DESIGN AND CONTROL OF A COMPACT 6-DEGREE-OF-FREEDOM

PRECISION POSITIONER WITH LINUX-BASED REAL-TIME CONTROL

A Dissertation

by

Ho Yu

Submitted to the Office of Graduate Studies of
Texas A&M University
in partial fulfillment of the requirements for the degree of

DOCTOR OF PHILOSOPHY

August 2009

Major Subject: Mechanical Engineering

DESIGN AND CONTROL OF A COMPACT 6-DEGREE-OF-FREEDOM

PRECISION POSITIONER WITH LINUX-BASED REAL-TIME CONTROL

A Dissertation

by

Ho Yu

Submitted to the Office of Graduate Studies of
Texas A&M University
in partial fulfillment of the requirements for the degree of

DOCTOR OF PHILOSOPHY

Approved by:

Chair of Committee,	Won-jong Kim
Committee Mmbers,	Alan Palazzolo
	Bryan Rasmussen
	Hamid A. Toliyat
Head of Department,	Dennis O'Neal

August 2009

Major Subject: Mechanical Engineering

ABSTRACT

Design and Control of a Compact 6-Degree-of-Freedom Precision Positioner with Linux-

Based Real-Time Control.

(August 2009)

Ho Yu, B.S., Hanyang University, Seoul, Korea;

M.S., Texas A&M University, College Station

Chair of Advisory Committee: Dr. Won-jong Kim

This dissertation presents the design, control, and implementation of a compact high-precision multidimensional positioner. This precision-positioning system consists of a novel concentrated-field magnet matrix and a triangular single-moving part that carries three 3-phase permanent-magnet planar-levitation-motor armatures. Since only a single levitated moving part, namely the platen, generates all required fine and coarse motions, this positioning system is reliable and potentially cost-effective. The three planar levitation motors based on the Lorentz-force law not only produce the vertical force to levitate the triangular platen but also control the platen's position and orientation in the horizontal plane. Three laser distance sensors are used to measure vertical, x-, and y-rotation motions. Three 2-axis Hall-effect sensors are used to determine lateral motions and rotation motion about the z-axis by measuring the magnetic flux density generated by the magnet matrix.

This positioning system has a total mass of 1.52 kg, which is the minimized mass to produce better dynamic performance. In order to reduce the mass of the moving platen, it

is made of Delrin with a mass density of 1.54 g/cm³ by Computer Numerical Controlled (CNC) machining. The platen can be regarded a pure mass, and the spring and damping effects are neglected except for the vertical dynamic. Single-input single-output (SISO) digital lead-lag controllers and a multivariable Linear Quadratic Gaussian (LQG) controller were designed and implemented. Real-time control was performed with the Linux-Ubuntu operating system OS. Real Time Application Interface (RTAI) for Linux works with Comedi and Comedi libraries and enables closed-loop real-time control.

One of the key advantages of this positioning stage with Hall-effect sensors is the extended travel range and rotation angle in the horizontal mode. The maximum travel ranges of 220 mm in x and 200 mm in y were achieved experimentally. Since the magnet matrix generates periodical sinusoidal flux densities in the x-y plane, the travel range can be extended by increasing the number of magnet pitches. The rotation angle of 12° was achieved in rotation around z. The angular velocities of 0.2094 rad/s and 4.74 rad/s were produced by a 200-mm-diameter circular motion and a 30-mm-diameter spiral motion, respectively. The maximum velocity of 16.25 mm/s was acquired from over one pitch motion. The maximum velocity of 17.5 mm/s in a 8-mm scanning motion was achieved with the acceleration of 72.4 m/s². Step responses demonstrated a 10-µm resolution and 6-µm rms position noise in the translational mode. For the vertical mode, step responses of 5 µm in z, 0.001° in roation around x, and 0.001° in rotation around y were achieved. This compact single-moving-part positioner has potential applications for precision-positioning systems in semiconductor- manufacturing.

of Him,

by Him,

and

for Him.

ACKNOWLEDGMENTS

Dr. Kun Ji, and Youngchul Na was essential for me to set up the Linux-RTAI-Comedi environment.

I would like to give my special thanks to my parents Mr. Seok-jong Yu and Mrs. Insun Kim for loving me forever.

TABLE OF CONTENTS

LIST OF TABLES

LIST OF FIGURES

FIGURE   Page

FIGURE
Page

FIGURE   Page

CHAPTER I

INTRODUCTION

1.1 Precision Motion Control

In modern nanoscale and microscale engineering applications, high-precision motion control is a key component for wafer steppers, surface profilometers, magnetic suspension stages, and scanned-probe microscopes. The research presented in this dissertation could be applicable to the wafer stepper stage in semiconductor manufacturing. The wafer stepper in semiconductor manufacturing is the crucial piece of equipment for photolithography-based processing. The step-and-repeat motions in the wafer stepper are the basic movements generated by the positioner. An optical source emits a deep ultraviolet (DUV) beam to a die site on the wafer through a photomask or reticle. The motion process in the wafer stepper stage requires not only the high resolution and precision, but also the multi-dimensional motion with large travel range and high control bandwidth [1–4].

A planar motor can be used as a good application for the wafer stepper stage. The advantage of a planar motor is that the multi-dimensional motion with large travel range can be provided with high precision. The Sawyer motor is the main type of the planar motor commercialized by Northern Magnetics and Megamation [5]. Features of the Sawyer motor are that the two-phase full-step is as coarse as the order of 250 µm and the

---

This dissertation follows the style and format of *IEEE Transactions on Automatic Control.*

position repeatability is as good as 5 µm. The Sawyer motor requires a tight air gap of less than 25 µm, so it should be operated with an ultrafine motor surface finish with precisely manufactured teeth. A drawback of the sawyer motor is that it has large the attractive force of 1800 N, large cogging force, and heating issues [6]. For instance, IBM printed-circuit-board assembly line uses Magamation's *x-y* stage, which has the order of 25 µm accuracy. Hinds, Nocito, and Pelta created an advanced model of the Sawyer motor for the purpose of the wafer stepper stage [7–8]. In this advanced design, the planar motor features permanent-magnet cubes as a stator, rather than the iron protrusions in the base plate of Sawyer motor. The first permanent-magnet planar motor that is orthogonally superimposed two conventional one-dimensional magnet arrays was proposed by Asakawa [9–10]. The magnetic levitation precision positioning stage presented in this thesis uses a stator of the superimposed Halbach magnet-matrix array, and a synchronous permanent-magnet planar motor (SPMPM), which has an advanced dynamic ability rather than the Sawyer motor or traditional permanent-magnet planar motors [11–18].

The laser interferometer is a conventional sensor for positioning devices that require high precision. The high resolution and low position noise on the sub-nanometer order is ideal for the precision positioning [1–4]. However, the laser interferometer has several drawbacks such as cost, complicated components, and limitations in its rotational sensing range. Since the laser beam is reflected by a mirror, the receiver easily loses the incoming beam when the stage exibits a big rotation angle. In addition, the maximum travel range is regulated by the size of the reflection mirror which needs to have very fine finish. Therefore, we propose using Hall-effect sensors for the multi-dimensional positioning

system in this research. It is not only the cost-effective, but also capable of large rotation motion with the good position resolution [19]. The precision positioner presented in this dissertation uses two-axis Hall-effect sensors for lateral motion in x and y and rotation about z with the positioning resolution on the order of micrometers. The vertical motions are detected by laser distance sensors (Nanogage 100). The SPMPMs as actuators in the positioner overcome the shortcomings of traditional planar motors [1–3]. Linux-based real-time control with RTAI and Comedi is used for performing the control algorithm.

1.2 Traditional Positioning Systems

Positioning stages are commonly used in motion control. The industry uses various different types of positioner to meet the requirement of positioning systems. For example, linear motor stages, which generate single-axis motions, are used in the applications that require one-dimensional motion. Positioning stages that use several actuators can generate multi-dimensional motions. In addition, rotation motions can be generated by rotary actuators. Positioning stages are classified by their required motion range and accuracy such as being a long-range scanning positioner or a high-precision positioner. Generally there are two types of the conventional positioners, which are crossed-axis-type gantry-type positioners [20–21]. A crossed-axis positioner has the stage axes on top of one another. The stepper motors as the actuator usually control the moving frames. To minimize the mechanical friction, some positioners employ air bearings, which require indispensable additional components. Figure 1-1 (a) and (b) show the conventional crossed-axis type positioners manufactured by Dnaher Motion and Aerotech, respectively.

<center>(a)   (b)</center>
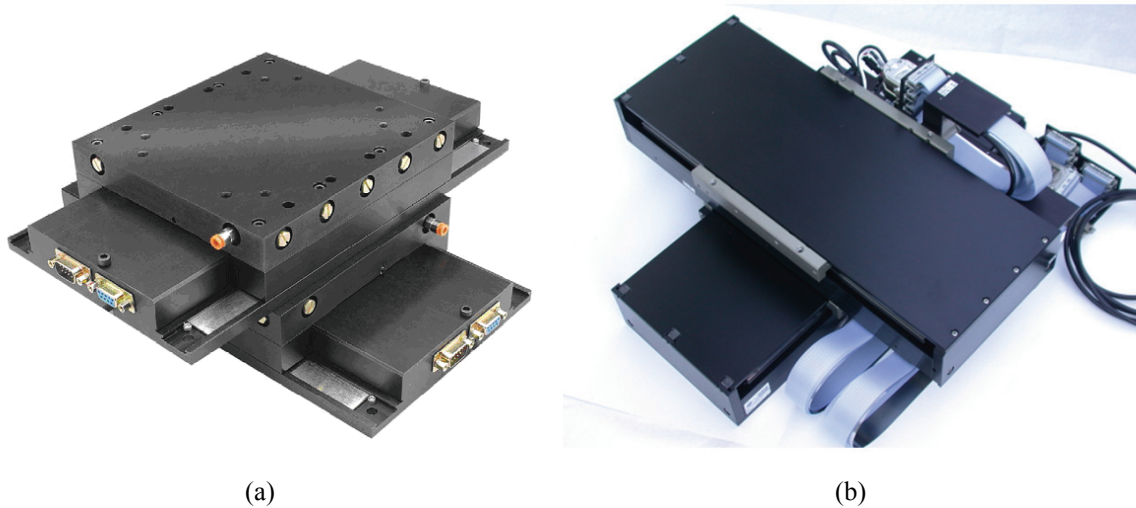
Figure 1-1: Crossed-axis type positioners (After (a) Danaher Motion [22] and (b) Aerotech corp. [23])

Gantry-type positionsers have a bridge-like frame shape and the positioner is contolled by actuators located at the end of the frame. This kind of positioner is used in scanners and plotters that do not require high precision motion control. Figure 1-2 presents a gantry type positioner of a robotic antenna stage in an anechoic chamber. Traditional positioners suffer from significant drawbacks including not being able to inherently generate rotational motions and the manufacturing cost is very high with respect to the mechanical bearing tolerance, which should be very accurate in the high precision motion generation. In addition, they need extra mechanical devices for an additional axis motion control. Although rotational motions could be produced by additional mechanical devices in Figure 1-3, the whole positioner's machine structure would be very complicated and bulkier since each axis of motion requires a dedicated actuator. As a consequence, a traditional positioning system could exhibit dynamic couplings, the lower operating speed, and be difficult to control [24].
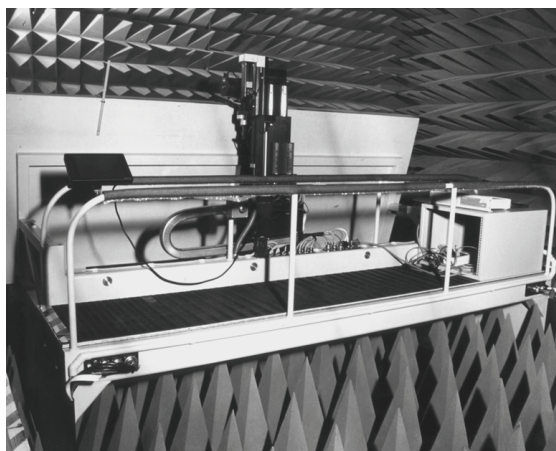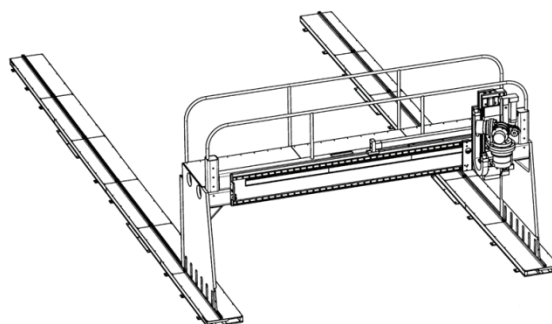
<div align="center">(a)   (b)</div>

Figure 1-2: Gantry type positioner of a robotic antenna stage in an anechoic chamber: (a) photograph and (b) schematic view [25]
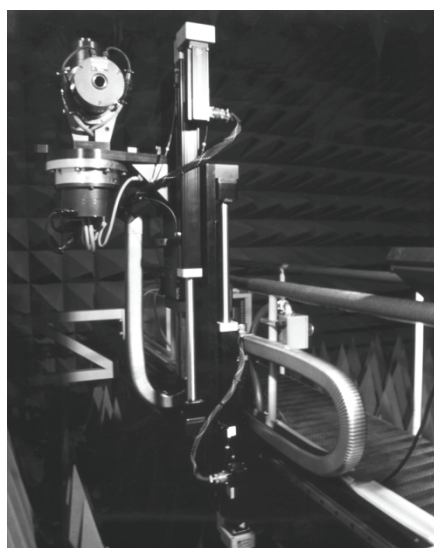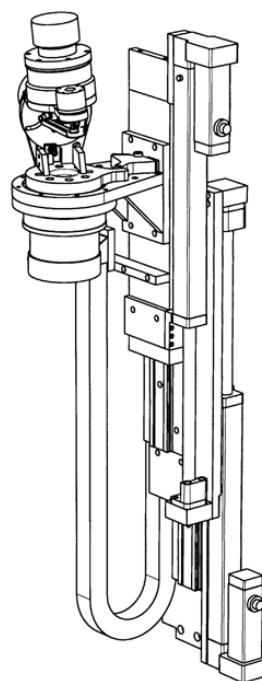
<div align="center">(a)   (b)</div>

Figure 1-3: Rotary type positioned: (a) additional rotary device in an anechoic chamber and (b) a schematic view [25]

1.3 Planar Motors and Magnetic Arrays

The crossed-axis-type, gantry-type, and rotary-type structures are commonly used methodologies to construct a precision positioning stage so far. As mentioned in the previous section, traditional stages use conventional actuators such as stepper motors and rotary motors, which can provide a single axis motion. Otherwise planar motors compared to the traditional actuators have the advantage of generating multi-dimensional motions. In addition, it can perform high-precision motion control by the levitation technology. Thanks to their single-moving frame, simpler structure, more compact body size, and the low manufacturing cost, planar motors are expected to be widely used in the planar positioning industry.

There are generally three types of planar motors such as variable-reluctance type, permanent-magnet matrix type, and induction type [26–30]. The permanent-magnet matrix type planar motor will be discussed in the following sub sections. Instead of using many salient teeth and iron protrusions in variable-reluctance (VM) motors such as the Sawyer motor, the planar permanent-magnet motors use the magnet matrices that generate magnet flux densities in the base plate. There are many kinds of magnet matrix designs that are proposed so far for planar permanent-magnet motors [31]. Figure 1-4 shows examples of the magnet matrices. The first magnet matrix proposed by Asakawa is in Figure 1-4 (a) [32]. It is direct superimposition of two orthogonal magnet arrays. Blank spaces represent the non-magnetic volume. Chitayat improve the magnet packing density from Asakawa's matrix by constructing the magnets in diagonal direction in Figure 1-4

(b). Magnet matrices by Ebihara et al. [15] and Cho et al. [33] are presented in Figure 1-4
(c) and (d), respectively.

(a)   (b)

(c)   (d)
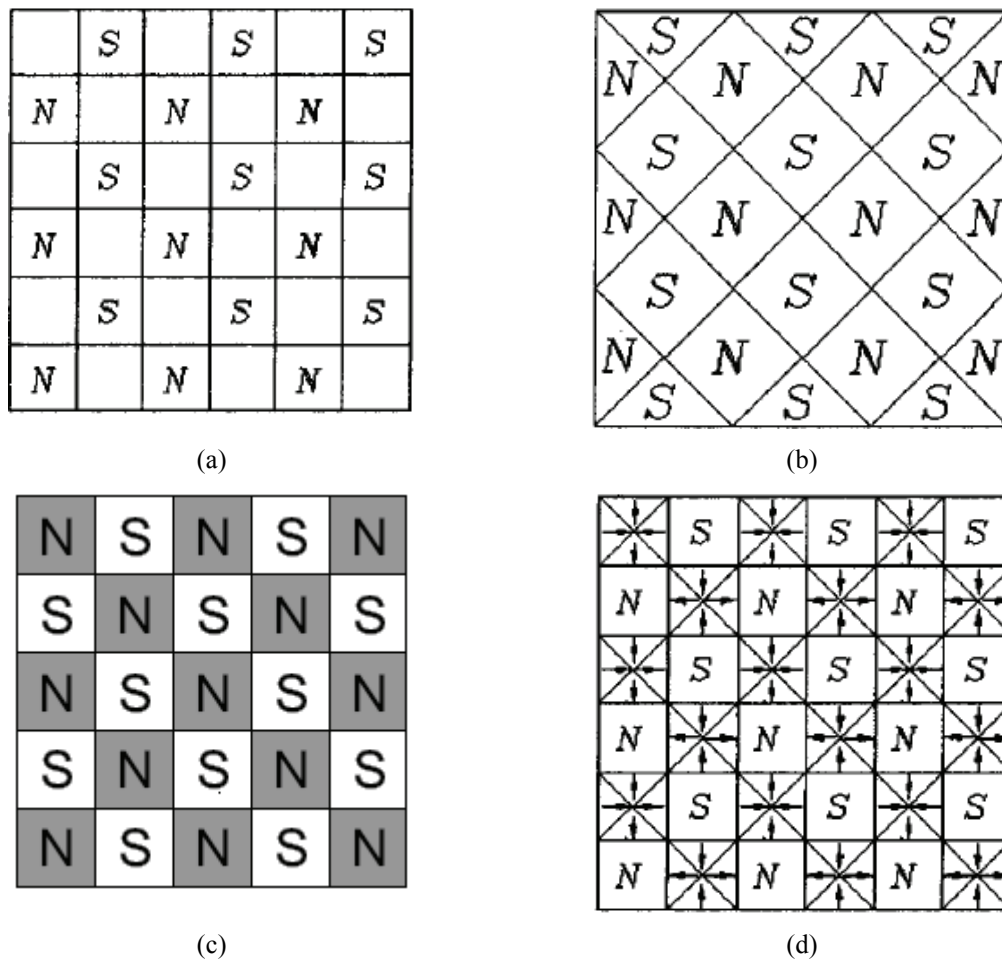
Figure 1-4: Conventional permanent magnet matrices. (a) Asakawa, (b) Chitayat, (c) Ebihara, and (d) Cho
[33]

Figure 1-5 presents the concentrated-field magnet matrix by Trumper et al. [34]. It
consists of two orthogonal Halbach magnet arrays that produce the constant magnetic
field for the synchronous permanent magnet planar motors (SPMPM). The compact-sized
multi-dimensional positioner was developed with this magnet matrix. The specification

and analysis of the Halbach magnet array and the superimposed concentrated-field magnet matrix will be discussed in Chapter II [35].
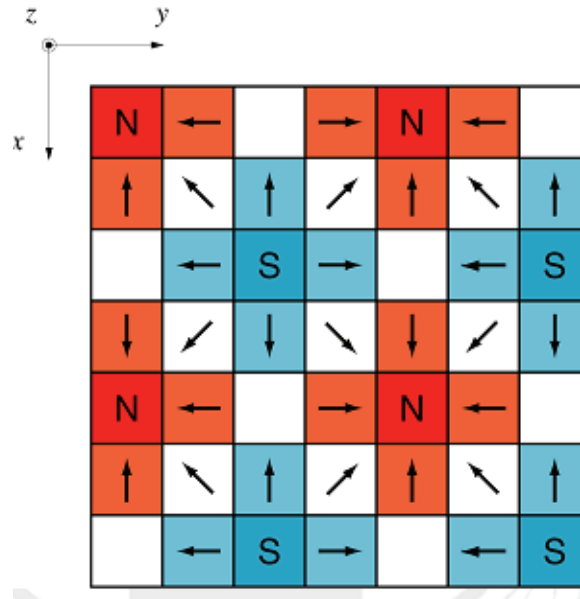
Figure 1-5: Concentrated-field permanent-magnet matrix [34]

1.4 Precision Positioning Stages

This section introduces several case studies of the precision positioning system. Prior to the planar motion stage, the linear position stage is introduced. The linear stage has a simpler design structure operating with a single axis than that of the planar stage, which generates multi-axis motions. Planar motion stages based on linear motors can generate multi-axis motions in a single frame, which has a simpler and more cost-effective design than those of traditional positing systems. In addition, piezoelectric materials can be used for the precision positioning stages. A flexure-based *xy* positioning stage with piezoelectric stacks is introduced in the last section.

1.4.1 Direct-drive Linear Brushless Permanent-Magnet Motor

Linear actuators used so far are of the hydraulic or pneumatic types, which are good for the applications requiring large force with respect to the small size. However, these actuators do not provide precision motion control. For the precision, the electric rotary motors are used with additional devices such as lead screws or linkages to convert the rotary motion to linear translation. This structure also has problems of a mechanical backlash and bulkier size by supplementary devices [36]. Hence, Kim and Murphy researched the tubular linear brushless permanent-magnet motor (LBPMM) for precision linear motion control, which is comprised of permanent magnets and current carrying coils [36–39]. Figure 1-6 (a) presents the experiment setup of tubular linear motor mounted on a precision optical table. The linear variable differential transformer (LVDT), which reads the position signal is connected to the linear motor. The LVDT consists of a single primary coil of wire with secondary coils placed on either side of the primary coil.
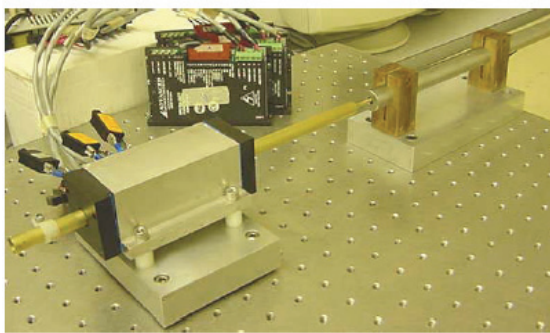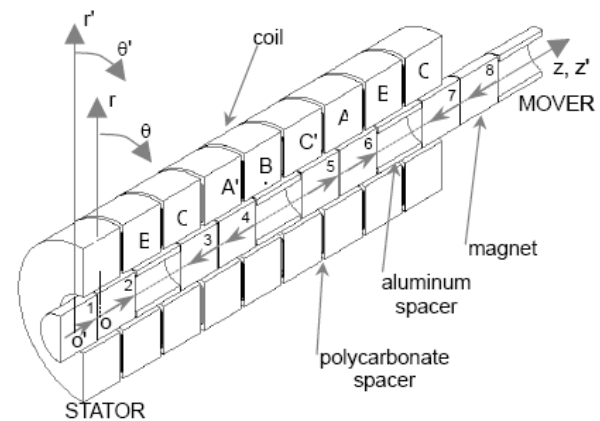
(a)   (b)

Figure 1-6: Tubular linear permanent-magnet motor: (a) photograph of an experimental setup and (b) sectional view of coils and magnets [36]

The analog position outputs from the LVDT flow to the digital signal prossesing (DSP) controller board through the conditioning circuit, a anti-aliasing filter, and the analog-to-digital converter. The LVDT features the analog output swing of 0–5 V, travel range of 10 cm, and the noise of 10 mV rms. The motor shows a rise time of 30 ms, a settling time of 60 ms, and 25% overshoot in the 5-mm step response. The maximum speed of 1.5 m/s and acceleration up to 10 g were acquired. It has a 10-cm travel range with respect to the LVDT and 26-N pull-out force. The advantage of the LBPMM is the compact size that is suitable for the robotic applications requiring moderate force and precision.

1.4.2 Magnetic Transportation Vehicle

The advantage of a magnetic levitation system is that it is contactless between the moving frame and the ground so it does not cause any friction, wear, and disturbances. Therefore, the system not only requires no lubricant, but can also generate fast speed and accurate motions. Applications of the magnetic levitation methodologies can be generally classified in two ways: One is precision positioning stages that use the high accuracy in the contactless frame. Another is maglev trains that take advantage of a fast speed without friction. This research introduces the latter case for the maglev trains. Former research of the maglev trains were commonly performed with the object of attaining high power and high speed, however they needed to move along a guide track or sidewall. So, Park and Beak proposed a maglev planar transportation vehicle (MPTV) [40]. Its goals were to achieve planar motions with high levitation, propulsion power, and to acquire a wide working range.
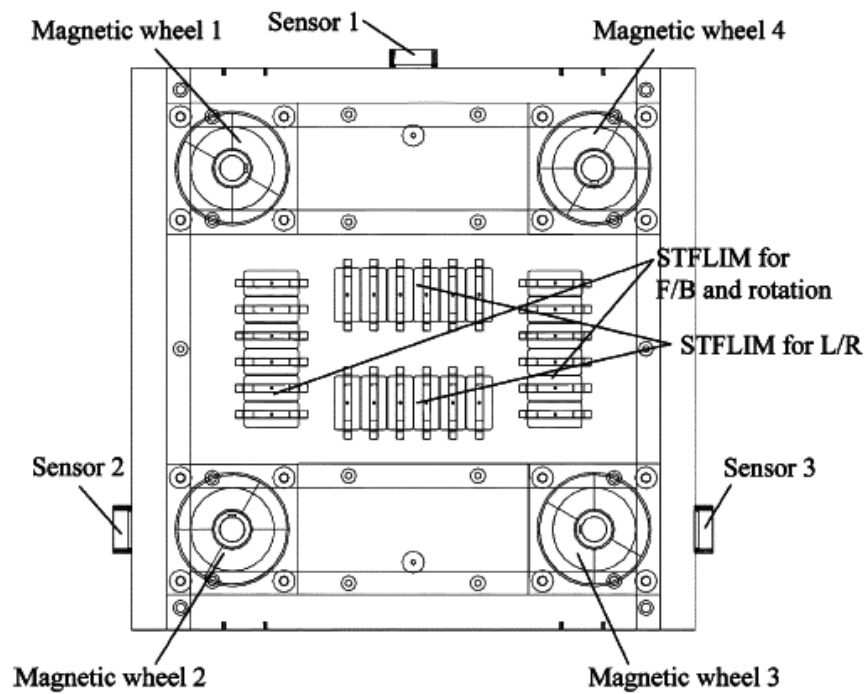
(a)
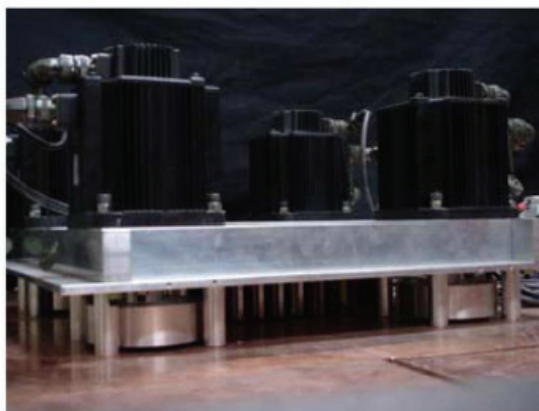
(b)
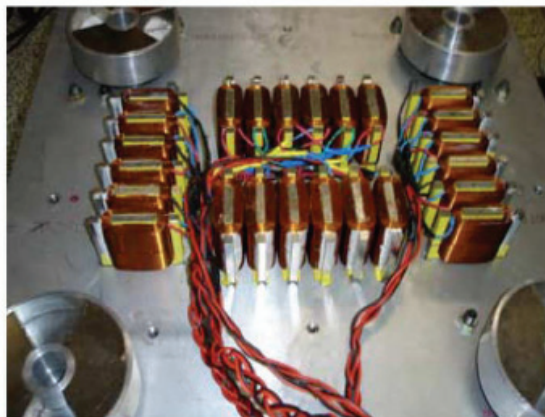
(c)

Figure 1-7: Two-dimensional maglev planar transportation vehicle; (a) schematic view, (b) side view, and (c) bottom view [40]

The schematic diagram of MPTV is shown in Figure 1-7 (a). It consists of four magnetic wheels with rotary machines for the levitation in Figure 1-7 (b) and four sets of single-side transverse flux linear induction motors (STFLIM) for propulsions in Figure 1-7 (c). The magnetic force is generated by rotating the magnetic wheels 1 and 3 in counterclockwise and the magnetic wheels 2 and 4 in clockwise at the same time with the same speed [41–45]. The different direction of motor rotations compensates for the net rotational moments of the MPTV. For the propulsions, two sets of STFLIMs are employed for the left and right motions, as well as the two sets of STFLIMs take charge of forward/backward (F/B) motions and rotation of the MPTV with two independent controllers. The size of MPTV is $770 \times 770 \times 384$ mm and it has a total mass of 170 kg. The MPTV can generate the maximum payload of 79 kg at the 10-mm levitation height and 122 kg at the 8-mm levitation height. The performance of approximately a 3.6-m/s propulsion speed with a 80-kg payload was achieved. By increasing the conductor, the travel range can be extended widely.

1.4.3 Philips Inverted Maglev Stage

The inverted planar maglev stage by Philips Applied Technology shown in Figure 1-8 is introduced in this section. The targets of stage development research are Extreme Ultra-Violet (EUV) lithography, nano-imprint lithography, and optical inspection. Figure 1-8 (a) and (b) shows the overall precision positioning stage views. The maglev stage adopted the fixed coils method referred to as "inverted" with Lorentz actuators that provide the motive forces. The moving coil type systems that carry the windings on the moving frame are called "conventional." Checker-board-pattern permanent magnets are l-

(a)   (b)
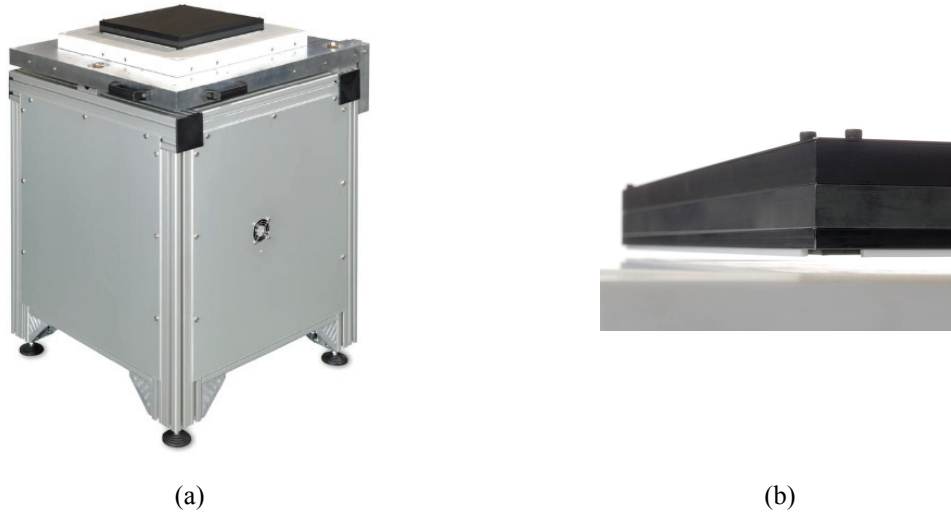
Figure 1-8: Magnetic levitation positioner by Philips [44]

ocated at the free-floating platform, and the fixed bed houses the coils. The load distribution over the coil of the inverted stage is not identical by the location of the positioner. On the other hand, the conventional stage carries an equal load over all the workspace, in spite of attached umbilical cables that support the power to the coils. In comparison, since the inverted stage's coils are embedded on the frame, the platen's moving is completely unrestricted. Philips Applied Technologies' engineers spent almost a decade developing control software "Soft Motion." The software pursuing efficient algorithms enables the maglev positioner to move in six axes with high precision. The metrology for the inverted planar stage is Hall sensors, which provide a positional accuracy of ±1 mm. For the practical stages, laser interferometer-based metrology and further software development will be developed [46].

1.4.4 Moving-Magnet Planar Actuator

Another moving magnet stage similar with the Philips precision positioning system is presented in this section. Jansen et al. proposed the moving magnet planar actuator as shown in Figure 1-9 (a) [47–50]. The motor stator is comprised of 84 coils with concentrated windings that are fixed on the machine frame and 24 coils are energized at the same time. The mover has a Halbach permanent-magnet array on the bottom place. The sets of active coils are changed with the location of the positioner during translations. The coils below and near the edge of the Halbach magnet array can only generate significant force and torque. Figure 1-9 (b) presents the switching mode between coil sets that change the mover's position. The active coils are represented dark gray, and it turns to the light gray as the positioner moves. In this example, between 15 and 24 coils are ac-

(a)   (b)
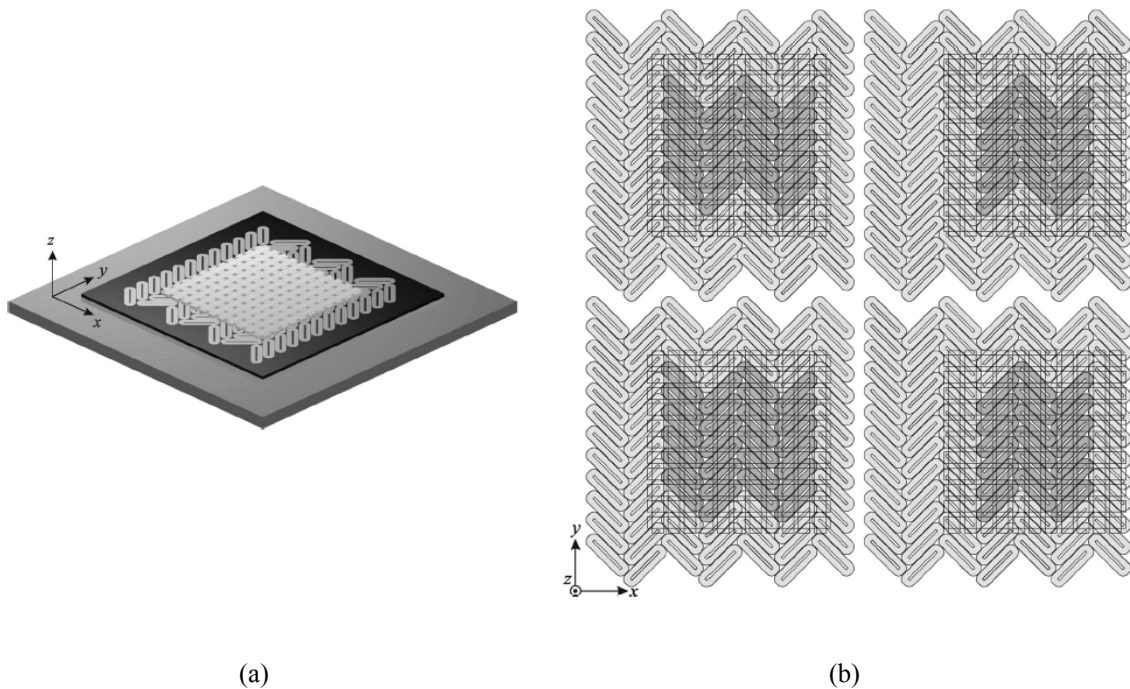
Figure 1-9: (a) Overview of the moving-magnet planar actuator and (b) active coils in translational motion [47]

tive by the location of mover. The rectangular-shaped coils on the bottom plate are placed in a herringbone pattern as illustrated in Figure 1-10 (a). Each coil is shifted over *cw* in both *x*- and *y*-directions. The dark gray coil group and the light gray coil group in Figure 1-10 (a) produce a position-independent force vector in the *yz* plane and in the *xz* plane, respectively. Figure 1-10 (b) shows the photograph of the planar actuator and measurement frame. The translator has a size of 300 × 300 mm in *xy* and the total mass of 8.2 kg. Eight eddy-current sensing probes measure the position displacements. The planar actuator has the travel range of 230 × 230 mm in *xy,* mechanical clearance of 1–2 mm. rotation angle of ±3 mrad, maximum speed of 1.4 m/s, and maximum acceleration of 14 m/s². The tracking error of the planar actuator is 30 μm in translation and 100 μrad in rotation.

| (a) | (b) |
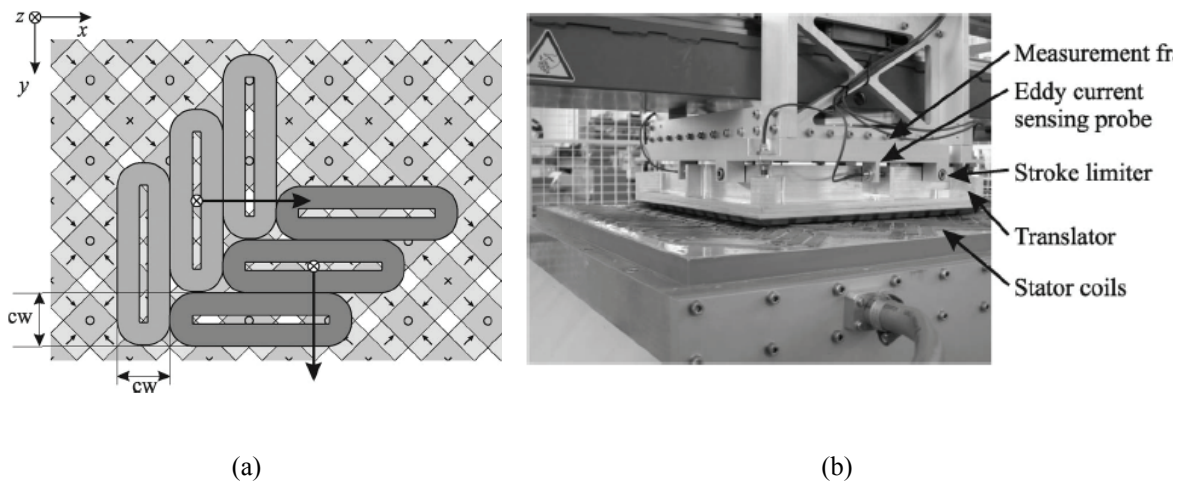
Figure 1-10: (a) Bottom view of a Halbach magnet array and two coil sets in a herringbone pattern and (b) photograph of the planar actuator and measurement frame [47]

1.4.5 Planar Actuator with Large Yaw Motion

Planar actuators that are being recently studied have a single moving frame providing multi-axis motions [51–54]. These planar actuators providing direct drive with multiple directional motions have the advantages of a simple structure, compact body size, and the effective energy consumption [55–57]. In precision positioning stages with planar actuators, however, controlling large yaw and translation simultaneously is not easy, because of the topologies of magnet array and sensors. Hence, Ueda and Ohsaki proposed a three-degree-of-freedom planar actuator with a small mover traveling large yaw and translational displacements [58]. Figure 1-11 (a) presents the fundamental structure of the planar actuator. The mover consists of two-dimensional Halbach magnet array that is free from wires in Figure 1-11 (b) [59]. The dimension of mover is 30 × 30 × 6 mm and the total mass is 37.3 g. Since the Halbach magnet array generates a quasi-sinusoidal and high flux density distribution on a single side, the actuator with Halbach magnet array can produce a large electromagnetic force with small force ripples [59–60]. Two sets of air-core three-phase armature conductors as stators are placed on a double-layered printed circuit board. The trusts in x and y can be generated independently and yaw directional torque is generated by the phase difference between the flux densities in the armature conductors. The d- and q-axis currents generate flux densities to produce proportionally the thrusts and torques. The perpendicular angle makes each axis operate independently. The paper proposed the decoupling control for the thrusts and torques. The planar actuator shows the 20-mm displacement in x- and y-directions, as well as 10° displacement in ϕ.

(a)　　　　　　　　　　　　　　　　　　　　　(b)
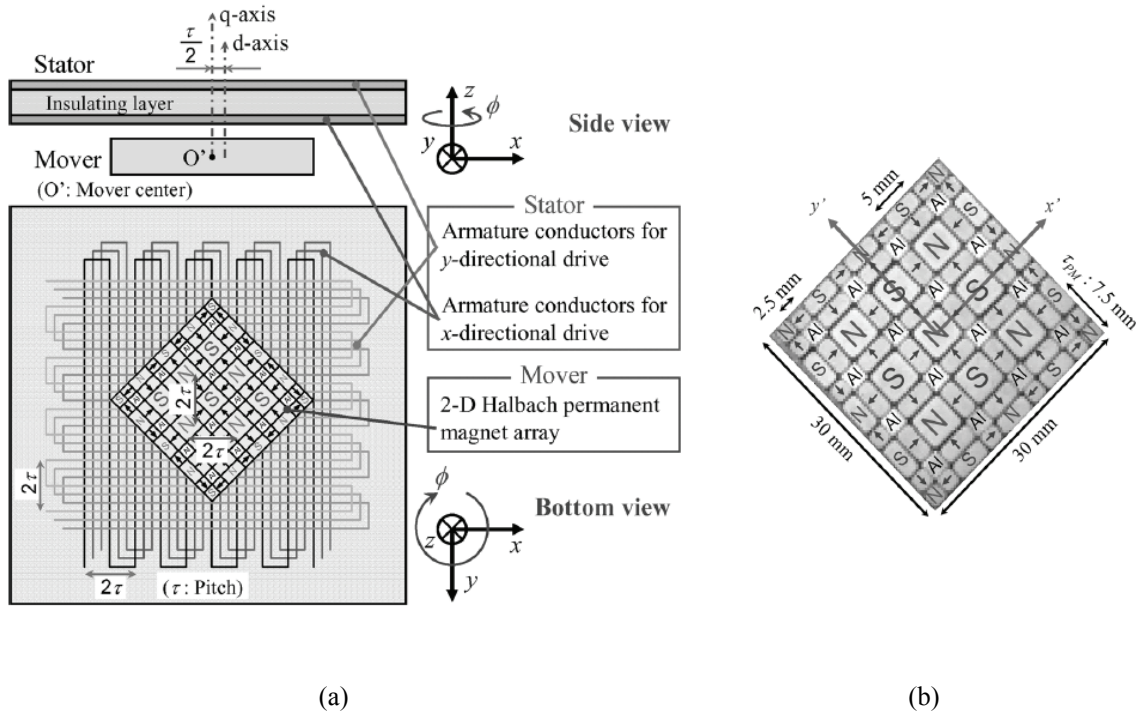
Figure 1-11: Planar actuator with a small mover: (a) fundamental structure and (b) the Halbach permanent-magnet array [58]

1.4.6 Piezoelectric Positioner

In precision-motion-control applications such as scanning-probe microscopy, lithography, nanometrology, and beam steering for optical communication systems, the actuator may contain piezoelectric materials [61–63]. Young et al. proposed a flexure-based xy stage for fast nanoscale positioning [64]. In the scanning-probe-microscopy applications, piezoelectric-tube scanners are commonly used due to their low costs. However, piezoelectric-stack-actuated stages that have larger moving range, greater mechanical bandwidth, and lower cross-coupling between axes are being considered for future piezoelectric precision positioning stages. In [65–66], two piezoelectric stacks as actuators control the xy motions with elastic deformation of flexure beams as shown in Figure 1-12. The concept of flexible mechanisms (flexures) became the base of the

design of the flexure-based nanopositioning stage. The design consists of the outer and inner sections. The outer frame was designed to maximize the displacement of piezoelectric stack actuators. The inner frame was designed to minimize the coupling between axes. The advantage of this stage is that no moving and sliding mechanical joints exist. As a result, the mechanical structure can be free from the problem of wear, backlash, and friction. The piezoelectric stacks are commonly used as actuators to drive flexure-based stage, because they have capabilities of repeatable nanometer resolution with high bandwidth, as well as generating high forces and acceleration. The basic principle of xy motion generations are represented in Figure 1-13 (a) and (b). Two piezoelectric-stack actuators located perpendicular to each other provide flexure deformations that cause displacements in x and y, respectively. The simulation results performed by ANSIS in x and y are also presented in Figure 1-13 (a) and (b). Capacitive sensors in each axis are used for measurement of flexure displacement. This flexure-based precision stage has the moving range of 25 × 25 µm with a high scanning speed, h-
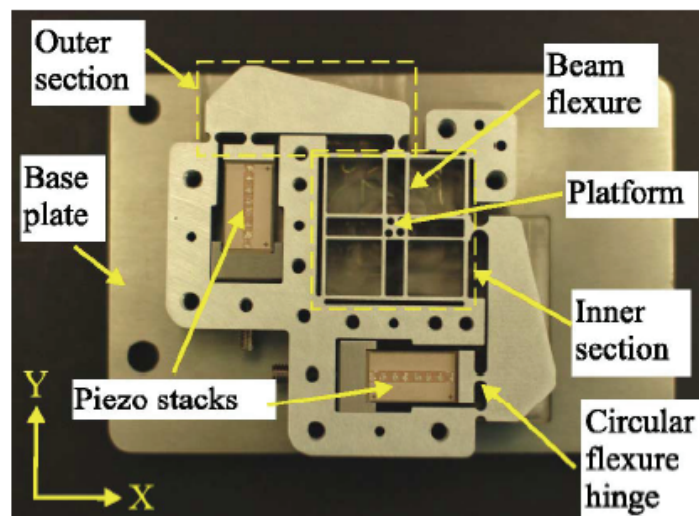
Figure 1-12: Flexure-based *XY* nanopositioning stage [64]

(a)   (b)
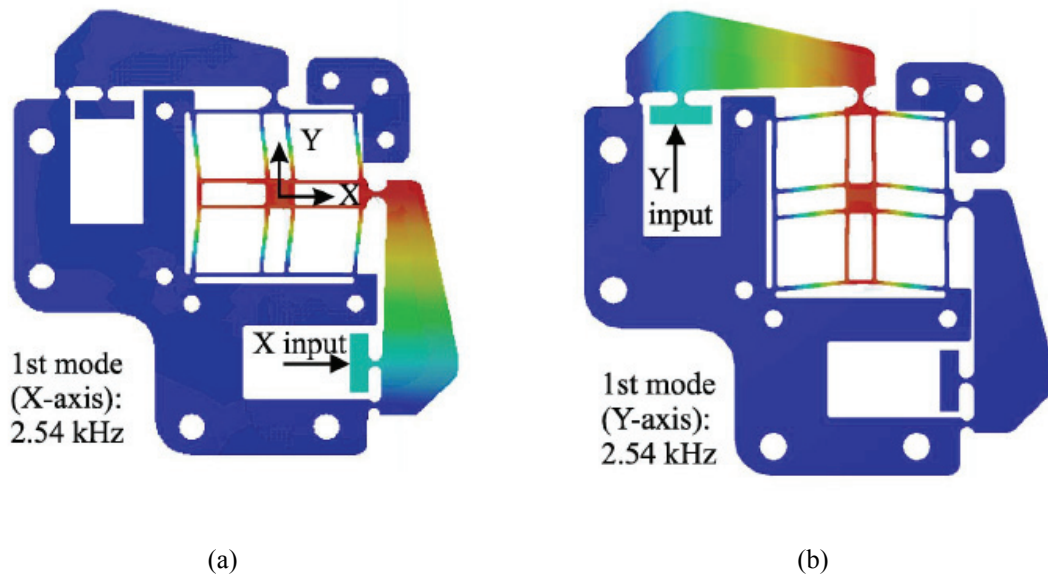
Figure 1-13: (a) ANSYS-based simulation in *x* and (b) in *y* [64]

igh resonance frequency of 2.7 kHz, 51-nm rms position error at 100 Hz, and low cross-coupling of −35 dB. Finite-element analysis (FEA) was used to determine the design factors such as resonant frequencies, travel range, and cross-coupling between axes [67–69].

1.5 Prior Arts

This section introduces several prior arts of precision positioning stages. First, Dr. Won-jong Kim's maglev stage, which has a rectangular moving frame with four linear motor sets is presented. The ATP stage researched by Tiejun Hu has different type stage from Dr. Won-jong Kim's. The triangular-shape moving frame carries three planar motors providing vertical and drive forces. Two compact maglev positioners studied by

Shobhit Verma are introduced. The ATP stage running solely on magnetic force and the Hall-effect sensor stage by Yusuke Kawato are also described.

1.5.1 High-Precision Planar-Maglev Stage

Figure 1-14 illustrates the planar maglev stage researched by Kim [3, 70–71] . This stage has capabilities of providing all the motions for the photolithography in semiconductor manufacturing. All 6-DOF motions can be generated with a single moving part in real-time control structures. This positioner is a moving-magnet type with the platen carrying Halbach magnet arrays on the bottom face. Four coil sets are attached to the fixed machine platform. Linear motors, which are the set of Halbach-type magnet array and the coil, can generate both suspension and drive forces. The advantage of a moving-magnet-type positioner is that the platen does not have umbilical cables or wires because all motor coil sets that require power sources are fixed on the machine frame. The overall mass of the platen including the magnet arrays is 5.6 kg. The levitation force against the gravity requires around 5.6 W at each motor. The rectangular shaped platen has four sets of the linear motor, in which two sets of motors are employed for the x-direction and the other two sets are employed for y-direction motion. The collaboration of four sets of linear motor generates the other 4-DOF. The travel range of 50 mm in x and y as well as 400 μm in z were achieved. For rotations, the positioner can provide milliradian-scale motions.

Figure 1-15 illustrates the laser interferometer setup for the maglev positioner. Laser interferometer setup consists of the laser head, beam splitters, beam benders, square mirrors, and receivers. Translations in 3-DOF are measured by the laser interferometers

with sub-nanometer resolution. The maglev stage has a position noise of 5 nm rms in x and y, as well as the acceleration of 10 m/s², was achieved at 50 Hz control bandwidth. The capacitance probes with nanometer resolution were used for the measuring of the vertical motions.
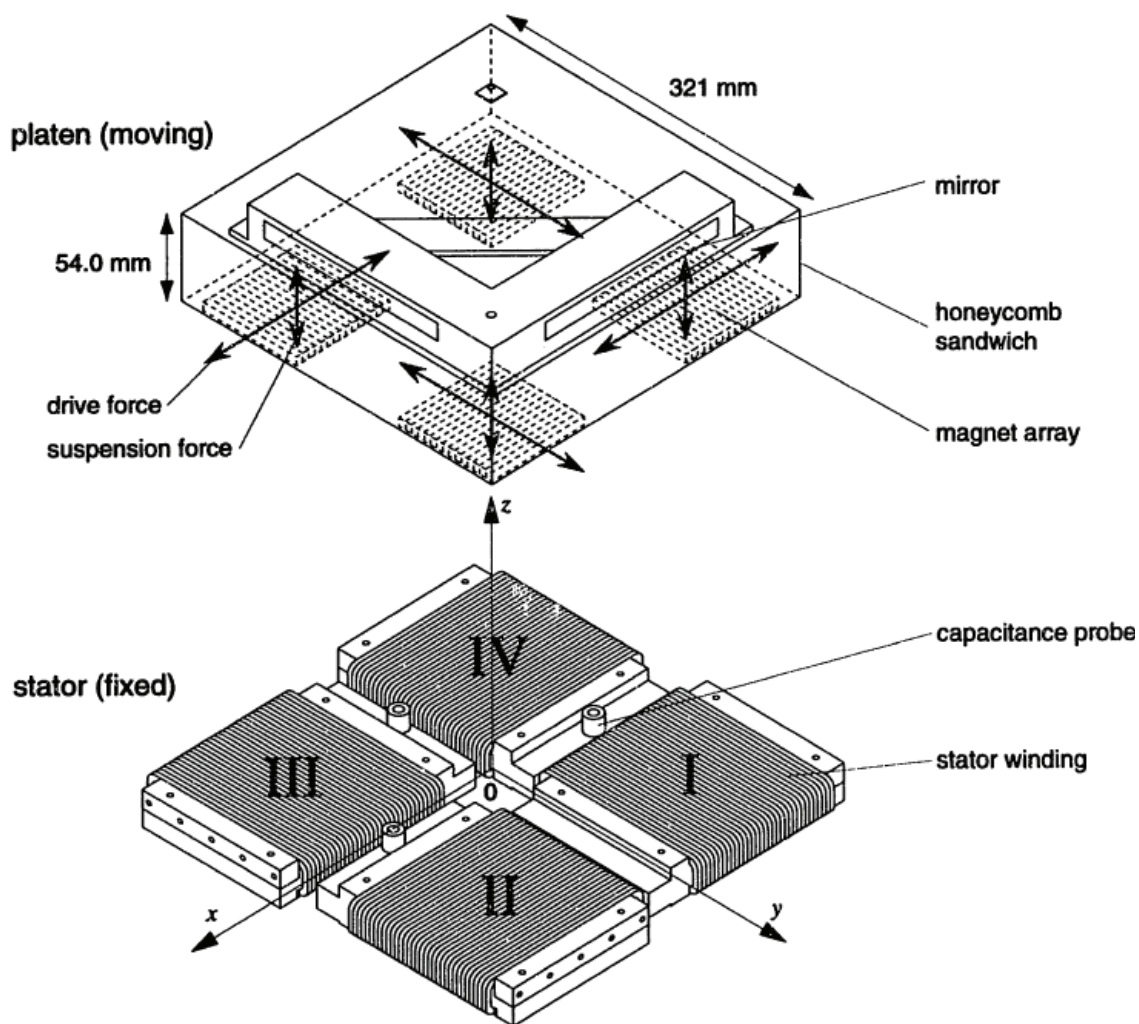
Figure 1-14: Planar maglev positioner [3]

Figure 1-15: Geometry of laser interferometer sensors [3]

1.5.2 Advanced Technology Program (ATP) Stage

Figure 1-16 shows the ATP precision positioning stage developed by Tiejun Hu, a former Ph.D student of Dr. Won-jong Kim [72–73]. It is a novel integrated 6-DOF high-precision positioning system consisting of a superimposed concentrated-field magnet matrix. Figure 1-16 (a) and (b) shows the top and bottom view, respectively. A triangular single-moving platen made of Delrin plastic carries three multi-phase windings, three aerostatic bearings for suspension, two stick mirrors for laser interferometers, and the three laser distance sensors for vertical movement. The total mass of the platen is 5.91-kg and the platen was run by three Synchronous Permanent Magnetic Planar Motors (SPMPM) on a patented concentrated-field magnet matrix with dimensions of 304.8 × 304.8 × 12.7 mm. The ATP stage used the laser interferometers shown in Figure 1-17 (a) for lateral position and velocity measurements. Since the laser interferometer is a relative position measurement device, the sensor data are calculated by the distance with respect to the initial position. The laser interferometer setup consists of the laser head in Figure 1-17 (b), the beam bender and splitter in Figure 1-17 (c), the interferometers and receivers manufactured by Agilent Technologies and the laser axis boards in Figure 1-17 (d). The prototype stage can generate the 20-nm positioning resolution and the 160 × 160 mm maximum travel range based on the VMEbus. The maximum velocity of 0.5 m/s and acceleration of 5 m/s² were generated. It can generate all 6-DOF, both fine and coarse motions with a single-moving frame [2].
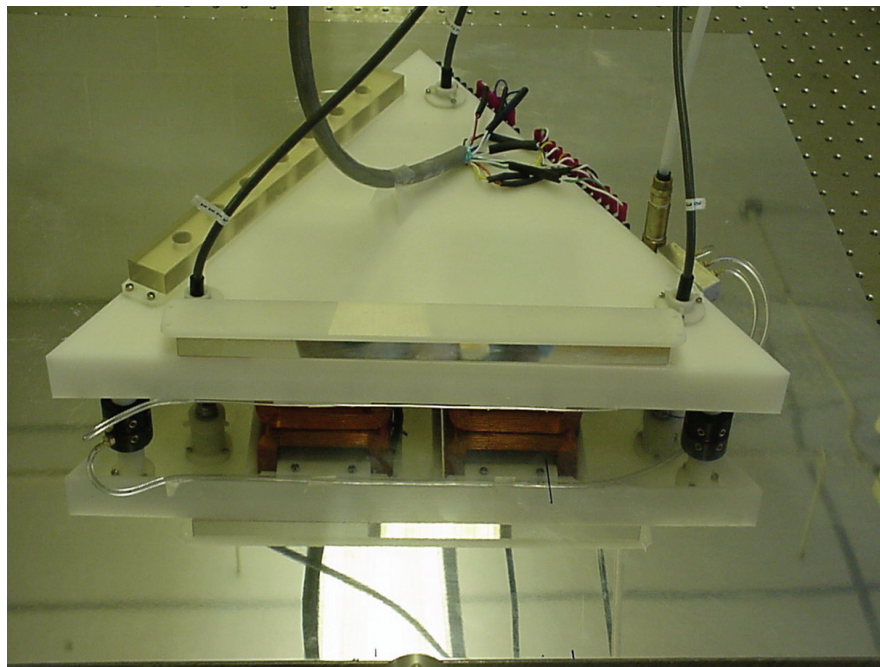
(a)
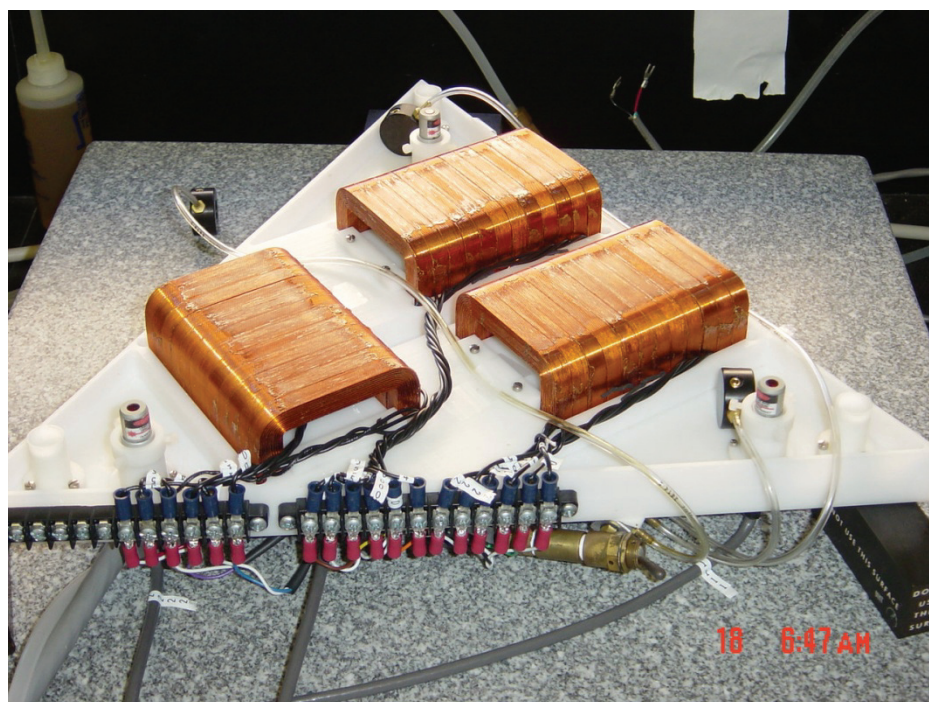
(b)

Figure 1-16: Advanced Technology Program (ATP) maglev stage [2]

(a)

laser interferometer for *x*   laser interferometers for *y* and ϕ

(b)   (c)   (d)
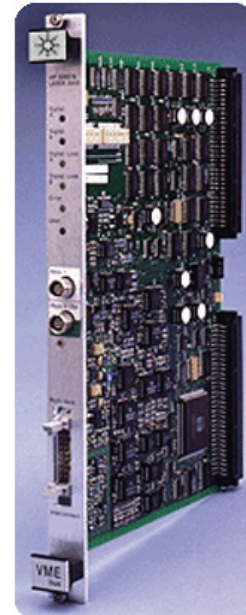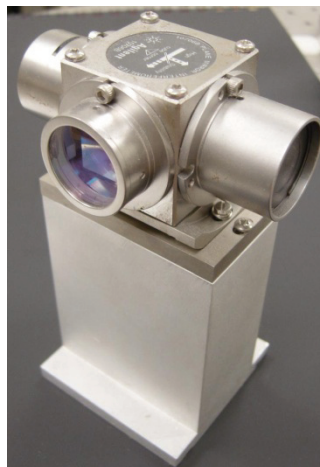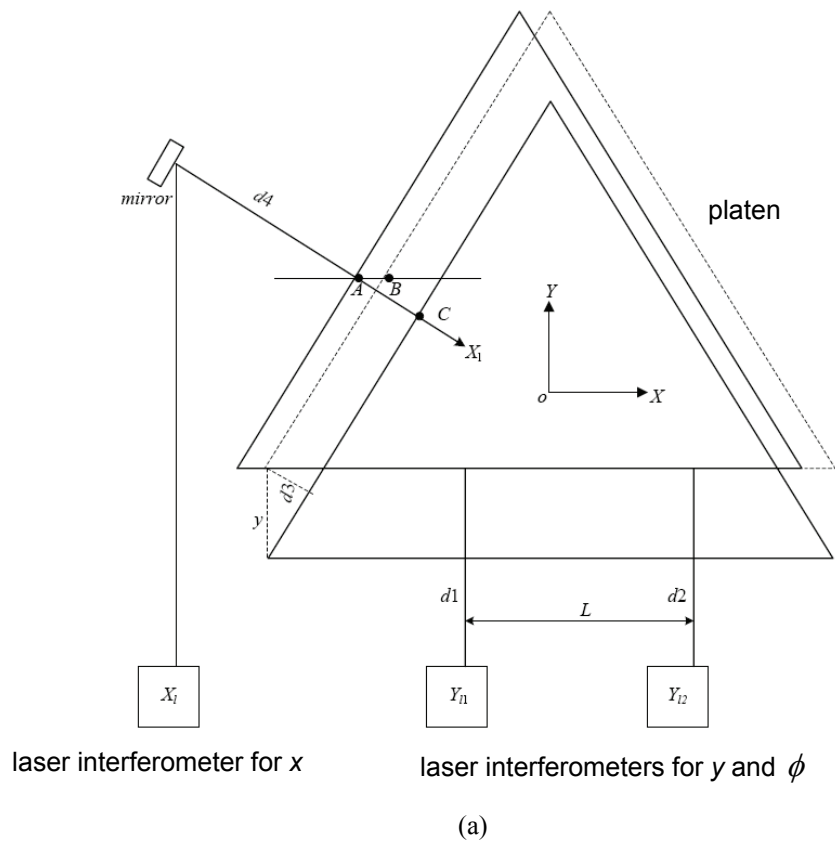
Figure 1-17: (a) Laser interferometer diagram [1], (b) laser head (HP 5517D), (c) beam bender (HP 10706B), and (d) VME bus laser-axis board (HP 10897B) (After optics and laser head data sheet of Agilent corp. an HP 10897 manual [74–75])

1.5.3 Compact Magnetic-Levitation Stage

The precision positioning stages researched by Shobhit Verma and Huzefa Shakir, former doctoral students of Dr. Kim, are introduced in this section [76–77]. The first stage is presented in Figure 1-18 (a), and its schematic view is in Figure 1-18 (b). The maglev stage used six single-axis actuators designed by Maheshwari [77], where the minimum number of actuators that can be generated 6-DOF. The actuator consists of a single magnet with a winding for vertical mode and two magnets with a winding for horizontal mode. The laser interferometers were used for the measurement in lateral motion and capacitace gauges were used in the vertical motion such as the levitation, roll, and pitch.

With the capacitance gauges, the capacitance between the probe and the positioner is measured and the distance to the target is calculated. The capacitance gauges, the ADE 2810 probe and 3800 OEM gauging module that have 1.3-nm resolution, manufactured by ADE technology was used in the experimental setup.

(a)   (b)
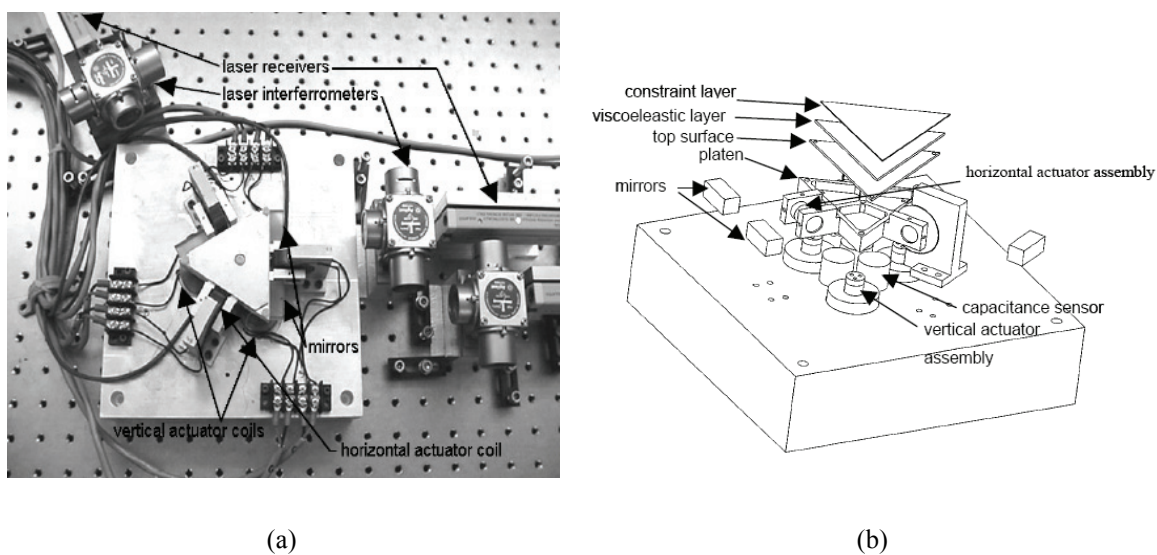
Figure 1-18: (a) The first-generation maglev stage and (b) its schematic view [77]

The capabilities of the first maglev stage are the position resolution of 5 nm and the position noise of 2 nm rms (root-mean-square). The maximum travel ranges are 300 μm in x-, y-, and z-direction and 3.5 mrad in rotations.

The second-generation maglev stage was fabricated by Verma. Figure 1-19 (a) and (b) show the photograph of the maglev stage and its schematic view, respectively. The overall shape of the stage had advanced to generate larger scale motions than those of the first stage. A single moving frame controls all 6-DOF motions. The difference in the mechanical frame compared to the first stage is that the second generation stage can be disassembled without any mechanical restrictions and generate large travel ranges in all axes, which are 15 times as wide as those of the first stage. The same methodologies of sensors were used with the first stage, such as the laser interferometers in horizontal motions and the capacitance gauges in vertical motions.

(a)   (b)
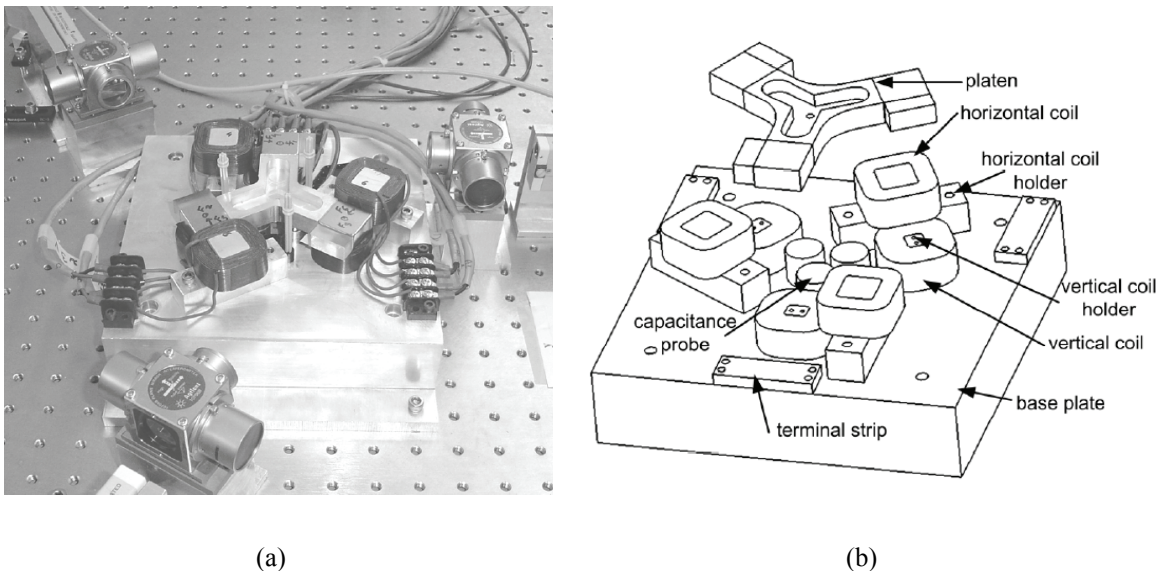
Figure 1-19: (a) The second-generation maglev stage and (b) its schematic view [77]

The mass of the platen is 0.267 kg and has the travel range of 5 × 5 mm in the *xy*-plane, 500 µm in *z*, and 0.1° in rotation. The advantage of the second-generation stage is not only that it has the extended travel range, but also its payload capacity, simplicity in mechanical design resulting in smaller number of mechanical parts than that of the first stage, and the its lower power consumption.

1.5.4 Maglev ATP Stage

My Masters research studied the magnetically levitated ATP stage [4]. Unlike the ATP stage, all 6-DOF motions are generated by magnetic forces. The overview of the maglev positioner is shown in Figure 1-20 (a) including three electromagnetic planar motors based on the Lorentz force law. Synchronous Permanent Magnet Planar Motors (SPMPM) not only produce vertical force to levitate the triangular platen but also control the platen's position and orientation in the horizontal mode. The experimental setup for the magnetic levitation and the levitation motion generation are shown in Figure 1-12 (b) and (c), respectively. Laser interferometers were used for the translations and the laser distance sensors were used for the vertical motions. The real-time digital controllers were designed and optimized for the positioner. The total mass of the platen is 5.91 kg, and it exhibits a maximum travel range of 120 mm × 120 mm in *x-y* plane and 100 µm in *z*. The position resolution of 20 nm and the position noise of 10 nm rms were demonstrated. The maglev positioner has the sub-microradian angular resolution around the *x*, *y*, and *z*-axes. A maximum velocity of 24.8 mm/s in *y* was achieved.
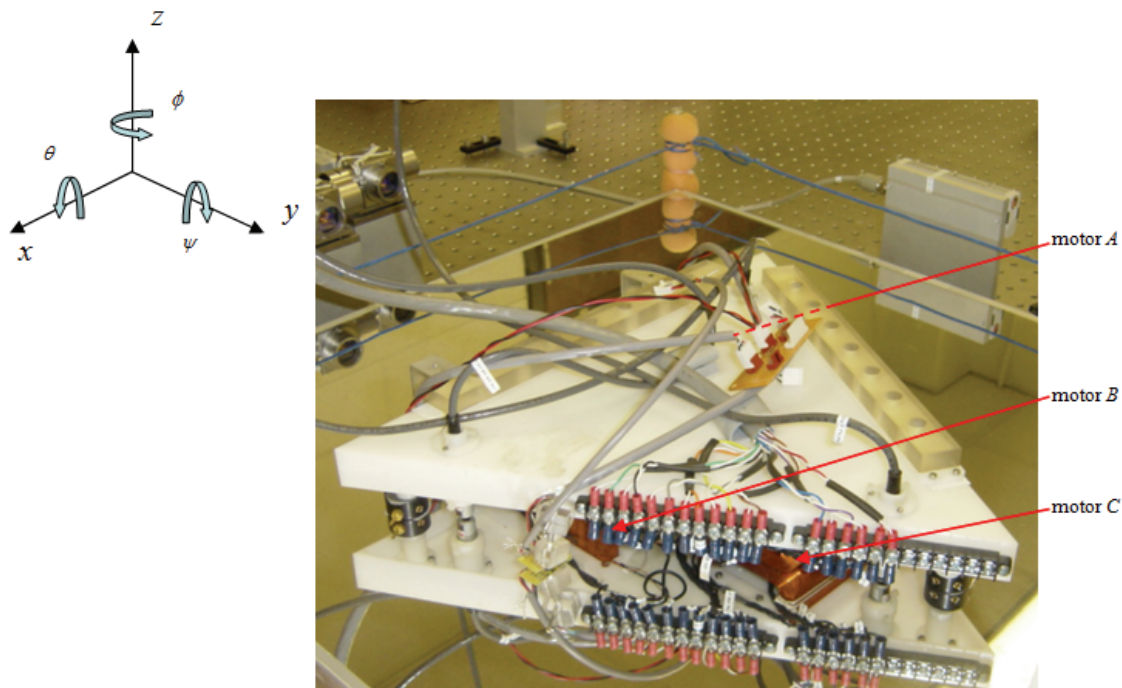
(a)
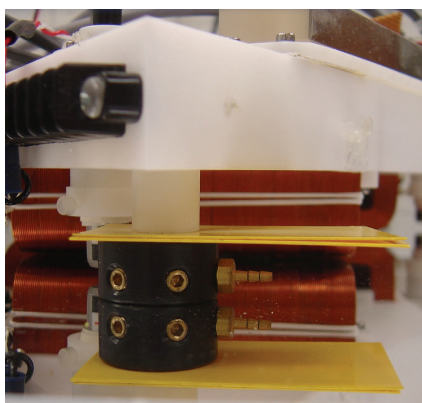
(b)
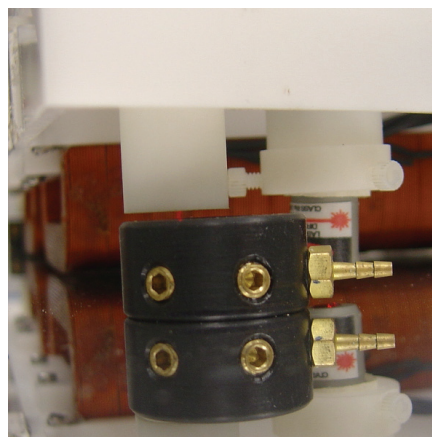
(c)

Figure 1-20: (a) A photograph of the 6-DOF maglev positioner with high precision. The triangular platen is placed on top of a mirror-finished aluminum plate. Beneath the aluminum plate is the concentrated-field magnet matrix. (b) Initial setting with two 0.04-inch-thick shims, and (c) under magnetic levitation without shims [4].

1.5.5 Multi-Dimensional Positioner with Hall-Effect Sensors

The last case study of the positioning system is the multi-dimensional positioner with Hall-effect sensors researched by Yusuke Kawato, a former master's student of Dr. Won-jong Kim [19, 78]. New sensing methodology for the precision positioner was introduced in this research. The overall view of the sensors mounted on the ATP stage is shown in Figure 1-21 (a) and Figure 1-21 (b) presents the closed-up view one of the Hall-effect sensors. For high precision positioning devices, laser interferometers, capacitance gauges, and the optical sensors are commonly used. These sensors have advantages of high resolution and low positioning noise. Their drawbacks are high manufacturing cost, complicated design, and limited travel range. For example, the laser interferometer system consists of the laser head, beam benders, splitters, beam reflection mirrors, and the receiver. The very fine surface finish of mirrors for a laser interferometer and a flat metal reference for a capacitance gauge that is crucial for acquiring good resolution. The whole set up of the laser interferometry for the maglev stage costs approximately $48,000 and the setup of the capacitance gauges costs approximately $15,000. The travel range is restricted by the size of the mirror. A laser interferometer is a relative sensor, and it is required for the initial position to be set whenever the positioner runs. On the other hand, the Hall-effect sensor is on absolute sensor regardless of the initial position setting. Although the Hall-effect sensor has a lower position resolution than that of laser sensors, its several advantages include low manufacturing cost, simple design, and extended travel range. A Gaussian Least Squares Differential Correction (GLSDC) algorithm estimated the unique position of the platen from sensors that read the magnetic flux density

generated by the magnet matrix. A recursive Discrete-time Kalman Filter (DKF) was used for the optimal estimates based on the GLSDC's position.
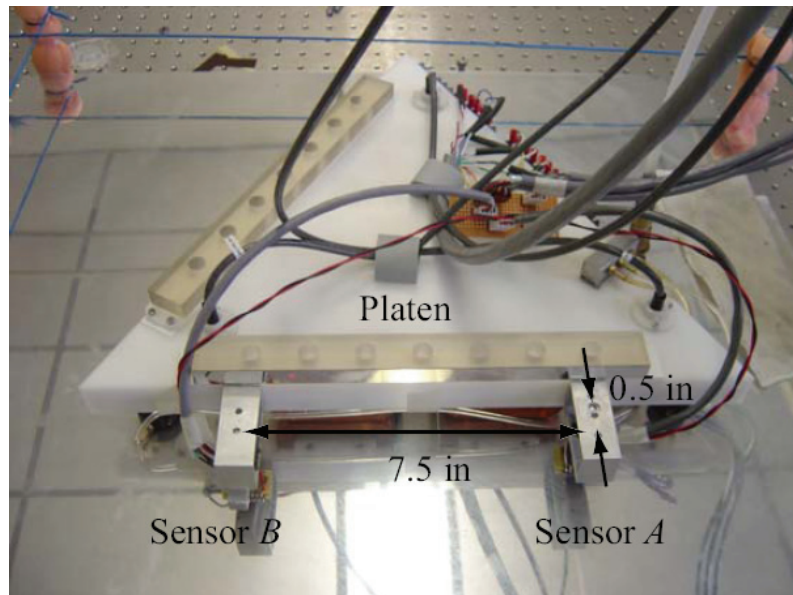
(a)
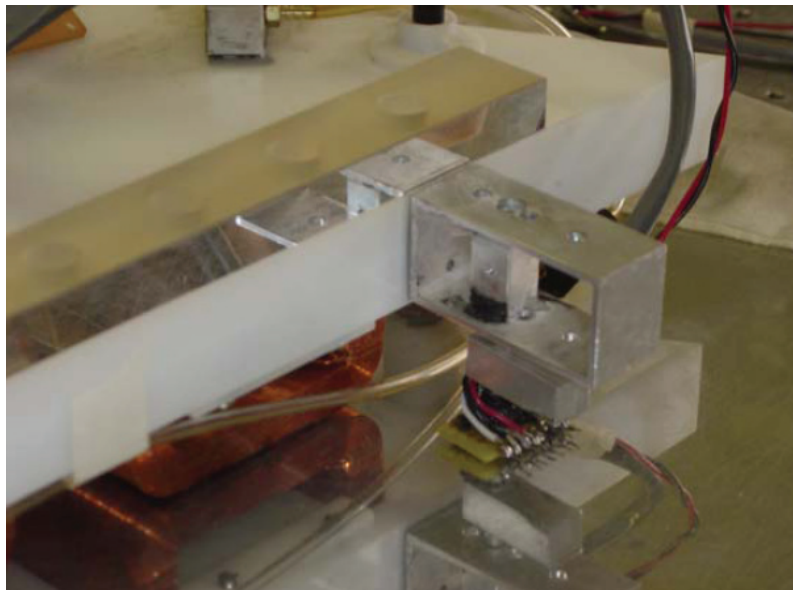
(b)

Figure 1-21: The experimental setup (a) Multi-DOF positioner with two sets of Hall-effect sensors mounted on the base and (b) close-up view of the mounted Hall-effect sensor [19]

1.6 Proposed Compact 6-DOF Positioner

Figure 1-22 (a) and (b) show the photograph of the multidimensional compact positioner and a perspective view of the positioning system, respectively. The positioning system consists of a single-moving frame made of Delrin, three planar motors, the base plate with the concentrated field permanent-magnet matrix, three aerostatic bearings, Hall-effect sensors, and the laser distance sensors as shown in Figure 1-22 (a).

The actuator for the multidimensional positioner is an SPMPM that can cover the downsides of traditional positioners. The moving frame, namely platen, can generate solely 6-DOF feedback motion control, as well as both fine and coarse motions required in the semiconductor industry. For the lateral motion measurement, 2-axis Hall-effect sensors were used instead of laser interferometers. Since the Hall-effect sensors are absolute position sensors, it is unnecessary to set up the initial position. it can also have unlimited travel range in translational motions. Besides, the Hall-effect sensor setup is cost-effective than that of laser sensors and has simple electronic structures without design constraints.

The compact precision positioner shows a 10-μm resolution with 6-μm rms position noise. The maximum travel range is 220 mm in x and 200 mm in y, which depend upon the size of magnets. Since the concentrated-field magnet matrix produces a periodical magnet flux density in the x-y plane, the maximum moving range in lateral motions can be easily extended.
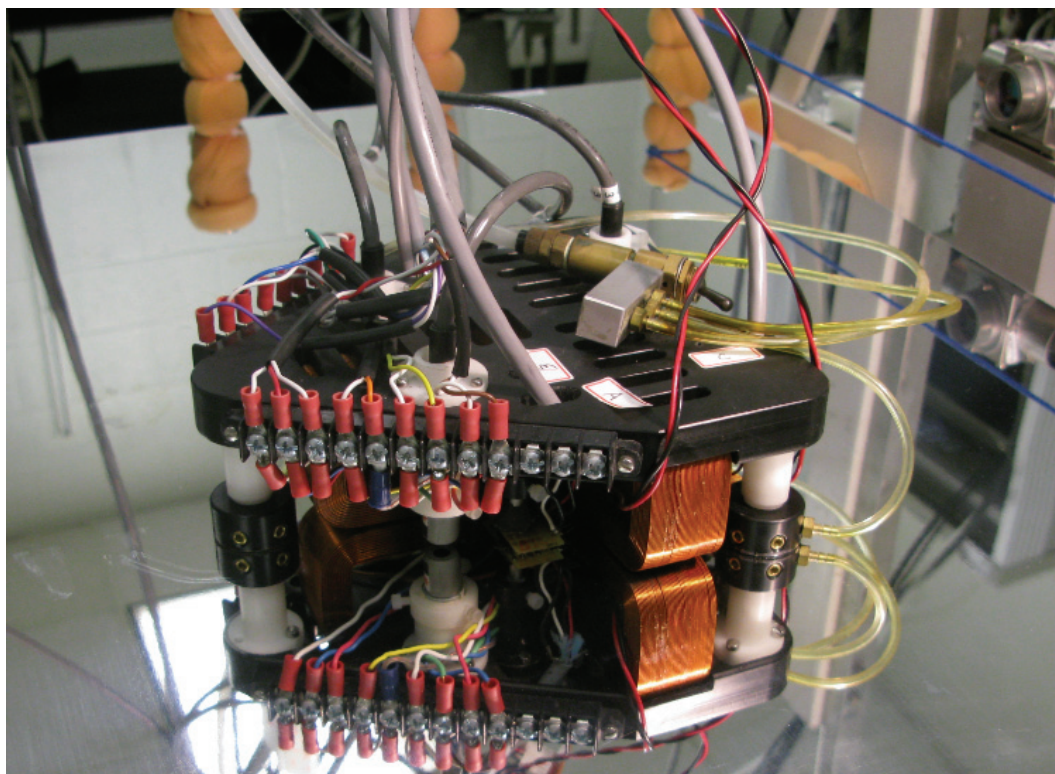
(a)
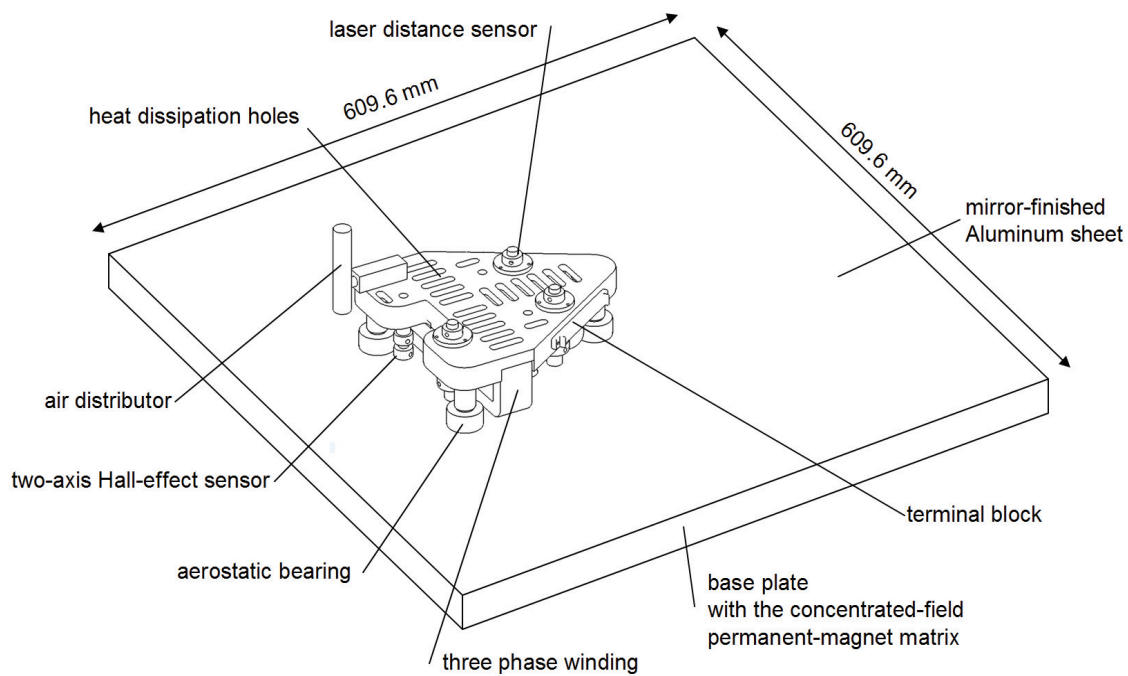
(b)

Figure 1-22: (a) Photograph of the positioner and (b) perspective view of the positiong system

The design objective of this positioner is that the minimized platen generates advanced dynamic performances with low cost. It is also demonstrated that there are several potential applyications in semiconductor-manufacturing positioning stage. A mechanically non-contact frame does not produce any wear particles from friction and leads to a long life span for all components. A single rigid moving frame with simple structure unlike in traditional positioners can have high natural frequencies, so better dynamic performances with high reliability in multidimensional positioning would be obtained.

1.7 Dissertation Overview

This dissertation includes a total of nine chapters: introduction, electromagnetic structure, design consideration, sensors, control software, mechanical design, system dynamics, controller design, results, and the conclusion and future work.

Chapter I presents a literature survey of precision positioning techniques. Features of traditional positioners commonly used in industry are presented. For the advanced precision-positioning actuators, the planar motors, which can generate multi-axis motions are studied. Since planar actuators have several advantages such as simple mechanical structures, low cost, and high precision, it is very useful technology in the future precision-positioning industry. Hence, many researches are as relating in this field. Several case studies of the precision positioner are introduced. Prior arts, which were achieved former students of Dr. Won-jong Kim are also presented.

Chapter II describes the electromagnetic structures and devices to run the precision positioner. The superimposed two-axis Halbach magnet array and harmonic magnetic flux densities are discussed. Multi-phase motor windings, power devices, and data acquisition boards are presented in this chapter.

Chapter III concentrated on the sensor systems for horizontal and vertical mode. Hall-effect sensors, which read the magnetic flux densities on the magnet array, are discussed with the sensing mechanisms. The laser distance sensors for the vertical mode and sensor dynamics are presented in this chapter.

Chapter IV shows control algorithms with the computer software for the signal processing. Linux-based real-time control system was designed and implemented using Real-Time Application Interface (RTAI) and Comedi. Control structure with the signal processing devices and programming architectures are developed.

Chapter V explains the mechanical design and assembly of the positioner. Design concepts, which were considered in the initial design processes, are presented. The compact positioner with high performance with a large travel range was the design objective. The specifications of the mechanical components are described in this chapter.

Chapter VI discusses the dynamic analysis and the system modeling of the positioner. The system dynamics based on the Newton's second law are derived in this chapter. The DQ-decomposition theory that decouples the horizontal and the vertical motions is introduced. Linearized force equations, basic motion generations with interactions of the planar motors, and the force allocations are discussed. State-space models for the advanced dynamic analysis are derived.

Chapter VII presents the control system design. A classical control algorithm is first applied in all six-axis motions. Root-locus plots, loop-transmission plots, and the closed-loop Bode plots are drawn using Matlab. Multivariable controllers based on the LQG methodology for the horizontal mode are designed.

Chapter VIII demonstrates the experimental results. Various step motions in all axes with perturbations in other axes are generated. Besides, long-range motions and large-angle motions are implemented.

The last chapter concludes this dissertation and suggests the future work for better performance. Appendices present several mechanical design specifications and programming codes.

1.8 Dissertation Contributions

This compact precision positioner was designed by SolidWorks. The design objective was to build a compact platen with while generating all 6-degree-of-freedom (DOF) motions. Therefore, the shape of the main body design was a little more complicated than the first-generation stage (ATP). The main body part, Hall-effect sensor mount, and winding holders were manufactured by a Roland CNC machine. The machining precision was 1 mill (25 μm).

As an operating system, the Linux Ubuntu was chosen and installed. Linux makes possible the use of a personal computer to perform real-time control rather than using a digital signal processor with a special computing system. The RTAI was installed based on Linux and works for the real-time current control with sensor signals. The data-

acquisition boards receive directly analog sensor signals and generate the voltage signals to the amplifiers. Comedi and Comedilib are the drive and the library for running data acquisition boards. The data acquisition boards NI-6703 and NI-6221 that support the Comedi drive were used. Nine input signals with Hall-effect sensors and laser distance sensors were obtained, and nine current output signals were generated for the 3 three-phase winding sets.

In order to obtain a proper position on top of the Halbach magnet array, the Hall-effect sensor position and the calibration are very important, since the magnet field shows nonlinearity. Kawato calibrated the sensed position with respect to the laser interferometer position [19]. The algorithm without the laser interferometer was studied and experiments were performed for the compact precision positioner.

Lead-lag controllers for six axes were designed and tested in the frequency domain. The LQG compensator was designed for the precision positioner. The LQG, as a Model Based Compensator (MBC) in multivariable system, provided good performances as well as high stability and robustness.

CHAPTER II

ELECTROMAGNETIC STRUCTURE

This chapter introduces the electromagnetic structures for the compact precision positioner. The positioner is operating above the concentrated-field magnet matrix that is the superimposition of two-axis Halbach magnet arrays. The magnetic field generated from a Halbach array is analyzed by Fourier series. Since the magnetic field is periodic, the positioner can generate the driving and the levitation forces.

2.1 Halbach Magnet Array

The magnet array in the base plate is employed as a stator. For the planar motor, the magnet array has a form of a plane. Magnetic arrays for the conventional permanent-magnet linear motors have both sides of the magnetic fields if there is no iron backing. Since the planar motor works only one side of the magnet array and the other side is wasted, an anti-symmetric magnetic field pattern is desired. Therefore, the type of magnet array that has stronger magnetic field on one side and weaker magnetic field on the other side is used for the planar motor. The magnet array first proposed by Halbach is the representative anti-symmetric single-side field magnetic array for use in undulators and particle accelerators [38]. Figure 2-1 shows the single axis Halbach array. Four blocks of magnets with the magnetization rotated by 90° in each other construct a single spatial pitch. Each adjacent magnet segment is rotated around an axis perpendicular to the direction, in which the array extends by a predetermined angle of 90° or 45°. The

advantage of Halbach magnet array is that it has $\sqrt{2}$ times stronger magnetic field than that of a conventional ironless magnet arrays with the same volume, which is power-efficient. Halbach magnet array illustrated in Figure 2-1 is for a single axis. To generate both planar and vertical motions, another Halbach magnet array is required. The concentrated-field magnet matrix that results from superimposing two orthogonal Halbach magnet arrays will be introduced in the following section.
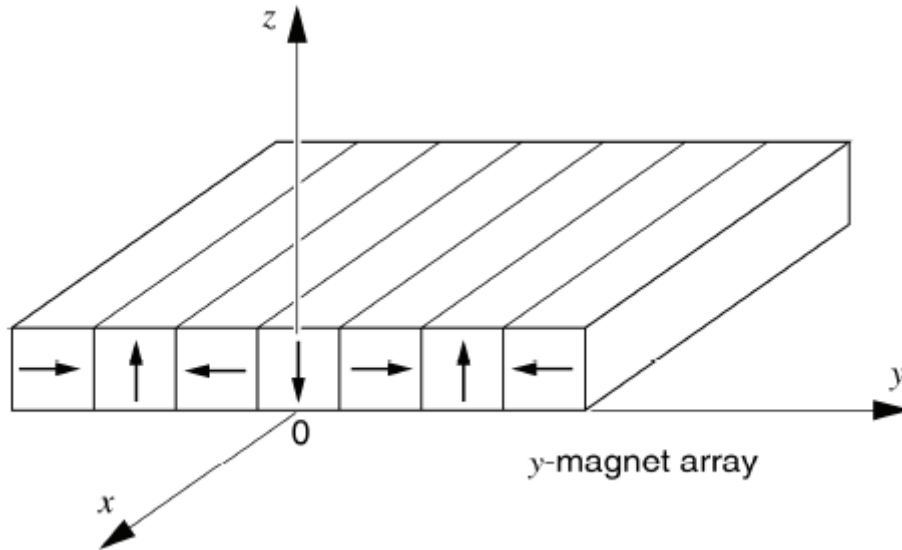
Figure 2-1: Halbach magnet array in y [3]

2.2 Magnetic Field Analysis

Halbach magnet array has a periodic geometry and the magnetic field so that Fourier series representation is suitable for analyzing the magnetic field. Melcher's notation is based on Fourier series analysis [19]. In this thesis, the strong side of the magnetic field is considered. In our positioning stage, the strong fundamental field is generated on the side faced with windings on platen. The Halbach magnet array magnetization using Fourier

series is first performed to model the magnetic flux on the magnet matrix. Figure 2-2 shows the magnetization of Halbach magnet array. The lateral and the vertical magnetization are represented in Figure 2-2 (a) and Figure 2-2 (b), respectively.

The vertical and the lateral magnetization components of the Halbach magnet array are represented by the complex Fourier coefficients [3, 19].
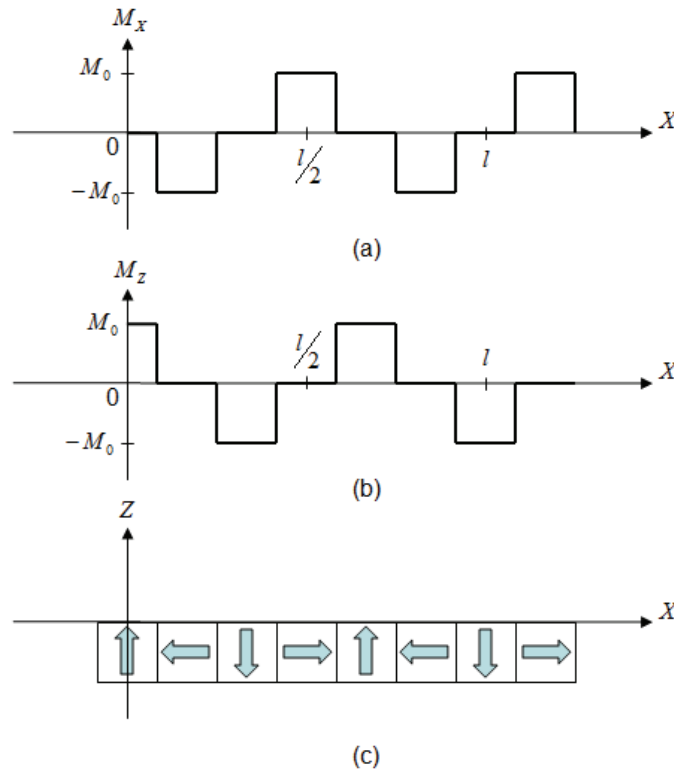
Figure 2-2 (a) Vertical, (b) lateral magnetization components with respect to x, and (c) single axis Halbach magnet array [3]

$$\widetilde{M}_{xn} = \frac{1}{l}\int_0^l M_x e^{jk_n x'} dx', \tag{2.1}$$

$$\tilde{M}_{zn} = \frac{1}{l}\int_0^l M_z e^{jk_n x'} dx', \tag{2.2}$$

where k_n is the spatial wave number as follows,

$$k_n = \frac{2\pi n}{l}, \tag{2.3}$$

The spatial wavelength of the magnet array is represented by l which is identified with the pitch of 50.97 mm. Halbach magnet array whose magnet has a square cross-section is presented as $\Delta = \frac{l}{4}$ shown in Figure 2-2.
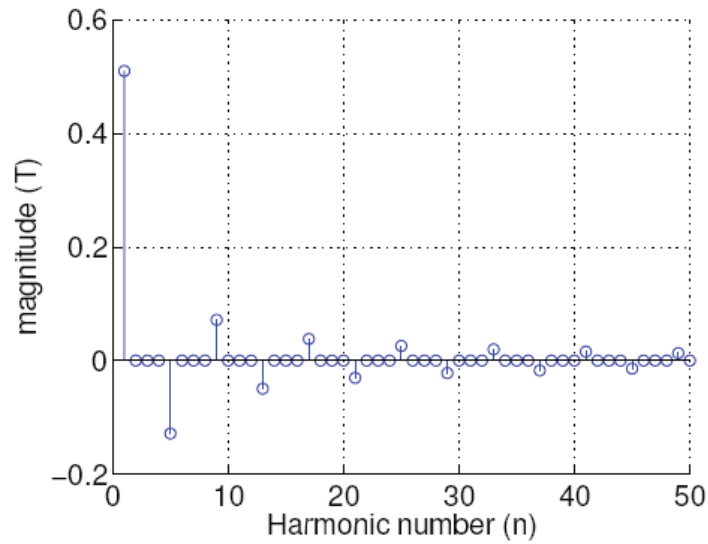
Figure 2-3: Fourier coefficients of the Halbach magnet array flux density [3]

The Fourier coefficients with peak magnetization of M_0 are as follows,

$$\tilde{M}_{zn} = \frac{\sqrt{2}M_0}{\pi|n|}, \quad n = \pm(8m+1) \text{ or } \pm(8m+3), \tag{2.4}$$

$$\widetilde{M}_{zn} = -\frac{\sqrt{2}M_0}{\pi|n|}, \quad n = \pm(8m + 5) \text{ or } \pm(8m + 7), \tag{2.5}$$

$$\widetilde{M}_{zn} = 0, \; n : \text{even}, \tag{2.6}$$

where m is a non-negative integer. Similarly, M_{xn} and M_{yn} are

$$\widetilde{M}_{xn} = \widetilde{M}_{yn} = j^n \widetilde{M}_{zn}, \tag{2.7}$$

The Fourier coefficients of the Halbach magnet array flux density on the strong side are shown in Figure 2-3. The total magnetization represented in (2.8–2.9) can be derived from equations (2.4–2.7).

$$M_z = \sum_{n=-\infty}^{\infty} (\widetilde{M}_{zn} e^{-jk_n y} + \widetilde{M}_{zn} e^{-jk_n x}), \tag{2.8}$$

$$M_x = 2\sum_{n=0}^{\infty} (\widetilde{M}_{xn} d^{-jk_n x}) = 2\sum_{n=0}^{\infty} \widetilde{M}_{xn} (\cos k_n x - j\sin k_n x), \tag{2.9}$$

After we define the magnetization components, the magnetic flux density with air gap Z_0 can be obtained. The following equations present the magnetic flux density using magnetoquasistatic (MQS) approximation,

$$\widetilde{B}_{zn} = \frac{\mu_0}{2} (j\widetilde{M}_{xn} + \widetilde{M}_{zn}) e^{-\gamma_n Z_0} (1 - e^{-\gamma_n \Delta}), \tag{2.10}$$

$$\widetilde{B}_{xn} = \frac{\mu_0}{2} (\widetilde{M}_{xn} - j\widetilde{M}_{zn}) e^{-\gamma_n Z_0} (1 - e^{-\gamma_n \Delta}), \tag{2.11}$$

where γ_n is the absolute value of the spatial wave number.

The field solutions for the magnet array at a plane Z_0 are shown in equations (2.10–2.11). Plugging in the equations (2.4–2.5) into the equations (2.10–2.11) will derive the Fourier coefficients of the magnetic flux density from the magnet array illustrated in Figure 2-3. In the ideal case Halbach magnet array, the strong side in Figure 2-2 (c) of the

magnet array generates the magnetic field of the fundamental, 5th, 9th,···, orders. The magnetic field is a superimposition of those harmonics. The 3rd-, 7th-, 11th-, ···, -order fields cancel out. A more purely sinusoidal field on the strong side of the Halbach magnet array can be generated from the explanations above. That means the planar motor may have little effect from the force ripple and obtain better power efficiency.

2.3 Concentrated-Field Magnet Matrix

The superimposition of two orthogonal Halbach magnet array produces a concentrated-field magnet matrix [3]. The constant magnetic field is measured by Hall-effect sensors [38]. Figure 2-4 (a) and (b) show the single-axis Halbach magnet arrays in x and y, respectively. The result of the superimposition is shown in Figure 2-4 (c) as a plane view. In addition, the magnet blocks are represented with an arrow have $1/\sqrt{2}$ remanence of the magnets noted with North (N) and South (S) poles, which are strong magnets. Shaded magnet blocks surrounding the North pole tip up 45° as shown in Figure 2-5 (a) and shaded blocks surrounding the South pole tip down 45° as shown in Figure 2-5 (b). Blank spaces mean that the magnet field is canceled out. As mentioned in the previous section, the Halbach magnet array has a stronger fundamental field, by a factor of $\sqrt{2}$, than the other side. Since the concentrated-field magnet matrix follows the linear superposition between two orthogonal magnet arrays, the basic principle of the Halbach magnet array is applicable to the two-dimensional magnet matrices. Higher power efficiency, than that of conventional magnetization patterns, can be achieved by using this kind of magnet array in the stationary base plate or a stator. One of the components

in determining the maximum travel range of the positioner is the size of the magnet matrix. The magnet matrix designed and manufactured by Dr. Won-jong Kim's former students Nikhil Bhat and Dr. Tiejun Hu consists of total 6 pitches in the *x*- and *y*-directions, respectively. By adding the number of pitches in each direction, the travel range of the positioner can be increased.

(a)

(b)

(c)
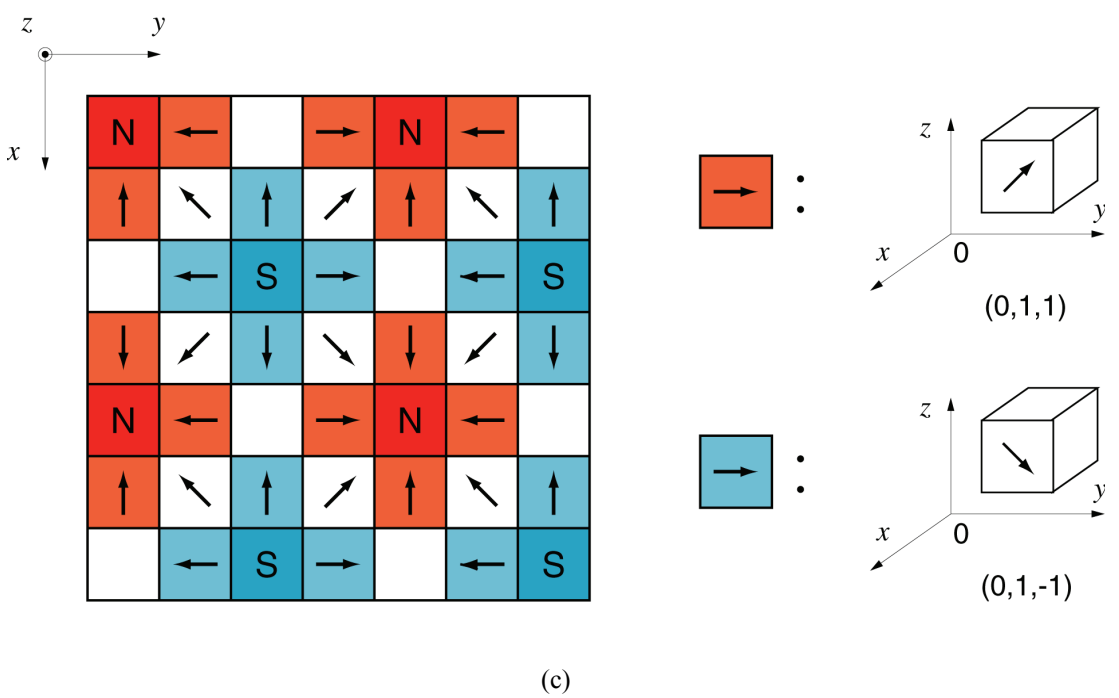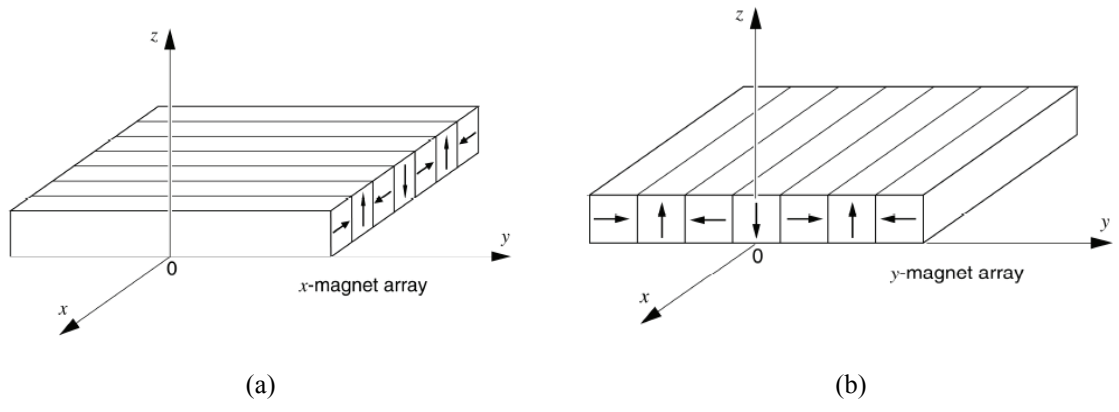
Figure 2-4: (a) Halbach magnet array in *x*, (b) in *y*, and (c) concentrated field magnet matrix [3]

(a)   (b)
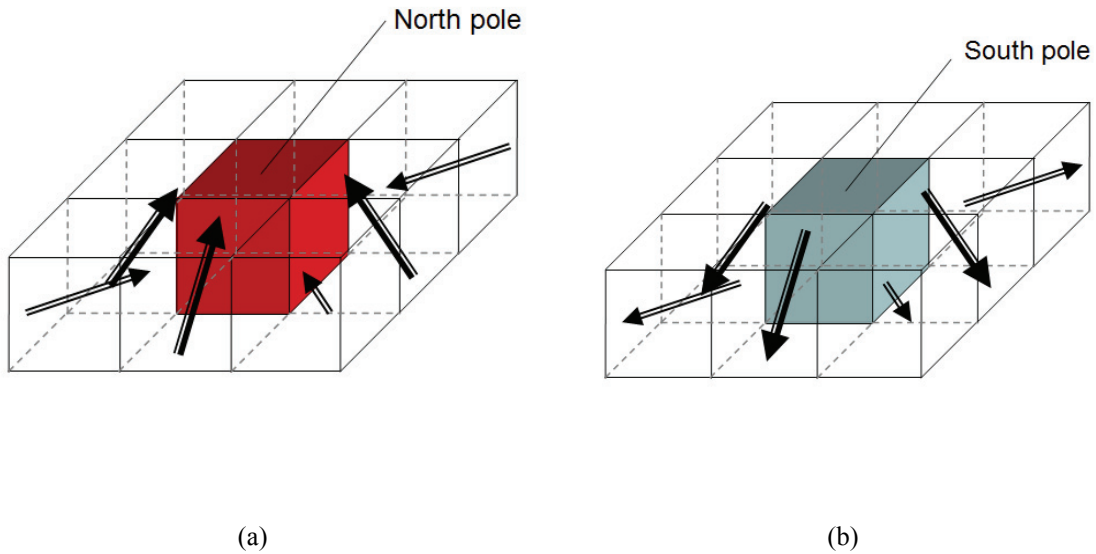
Figure 2-5: 3-D views of the concentrated-field magnet matrix

2.3.1 Flux Density Representation

From the definition of the Fourier series in previous chapter, the total magnetic flux densities of the Halbach magnet array on the fundamental strong side are presented as follows,

$$B_z = \sum_{n=0}^{\infty} \widetilde{B}_{zn} \left(e^{-jk_n x} + e^{-jk_n y} \right), \tag{2.12}$$

$$B_x = 2 \sum_{n=0}^{\infty} \widetilde{B}_{xn} e^{-jk_n x}, \tag{2.13}$$

Figure 2-6 (a), (b), and (c) present the total magnetic flux density in x, y, and z, respectively. According to the previous analysis, the magnetic flux density decays exponentially with respect to the air gap.
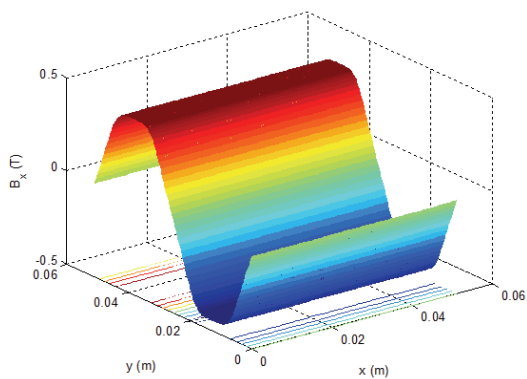
(a)
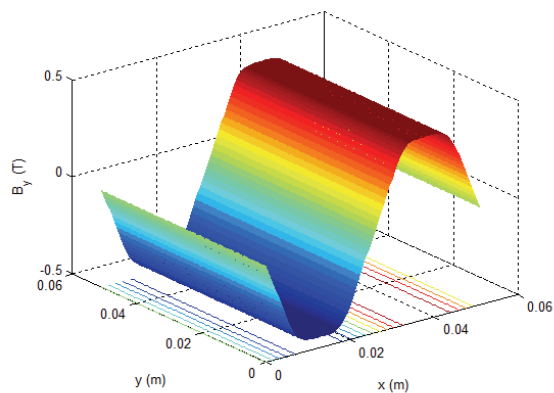
(b)
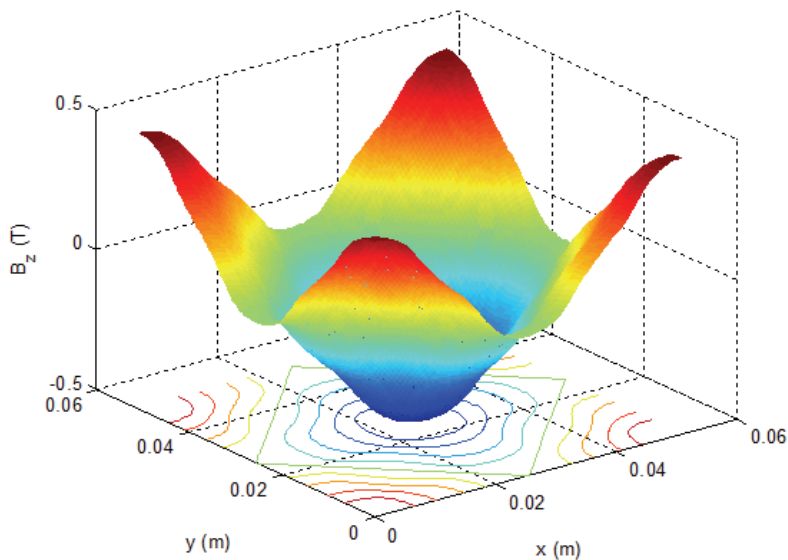
(c)

Figure 2-6: Flux density representation (a) in *x*, (b) in *y*, and (c) in *z* [19]

2.3.2 Neodymium-Iron-Boron Magnet Block

The prototype concentrated-field magnet matrix consists of a number of magnet blocks of neodymium-iron-boron (NdFeB). Neodymium-iron-boron magnets are a sort of rare-earth magnetic material that has high remanence, coercive force, and maximum energy. NdFeB consists of two atoms of Neodymium (Nd), 14 atoms of Iron (Fe), and one atom of Boron (B) so that their chemical composition is $Nd_2Fe_{14}B$. However, it is commonly abbreviated as NdFeB in industry. Since it is easy to be manufactured by the size and the shape, NdFeB has been widely used in commercial products in industry since the mid 1980's.

The grade in strength of Neodymium magnets exist from N24 to the strongest, N55. The magnetic energy product is represented after the N, and the customizing unit is megagauss-oersteds (MGOe) (1 MGOe = 7958×10^3 T·A/m = 7958 kJ/m³). N48 has remnant static magnetic field of 1.38 T. Sintering, compression bonding, injection molding, and extrusion are commonly used method to manufacture NdFeB. The highest energy magnet product of up to 48 MGOe can be formed by the sintering, though the maximum strength would be theoretically 64 MGOe. The lower energy magnet product of up to 10 MGOe can be formed by the bonding. Most of NdFeB magnets are anisotropic and the orientation direction can be magnetized in the magnet block. However, the NdFeB material tends to corrode easily in humid environments so that the surface treatment is necessary such as a thin film coating. The method of nickel coating around the NdFeB magnet is not appropriate, because the epoxy will not bond well to the magnet with a nickel coating. So, the prototype magnet matrix was chosen to use the phenolic resin coating against corrosion, which is also good for epoxy adhesion. NdFeB

is a very strong magnet relative to their mass and cost-effective relative to other magnet materials. A Neodymium magnet can hold up 1300 times its own weight. Nonetheless, it has a weak point of not only the corrosion but also the hardness. In other words, the neodymium magnet is mechanically fragile. The temperatures over 150°C or under impact as a result of their own acceleration may break the magnet blocks so that it requires very careful treatment. In addition, it is sensitive about the temperature, where it loses their magnetism above its Curie temperature. Table 2-1 shows properties of neodymium-iron-boron magnet.

Neodymium-iron-boron magnets have become popular in high technology applications require high performance magnets such as motors, trigger sensors and switches, computer hard drives, transducers in many headphones, and microwave components over the last 10 years. For the small size of the electronic and mechanical components recently, the high-energy magnetic materials such as NdFeB have been useful [77].

Table 2-1. Properties of neodymium-iron-boron magnet

	Unit	Value
Curie temperature	°C	310~370
Maximum operating temperature	°C	80~180
Resistivity	μ-ohm-cm	160
Hardness	Hv	560~580
Density	g/cm³	7.4
Thermal conductivity	kcal/m-h-°C	7.7
Young's modulus	MPa	1.73×10^3
Bending strength	MPa	2.45
Temperature coefficient of Br	%/°C	−0.12~ −0.10
Temperature coefficient of iHc	%/°C	−0.6
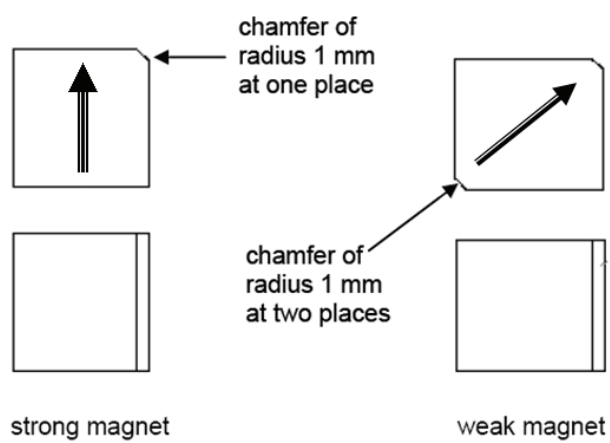
(a)
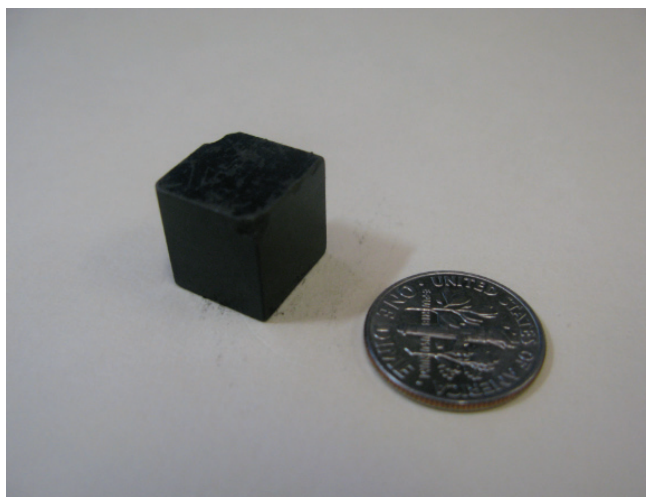
(b)

Figure 2-7 (a) Magnet specifications [1] and (b) photograph of a magnet compared to a dime

Figure 2-7 (a) illustrates the Neodymium-iron-boron magnet specification. The magnet matrix consists of two kinds of magnet. One is a strong magnet which has a 90° magnetization. The strong magnet material is NdFeB50 with a residual flux density of 1.43 T. The other is a weak magnet block which has 45° magnetization angle. NdFeB30 is used for the weak magnet blocks with a residual flux density of 1.10 T. The dimension of both blocks is $0.5 \times 0.5 \times 0.5$" with a dimensional tolerance of ±0.002". The number of chamfer distinguishes two magnet blocks, where the strong magnet has a single chamfer, otherwise the weak magnet block has two chamfers at the edges. The picture of the magnet block is shown in Figure 2-7 (b). The size of a magnet block is compared with the size of a dime.

2.3.3 Magnet Matrix Structure

The design and fabrication of the concentrated-field magnet matrix was based on Dr. Won-jong Kim's US patent [34]. Manufacturing of the magnet matrix and the base plate was performed by Bhat and Hu. PC-7 epoxy was used to glue magnets, because it has very well adhesive property to the phenolic resin coating around the magnet blocks. Figure 2-8 presents the part of epoxy glued magnet blocks with a dimension of 1 pitch × 1 pitch. 4 magnet blocks compose 1 pitch of 50.97 mm. Vacant spaces in the concentrated-field magnet matrix in Figure 2-4 were filled with the aluminum spacers. The thickness of epoxy among magnet blocks is 0.01". The total magnet array includes 432 weak magnet blocks, 72 strong magnet blocks, and 72 aluminum spacers. Figure 2-9 (a) presents the picture of total magnet array by Hu. The base plate was made of aluminum with dimension of $24 \times 24 \times 1.5$" illustrated in Figure 2-9 (b) with the total

magnet matrix. Figure 2-9 (c) shows the side view of the magnet matrix before the epoxy cover.
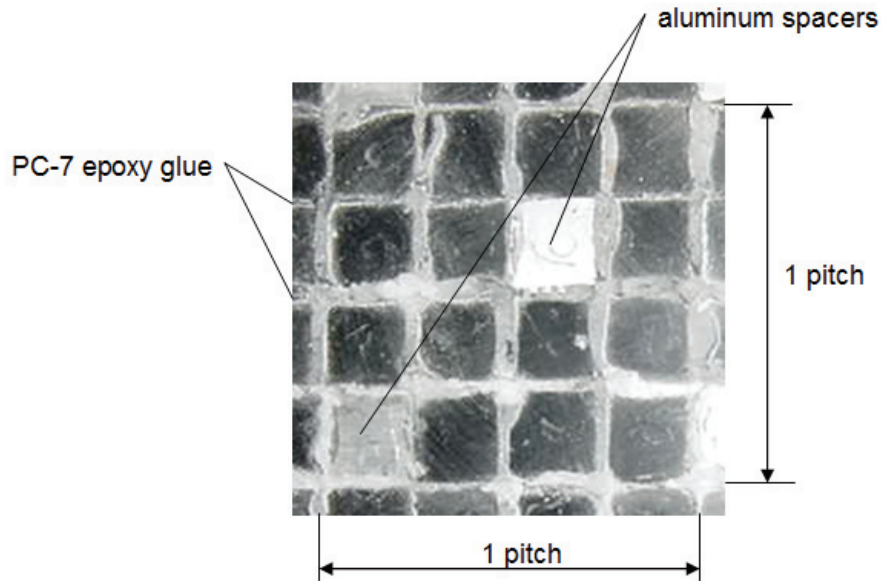
Figure 2-8: 1 pitch magnetic array [1]

On top of the magnet matrix, the 0.02" epoxy layer was covered shown in Figure 2-10 (a). It is required very fine surface finish on the epoxy and the base plate, because the air bearing suspension is critical in providing the levitation for the positioner. After the base plate with the magnet matrix was machined flat enough, the mirror finished aluminum sheet shown in Figure 2-10 (b) was covered on top of the base plate. The aluminum sheet purchased from MacMaster has roughness of 0.1 μm and dimension of $24 \times 24 \times 0.04$". The eddy-current damping effect may happen between the aluminum sheet and the base plate. It causes the aluminum bending to prevent the platen from moving smooth. Therefore, it should be careful to place the aluminum sheet over the base plate.
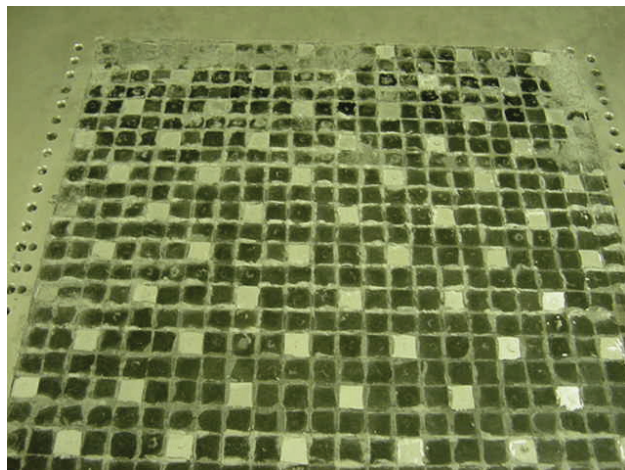
(a)
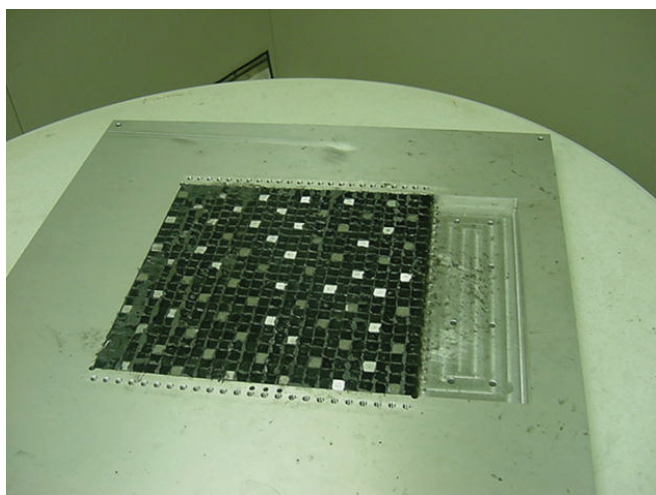
(b)
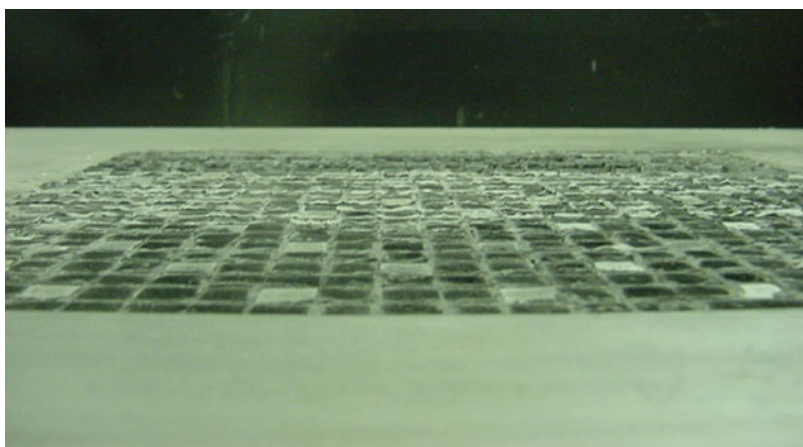
(c)

Figure 2-9: Pictures of the magnet matrix [1]
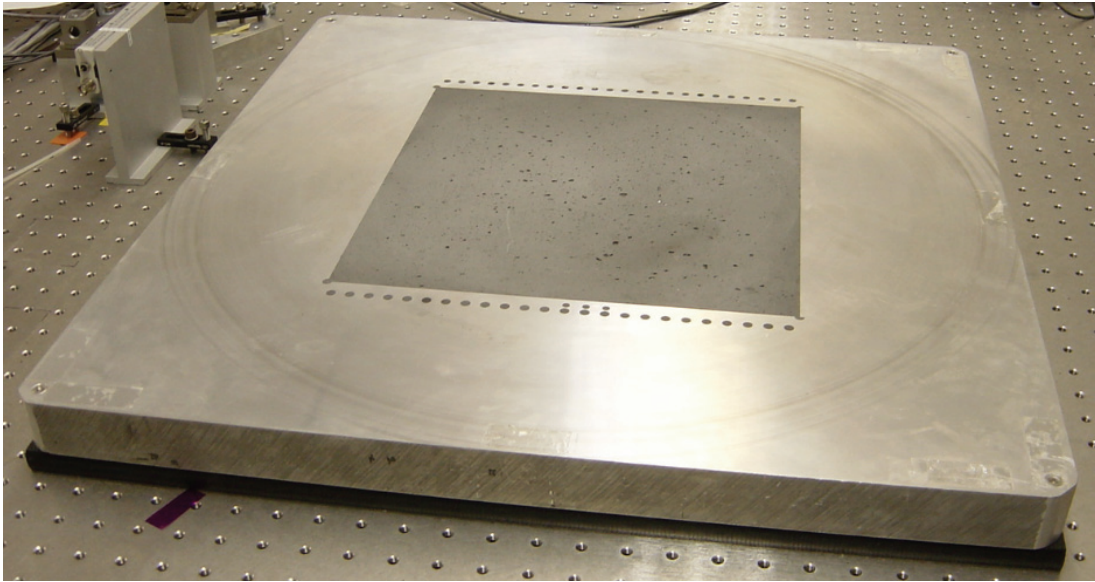
(a)
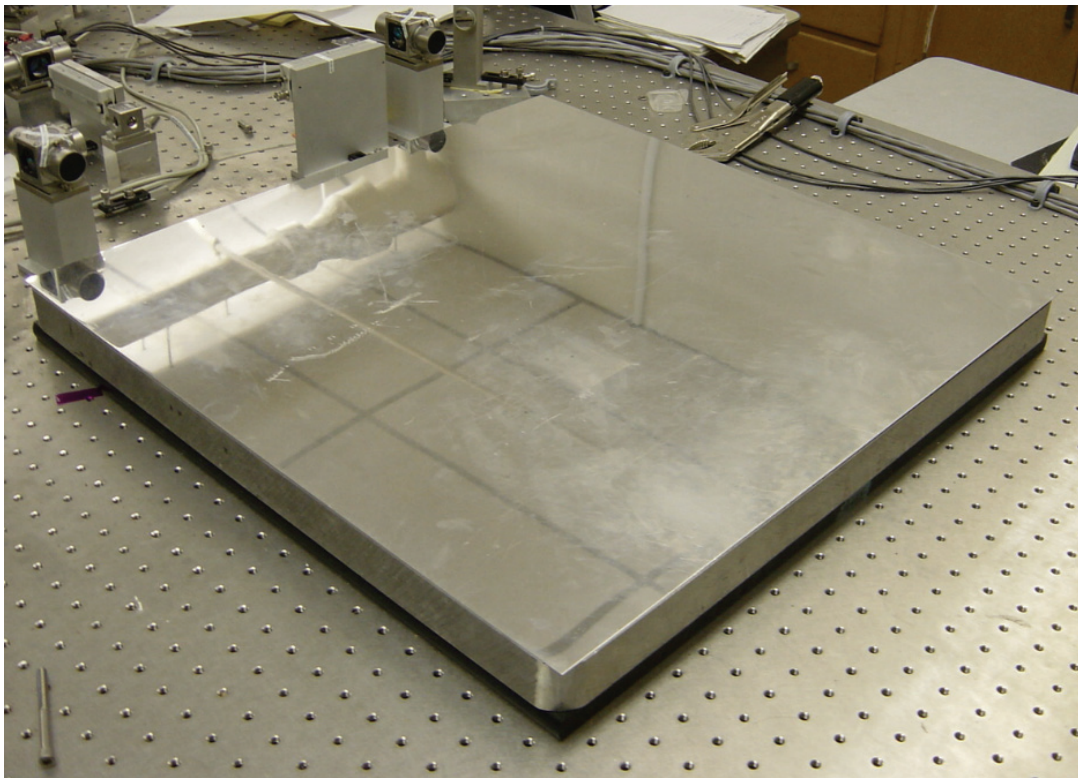
(b)

Figure 2-10: Pictures of the magnet matrix [1]

Table 2-2 shows parameters of the concentrated-field magnet array. As we can see in Table 2-2, the total magnet array size is 304.8 × 304.8 mm in the middle of the aluminum base plate which has a dimension of 609.6 × 609.6 mm. The maximum travel range which can be generated by the positioner depends on the size of the magnet array.

Table 2-2. Parameters of the magnet matrix

Specification	Unit	Value
Pitch, l	mm	50.977
Magnet array width, w	mm	12.7
Magnet matrix size	mm	304.8 × 304.8
Number of magnet pitches, N_m		2
Magnet thickness, Δ		$l/4$
Magnet remanence	T	$B_r = \mu_0 M_0 = 0.71$
Base plate size	mm	609.6 × 609.6

2.4 Motor Windings

The positioner carries three planar motors on the bottom face of the body. Each planar motor consists of three phases, with which the positioner totally include nine winding sets as illustrated in Figure 2-11. The dimension in inch and the shape of the stator winding are shown in Figure 2-11 (a). The thickness of the winding set is 0.3345" and the offset is ±0.001". A single winding has three hundred and five turns with AWG#24 heat bondable wire (diameter of 0.0213"). To achieve optimal motion performances with a planar motor, the flatness process of the bottom surface is crucial. Design work of the winding set

performed by Hu took care of several parameters such as, the thickness of wire, the number of layers, the number of turns, the peak phase current, and the terminal voltage. Table 2-3 presents the specifications of the winding set.

Table 2-3. Parameters of the winding

Specification	Unit	Value
Number of phases		3
Wire specification		AWG#24
Wire resistivity	Ω/m	0.08422
Number of turns		305
Cross sectional area of a winding	m²	8.6524×10^{-5}
Winding thickness	Γ	$l/5$
Phase inductance	mH	15.264
Phase resistance	Ω	4.98
Nominal phase current	A	0.5674
Maximum phase current	A	1.26
Nominal phase voltage	V	2.837
Maximum phase voltage	V	6.525
Turn density, η_0	Turns/m²	3.5246×10^6
Nominal peak current density	A/m²	2×10^6
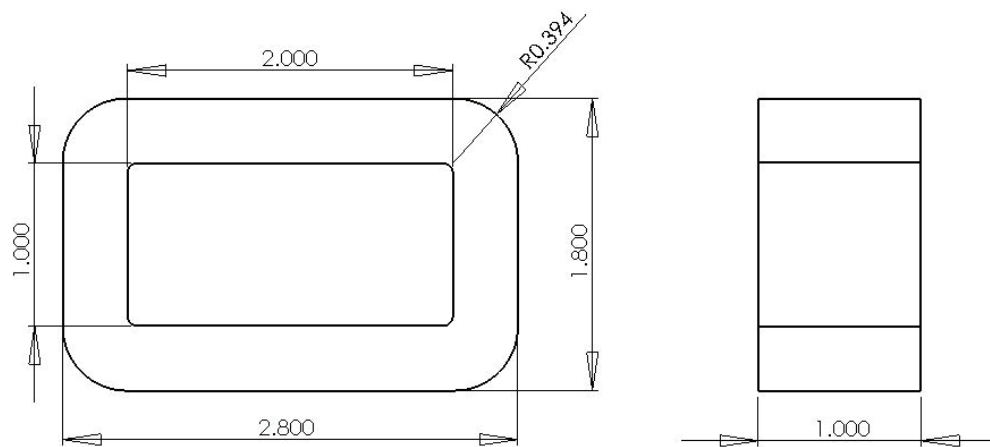
Figure 2-11: Dimension of a coil in three-phase winding

2.5 Power Amplifier

As mentioned in the previous section, the positioner includes total 9 three-phase winding sets. Nine independent channels control the winding actuator for the positioner's motion generation. The source components that control winding set are the currents from the amplifiers. In this system, total nine-channel power amplifiers are required to supply individual phase currents. The programming code RTAI and Comedi deal with the voltage signals from the analog-to-digital converters. It also generates the voltage commands to the digital-to-analog converters. In the middle of the winding set and the converters, the power amplifiers supply the exact amount of current flowing to the winding set from the voltage sources. The power amplifier's dynamics is a critical issue for the current signal control.

2.6 Power Supplies

Two linear power supplies of LZS-250-3 manufactured by LAMBDA Electronics[1] are used. It is manufactured as rugged mechanical and superior thermal design. Besides, wide range adjustment of output and protecting transient input voltage are the feature of this power supply. The linear power supplies have 5 mV ripple errors. On the other hand, the switching-type power supplies have the ripple errors of 150 mV. Figure 2-12 (a), (b), and (c) show the picture of the linear power supply in the top, the front, and the back, respectively. The specification of LZS-250-3 is presented in Table 2-4.

Table 2-4. Specifications of LZS-250-3 power supply

Specification	Unit	Value
Output voltage range	V	18.0~29.4
Nominal voltage	V	24
Maximum output current (40°C)	A	12.5
Maximum output current (50°C)	A	11.3
Maxmum output current (60°C)	A	10
Ripple and noise (20 MHz handwidth)	mV	100 (peak to peak)
		10 (RMS)

The power OP Amp ratings and the maximum output current to the planar motors determine the current and voltage ratings of the power supply. The maximum current in winding that we measured was 1.29 A. Since the positioner carries total nine phases in planar motors, the maximum input current should be more than nine times of the maximum current of a single phase winding that is 11.61 A.

---

[1] LAMBDA Americas, 3055 Del Sol Blvd, San Diego, CA 92154

(a)
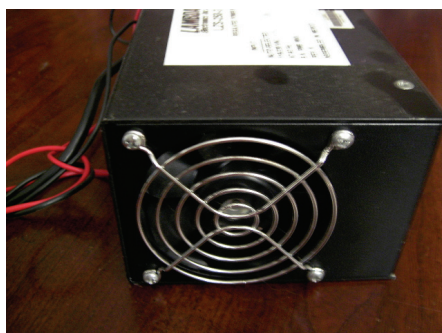
(b)
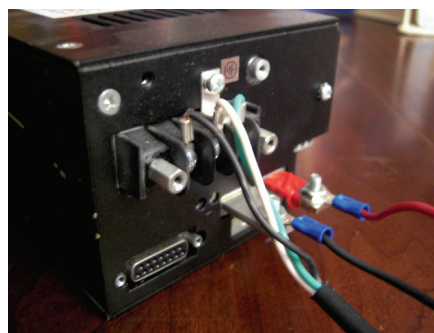
(c)

Figure 2-12: LZS-250-3 Power supply

2.6.1 Power OP Amp

Nine linear power OP Amp PA12A manufactured by Apex [2] are used. The specifications of the power OP Amp satisfy the current and the voltage swing for the power amplifier circuits. Figure 2-13 (a) shows the picture of OP Amp, PA12A, and Figure 2-13 (b) shows its 8-pin connection lines. Table 2-5 presents the specifications of power OP Amp. This power OP Amp is commonly used in motor, power transducers, temperature controls, programmable power supplies, and audio amplifiers [79].

---

[2] Apex Microtechnology Corp., 5980 N. Shannon Road, Tucson, Arizona 85741

(a)
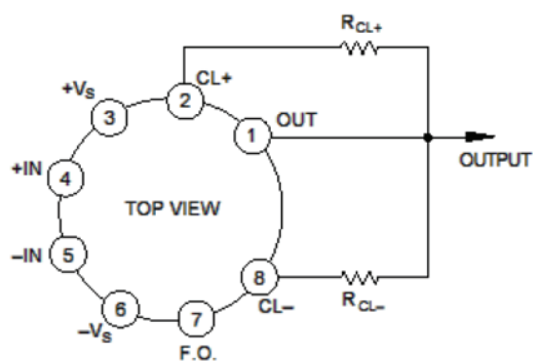
(b)

Figure 2-13 (a) Photograph of PA12A power OP Amp and (b) its 8-pin connections [79]

Table 2-5. Specifications of PA12A power OP Amp [Apex PA12 data sheet]

Specification	Unit	Value
Low thermal resistance	°C/W	1.4
Wide supply range	V	±10 to ±50
High output current	A	±15 peak
Maximum supply voltage, +Vs to -Vs	V	100
Power dissipation	W	125
Operating temperature range	°C	−55~125

2.6.2 Power Amplifier Circuit

The power amplifier circuit illustrated in Figure 2-14 was designed by Hu [1]. The differential amplifier, feedback amplifier, and power booster form a circuit. Parameters of the resistance are presented in Table 2-6. Resistors R_1, R_2, R_3, and R_4 serve on the differential amplifier which blocks common-mode input signals and works as a low pass. A feedback amplifier serves on to stabilize the current control loop.

The current-sensing resistor R_{10} measures the current flowing through the winding in real time. The amplifier closed-loop bandwidth of 1.3 kHz was obtained.
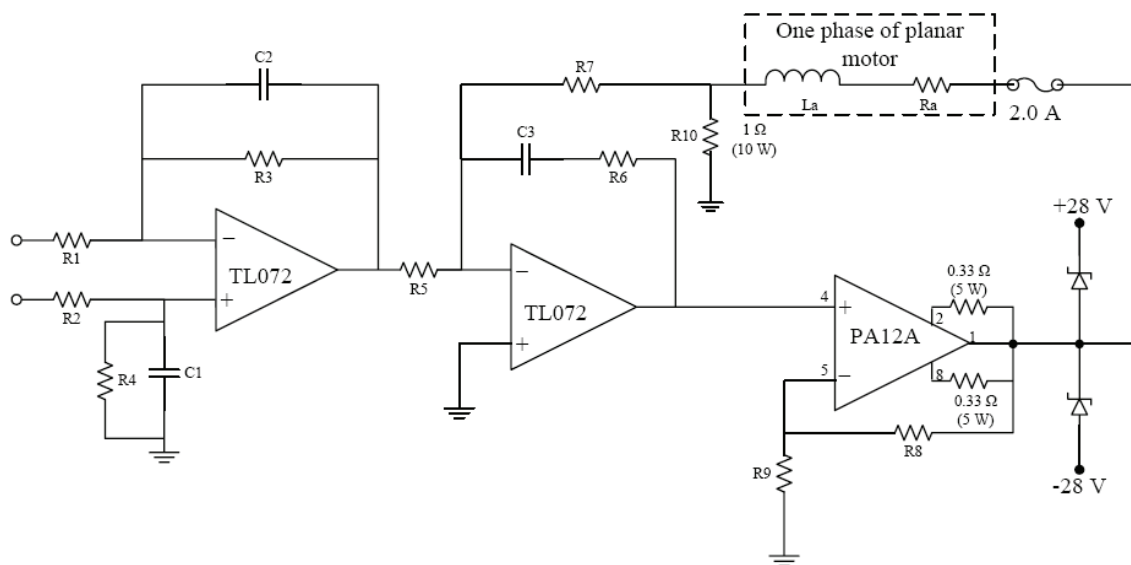
Figure 2-14: Power amplifier circuit [1]

Table 2-6. Specifications of the power amplifier circuit

Specification	Unit	Value	Specification	Unit	Value
R_1	kΩ	10 ± 0.001	R_9	kΩ	10 ± 0.001
R_2	kΩ	10 ± 0.001	R_{10}	Ω	1
R_3	kΩ	10 ± 0.001	C_1	μF	0.01
R_4	kΩ	10 ± 0.001	C_2	μF	0.01
R_5	kΩ	10 ± 0.001	C_3	μF	0.01
R_6	kΩ	82	Ra	Ω	19.44
R_7	kΩ	1.3	La	mH	15.26
R_8	kΩ	10 ± 0.001			

After the power amplifiers was connected to planar motors, voltage and current tests were performed. Each single winding was connected to the power amplifiers individually. Then the capabilities of supplying appropriate amount of current were checked by digital multimeter. A single winding has a resistance of 4.98 Ω. The power amplifier receives the voltage signal sources from the digital-to-analog converter (DAC). Feedback control is performed as voltage signals on RTAI and Comedi. The maximum voltage sensing of the DACs is ±10 V. Tables 2-7 and 2-8 show the voltage and the current test results. The maximum output current from the power amplifier is 1.29 A when the DAC output voltage reaches the maximum value of 10 V.

Table 2-7. Power amplifier and D/A converters current test results

Input voltage on Comedi	A1 (A)	A2 (A)	A3 (A)	B1 (A)	B2 (A)	B3 (A)	C1 (A)	C2 (A)	C3 (A)
1V	0.12	0.12	0.12	0.13	0.12	0.12	0.12	0.13	0.13
2V	0.245	0.245	0.245	0.255	0.245	0.25	0.245	0.25	0.25
3V	0.38	0.375	0.375	0.38	0.37	0.38	0.375	0.375	0.38
4V	0.5	0.5	0.5	0.51	0.5	0.51	0.5	0.51	0.51
5V	0.625	0.625	0.625	0.635	0.625	0.64	0.63	0.63	0.64
6V	0.75	0.755	0.76	0.77	0.755	0.775	0.76	0.765	0.765
7V	0.885	0.88	0.89	0.9	0.88	0.9	0.88	0.89	0.89
8V	1.01	1.01	1.01	1.03	1.01	1.02	1.01	1.02	1.02
9V	1.14	1.13	1.15	1.16	1.14	1.17	1.14	1.15	1.16
10V	1.255	1.26	1.27	1.29	1.26	1.29	1.27	1.28	1.29

Table 2-8. Power amplifier and D/A converters voltage test results

Input voltage on Comedi	A1 (V)	A2 (V)	A3 (V)	B1 (V)	B2 (V)	B3 (V)	C1 (V)	C2 (V)	C3 (V)
1V	0.629	0.636	0.608	0.65	0.606	0.646	0.616	0.648	0.64
2V	1.258	1.263	1.241	1.287	1.235	1.288	1.248	1.284	1.28
3V	1.887	1.889	1.875	1.926	1.867	1.932	1.882	1.923	1.922
4V	2.542	2.542	2.535	2.593	2.528	2.606	2.544	2.592	2.594
5V	3.191	3.191	3.191	3.25	3.186	3.27	3.207	3.25	3.26
6V	3.91	3.91	3.92	4	3.92	4.02	3.93	4.01	4.01
7V	4.42	4.43	4.45	4.52	4.46	4.58	4.49	4.57	4.58
8V	5.19	5.19	5.23	5.33	5.27	5.33	5.27	5.34	5.37
9V	5.82	5.83	5.89	6.01	5.93	6.1	5.98	6.08	6.11
10V	6.32	6.33	6.39	6.53	6.47	6.67	6.56	6.7	6.76

2.7 Data Acquisition

As mentioned in the previous section, feedback signals from sensors are controlled as voltage signals on programs. Digitized signals with sampling frequency of 800 Hz

circulate the feedback control loops through the power amplifiers, planar motors, Hall-effect sensors, and laser distance sensors.
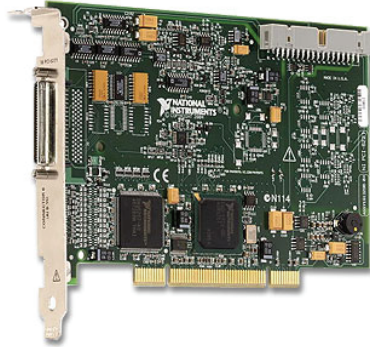
(a)   (b)
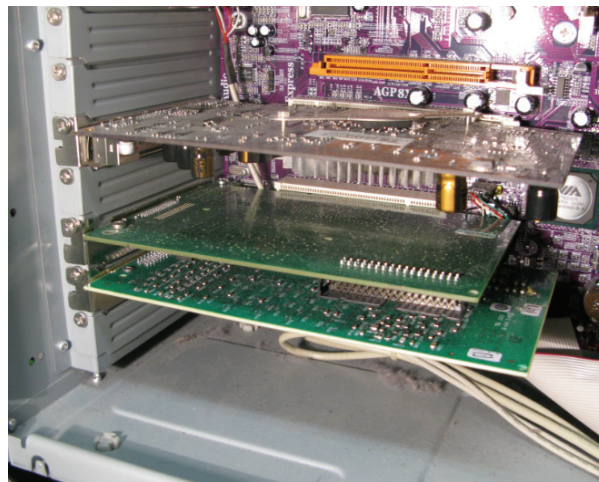
(c)

Figure 2-15: Photographs of (a) NI PCI-6221, (b) NI PCI-6703, and (c) mounted boards on PC

As an analog-to-digital converter (ADC), NI PCI-6221 board manufactured by National Instrument (NI) shown in Figure 2-15 (a) is used. The NI PCI-6221 ADC supports 16-bit, 250 kS/s 16 analog output channels, 24 digital I/Os, two 16-bit analog outputs and 32-bit counters. All analog voltage signals from three 2-axis Hall-effect sensors and three laser distance sensors come through this board and are converted to

digital signals. As a DAC, NI-6703 board manufactured by NI shown in Figure 2-15 (b) is used. This DAC board supports sixteen 16-bit analog output voltage channels with ±10 V and 8 digital I/O lines. Figure 2-15 (c) shows the picture of two converters mounted in the personal computer chassis. These two data acquisition boards are supported by Comedi drivers of "ni_pci.mio" and "ni_670x" for the real-time control. Although commonly used data acquisition board such as NI-6221 has both of analog input and output channels, the dual data acquisition boards were adopted. This will be elaborated in the following chapter.

For the convenience of signal cable connection, a CB-68LP connector manufactured by NI is used. Each data acquisition board has their own connectors. The numbers represented on the board correspond with data channels on data acquisition board to distinguish channels. In addition, screws placed on the pins give convenience to connect and disconnect data signal cables just using a screw driver. Figure 2-16 presents two connectors for two data acquisition boards. The left side is the DAC connection of NI-6703 and output data signal cables connected to the power amplifiers. The right side is the ADC connection of NI-6221 and input data signal cables from laser distance sensors and 2-axis Hall-effect sensors.

SHC68-68-EPM shielded signal cables that has 68 pins are used between the data acquisition boards and the connector blocks. It consists of individually shielded twisted pairs for the analog inputs and outputs as well as the twisted pairs for critical digital I/O separately. In addition, it reduces crosstalk.
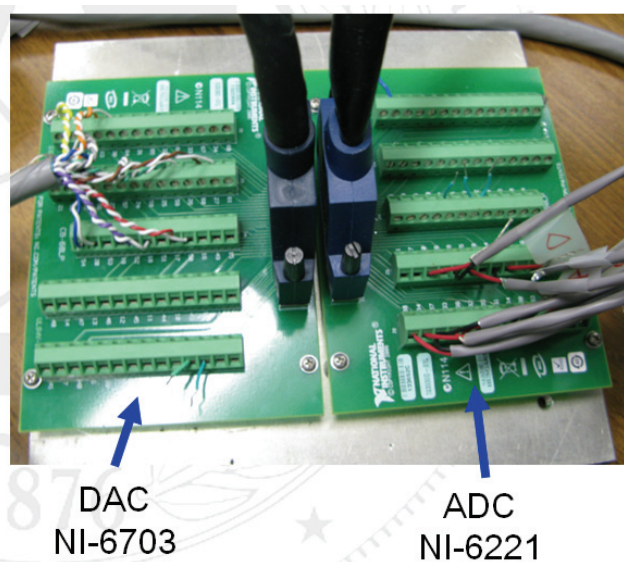
Figure 2-16: NI-6703 and NI-6221 connectors with signal cables

2.8 Power Connection Switches

The real-time control running on a personal computer is not always stable in every time when the program runs. For instance, the computing system is sometimes shut down while the power amplifier and the planar motor winding set are still running. Besides, if the programming code of RTAI is stopped on purpose in the middle of iterations, previous step output voltage signal commands will not become zero values automatically. Hence, keeping running the power amplifier and planar motors with typical current values generates heat on the winding set, which affects the accuracy. The power switch set is connected all 9-channel power amplifiers. If emergencies may happen in the maglev system, it can cut off all power sources going to the power amplifiers and windings. Figure 2-17 presents the power switch set and it consists of five toggle switches.

Figure 2-17: Power switch set

CHAPTER III

SENSORS

The precision positioner was designed to generate 6-DOF motions supported by three 3-phase planar motors. Each planar motor can generate two decoupled and orthogonal forces in horizontal and vertical directions. Three sensors for the translational motions and three sensors for vertical motions are required to achieve the feedback controls in each axis. In this chapter, Hall-effect sensors that measure the magnetic flux density from the concentrated-field permanent magnet matrix for translational motions are introduced and laser distance sensors for vertical motions are followed. Sensor equations explain the basic principles how each sensor operates to measure the unique position.

3.1 Hall-Effect Sensor

The Hall-effect was discovered by Dr. Edwin Hall in 1879 at Johns Hopkins University in Baltimore. When the magnetic field is perpendicular to the one face of a thin rectangle of gold while current was flowing through, he found that the voltage was proportional to the current flowing through the conductor [80]. Hall-effect sensors were manufactured in the 1950s with semiconductor materials. Cost, however, was a disadvantage. In 1965, a practical and low-cost solid-state sensor was developed by Vorthmann and Maupin of Micro Switch Sensing and Control. Thus, Hall-effect sensors could then be integrated on a single silicon for low-cost and high-volume applications.

3.2 Hall Sensor Theory

The Hall-effect is used with the magnetic field sensor for measuring the magnitude of the magnetic flux density. The conductor in the Hall-effect sensor is placed into the magnetic field. A voltage is proportionally generated perpendicular to both the current and the field. The principle of the Hall-effect sensor is presented in Figure 3-1, which represents the single-axis Hall-effect sensor. The thin plate is the semiconducting material (Hall element) and the current element passes through the plate. A perpendicular angle is required between the direction of the current and the output connections. Figure 3-1 (a) presents the case when no magnetic flux occurs. The current distribution is uniform and potential differences do not take place. On the other hand, Figure 3-1 (b) shows the Hall-effect principle when the magnetic field passes through the current-carrying conductor. The magnetic field presents perpendicular to the current flowing and a Lorenz force is applied on the current. The magnetic force interrupts the uniform current distribution. Potential differences from the disturbed current occur so that the voltage output is generated. This voltage is called the Hall voltage (V_H), which is based on the interaction of the magnetic field and the current. Equation $V_H \propto I \times B$ shows the relationship between the Hall-effect sensor output voltage and the interaction of the current. Hall-effect sensors are generally used for proximity switching, positioning, speed detection and current sensing applications. For example, they are used in servo motor control, the overflow current measurement, power supply control, and the timing speed of wheels and shafts such as an internal-combustion engine ignition timing device

(a)

(b)
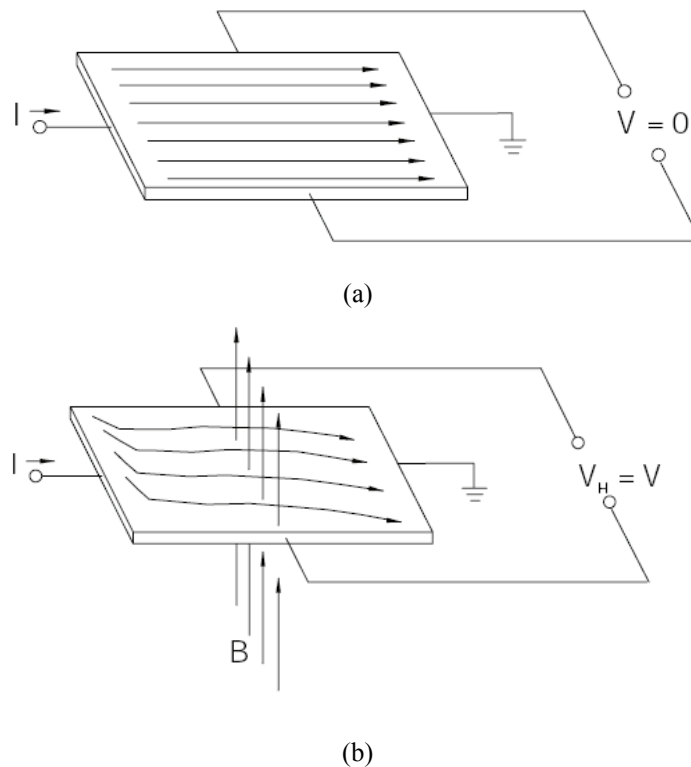
Figure 3-1: (a) Hall-effect sensor without magnetic field and (b) with magnetic field present [19]

or a tachometer. Figure 3-2 illustrates the basic principle of Hall-effect sensor methodology for a rotating machine. The pictured wheel carries two equally spaced magnets and the voltage from the sensor peaks twice for each revolution. This arrangement is commonly used to regulate the speed of disk drive. The advantages of the Hall-effect sensors are that they are contactless, small in size, reliable, low-cost, and insensitive to harsh and polluted environmental conditions. In addition, the Hall-effect sensor can measure both a direct current (DC) and an alternating current (AC). It is also totally insulated by the measured semiconducting materials, as well as power loss from the sensor is almost zero. The Hall-effect sensor was chosen for this research as the positioning sensors because it has fast signal responses and high linearity between the voltage output and the current flowing. The simple structure produces the high reliability

as well. On the other hand, the Hall-effect sensor has limited accuracy due to the offset, noise, temperature, and aging effects.
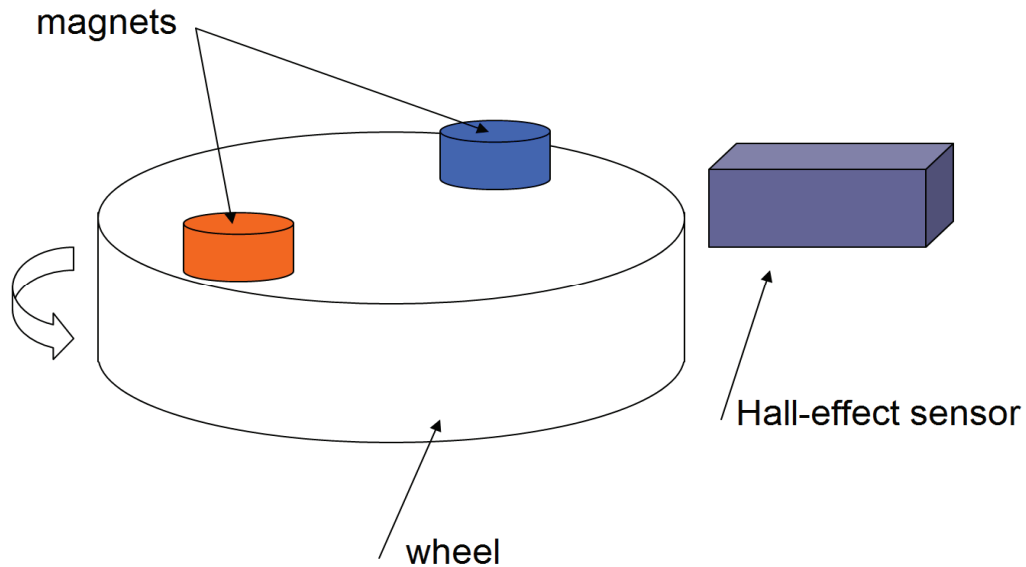
Figure 3-2 Basic principle of Hall-effect sensor for the rotating machinery

3.3 Laser Interferometer

Laser interferometer is commonly used methodology in the precision positioning. Figure 3-3 shows the schematic view of the laser interferometer for the ATP project. Three laser interferometers are employed for the 3-DOF lateral position measurements in x, y, and rotation around z. The overall system consists of the laser head that generates a laser source, three laser interferometers, beam benders, beam splitters, laser receivers, stick mirrors, and the laser-axis boards. The laser head manufactured by Agilent [3] (5517D) generates the HeNe laser source at the wavelength of 632 nm. The Agilent 10897B laser-axis board has the resolution of 0.6 nm. The laser interferometer produces 35-bit position data and 24-bit velocity data. ATP stage performed by Tiejun Hu, a

formal doctoral student of Dr. Won-jong Kim, adopted this sensing method and Pentek

4284 DSP board[4] that reads the position and the velocity measurement data through the

VMEbus.
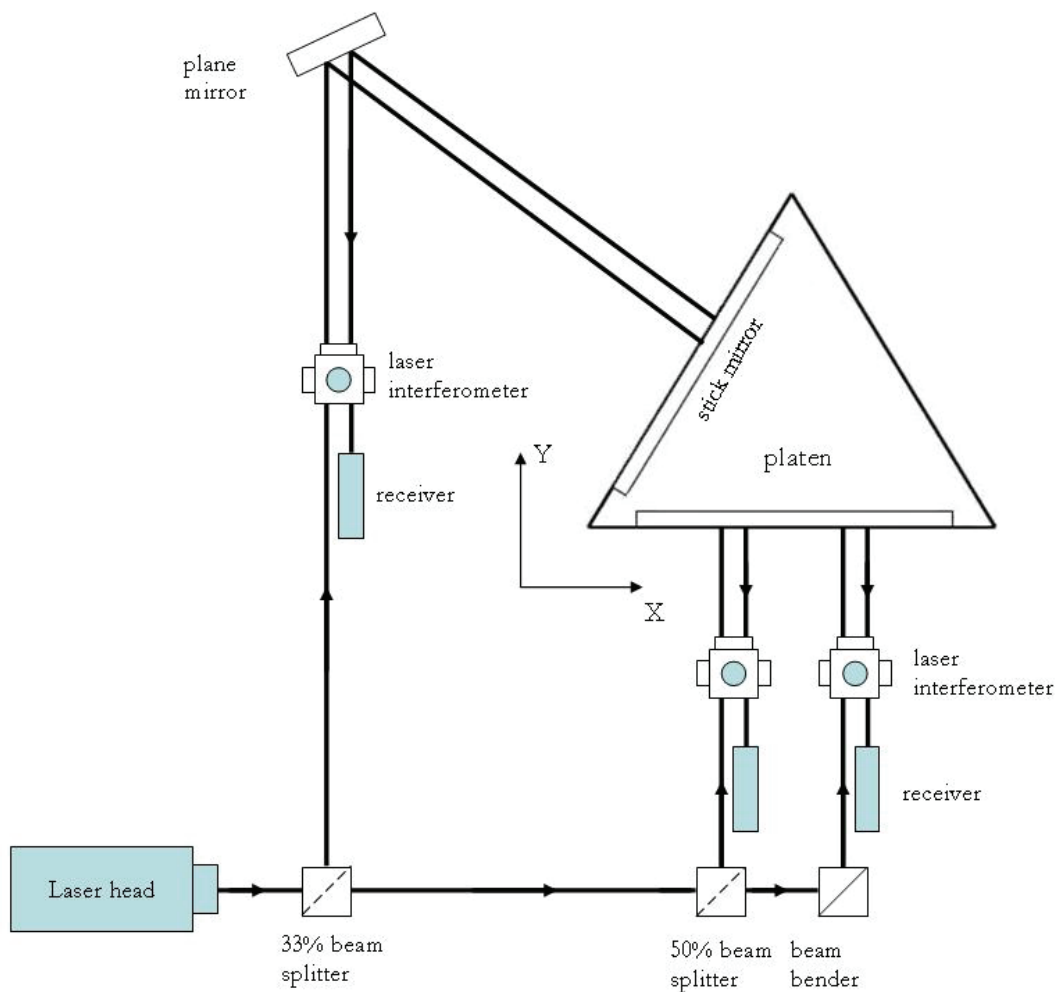
Figure 3-3: Schematic view of the laser interferometers on ATP stage

[3] Agilent Technologies, Inc. 395 Page Mill Rd. Palo Alto, CA 94306

[4] Pentek, Inc. One Park Way, Upper Saddle River, NJ 07458

3.4 Instrumentation

3.4.1 Two-Axis Hall-Effect Sensor

The Hall-effect sensor 2D-VD-11SO manufactured by Sentron AG[5] is used for the lateral position measurement [81]. Figure 3-4 (a) shows the photograph of the Hall-effect sensor mounted on the data connection board, which is 8-pin, surface-mount, small-outline integrated circuit (SOIC). Each Hall-effect sensor has two orthogonal axes, where the sensor measures the magnetic flux density of two independent perpendicular axes on the chip's surface as illustrated in Figure 3-4 (b). Table 3-1 presents the specifications of the sensor. The 2 mA constant current source or the 5 V constant voltage source is necessary to run 2D-VD-11SO as a power source.

Figure 3-5 (a) shows the Hall-effect sensor mounted on the IC board, as well as the power and the data cable connections. The IC board is the 9082 8-pin SOIC. The board dimension of 0.6×1.1 in and the details of pin connection are illustrated in Figure 3-5 (b).

3.4.2 Hall-Effect Sensor Power Supply

Hall-effect sensors operate with the power supply circuit, an amplifier, and a low-pass filter to prevent aliasing. The experimental setup includes three sets of power supply circuits for each Hall-effect sensor.

Each Hall-effect sensor requires a 5 V constant voltage source or a 2 mV constant current source. Both of power sources were tested by Yusuke Kawato, Dr. Kim's previous master's student. The current power source showed a smaller sensor output fluc-

---

[5] Sentron AG, Baarerstrasse 73 CH – 6300 Zug, Switzerland
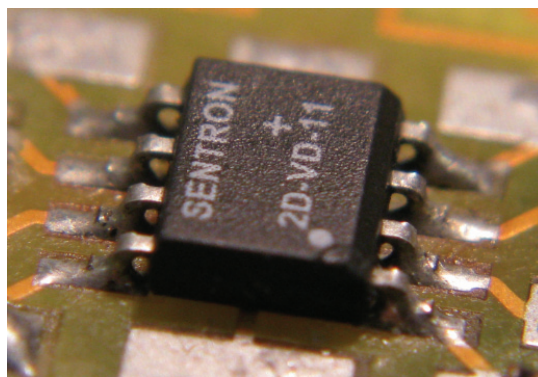
(a)

(b)

Figure 3-4: (a) Photograph of 2-axis Hall-effect sensor and (b) its schematic views [82]

Table 3-1. Specifications of 2D-HD-11SO 2-axis Hall-effect sensor

Specification	Condition	Value
Input resistance	$B = 0$ mT, $I_c = 2$ mA	2.2 kΩ
Output resistance	$B = 0$ mT, $I_c = 2$ mA	8.5 kΩ
Output voltage	Constant Current Drive $B = 1$ T, $I_c = 2$ mA	400 mV
Offset voltage	$B = 0$ mT, $I_c = 2$ mA	± 3 mV
Sensitivity	$I_c = 2$ mA	400 mV/T
Magnetic sensitive volume		$0.25 \times 0.25 \times 0.20$ mm
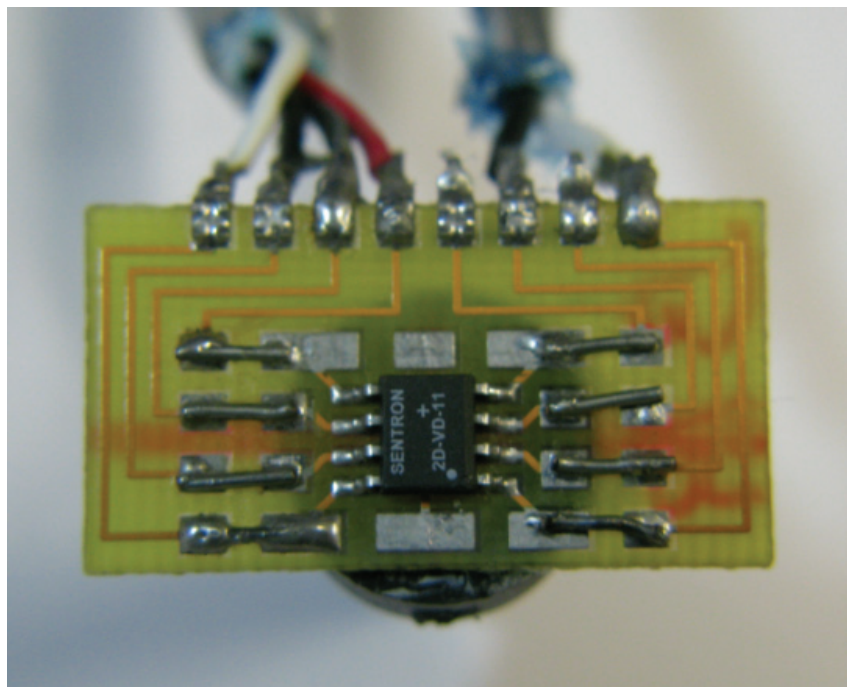
(a)

IN-LINE COMPONENT
MOUNTING PADS ACCEPT
0805, 1206, MINI-MELF,
A-TANTALUM, AND OTHER
2-TERMINAL SMD DEVICES

.600 in.

MOUNTING
PAD FOR
BYPASS
CAPACITOR
ACROSS I.C.
TERMINALS 4-8

BOARD WIDTH
1.10 in.
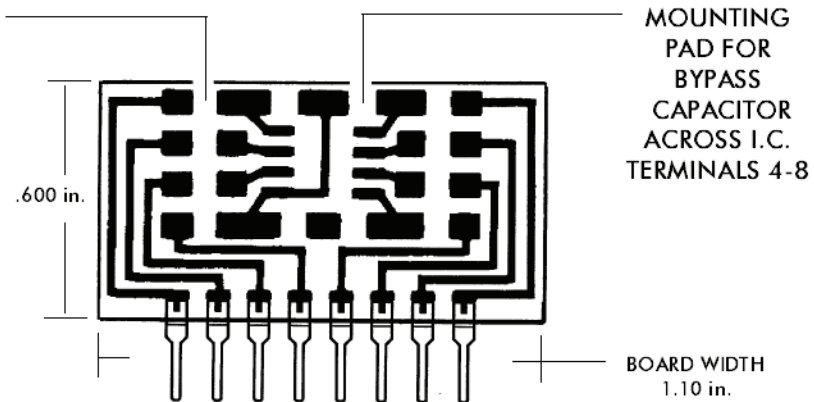
(b)

Figure 3-5: (a) Photograph of Hall-effect sensor with cable connection and (b) data connection board [83]

tuation. The sensor noise by the sampled standard deviation is 5.76 mV. To regulate the current source, the current regulator diodes CR200 manufactured by Vishay Siliconix [6] were used. The power supply circuit with CR200 diodes provides the 2-mA constant current and it guarantees ±10% tolerance with good temperature stability. Figure 3-6 (a) shows the picture of three sets of the power supply circuits and the circuit diagram is illustrated in Figure 3-6 (b).

3.4.3 Amplifier and Analog Filter

The photograph of implemented amplifier and analog filter circuit is shown in Figure 3-8 (a), and Figure 3-8 (b) is the circuit diagram. The OP Amp TL072ACP manufactured by Texas Instruments [7] is used. To reduce the common-mode noise, the differential amplifier was used in the left part of Figure 3-8 (b). The amplifier is shown in the right part of the circuit diagram. It requires ±15 V power source, which is supported by the power supply E3646A manufactured by Agilent. An anti-aliasing filter that is the low-pass filter with the frequency of 200 Hz is placed after an amplifier circuit. This hinders not only aliasing signals, but also the high frequency noise going into the ADC. Sensor noise of 1 mV is measured after the low-pass filter. All Hall-effect sensor outputs after amplifiers and analog filters are connected directly to the NI-6221 ADC board. The specifications of the amplifier and the analog filter circuit are presented in Table 3-2.

---

[6] Vishay Intertechnology, Inc. 63 Lincoln Highway, Malvern, PA 19355-2120

[7] Texas Instruments Inc. 13532 N. Central Expressway, M/S 3807 Dallas Texas 75243-1108

(a)

Y-channel analog output

X-channel analog output

amplifier and
low-pass filter

8 7 6 5

Bx

By

1 2 3 4

2-axis
Hall-effect sensor
2D-VD-11SO

diode CR200

9 V battery

GND
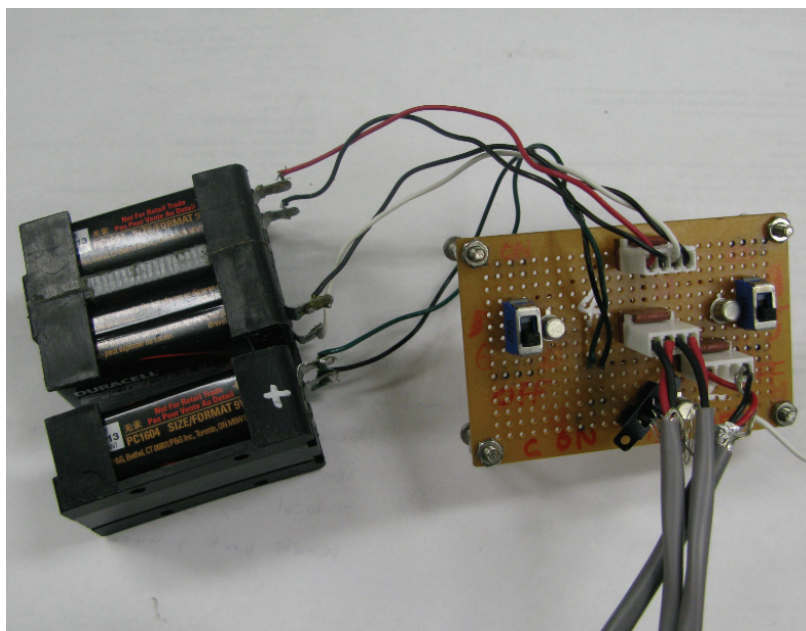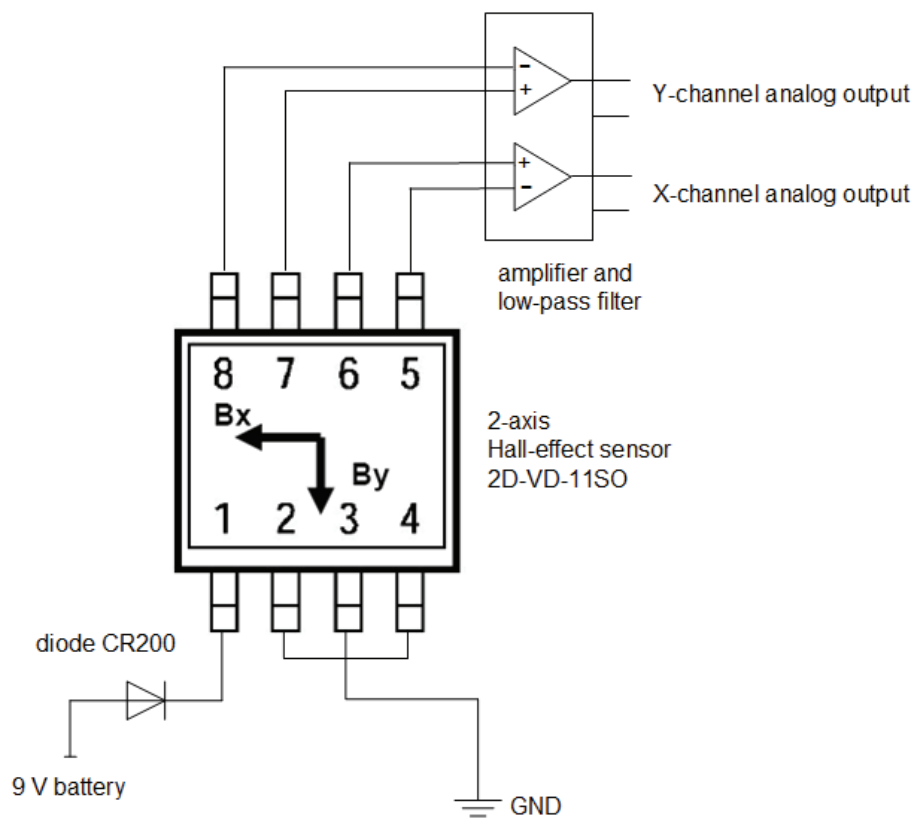
(b)

Figure 3-6: (a) Photograph of sensor power supply and (b) Hall sensor power supply circuit [19]
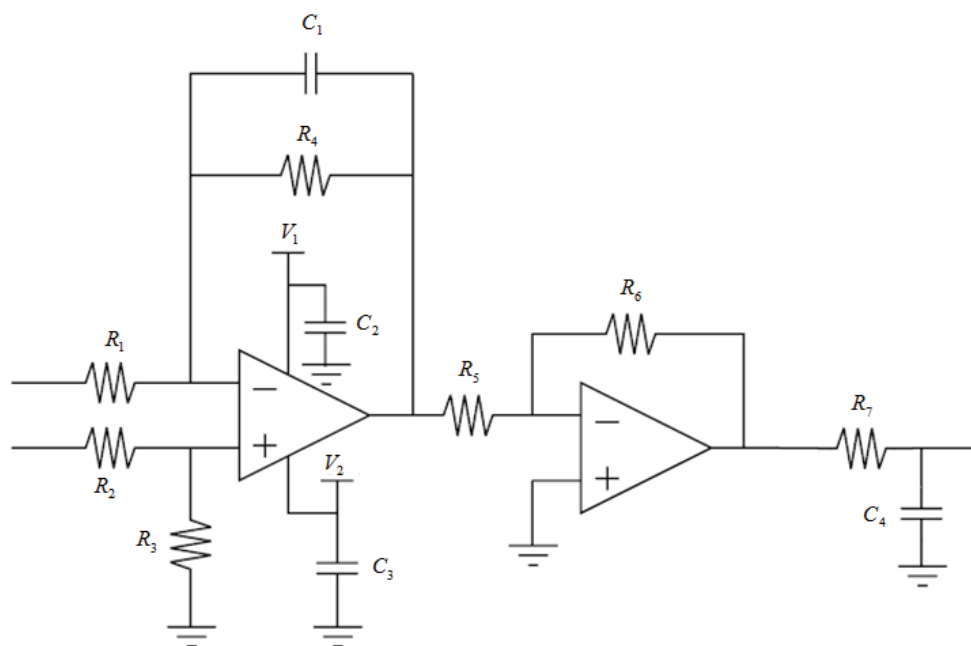
Figure 3-7: Amplifier and filter circuit [19]

Table. 3-2 Specifications of the amplifier and the filter circuit

Specification	Unit	Value	Specification	Unit	Value
V_1	V	15	R_2	kΩ	10
V_2	V	−15	R_3	kΩ	10
C_1	pF	820	R_4	kΩ	10
C_2	μF	0.01	R_5	kΩ	1.3
C_3	μF	0.01	R_6	kΩ	27.4
C_4	μF	0.07	R_7	kΩ	10
R_1	kΩ	10			

3.5 Sensing Methodology

The concentrated-field magnet matrix introduced in the previous chapter generates continuous and periodic sinusoidal magnetic flux density in each axis. The magnetic flux densities are measured by Hall-effect sensors to identify the platen's position. Figure 3-8 shows sinusoidal magnetic flux densities of four pitches in x, y, and z, respectively. The actual magnetic matrix has a total of 6×6 pitches in x-y plane.

(a)

(b)

(c)
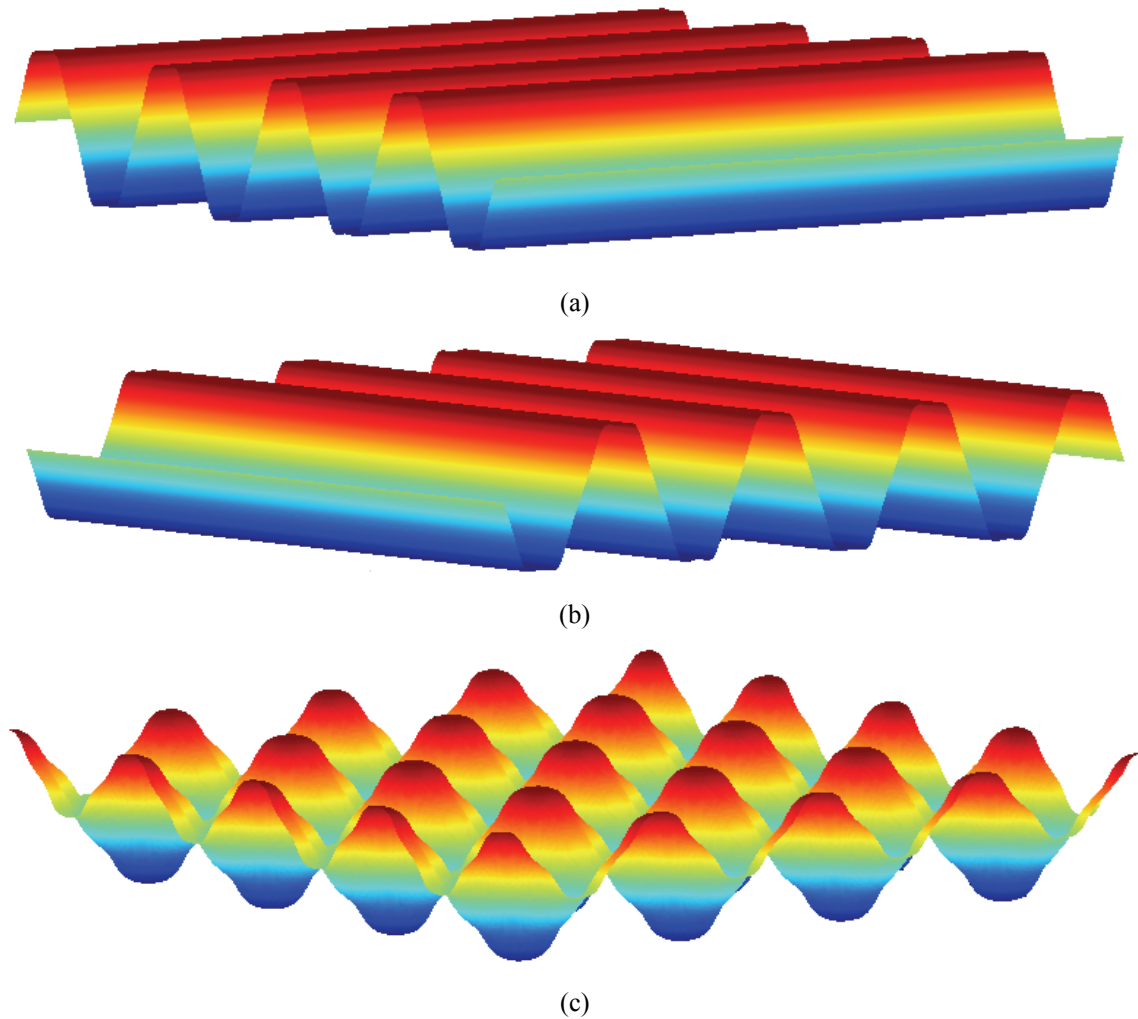
Figure 3-8: Magnetic flux density of 4 pitches in (a) x, (b) y, and (c) z

A single Hall-effect sensor cannot detect the unique position of the platen, because there are two of the same magnitude points in one pitch sinusoidal magnetic flux density. Therefore, two Hall-effect sensors collaborate for one-axis motion. Moreover, it is used to determine the direction of motion with the phase lag between two hall-effect sensors.

As we can see in Figure 3-8, the magnetic flux density has symmetric and periodic forms. These make the positioner move long range over one pitch. In this case, it is crucial to have specific a sensor position gap that causes the phase lag as follows,

$$\left(\frac{1}{4} + \frac{1}{2} n \right) \times \text{pitch}, \ n = 1, 2, 3, \dots \tag{3.1}$$

If the sensor position gap exists following by equation (3.1), one of the sensors is always located at the detectable intervals drawn by thick line in Figure 3-9. Those detectable intervals are sensitive measurement intervals. The periodic and sinudoial magnetic flux density is converted to the voltage signal by the Hall-effect sensor.

Since we are using the sensitive intervals, the sensor switching should happen at every quarter pitch. Thick lines in the figure represent the intervals where Hall-effect sensors operate. The key point of the sensor switching is to generate the continuous sensor signal without interruption.

Figure 3-10 illustrates how the Hall-effect sensors collaborate to generate single-axis motion. On the normalized sinusoidal wave, the sensitive intervals detected by each Hall-effect sensor are denoted by the thick lines. For example, Figure 3-10 (a) shows that the sensor B enters the sensitive interval and the data from the sensor B are going to be obtained. The sensor B produces the positioning data in the sensitive interval in Figure 3-10 (b). Lastly, the measuring sensor switches in Figure 3-10 (c). The sensor B steps out

from the sensitive interval and the sensor A enters the sensing interval at the same time. This sensor switching happens repeatedly when the platen moves over a pitch.
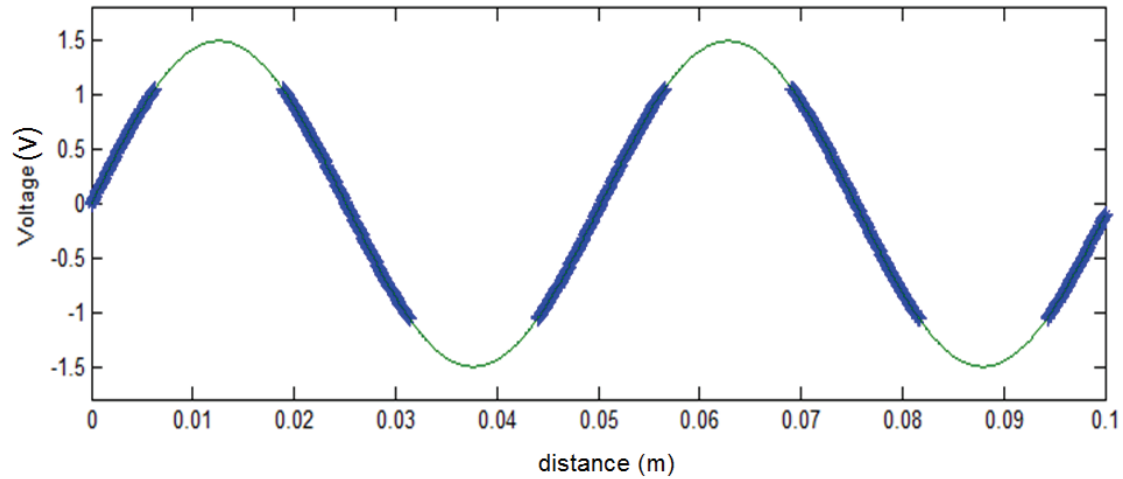
Figure 3-9: Measurement interval in the voltage signal with respect to the magnetic flux density

Figure 3-11 illustrates the sections of the sensor position with phase difference. Two sinusoidal waves indicate the voltage signals of magnetic flux densities from Hall-effect sensors A and B in x and sensors A and C in y. According to the Hall-effect sensor position in equation (3.1), two waves of magnetic flux densities have a phase difference of 90°. A pitch of magnetic flux density can be separated by eight sections in Figure 3-11. The collaboration of two Hall-effect sensors makes sensor measurements become continuous over a pitch using only sensitive interval in sinusoidal waves.

Each Hall-effect sensor has two axis measuring orthogonal directions. Three Hall-effect sensors produce a total of six voltage data, however, the positioner uses four axes to generate translations in x and y such as V_{ax}, V_{bx}, V_{ay}, and V_{cy}. Figures 3-13 and 3-14 present the voltage data with respect to the magnetic flux densities in x and y, respectively. Each plot explains that the magnet matrix has six pitches in both axes. The

(a)

(b)

(c)
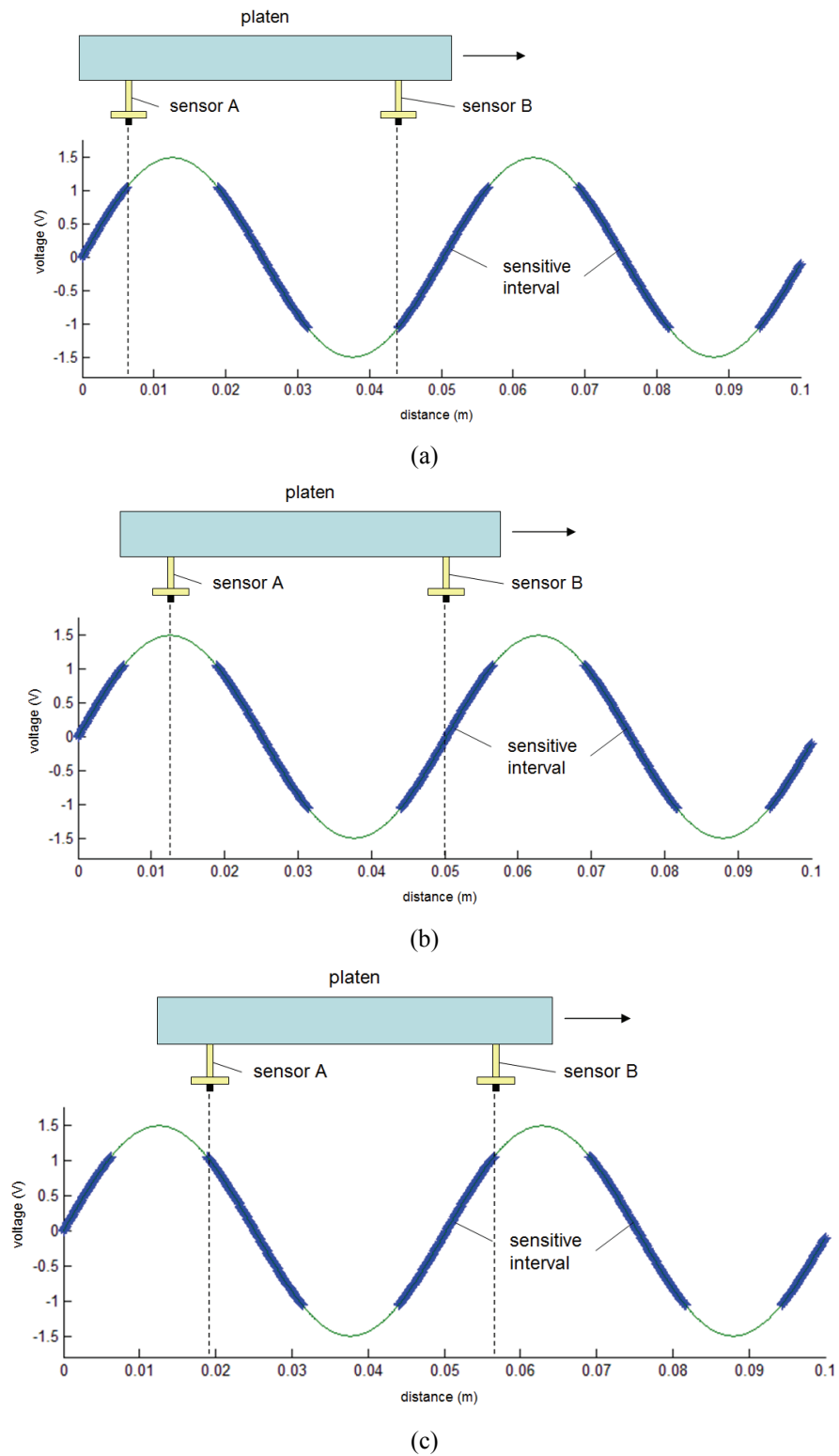
Figure 3-10 : Illustration of the sensor switching and collaboration principle
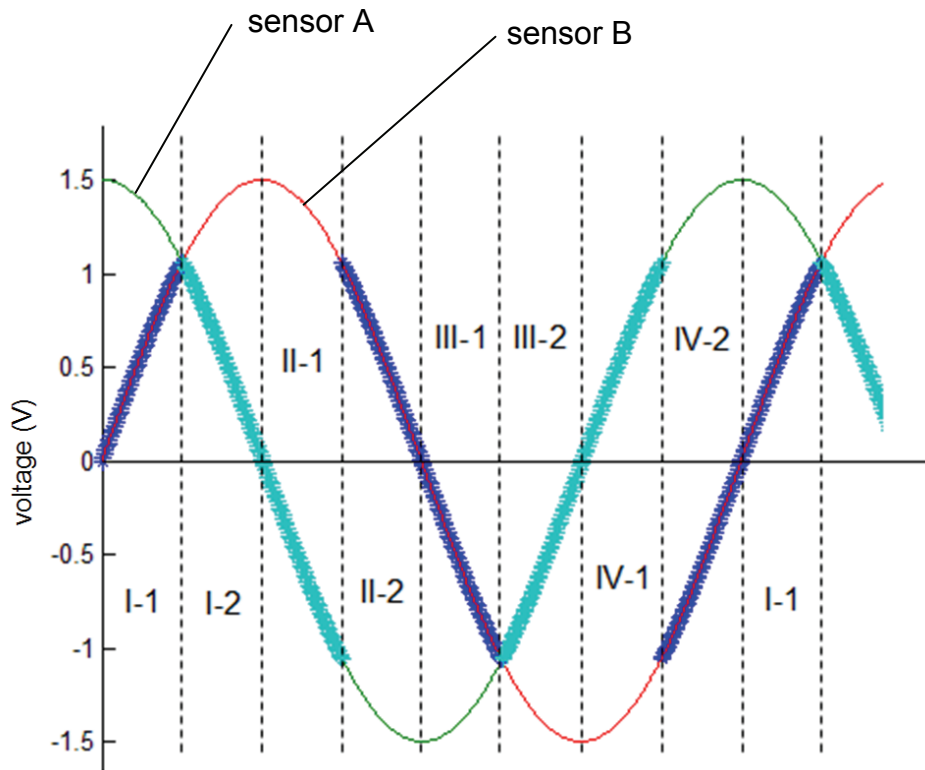
Figure 3-11 : Sensor position arrangement

voltage data were obtained through the single axis scanning motion in six different positions depending on pitches in Figure 3-12. The following Figures 3-13 and 3-14 illustrate the scanning results in the *x-y* plane. Two figures show the almost identical plots, which imply that the magnetic flux densities are uniformly generated at every pitch. However, manufacturing errors might cause the nonlinearity of flux density, for example, the strong forces among magnets bring on the misalignment of the magnet blocks.

Voltage data directly from the Hall-effect sensors need to be normalized. The values of $\tilde{a}_x$, $\tilde{b}_x$, $\tilde{a}_y$, and $\tilde{c}_y$ represent the normalized data become identical with the constants of ω_{ax}, ω_{bx}, ω_{ay}, and ω_{cy} and the offset values of $V_{axoffset}$, $V_{bxoffset}$, $V_{ayoffset}$, and $V_{cyoffset}$. The normalization result is presented in Figure 3-15.

$$\tilde{a}_x = \omega_{ax} \cdot V_{ax} + V_{axoffset} \,, \tag{3.2}$$

$$\tilde{b}_x = \omega_{bx} \cdot V_{bx} + V_{bxoffset} \,, \tag{3.3}$$

$$\tilde{a}_y = \omega_{ay} \cdot V_{ay} + V_{ayoffset} \,, \tag{3.4}$$

$$\tilde{c}_y = \omega_{cy} \cdot V_{cy} + V_{cyoffset} \,, \tag{3.5}$$
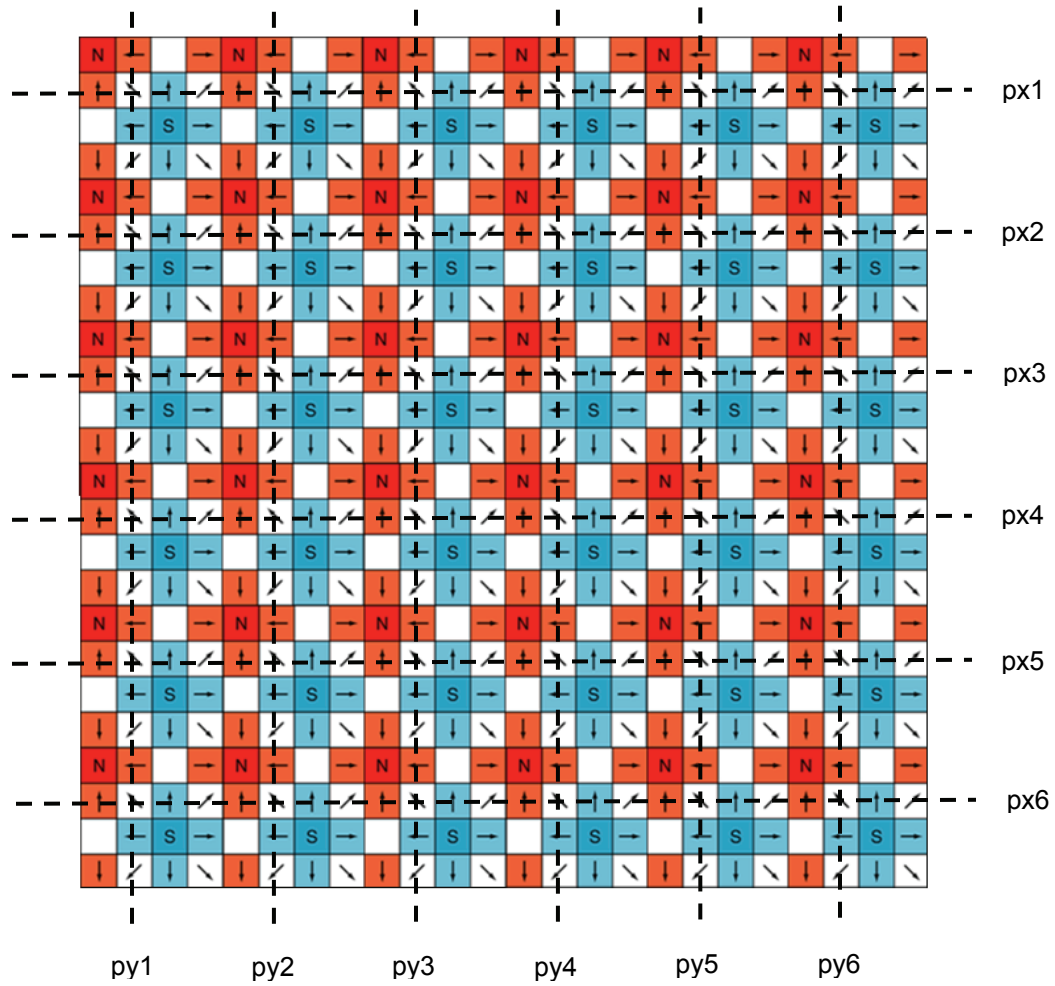
Figure 3-12: Notation of the magnet piches in the *x-y* plane
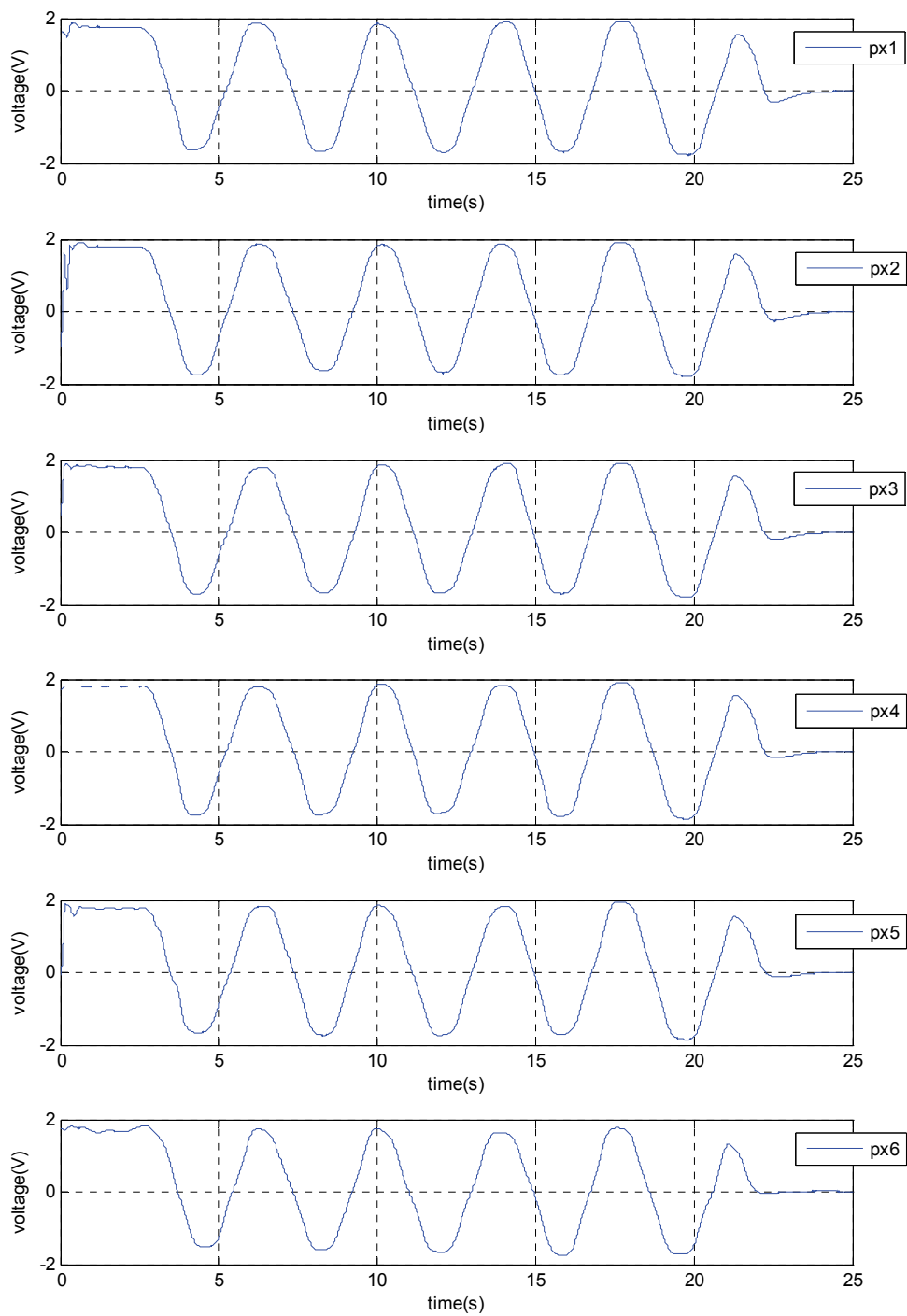
Figure 3-13: Voltage profile of the magnetic flux density in *x*
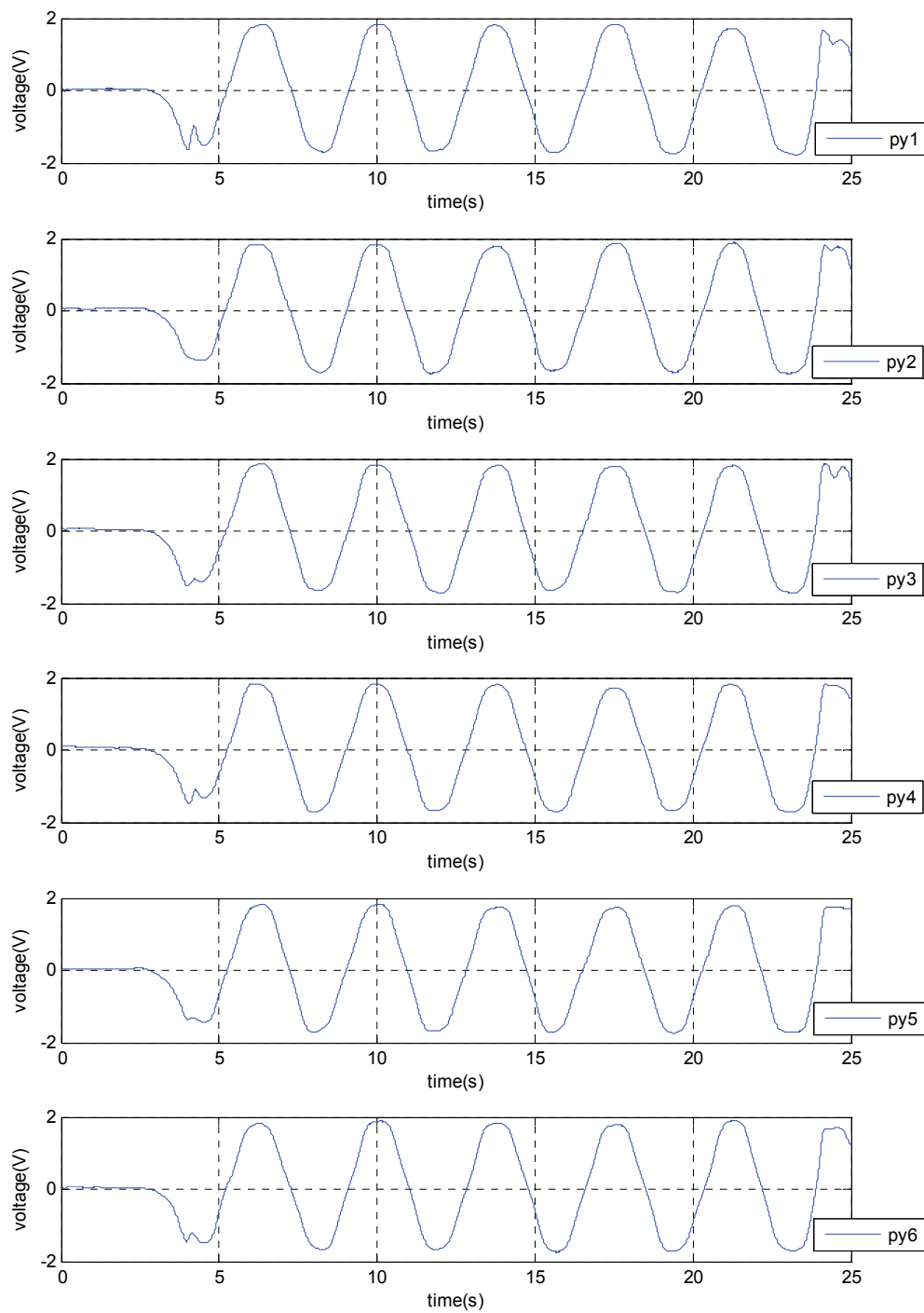
Figure 3-14: Voltage profile of the magnetic flux density in *y*
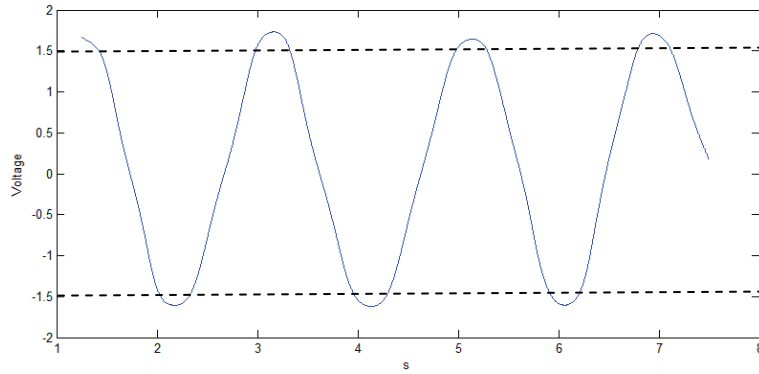
(a)
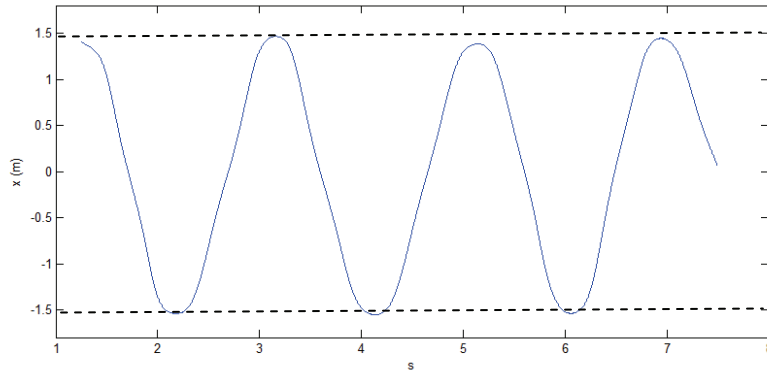
(b)

Figure 3-15: (a) Rough voltage output from Hall-effect sensor in x and (b) output after the normalization

The values of a_x, b_x, a_y, and c_y in equation (3.6–3.9) represent the sine values from the

normalized data

$$a_x = \sin(\omega_{ax} \cdot V_{ax} + V_{axoffset}),$$

(3.6)

$$b_x = \sin(\omega_{bx} \cdot V_{bx} + V_{bxoffset}),$$

(3.7)

$$a_y = \sin(\omega_{ay} \cdot V_{ay} + V_{ayoffset}),$$

(3.8)

$$c_y = \sin(\omega_{cy} \cdot V_{cy} + V_{cyoffset}),$$

(3.9)

The equations (3.10–3.13) are the time derivative terms of normalized data.

$$\Delta x_a = \frac{da_x}{dt}, \tag{3.10}$$

$$\Delta x_b = \frac{db_x}{dt}, \tag{3.11}$$

$$\Delta y_a = \frac{da_y}{dt}, \tag{3.12}$$

$$\Delta y_c = \frac{dc_y}{dt}, \tag{3.13}$$

A pitch of the magnetic flux density wave consists of eight distinguished sections that are adopted with different rules. These eight sections in single pitch are repeated over the entire magnet matrix, which has a total of six pitches in the *x-y* plane.

(a) I-1: In this region, the sensitive interval of sensor A and values of ω_{ax} and ω_{ax} are used with a scalar of α in *x*- and *y*-direction. Sensor data Δx_b in *x* and Δy_c in *y* compensate the variables of Δx_d and Δy_d with scaling factor of β.

$$\Delta x_d = \alpha \cdot \Delta x_a - \beta \cdot \Delta x_b, \tag{3.14}$$

$$\Delta y_d = \alpha \cdot \Delta y_a - \beta \cdot \Delta y_c, \tag{3.15}$$

(b) I-2: Both sensors have positive voltage signals. The sensitive interval that is the negative time derivative terms from sensor B in *x* and sensor C in *y* are mainly used with a scaling factor of α.

$$\Delta x_d = \beta \cdot \Delta x_a - \alpha \cdot \Delta x_b, \tag{3.16}$$

$$\Delta y_d = \beta \cdot \Delta y_a - \alpha \cdot \Delta y_c, \tag{3.17}$$

(c) II-1: The positive voltage signal from sensor A and the negative voltage signal with negative time derivative from sensor B in *x* and sensor C in *y* exist in this

interval. The main sensors in the sensitive interval are identical with the previous section I-2.

$$\Delta x_d = -\beta \cdot \Delta x_a - \alpha \cdot \Delta x_b, \tag{3.18}$$

$$\Delta y_d = -\beta \cdot \Delta y_a - \alpha \cdot \Delta y_c, \tag{3.19}$$

(d) II-2: Like section II-1, the positive voltage signal from sensor A and the negative voltage signal from sensor B or C exist. The main sensor measuring the magnetic flux density is switched to sensor A. Both of sensor's time derivative terms are negative.

$$\Delta x_d = -\alpha \cdot \Delta x_a - \beta \cdot \Delta x_b, \tag{3.20}$$

$$\Delta y_d = -\alpha \cdot \Delta y_a - \beta \cdot \Delta y_c, \tag{3.21}$$

(e) III-1: Both sensors' voltage signals are negative, though the time derivative term from sensor B or C turns to the positive. The mainly using sensor in the sensitive interval and its sign of time derivative term are not changed from section II-2.

$$\Delta x_d = -\alpha \cdot \Delta x_a + \beta \cdot \Delta x_b, \tag{3.22}$$

$$\Delta y_d = -\alpha \cdot \Delta y_a + \beta \cdot \Delta y_c, \tag{3.23}$$

(f) III-2: In this section, the measuring sensor in the sensitive interval is switched to sensor B in x and sensor C in y. Voltage sensor signals from both of sensors are negative position. The positive time derivative in sensor B or C's signal and the negative time derivative in sensor A's signal are achieved.

$$\Delta x_d = -\beta \cdot \Delta x_a + \alpha \cdot \Delta x_b, \tag{3.24}$$

$$\Delta y_d = -\beta \cdot \Delta y_a + \alpha \cdot \Delta y_c, \tag{3.25}$$

(g) IV-1: The voltage signal from sensor A keeps remaining negative, but the voltage signal from sensor B or C turns to positive position. The main sensor keeps same with the previous section, III-2. Both of time derivative terms are positive.

$$\Delta x_d = \beta \cdot \Delta x_a + \alpha \cdot \Delta x_b, \tag{3.26}$$

$$\Delta y_d = \beta \cdot \Delta y_a + \alpha \cdot \Delta y_c, \tag{3.27}$$

(h) IV-2: It is the last section in a pitch to generate extended motion generation in the *x-y* plane. Both of the sensor voltage signals are positive and the sensor A measures mainly the magnetic flux density in the *x-y* plane. The positive time derivative from sensor A and the negative time derivative from the sensor B or C exist in this section.

$$\Delta x_d = \alpha \cdot \Delta x_a + \beta \cdot \Delta x_b, \tag{3.28}$$

$$\Delta y_d = \alpha \cdot \Delta y_a + \beta \cdot \Delta y_c, \tag{3.29}$$

The eight distinct sections in a single pitch are repeated on the magnet matrix because the magnetic flux density is periodic in space. Hence, the positioner can generate unrestricted motions in the *x-y* plane with respect to the size of the magnet matrix.

3.6 Filtering

The position data calculated from the Hall-effect sensors need to filter out the noise. So, a recursive discrete-time Kalman filter (DKF) was used [19]. The DKF provides the estimates of the velocity values in *x*, *y*, and ϕ, which are used in the design of multivariable control in horizontal mode.

The state values are,

$$\bar{k} = \begin{bmatrix} x & y & r \end{bmatrix}^T \tag{3.30}$$

$$\bar{x}_n = \begin{bmatrix} \bar{k} \\ \dot{\bar{k}} \\ \ddot{\bar{k}} \end{bmatrix} \tag{3.31}$$

The output values of positioner in x, y, and the rotation of z are in equation (3.30). The dynamic model in continuous time is presented as follows,

$$\begin{bmatrix} \dot{\bar{k}}(t) \\ \ddot{\bar{k}}(t) \\ \dddot{\bar{k}}(t) \end{bmatrix} = \begin{bmatrix} 0 & I_{3\times3} & 0 \\ 0 & 0 & I_{3\times3} \\ 0 & 0 & 0 \end{bmatrix} \begin{bmatrix} \bar{k}(t) \\ \dot{\bar{k}}(t) \\ \ddot{\bar{k}}(t) \end{bmatrix} + \begin{bmatrix} 0 \\ 0 \\ I_{3\times3} \end{bmatrix} \bar{w}(t), \tag{3.32}$$

$$\widetilde{y}(t) = \begin{bmatrix} I_{3\times3} & 0 & 0 \end{bmatrix} \begin{bmatrix} \bar{k}(t) \\ \dot{\bar{k}}(t) \\ \ddot{\bar{k}}(t) \end{bmatrix} + \bar{\theta}(t), \tag{3.33}$$

where values $\bar{\theta}(t)$ are the measurement noise from the Hall-effect sensors, which are assumed as zero-mean Gaussian noise.

$$\bar{\theta}(t) \sim N(0, R_k). \tag{3.34}$$

R_k and w(t) are the error covariance matrix and the process noise presented in Chapter VII.

The discrete time model is,

$$\bar{x}_{n+1} = \begin{bmatrix} I_{3\times3} & (\Delta t)I_{3\times3} & \frac{1}{2}(\Delta t)^2 I_{3\times3} \\ 0 & I_{3\times3} & (\Delta t)I_{3\times3} \\ 0 & 0 & I_{3\times3} \end{bmatrix} \bar{x}_n + \begin{bmatrix} \frac{1}{6}(\Delta t)^3 I_{3\times3} \\ \frac{1}{2}(\Delta t)^2 I_{3\times3} \\ (\Delta t)I_{3\times3} \end{bmatrix} \bar{w}_n = A\bar{x}_n + \Gamma\bar{w}_n, \tag{3.35}$$

$$\widetilde{y}_n = \begin{bmatrix} I_{3\times3} & 0 & 0 \end{bmatrix}\bar{x}_n + \bar{\theta}_n = C\bar{x}_n + \bar{\theta}_n, \tag{3.36}$$

where Δt is the integration time in real-time control. The error covariance matrix Q_n from the noise $\overline{w}_n$, which is the positive constant matrix is presented in equation (3.37) [84].

$$Q_n = \begin{bmatrix} q_x & 0 & 0 \\ 0 & q_y & 0 \\ 0 & 0 & q_r \end{bmatrix}, \tag{3.37}$$

where values are determined experimentally as $q_{(x,y)} = 100 \text{ m}^2/\text{s}^6$ and $q_r = 10^5 \text{ rad}^2/\text{s}^6$. The filter dynamics is related to the size of value q. Small values of q can filter out the noise effectively, however it cause the slow convergence with small bandwidth. Large values of q have high speed of convergence, but it cannot filter out noise well. There is a design trade-off, where large q causes the big overshoot. The bandwidth of the filter needs to be much faster than the controller and effectively filter out the noise at the same time. The bandwidth of a DKF was set at 50 Hz in x and y, as well as at 100 Hz in the rotation around z [19].

$$P_{n+1} = A_n P_n A_n^T + \Gamma_n Q_n \Gamma_n^T, \tag{3.38}$$

$$P_0 = p_0 I_{9 \times 9}, \tag{3.39}$$

where P is equal to the covariance matrix of the optimal estimation error. The initial value of $p_0 = 1 \times 10^{-8} \text{ m}^2$ was determined by experiments to obtain good convergence [19]. The gain matrix is

$$K_n = P_n C_n'^T (C_n P_n C_n^T + R_n)^{-1}. \tag{3.40}$$

Figure 3-15 (a) and (b) illustrate the output results that are obtained directly by Hall-effect sensors with the zero position in x and after DKF, respectively. In Chapter VII, all experimental results will be shown as the filtered data.
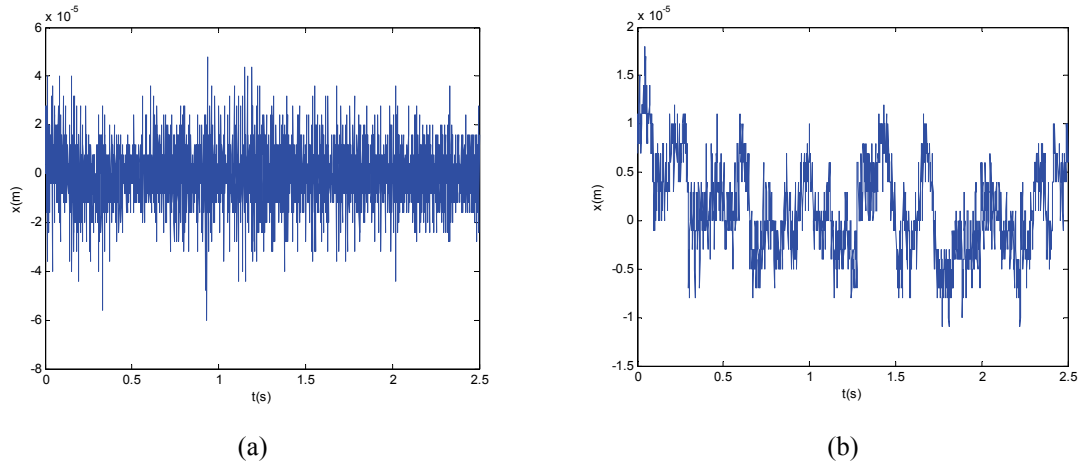
Figure 3-16: Zero position outputs in *x*: (a) Hall-effect sensor data and (b) after filtering

3.7 Laser Distance Sensor

3.7.1 Instrumentation

The vertical mode position feedback is performed by three laser distance sensors (Nanogage 100). The vertical mode includes a translation in *z*, pitch, and roll. Non-magnetic body parts of the sensors do not affect anything on magnetic field and the planar motors working. Figure 3-17 presents the laser distance sensor and its measurement range, respectively. The entire signal-capture range of the laser distance sensor is ±400 μm. However, the area in which the laser sensor can measure linearly is 100 μm in the middle of the signal-capture range. A three-colored LED light indicates the sensor position–red indicates the sensor position loses signals, yellow turns on within the capture range, and green indicates that the sensor is placed at the proper position near the zero crossing. By experimental calibrations, laser distance sensors transmit the voltage signal of ±5 V to the ADC. Specifications of the laser distance sensor are presented in Table 3-3.

Table 3-3. Specifications of the laser distance sensor

Specification	Unit	Value
Linear measurement range	μm	100
Signal capture range	μm	800
Resolution	nm	15
Bandwidth	kHz	100
Sensor head standoff	mm	3
Perpendicular tolerance	degree	± 0.1
Surface reflectivity for full resolution	%	4~ 100
Sensor body length	mm	58.7
Maximum sensor diameter	mm	15.9
Measurement spot diameter	μm	100

Large bandwidth of 100 kHz makes the Nanogage 100 sensor suitable for high speed run-out or vibration measurements. The large 3-mm laser head stand-off has benefits in several applications such as the handling equipment requires additional clearance like semiconductor wafers. In addition, the sensors are insensitive to temperature as well as the small size of sensor (2.31 in length and 0.623 in diameter) gives the convenience of installation and equipment development.

Figure 3-18 illustrates the basic working principle of the laser distance sensor. The laser distance sensor is a folded optical triangulation sensor composed of a bi-cell detector and has precisely controlled focal spot size. The Automatic Gain Controlled (AGC) laser diode source and the bi-cell detector have a 10 micron gap. The laser beam from the diode is reflected by the target area and then it goes into the detector. The output voltage that is proportional to the vertical displacement is generated by the laser signals from the bi-cell detector. The size of detector and focal spot determines the linear measu-

(a)
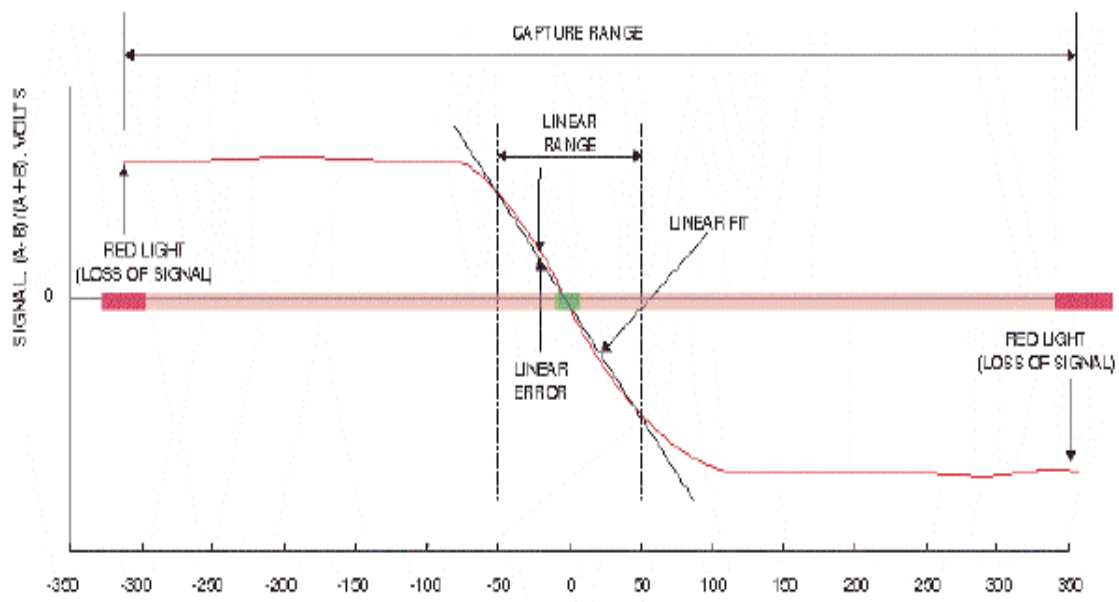
(b)

Figure 3-17: (a) Laser distance sensor (Nanogage 100) and (b) its linear measurement range [OPTRA datasheet]
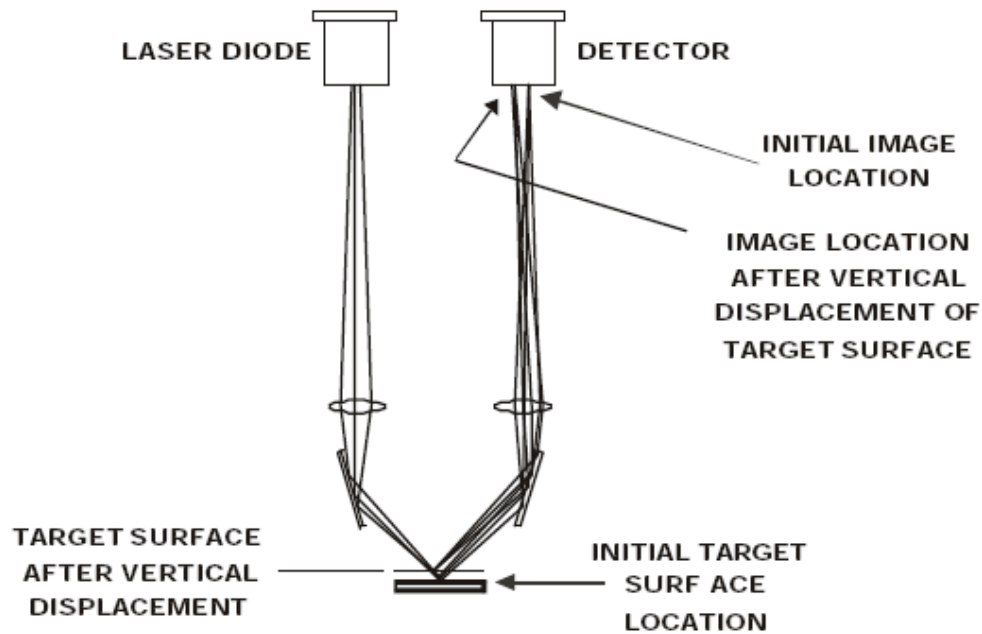
Figure 3-18: Basic principle of the laser distance sensor [85]

rement range of sensors unlike triangulation sensors based on position-sensing detectors. The linearity with respect to the voltage output is finally defined by the numerical calibration and corrections [85].

3.7.2 Sensor Positions and Dynamics

According to the equation (3.1), the sensor position gap of 63.5 mm as illustrated in Figure 3-19 was decided and the phase lag of 90° occurs between sensors. Figure 3-18 shows the location of three Hall-effect sensors on the platen with respect to the center of mass. Its specifications are represented in Table 3-4.

The planar motion control in the *x-y* plane is achieved with similar methodology because each axis of the magnetic fields is independently placed in an orthogonal direction. The vertical mode in θ, ψ and z is controlled by feedback from laser distance

sensors as presented in the previous section. Three laser distance sensors are located on the body part illustrated in Figure 3-20. The origin in the coordinate is presented as O that corresponds to the center of mass and each laser distance sensor are noted at 1, 2, and 3. The distances from the origin to each sensor position in x are denoted as $l_{(1,2,3)x}$ and the distances between the origin and the laser distance sensor positions in y are similarly represented as $l_{(1,2,3)y}$. Table 3-5 shows variables of sensor distance values. The photograph of the Hall-effect sensor and laser distance sensor mounted on the platen are shown in Figure 3-21.

According to the values in Table 3-5, sensor equations are derived from the laser distance sensors' geometric parameters. The laser distance sensors (Nanogage 100) produce the displacement information for the position sensing. The relationship between sensor readings and vertical motions are presented as follows,

$$
\begin{bmatrix} l_1 \\ l_2 \\ l_3 \end{bmatrix} = \begin{bmatrix} l_{1y} & l_{1x} & 1 \\ l_{2y} & -l_{2x} & 1 \\ -l_{3y} & -l_{3x} & 1 \end{bmatrix} \begin{bmatrix} \theta \\ \psi \\ z \end{bmatrix} = \begin{bmatrix} 37.02 & 30.61 & 1 \\ 37.02 & -28.73 & 1 \\ -48.97 & -34.68 & 1 \end{bmatrix} \begin{bmatrix} \theta \\ \psi \\ z \end{bmatrix},
\tag{3.41}
$$

The vector $\begin{bmatrix} l_1 & l_2 & l_3 \end{bmatrix}^T$ denotes the each sensor reading, and the displacement of the vertical mode is represented as the vector $\begin{bmatrix} \theta & \psi & z \end{bmatrix}^T$. The rotation around x, the rotation around y, and the translation in z are shown as θ, ψ, and z, respectively. By taking inverse coefficient matrix transformation, we can obtain the equation (3.42),

$$
\begin{bmatrix} \theta \\ \psi \\ z \end{bmatrix} = \begin{bmatrix} -1.16606 & 12.7953 & -11.6293 \\ 16.852 & -16.852 & 0 \\ 0.527327 & 0.042158 & 0.430515 \end{bmatrix} \begin{bmatrix} l_1 \\ l_2 \\ l_3 \end{bmatrix},
\tag{3.42}
$$
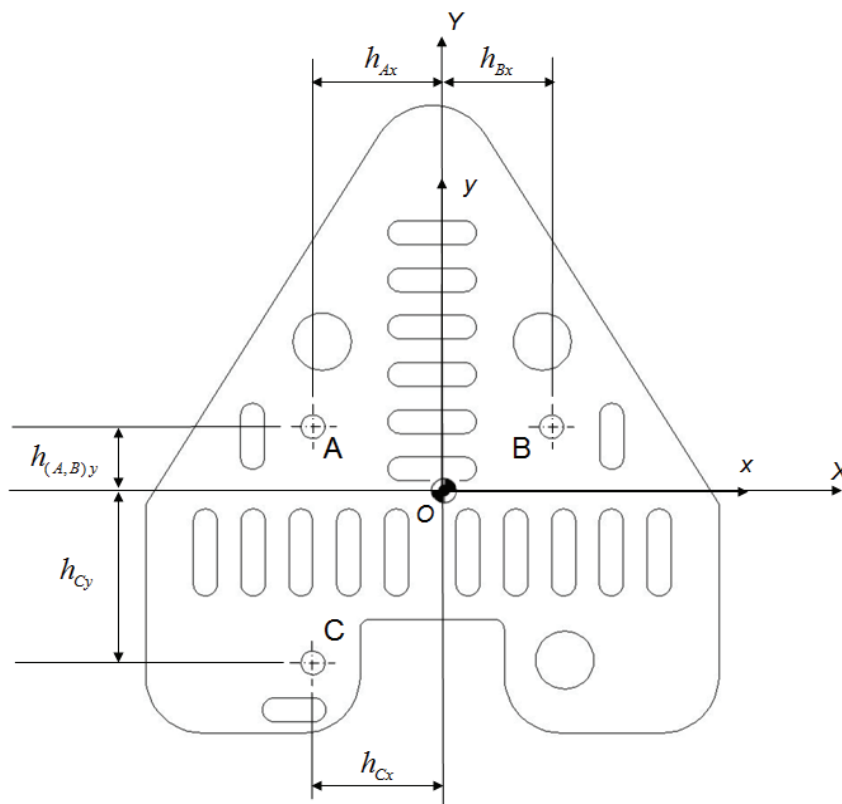
Figure 3-19: Hall-effect sensor locations

Table 3-4 Hall-effect sensor locations from the origin

Variables	Distance (mm)
h_{Ax}	33.57
h_{Bx}	30.81
h_{Cx}	33.57
h_{Ay}	13.77
h_{By}	13.77
h_{Cy}	49.73
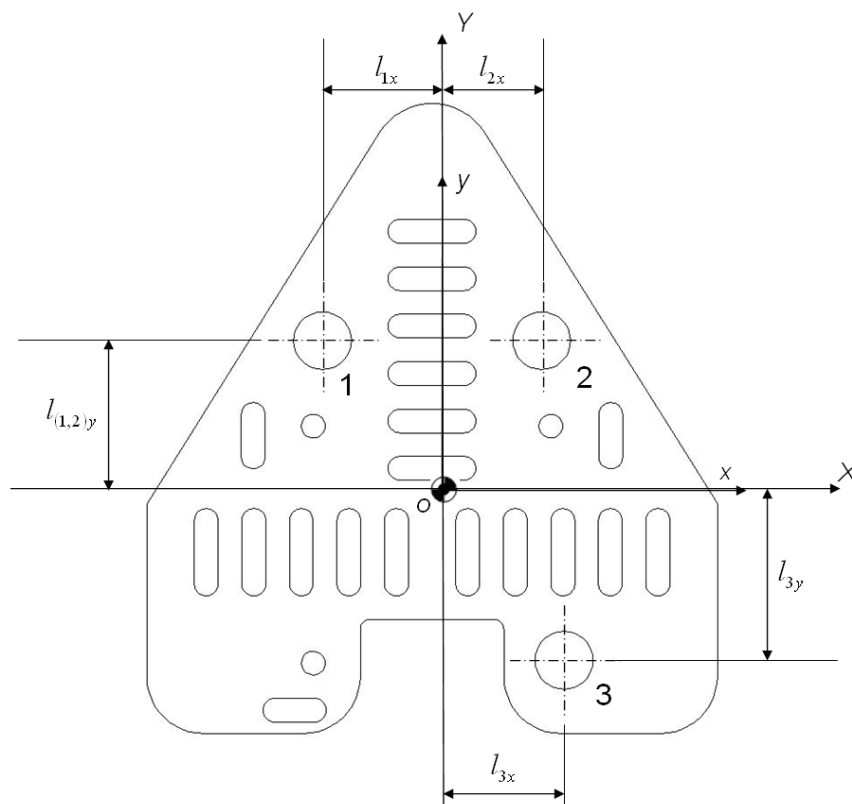
Figure 3-20: Laser distance sensor locations

Table 3-5. Specifications of the laser distance sensor locations

Variables	Distance (mm)
l_{1x}	30.61
l_{2x}	28.73
l_{3x}	34.68
l_{1y}	37.02
l_{2y}	37.02
l_{3y}	48.97

From the transformation matrix (3.42), the levitation motion is presented by the location of the laser distance sensors.

$$z = 0.527327l_1 + 0.042158l_2 + 0.430515l_3,$$
(3.43)

laser distance sensor
(Nanogage 100)

Hall-effect sensor and data
connection board
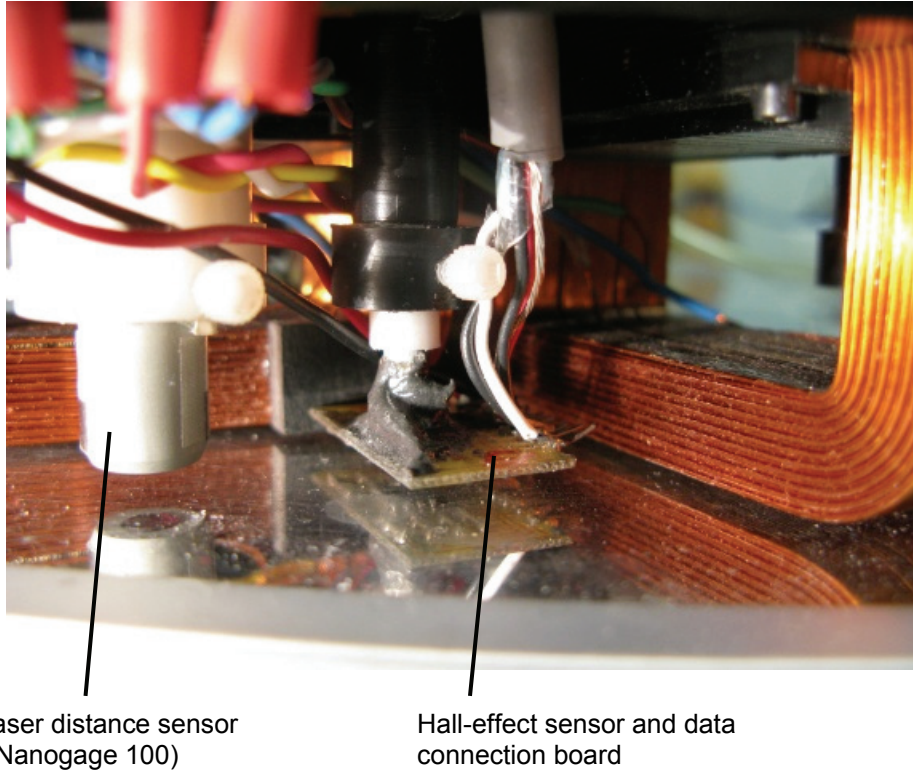
Figure 3-21: Photograph of the laser distance sensor and the Hall-effect sensor

3.7.3 Anti-Aliasing and Voltage-Clamp Circuit

The anti-aliasing filter to avoid aliasing is shown in Figure 3-22. It is the first-order low-pass analog filter with the cut-off frequency of 1 kHz. Table 3-6 presents specifications of the anti-aliasing filter. Two clamping diodes regulate the output voltage

of ±5 V, which was the input swing of ADCs. The purpose of the clamping circuit is to

protect ADCs from the over-voltage.
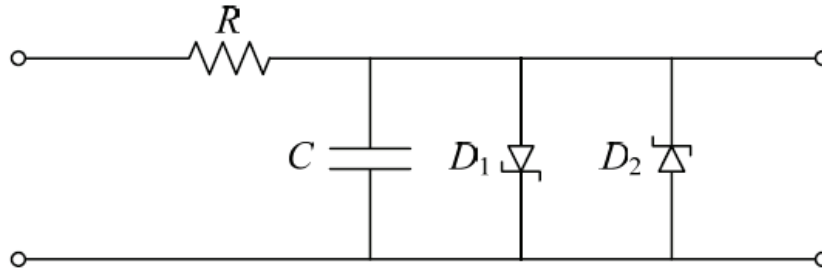
Figure 3-22: Anti-aliasing and voltage-clamp circuit [19]

Table 3-6. Specifications for anti-aliasing filter

Specification	Unit	Value
R	kΩ	10
C	μF	0.015

CHAPTER IV

CONTROL SOFTWARE

This chapter introduces the control algorithm with the computer software to run the positioning system in real time. A Linux-based digital control system was designed and implemented with sampling frequency of 800 Hz. The multi-dimensional precision positioning system in real-time digital control environment was built, tested, and implemented using RTAI for Linux. The real-time system includes the use of Linux kernel of Ubuntu, RTAI, Comedi, Comedi libraries, and C-code. Two data acquisition boards were employed for converting data between analog and digital signals in the control routine. The programming architectures are presented with flow charts.

4.1 Real-Time Control

The meaning of "real-time" can be defined in various ways. However, only two types of the real-time can be generally specified in computer science literature, that of the soft and hard real-time systems [86–89].

First, the soft real-time system depends on the desired schedule. This system can use the average case performances to compensate for bad performances. Therefore, it happens to miss actual data for the interpolation. For instance, missing a frame, from time to time, in a video display does not affect the overall visual of a movie.

On the other hand, the hard real-time system makes sure the given time limit and should have bounded latencies. The timing deadline determined by the user should be

obeyed in a typical routine. Compensation and interpolation as it does in a soft real-time system are not allowed. In this research, the hard real-time magnetic precision positioning system is controlled by RTAI running on Linux. RTAI guarantees hard real-time scheduling by setting timing deadlines.

4.2 Linux and Ubuntu

Linux is used as an operating system to control real-time task for the following reasons. First, Linux is an open-source code that can be downloaded and installed without cost. Secondly, it supports the real-time user interface and shows good performances, and has useful functions and development tools. A Pentium 4 processor computer was used in our system with user interface. In addition, Linux has the advantage of providing safety against viruses and network problems. There are various Linux distributions that are open-source such as Redhat, Mandrake, Caldera, Suse, and Ubuntu.

Ubuntu with RTAI has been installed and demonstrated with the user interface for our real-time control system. The reasons we choose Ubuntu are that it is fast and easy to install, and it supports the Firefox web browser and Opera, making it easy to access the internet. Ubuntu has well arranged tools and graphics. Moreover, it makes other software to be installed easy and it supports hardware application well. For instance, the NI-6221 and NI-6703 data acquisition boards are used in our real-time system. Lastly, Ubuntu occupies lower memory space compared to other operating systems, so that a personal computer with low memory capacity can be used.

4.3 RTAI

RTAI is a kernel modified package of Linux. Dipartimento di Ingeneria Aerospaziale Politecnico di Milano (DIAPM) developed RTAI for the purpose of a real-time operating environment solution. It supports the time critical components needed for real-time control and is suitable for the hard real-time system that needs to be preemptive and deterministic. One of the reasons that RTAI was developed is that Linux alone is not enough to fully support the real-time. Even though Linux has many advantages, such as hardware management, event polling, peripheral interrupts, scheduler classes for process activation and priorities, interprocess communication, and implementation of the network protocols. The real-time operating environment can be established by RTAI that modifies the Linux kernel. For instance, interrupt handling and scheduling policies in kernel behavior need to be changed for a real-time performance. Low latency and timing predictability are required.

Linux kernel and RTAI basically perform same, but RTAI additionally has the ability of a real-time OS. Linux is operated only when the real-time kernel is inactive, because Linux OS kernel is recognized as an idle task by the real-time scheduler, and the real-time task is performed first in the task priority.

The real-time system always reacts to an interrupt. The peripheral interrupts are detected by the RTAI interrupt dispatcher and rearranged to Linux. The real-time kernel stops the interrupts during the processing and it decides the priority for the dispatch. The real-time interrupt handler occurs in proper time, and the interrupt pending status happens without a real-time interrupt handler. The pending interrupt status switches to an enable

status with the Linux interrupt handler, when Linux calls an enable interrupts. Hence, the interrupt is always able to work.

RTAI makes that the real-time system modular and extensible. The scheduler module can find the appropriate alternative module for satisfying the requirements, when the scheduler is executed unsuitably. Real-time system modules use the kernel address space for the purpose of minimizing the task switch time. Additionally, there are several advantages of RTAI. The installation of the real-time system part depends on the Linux loadable module mechanism. The non-real-time operation of loading and unloading modules can be performed by Linux. RTAI also offers the dynamic memory allocation as well as the one-shot and periodic schedulers. It supports UniProcessor, MultiProcessor, and Symmetric Multi-Processor. Remote Procedure Calls (RPCs), shared memory, traditional real-time inter process communications (IPCs), mailbox, first-in-first-outs (FIFOs) are the features of RTAI. Technical performance of RTAI follows below [90–94],

- Context switch time of 4 µs

- Interrupt response of 20 µs

- Periodic tasks of 100 kHz

- One-shot task rates of 30 kHz

4.4 Comedi

Comedi is an acronym for Control and Measurement Device Interface [90]. The Comedi was used to achieve the Input and Output (I/O) interface with the hardware

components such as the positioners, amplifiers, and the data acquisition boards. Comedi is an open-source device driver code like Linux and supports various kinds of driver structures for data acquisition devices. The Comedi open-source project supports an Application Program Interface (API). A standard Linux kernel and RTAI can be used with Comedi. It can develop tools, libraries, and drivers for the data acquisition boards. There are two Comedi packages: comedi and comedilib. The comedi implements the kernel space functionality and comedilib is applied for the user space access for using the device functions [90]. Comedi functions activate the devices which are ADC and DAC boards. For reporting purposes names were designated for the devices in the real-time task. ADC is referred to as "it" and DAC is referred to as "it2". The Comedi devices are referred to as "comedi0" and "comedi1", respectively. The signal type should be defined such as analog I/O and digital I/O. The digit "0" and "1" refer to the analog I/O and the digit "2" refers to the digital I/O in the sub device operation [86].

4.5 Control Structure

Figure 4-1 shows a schematic diagram of the control structure of the multidimensional positioning system. This diagram generally illustrates how the control and sensor signals flow and how they are processed. The real-time control system running on the PC acquires analog data from sensors such as vertical laser sensors (NANOGAGE 100) and 2-channel Hall-effect sensors through the analog-to-digital data acquisition board (NI-6221). A Pentium 4 processor personal computer with a 1 Gigabyte memory compiles C programming codes that include the real-time control routine and digital signal

processing. The C codes working with RTAI and Comedi functions process all the position measurement data and compute the control outputs in order to run the positioner in real time. The user interface to control the platen's position and velocity is developed with C codes. The position data computed from PC flow to the digital-to-analog converter (DAC) of NI-6703, which supports sixteen 16-bit analog output voltage channels with ±10 V and 8 digital I/O lines. The positioner loads a total of three planar motors consisting of three-phases, so the whole system requires nine analog channels covered by NI-6703. Nine independent control output signals from DAC go into the power amplifiers that were designed by Hu [1]. The power amplifiers supply commanded phase currents to the each planar motor winding. The real actuation forces to control the movement of the platen are generated.
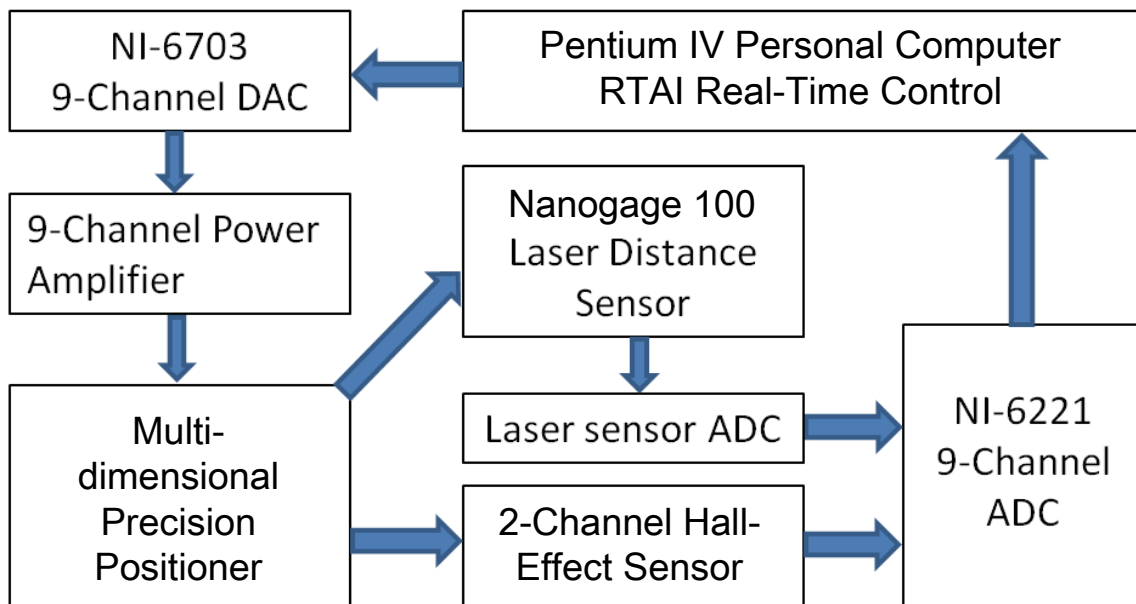
Figure 4-1 Block diagram of the control structure

The multi-dimensional positioning system requires at least nine input channels and nine output channels. The nine analog output channels are for the three 3-phase planar motors. Nine input channels are occupied with three vertical laser sensors and three 2-channel Hall-effect sensors carried in the positioner. Therefore, the data acquisition board requires at least nine independent analog input and output channels. NI-6703 board supports only 16 analog output channels so that an additional data acquisition board is required. NI-6221 board has 16-bit, 250 kS/s 16 analog output channels, 24 digital I/O, two 16-bit analog outputs and 32-bit counters. Therefore, two different data acquisition boards, ADC and DAC converters, were chosen, because nine independent analog input and output channels can not be supported with a single board. Another reason NI boards are used is that the data acquisition board should run with Comedi drivers, which are "ni_pci.mio" and "ni_670x." NI-series data acquisition boards supports Comedi drivers well. The best choice for the data communication is actually to use a single data acquisition board that has both of input and output channels, because a single board data processing does not have an inter-boards time delay. However, there is no choice of single data acquisition boards supporting nine analog inputs and outputs channels simultaneously. Hence, a dual real-time board control system was created even though a dual-board type is slower than a single-board type. The signal processing delay exists for communicating between two boards, because two different board drivers are run and compiled in the same time. In addition, C programming code should open both of A/D and D/A board drivers with Comedi functions so that it takes more execution time. It also requires terminating individually two drivers and devices on program.

The anti-aliasing filter is implemented to prevent aliasing by sampling right after the output signals from laser distance sensors (Nanogage 100). All position measurement signals from laser distance sensors flow to the ADC board (NI-6221) with the signals from 2-axis Hall-effect sensors as illustrated in Figure 4-1. Therefore, all sensor position, voltage, and current signal flows perform a control system feedback as explained above.

Before the current sources are generated by the amplifiers, the voltage sources are controlled by the DAC board. The amplifiers convert the voltage to the current sources. In addition, the sensor signals that are presenting the voltage sources are converted by the ADC board, vice versa. Comedi uses the converting command of "lsampl_t" between signal samples and voltages in both DAC and ADC. The largest sample values and the number of available ranges need to be defined with the maxdata and range functions [94].

4.6 RTAI and Comedi Installation

This section introduces an order and key structures of programming installation. The operating system of Linux, Ubuntu version 6.10, was installed followed by the installation of RTAI version 3.4. Since there is no gcc compiler in RTAI-3.4, an additional gcc-3.4 and its compiler packages are recommended to avoid errors while compiling the RTAI and Comedi, though the latest version of gcc is 4.1.2. A vanilla GNU/Linux kernel is required to be installed to compile the RTAI and Comedi. Before the Comedilib and Comedi are installed, the hardware such as NI-6221 and NI-6703 need to be installed. In the middle step of the installation, there are several procedures to recognize the current hardware. The version of Comedilib-0.8.0 and Comedi-0.7.74 were

used. Since the multi-dimensional positioner uses two data acquisition boards, the dual Comedi driver should be compiled.

4.7 Control Routine

This section presents the digital control routine written in C that includes RTAI and Comedi commands with flowcharts. There are four general sections in the control routine such as the main program, the demonstration routine, the calibration of Hall-effect sensors, and the calibration of the laser distance sensors.

a) Main program

The main body section of the whole control routine is shown in Figure 4-2. The main program incorporates the channels, the voltage signal converting functions, and the signal handling functions. First, all the variables, constant values, sensors channel allocations, and the input/output (I/O) device settings are initialized. Then, the signal handling structures are initialized. For example, the directories and addressees of data are determined, and all data for 6-DOF are saved with different paths at the same time. The Comedi commands are used to read input data from the data acquisition board and regulate the data size. The six calibration values for three two-axis Hall-effect sensors are located in the main program, because they are applied to all demonstrations. The sampling frequency is controlled before the demonstrations, and all digital compensators use this same frequency. Controlling the sampling period with a nano-second unit determines the overall sampling frequency. Finally, the Com-
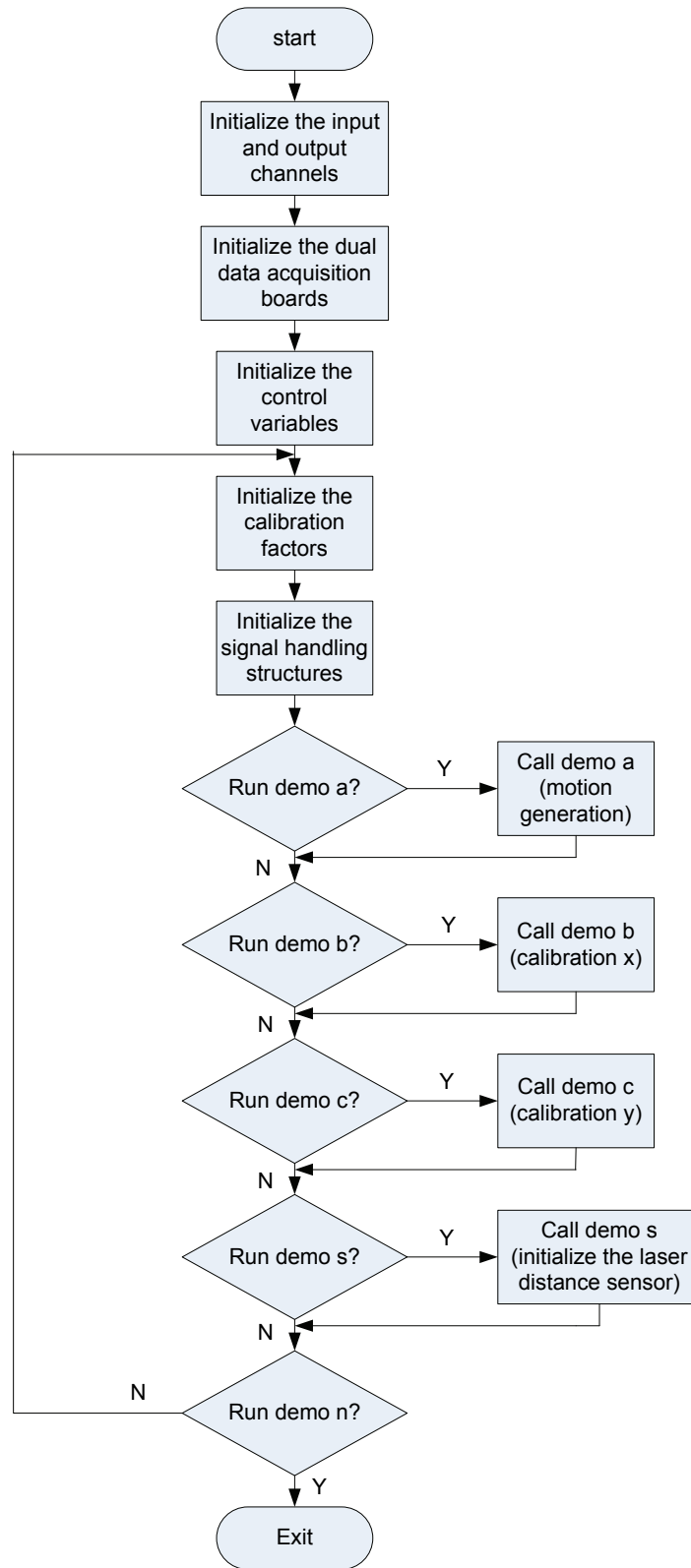
Figure 4-2: Flowchart of the main program

edi commands terminate the program normally and write real-time data through the output channels for the devices that are used at the end of the main body.

b) Demonstration routine

Actual motion generations are performed in this routine. Demonstration routines shown in Figure 4-3 include the several sizes of step responses, linear large scanning motions, and circular motions. The raw data from Hall-effect sensors and laser distance sensors are first acquired. These data are calibrated with the factor designated in the main program. The factors are determined by recursive calibrations for three Hall-effect sensors and three laser distance sensors. The calibrated voltage signals go through the motion generation routine and the implemented real-time digital controllers. This iteration loop is repeated 800 times per second. Nine different voltage data for the nine windings and the voltage signal is converted to a current signal through the amplifiers that are generated in a single sampling period. All six motion profiles are saved as text files. Finally, the Comedi commands write the output data to digital-to-analog converter.

c) Hall-effect sensor calibration routine

This routine presented in Figure 4-4 is constructed only for the calibration of Hall-effect sensor signal in x and y. As mentioned above, the sensor calibration is crucial for the precise motion generation. The Hall-effect sensors read the magnetic flux density from the concentrated field magnet matrix as voltage signals. Two Hall-effect sensors collaborate to identify the platen's position in a single axis. It is important to

```
                    ┌──────────┐
                    │  Start   │
                    └────┬─────┘
                         │
    ┌────────────────────▼────────┐
    │   ┌──────────────────┐      │
    │   │  Set sensor      │      │
    │   │  data input      │      │
    │   │  channels        │      │
    │   └──────────────────┘      │
    │                             │
    │   ┌──────────────────┐      │
    │   │  Calibrate laser │      │
    │   │  distance sensor │      │
    │   │  positions       │      │
    │   └──────────────────┘      │
    │                             │
    │   ┌──────────────────┐      │
    │   │  Calibrate 2-axis│      │
    │   │  Hall-effect     │      │
    │   │  sensor positions│      │
    │   └──────────────────┘      │
    │                             │
    │   ┌──────────────────┐      │
    │   │  Read position   │      │
    │   │  data from laser │      │
    │   │  distance sensors│      │
    │   └──────────────────┘      │
    │                             │
    │   ┌──────────────────┐      │
    │   │  Read position   │      │
    │   │  data from 2-axis│      │
    │   │  Hall-effect     │      │
    │   │  sensors         │      │
    │   └──────────────────┘      │
    │                             │
    │   ┌──────────────────┐      │
    │   │  Digital         │      │
    │   │  compensators    │      │
    │   └──────────────────┘      │
    │                             │
    │   ┌──────────────────┐      │
    │   │  Run demo a      │      │
    │   └──────────────────┘      │
    │                             │
    │   ┌──────────────────┐      │
    │   │  Print position  │      │
    │   │  data            │      │
    │   └──────────────────┘      │
    │                             │
    │   ┌──────────────────┐      │
    │   │  Save each axis  │      │
    │   │  position data   │      │
    │   └──────────────────┘      │
    └──────────┬──────────────────┘
               │
    ┌──────────▼───────┐
    │  Set output data │
    │  with Comedi     │
    │  commands        │
    └──────────┬───────┘
               │
         ┌─────▼────┐
         │   End    │
         └──────────┘
```
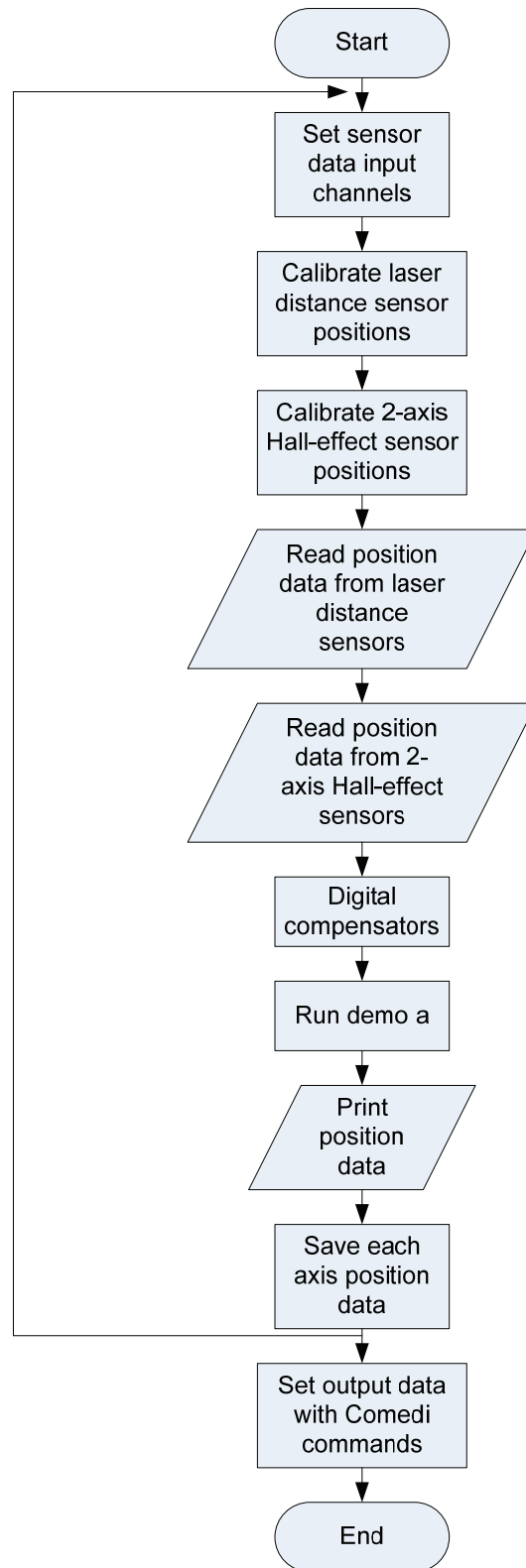
Figure 4-3: Flowchart of the demonstration routine

Keep the same voltage magnitude in two Hall-effect sensors. The channel setting and input sensor data readings are basically the same as the demonstration routine. Linear motions of 200 mm in x and y are performed with open-loop control, while the Hall-effect sensors read the voltage data. Recursive data reading and calculation in MATLAB extract the calibration values.

d) Laser distance sensor calibration routine

Vertical motion generation requires three laser distance sensors. The linear measurement range of the laser distance sensor is just 100 μm. So, accurate calibration and sensor height adjustment is required. The initial position of the sensor is the most appropriate to be located at the center of the linear range, where the LED turns on the green light. Channels for the laser distance sensors are used in this routine. Each sensor should be calibrated and adjusted individually while the iteration loop runs in Figure 4-5. After the individual sensor calibration and the height adjustment are finished, the overall initial sensor position by the geometrical dynamics should be checked. This routine runs with same sampling frequency with other routines.

```
       ┌─────────┐
       │  Start  │
       └─────────┘
            │
            ▼
   ┌─────────────────┐
   │   Set sensor    │
   │  data input     │
   │   channels      │
   └─────────────────┘
            │
            ▼
   ╱─────────────────╱
  ╱  Read position  ╱
 ╱  data from 2-   ╱
╱  axis Hall-effect╱
╱     sensors     ╱
 ─────────────────
            │
            ▼
   ┌─────────────────┐
   │ Calibrate 2-axis│
   │ Hall-effect     │
   │ sensor positions│
   └─────────────────┘
            │
            ▼
   ┌─────────────────┐
   │  Run open loop  │
   │  demo in x & y  │
   └─────────────────┘
            │
            ▼
   ╱─────────────────╱
  ╱      Read       ╱
 ╱   sensor data   ╱
  ─────────────────
            │
            ▼
   ┌─────────────────┐
   │   Save data     │
   └─────────────────┘
            │
            ▼
   ┌─────────────────┐
   │ Set output data │
   │  with Comedi    │
   │   commands      │
   └─────────────────┘
            │
            ▼
       ┌─────────┐
       │   End   │
       └─────────┘
```
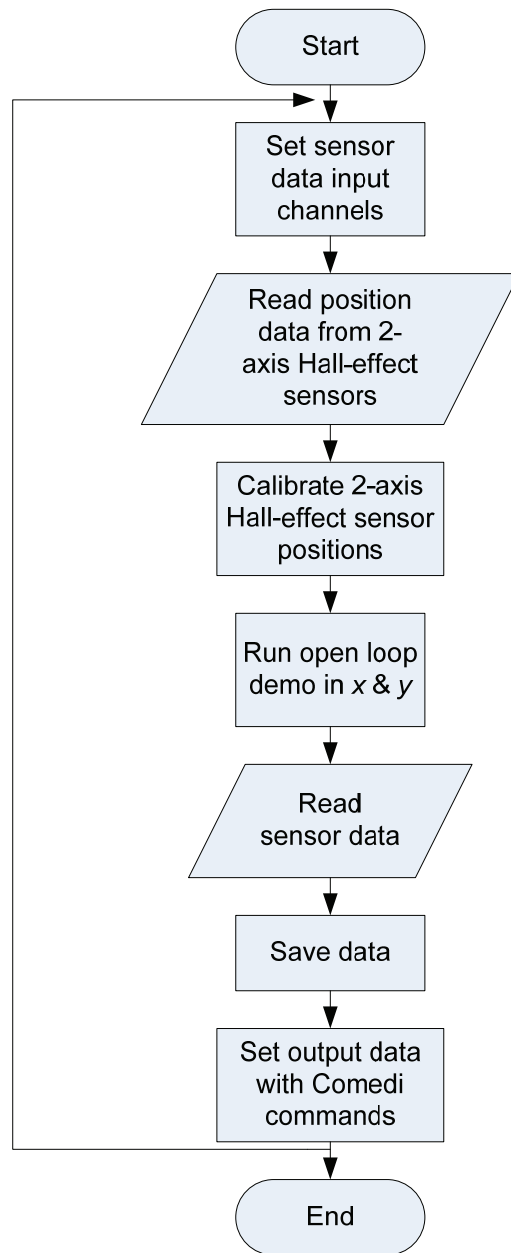
Figure 4-4: Flowchart of the sensor calibrations in x and y
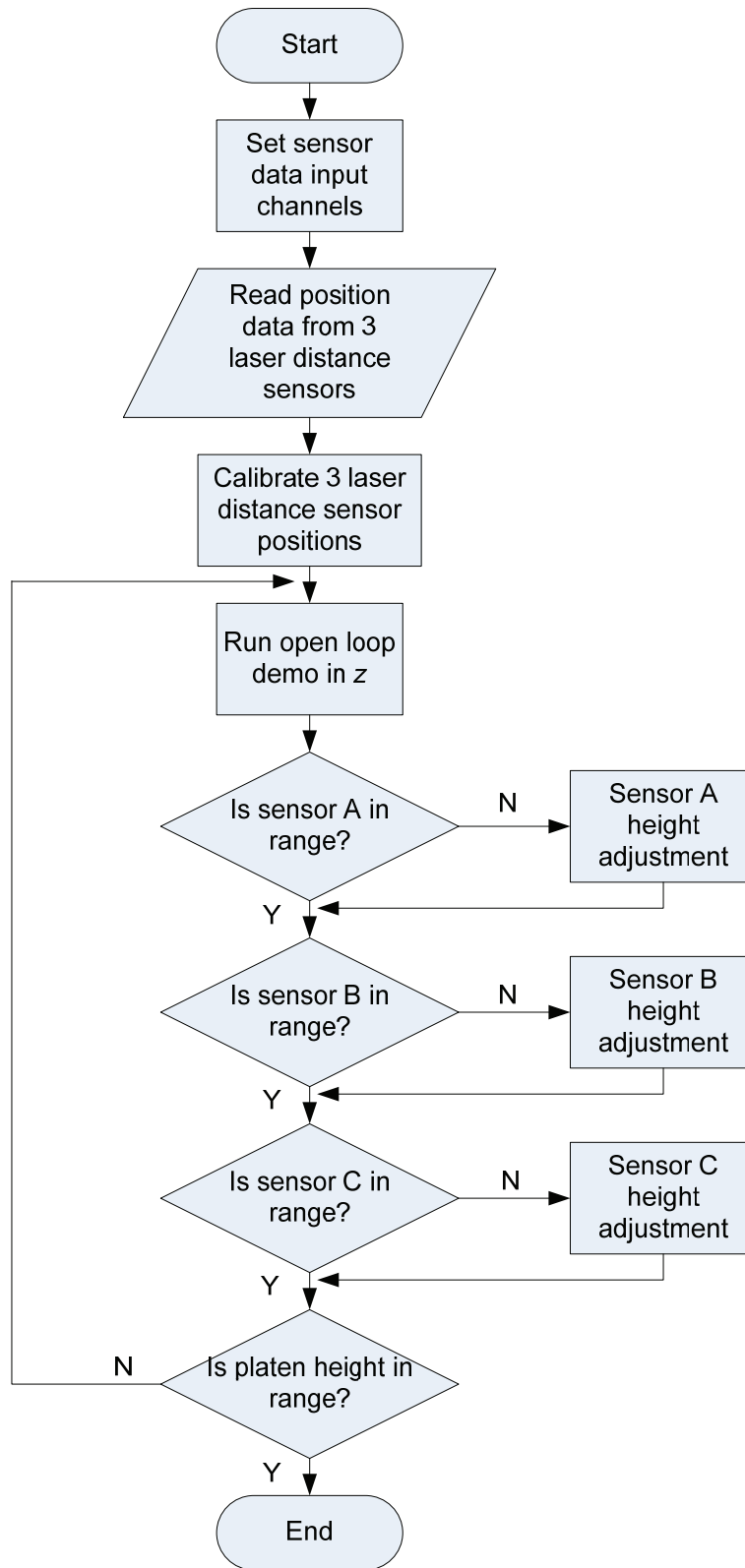
Figure 4-5: Calibration and initialization of the laser distance sensors

CHAPTER V

MECHANICAL DESIGN

In this chapter, the detailed mechanical designs and fabrication processes of the moving platen are discussed. The overview of the magnet matrix, the design of planar motor windings, overall design concepts, the design objective of positioner are first illustrated and then, the machining processes of each part are presented. The mechanical fabrication and the assembly of each component are also presented. Each part includes pictured views and schematic figures with dimensions for better understanding. English units are used for dimensions of mechanical parts.

5.1 Platen

The platen is the single moving part, comprised of a main body made of Delrin, driving planar motors which consist of three coils, three aerostatic bearings, three laser sensors for vertical motions, three Hall-effect sensors for the lateral motions, and two terminal blocks for wire connection. For the purpose of the advanced performance, the platen was designed as compact and light as possible loading all those components. The platen should be considered to set additional devices for wafer such as wafer holders (vacuum or electrostatic chucks) and sensors for alignment for applying in semiconductor manufacturing. However, this research concentrates on the positioner performances without the load.

5.1.1 Magnet Matrix

As discussed previous chapter, the concentrated field magnet matrix array is used as a stator for the precision positioner. This magnet matrix consists of two orthogonal Halbach magnet array so that it generates periodic sinusoidal magnetic flux densities in the *x-y* plane.
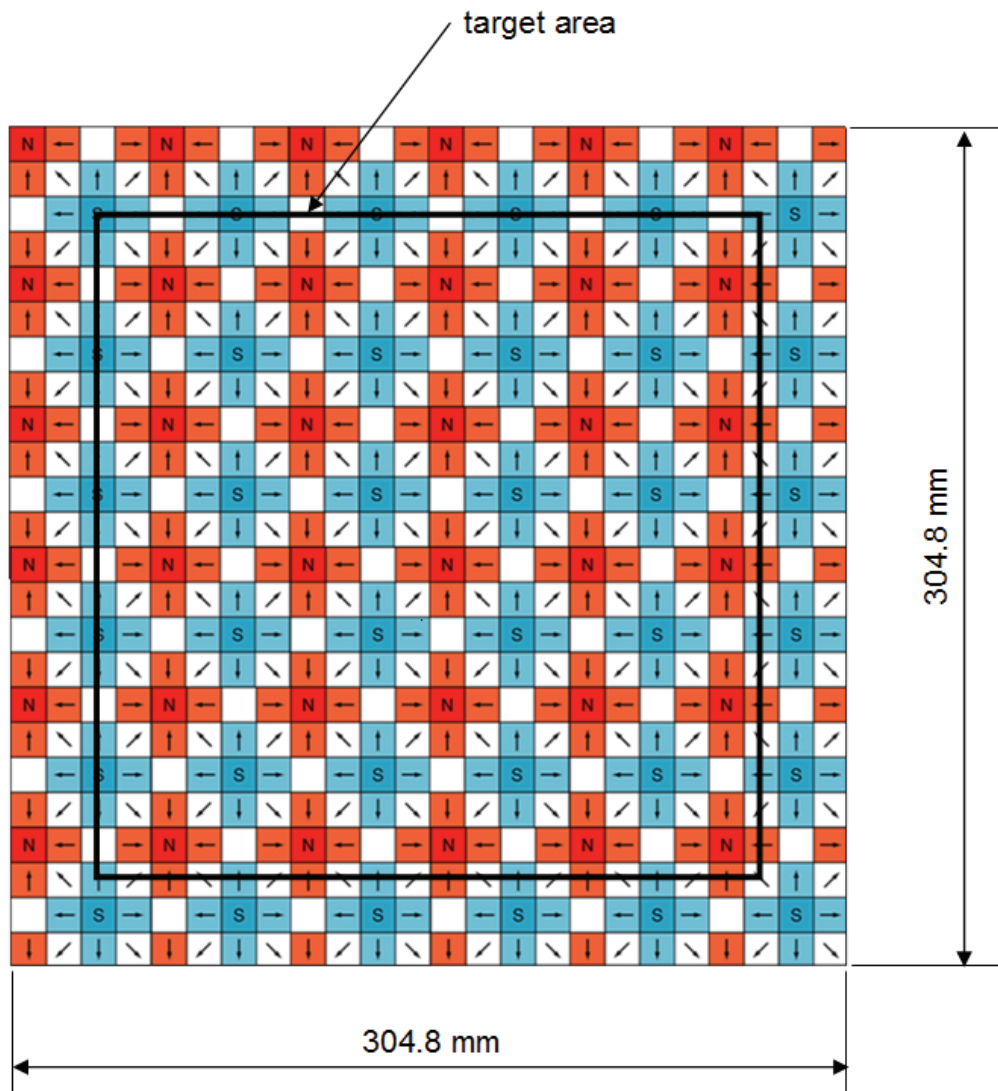
Figure 5-1: Overall view of the magnet matrix

Yusuke Kawato performed the study of position control with Hall-effect sensors, which are illustrated in Chapter I. He made the positioner move within one by one pitch. Hence, one of the goals of this research was to extend and maximize the travel range of the positioner. Figure 5-1 shows the overall view of the magnet matrix, which has six pitches of magnetic flux densities in each axis. The total size of magnet array is 304.8 × 304.8 mm. The target area where the platen can generate plane motions in Figure 5-1 was supposed to be maximum 240 × 240 mm in the *x-y* plane. The planar motor's geometry does not allow the positioner to move the whole area on top of the magnet matrix. In addition, the magnitudes of magnetic flux density at the ends of magnet array are not same with those of the inside magnet array.

5.1.2 Optimal Design of Triangular Body

There are two design principles to construct the frame for planar actuators. One is that the winding is employed as a stator. Another is that the permanent magnet array is adopted as a stator. There are trade-offs between these two design principles. In the former case, the permanent magnet array is supposed to be attached on the mover and the coils are fixed on the machine frame. An advantage of the moving permanent magnet array is that the platen does not need to load any umbilical cables so that the system is able to avoid unbalanced external forces. However, it has drawbacks of the high power loss. That is because the just interacted area between the permanent magnet and the windings can generate magnetic force. The rest of area of windings without any interaction dissipates the power. The lager the winding is used as the stator, the more power the system would lose. In addition, if the platen carries several permanent magnet

matrices at the bottom for generating multi degree-of-freedom dynamics, the whole system should become much heavier than the moving coil frame. On the other hand, the moving coil platen has advantages such as the whole system has light weight so that the platen is able to perform advanced dynamic movements and consume less power. By extension of the permanent-magnet matrix, the maximum travel range will be increased easily. As a result, the moving winding design has been chosen with several advantages above, although the platen carries umbilical cables connected for the power source and sensors.

The goal of mechanical design is the minimization of the stage and generating advanced dynamic performances with Hall-effect sensors compared to the prior arts [1–4]. The body of the positioner was designed by Solidworks [8]. The precision positioner fundamentally consists of a main triangular body made of Delrin, which has the mass density of 1.54 g/cm², three air suspended bearings manufactured by Nelson Air corp., three vertical sensors (Nanogage 100), three Hall-effect sensors [78], three windings, and two terminal blocks for wire connections. Each planar motor is comprised of three phases. Two windings that are located at the bottom of the triangle in Figure 5-3 generate driving forces in the *y*-direction and one at the top of the triangle in the vertical direction generate driving forces in the *x*-direction. All three windings generate magnetic suspension forces at the same time. The planar motors provide not only levitation forces, but also rotation motions of roll, pitch, and yaw with interactions among motors. As a result, the precision positionr is able to generate all 6-DOF motions.

-----

[8] SolidWorks Corporation, 300 Baker Avenue, Concord, MA 01742

The most compact platen design including all parts presented in the previous paragraph is geometrically the triangle. For simple machining process in manufacturing, the body part should be an equilateral triangle like the previous ATP project [1]. However, to minimize the mass of the platen, the modified shaped triangular body was designed, which is composed by the round edges and protrusions. The complicated designs of holes, pockets, round edges, and protrusions were manufactured by the CNC machines. Hence, the most compact platen design in Figures 5-2 and 5-3 could be achieved.
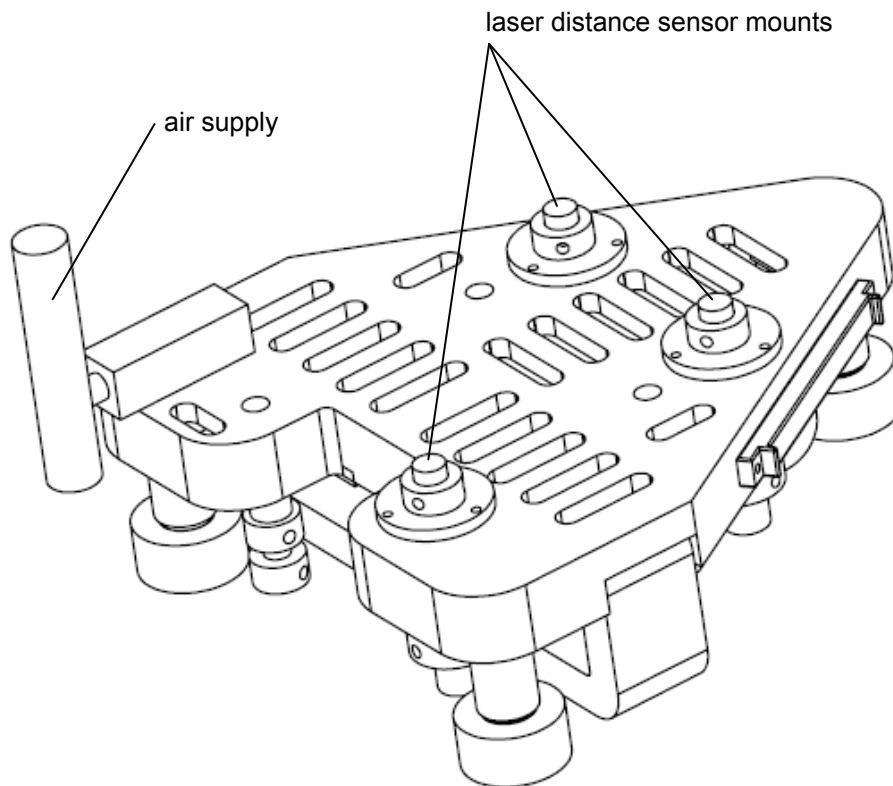
Figure 5-2: Top view of the assembled platen
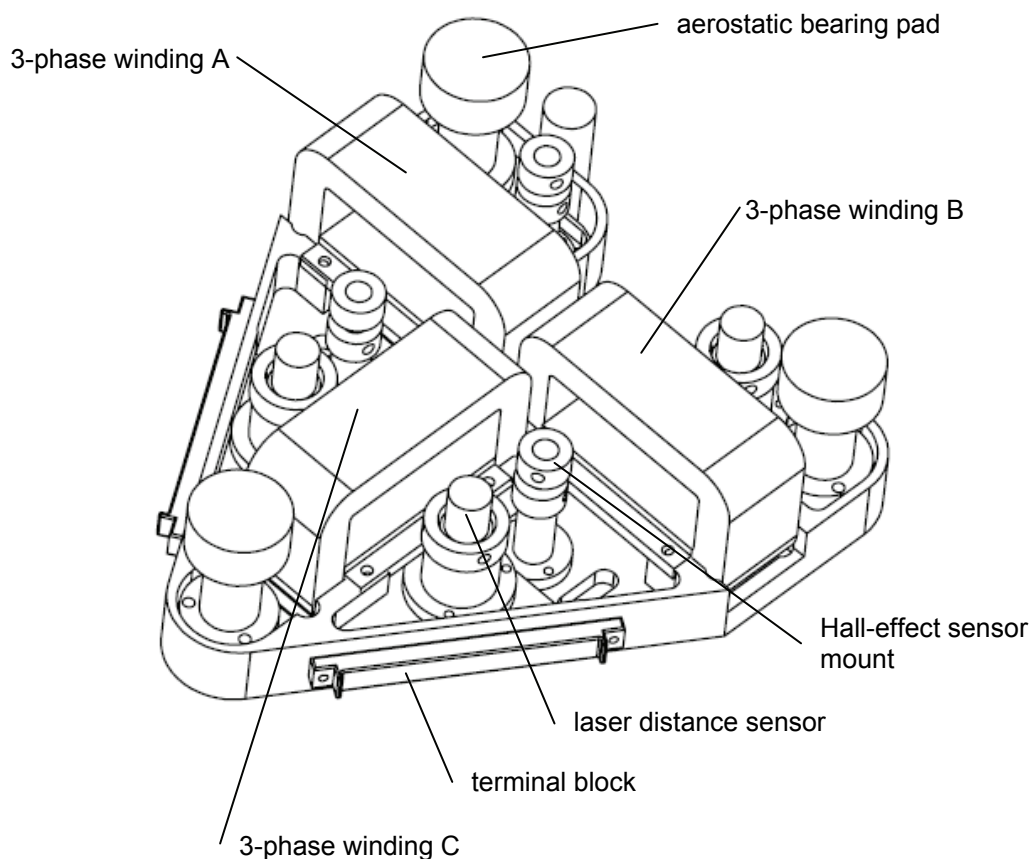
Figure 5-3: Bottom view of the assembled platen

As mentioned above, the platen was designed as small as possible loading all three Hall-effect sensors, three vertical sensors (Nanogage 100), and three air-bearing pads with mounts. To reduce the platen mass, many holes were made all the way through the body. These holes not, but also dissipate the heat generated by the coils. Since the three-phase coils are attached beneath the plastic body, the high temperature heat may affect the Delrin plastic body structure and/or cause the bending of aluminum plate, which covers the magnet array. The effective working area of winding, which produces the

magnetic force with respect to the magnetic flux density, is 2×1 in on the bottom place in Figure 5-4.
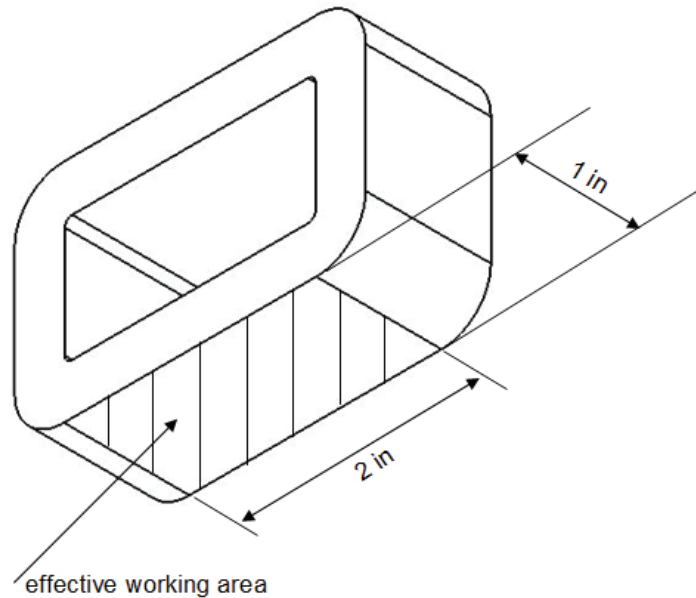
Figure 5-4: Effective working area of the winding

According to the Kawato's research [19], the Hall-effect sensors should have gaps based on equation (3.1) between sensors to measure. The smallest sensor gap of 2.5 inches in the compact body was chosen. Three aerostatic bearings support the platen at the end of round edge for the best dynamic movement in stability. It generates not only the vertical forces against the gravity for levitation, but also it prevents the platen from rolling and pitching in fast stepping motions. The rest of spaces are occupied with three laser distance sensors for the vertical mode control. The laser distance sensors are located as far as possible to minimize geometric errors. All 3 three-phase windings and Hall-effect sensors have several wire connections with a chassis, which include power supplies,

A/D, and D/A converters. Extra three holes beside hall-effect sensor mounts help that wire rearrangement on the platen, which reduce the interruptions in the dynamic motion. In order to achieve simple and accurate manufacturing during the CNC machining, a single end-mill that has 6 mm diameter cut a whole body without changing the tools.

Figure 5-2 shows the perspective top view of the positioner. It carries the air distributor for the aerostatic bearings. Three top mounts for the laser distance sensors are attached on top of the platen with 2-56 screws. Figure 5-3 illustrates the bottom view of the positioner. Three winding sets, aerostatic bearings, hall-effect sensors, and laser distance sensors occupy each pocket.

5.2 Machining Process

5.2.1 Delrin Plastic

Delrin is used as materials for the platen body, aerostatic mounts, Nanogage mounts, and Hall-effect sensor mounts, because it is light. Delrin is the brand name of an acetal resin engineering plastic. DuPont [9] synthesized it first around 1952, filed the patent of Delrin in 1956, and produced it in 1960. It is popular for the alternative material instead of metal. It is used for the bearing-replacement in caster and wheels, due to the resistance to liquids and low coefficient of friction. Excellent durability also makes available Delrin to be material as guitar picks. Additional applications include engineering field such as gears, ski bindings, fasteners, and lock systems. Delrin is the wear-resistant plastic that can be operated in temperature in excess of 200ºF. Machining of Delrin follows the tradi-

---

[9] E. I. du Pont de Nemours and Company, Wilmington, Delaware, USA

tional methods such as turning, of Delrin are polyoxymethylene (POM), acetal resin, milling and drilling. Sharp tools are required but no lubricant is necessary. Other names polytrioxane and polyformaldehyde. Mass density of Delrin is 1.54 g/cm³. Figure 5-5 shows the chemical formula of paraformaldehyde.
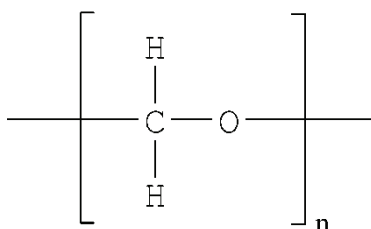
Figure 5-5: The chemical formula of Paraformaldehyde

5.2.2 CNC

After the triangular body was designed with Solidworks, the computer numerial controlled (CNC) machine manufactured by Roland[10] in Dr. Creasy's lab was used for cutting the body in Figure 5-6 [95]. A single-tool cutting design make possible the 6 mm diameter end mill (6 mm×38×76M) manufactured by Ultratool cut the whole platen body. Basically, the CNC cutting consists of five steps. First, the overall body cutting was performed along the outside edge. Second step is the pocket 1 for air suspended bearings and vertical sensor mounts, which has the depth of 0.2 in. Third is the pocket 2 for planar motors and Hall-effect sensors, which has the depth of 0.4 in. Forth is the drillings for ventilating halls, Hall-effect sensor mounts and cable paths. Final is the lathe cutting on top of the body platen. Figure 5-7 shows the perspective view of main pockets for and holes on the body with the CNC cutting. All measurements of pockets and the holes are presented in Figures A-1 to A-4 in Appendix A.
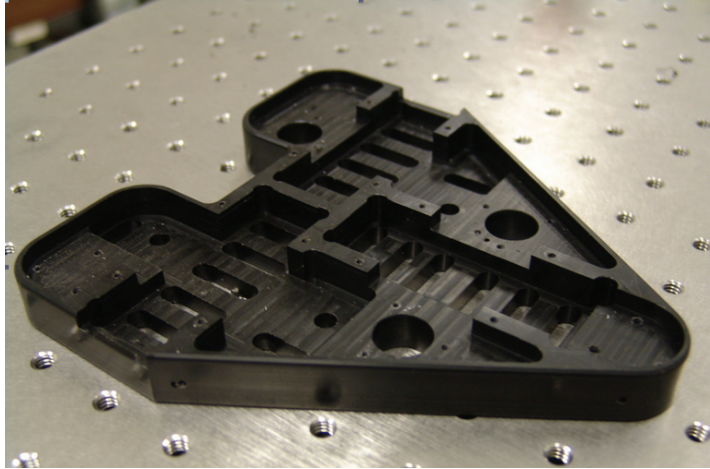
Figure 5-6: Photograph of the bottom view of the plastic body

pocket 1: 0.2" depth

pocket 2: 0.4" depth

pocket 1: 0.2" depth
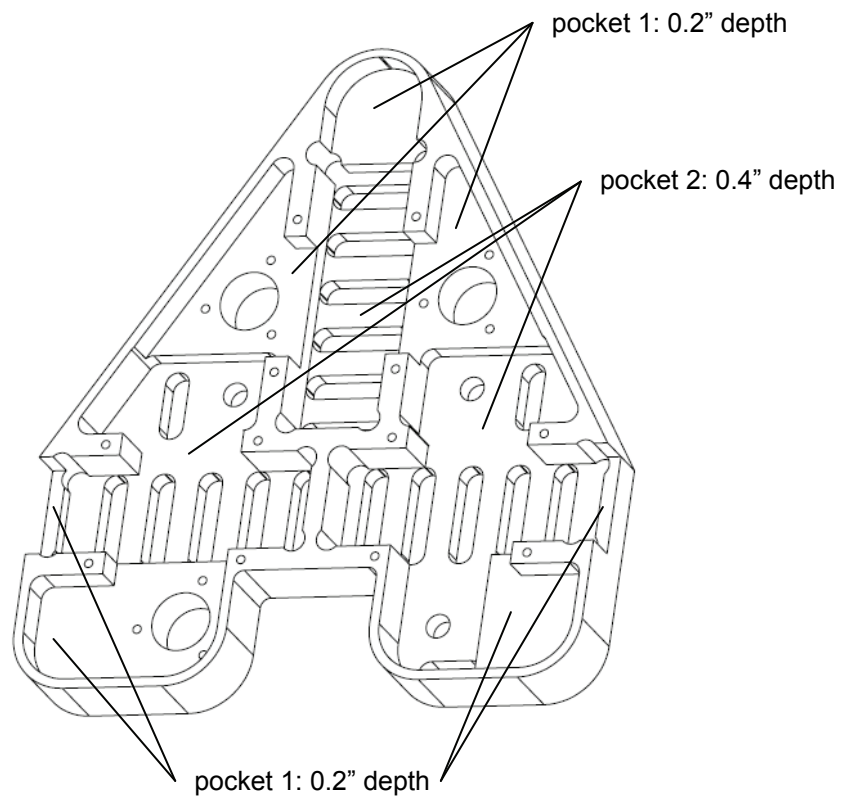
Figure 5-7: Pockets 1 and 2 for the CNC machining

---

[10] Roland DG Corporation, Headquarter, 1-6-4 Shinmiyakoda, Kita-ku, Hamamatsu-shi, Shizuoka-ken, 431-2103 Japan

5.2.3 Drilling and Tapping for Mount

Figure A-5 in Appendix A illustrates the drilling and tapping size and locations for Nanogage 100 sensor mounts and winding mounts. Both of them are mounted with 2-56 screws. Each sensor mount was fixed by 3 screws at 120º, and each winding mount includes 4 screw sets for assembly. In addition, Nanogage 100 sensor mounts at the top also use 2-56 screws. Aerostatic bearing mounts, Hall-effect sensor mounts and terminal blocks are assembled with 4-40 screws.

5.3 Assembling Process

5.3.1 Actuators

The precision positioner requires both fine and coarse 6-DOF motions. The chosen actuator is SPMPM. This actuator generates neither cogging force nor attraction forces. Figure 5-8 (a) shows the picture of single phase winding. Each planar motor is comprised of three single windings. The commutation law among motor phases is presented in Chapter VI. Figure 5-8 (b) and (c) present the pictures of the winding mount that was manufactured by CNC machine and winding assembly, respectively.

The winding set and its dimensions are shown in Figure 5-9 (a). Figure 5-9 (b) shows the schematic view of the assembled winding mount. I designed it for assembling winding sets on the platen using 2-56 screws without any glues. The dimension of the winding mount is illustrated in Figure A-6 in Appendix A.

(a)

(b)

(c)
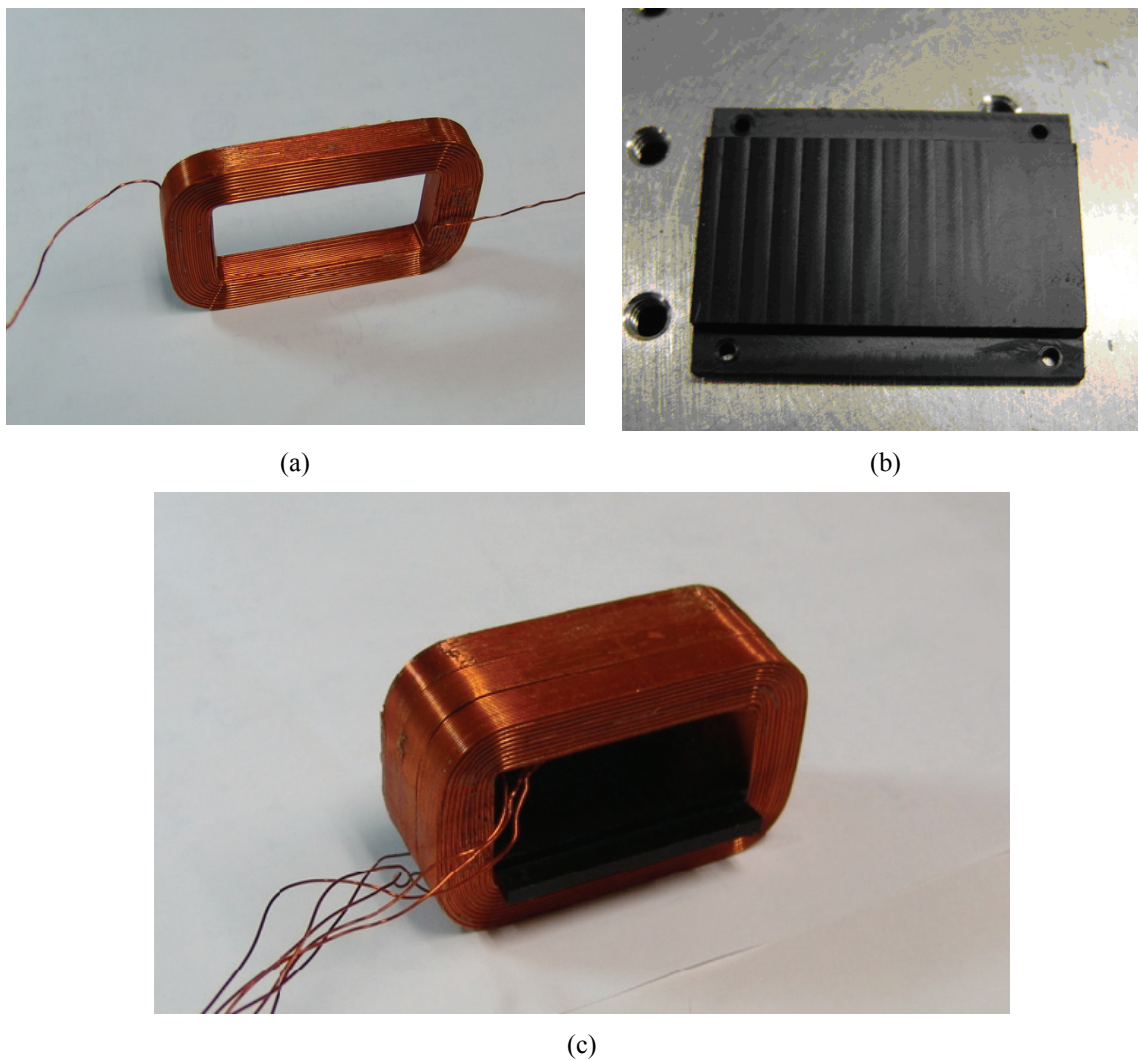
Figure 5-8: Photographs of the planar motor winding, (a) a single phase winding, (b) winding mount, and (c) winding assembly

(a)

three phase synchronous winding

Delrin plastic winding mount
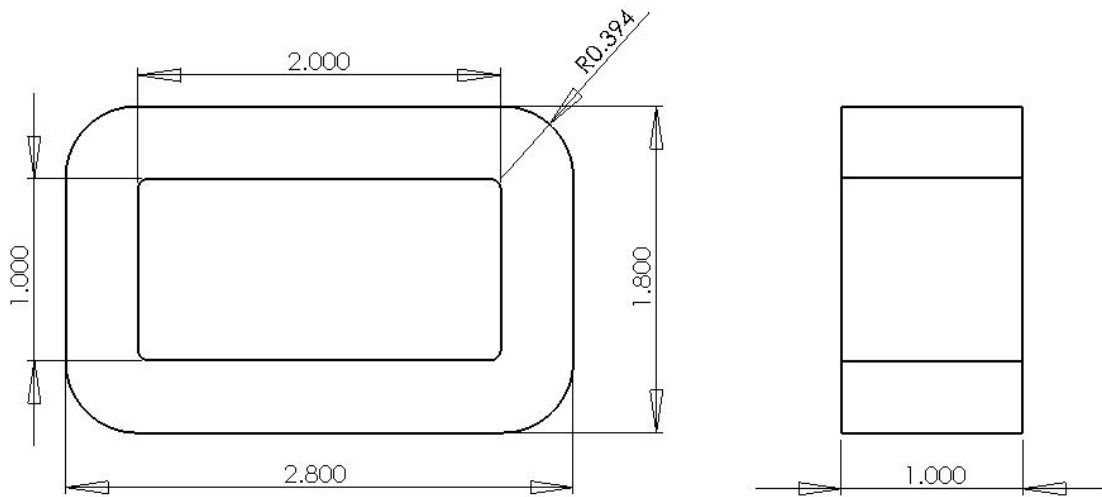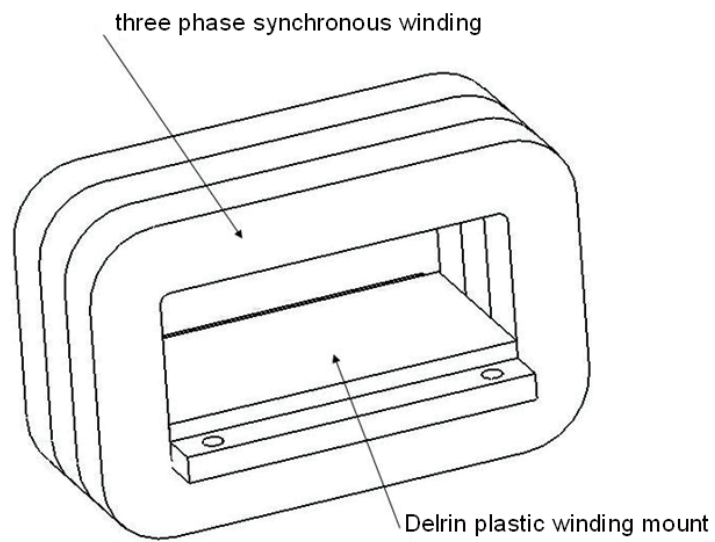
(b)

Figure 5-9: (a) dimension of winding and (b) winding assembly

5.3.2 Vertical Sensor Mount

The bottom mount for Nanogage 100 made of Delrin is shown in Figure A-7 in Appendix A. The standoff of 3 mm is required for the proper operation of Nanogage 100. The bottom mount was designed to keep the standoff constant. In addition, three set of 4-40 screws make the sensor height be adjustable. For the purpose of acquiring the perpendicular tolerance of $\pm 0.1°$, another mounts that fix the Nanogage 100 on top were required as shown in Figure 5-1. Three sets of 4-40 screws were also used for sensor height adjustment. Dimensions of top sensor mounts is illustrated in Figure A-8 in Appendix A. Figure 5-10 shows the assembly of Nanogage 100 for the vertical laser distance measurements. Three sets of Nanogage 100 mounts are fixed on the platen with each of three 2-56 screws.
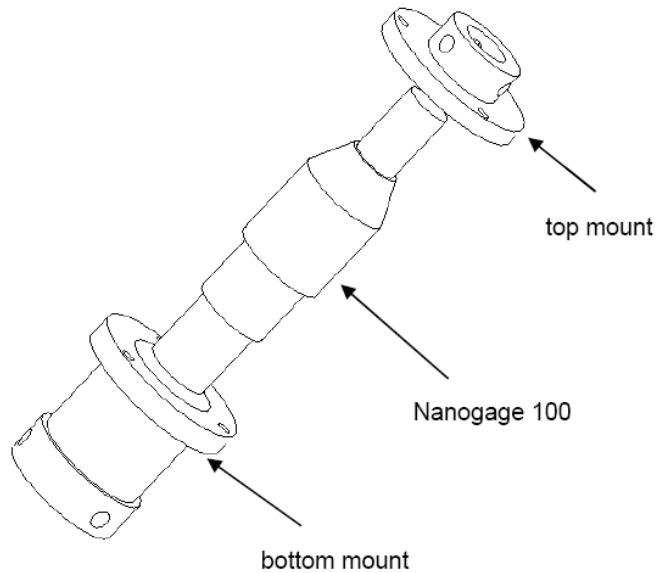
Figure 5-10: Nanogage 100 assembly [1]

5.3.3 Aerostatic Bearing

The platen is levitated by not only magnetic force but also aerostatic bearings against gravity. The three aerostatic bearings FP-C-010 manufactured by Nelson Air Corporation[11] are used at the edges of the platen in Figure 5-11. Air pressure of 20–90 psi is required for supporting up to the load of 10 kg. In order to support aerostatic-bearings, Delrin plastic mounts and ball joints are used. The ball joints between the aerostatic bearing pad and the Delrin mount are used as not only the connectors, but also adjust the height of platen and keep the constant gap of 0.03 in between winding sets and the ground. The ball joint is made of Delrin plastic and has the radius of 0.25 inch. For adjusting the overall platen height, it was ground with a sand paper to have a hemisphere shape as shown in Figure 5-12. The assembly of the ball-joint mounting with aerostatic bearing is shown in Figure 5-12. The aerostatic bearing consists

of the bearing pad, the ball-joint and the mount without screw fixed. Figure 5-13 shows the picture of aerostatic bearing mount and specifications of the mount is presented in Figure A-9 in Appendix A. 4-40 screws were used to fix the mounts on the platen. Figure 5-14 shows the schematic views of assembled mounts on the body. The assembly of motor winding is illustrated in Figure 5-14 (a). The views of Nanogage mounts and aerostatic bearing mounts are presented in Figure 5-14 (b) and (c), respectively.

---

[11] Nelson Air Corp., 559 Route 13 South, Milford, NH 03055
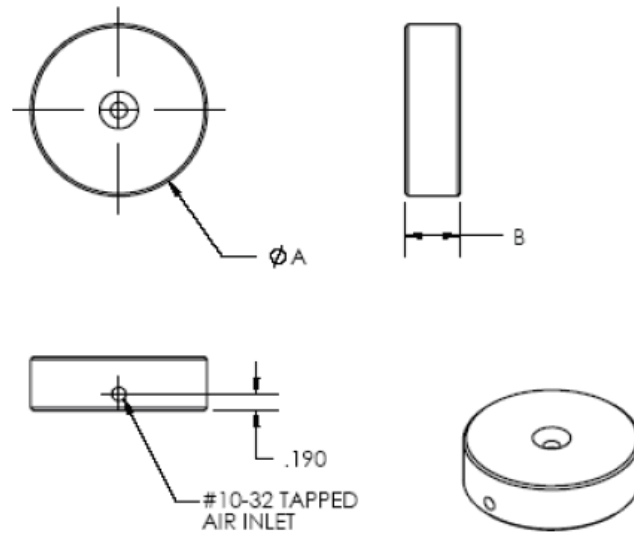
(a)

(b)

Figure 5-11: Aerostatic bearing, (a) dimensions and (b) photograph [after Nelson Air Corp.]
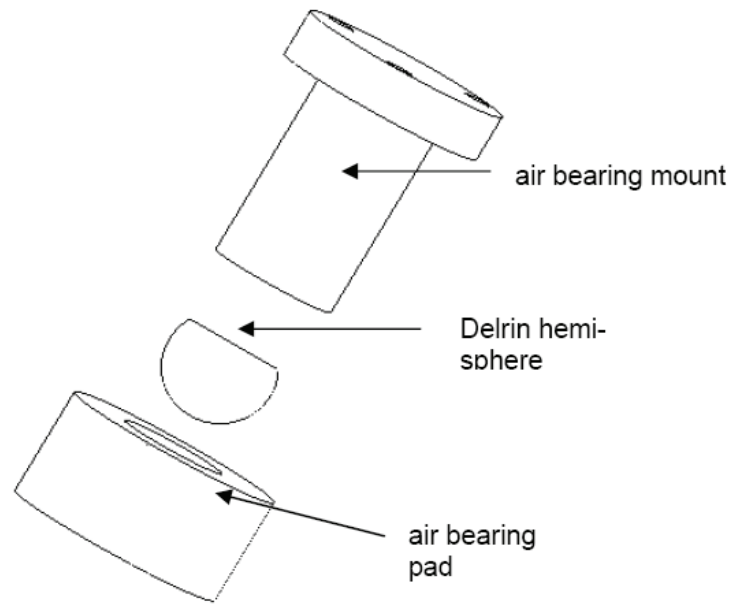
Figure 5-12: Assembly of the aerostatic bearing mount [1]
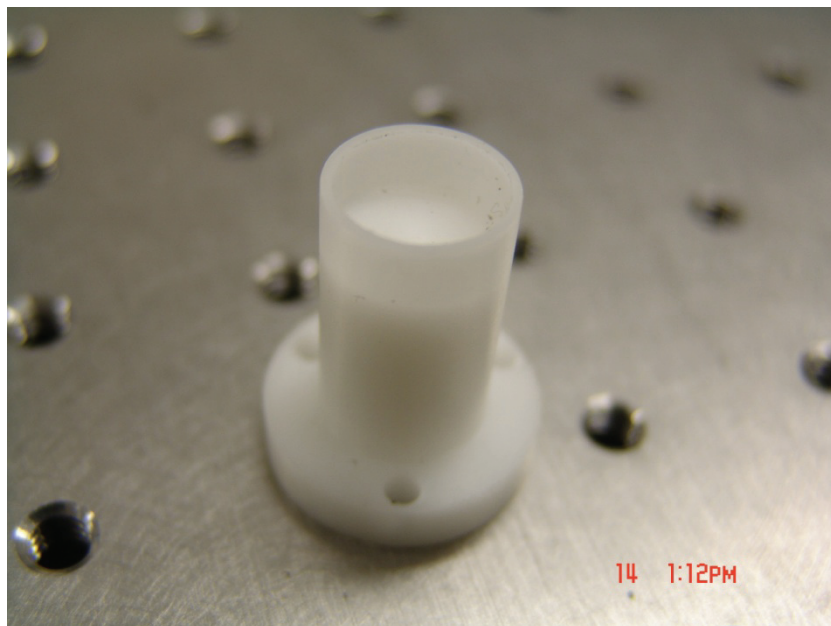
Figure 5-13: Photograph of the aerostatic bearing mount
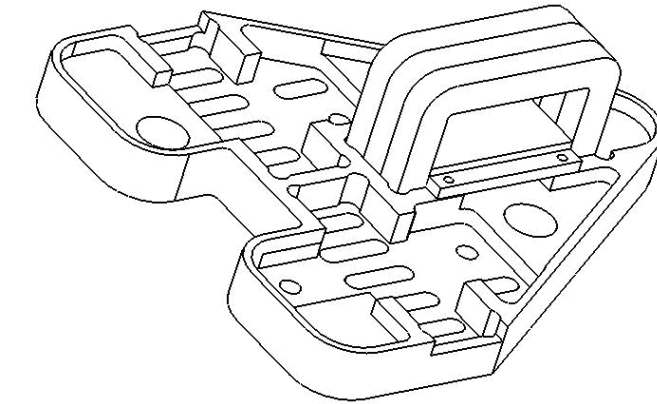
(a)
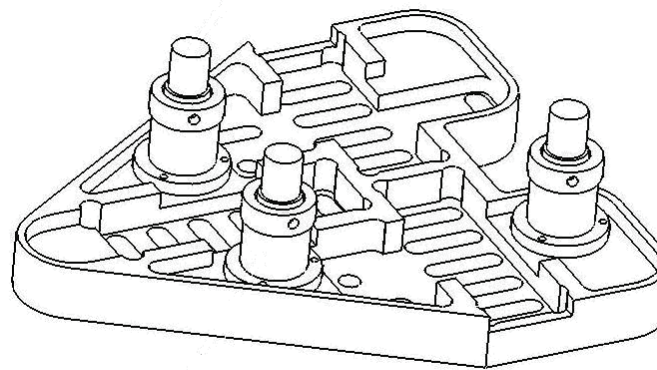
(b)
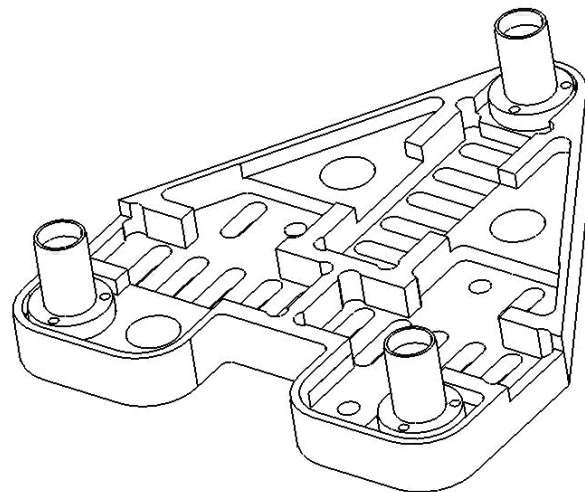
(c)

Figure 5-14: (a) Windings mounted on the body pocket, (b) Nanogage 100 mounted on the platen, and (c) aerostatic bearings mounted on the platen

5.3.4 Terminal Block

There are three planar motors in the positioner, where each planar motor consists of three windings. Hence, a total of nine windings are used as actuators to generate driving and the levitation forces. Each of winding includes two ends so that the platen needs a total of 18 pin connections. Therefore, two terminal blocks, which has 12 pin connectors in Figure 5-16 are attached on each side of the platen with 4-40 screws.
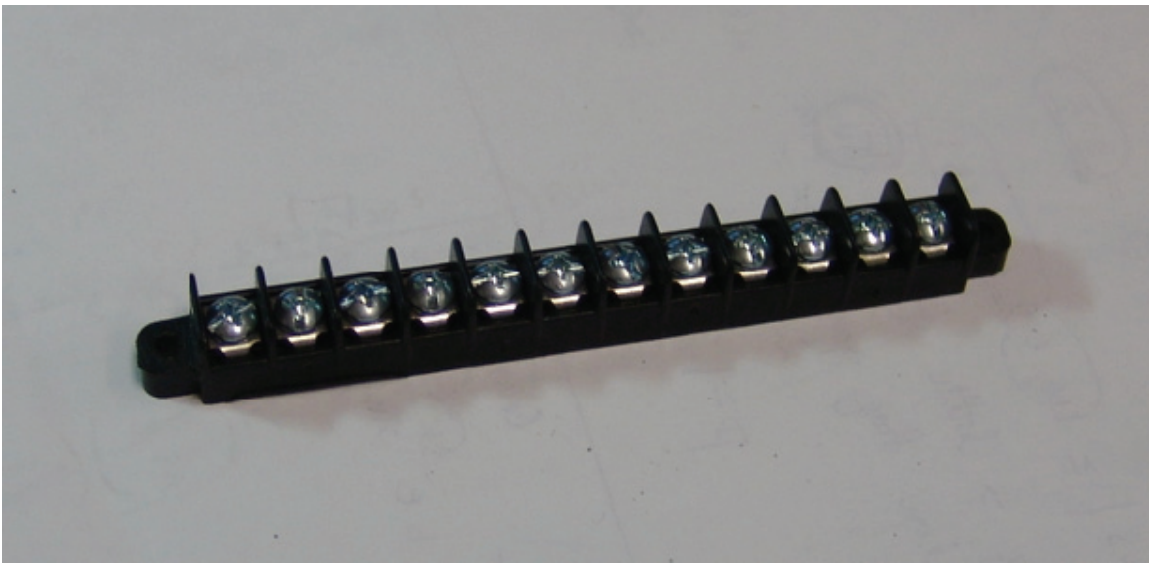
Figure 5-15: Picture of the terminal block

5.3.5 Hall-Effect Sensor Mount

Three Hall-effect sensors for the lateral motion measurement are used in this project. As shown in Figure A-2 in Appendix A, three clearance holes of diameter 0.250 inches for mounts were drilled with the CNC machine on the platen. The Hall-effect sensor consists of the sensor chip, the sensor data board, the sensor holder, the holder bar, and the mount. The fabrication of sensor boards is presented in Chapter III. The circuit board

of Hall-effect sensor and board holder are glued. The sensor holder and the holder bar are fixed with 4-40 screws and another 4-40 screw placed on the mount make the sensor bar be adjustable to the correct position. All of the holders, the bars, and the mounts are made of Delrin. Hall-effect sensor mounts are fastened on the pocket 2 in Figure 5-7 on the platen with 4-40 screws. Figure 5-16 shows the view of the Hall-effect sensor mounts attached on the platen and it also shows that the sensor bar and the holder can be adjusted upside and down like cylinder for the proper standoff distance. Dimensions of the Hall-effect sensor mount, holder, and bar are presented in Figures A-10 and A-11 in Appendix A.

5.3.6 Whole Platen Assembly

Figure 5-17 presents the platen assembly process. First, two terminal blocks were attached on each side of the platen body. Then laser-distance-sensor and aerostatic-bearing mounts were assembled with screws. Planar motors A, B, and C with the motor mounts were fixed on the platen in turn. The Hall-effect sensor mounts were attached, and the wires were covered by the heat-shielding tubing with different colors to distinguish each phase. Nine different channel outputs from DACs pass through each amplifier and reach the positioner. Figure 5-18 shows the assembled positioner and wire connections on the bottom side. The exploded top view, the exploded bottom view, and the exploded whole platen assembly are illustrated in Figures 5-19, 5-20, and 5-21, respectively. Finally, the schematic side view of the platen is presented in Figure 5-22.
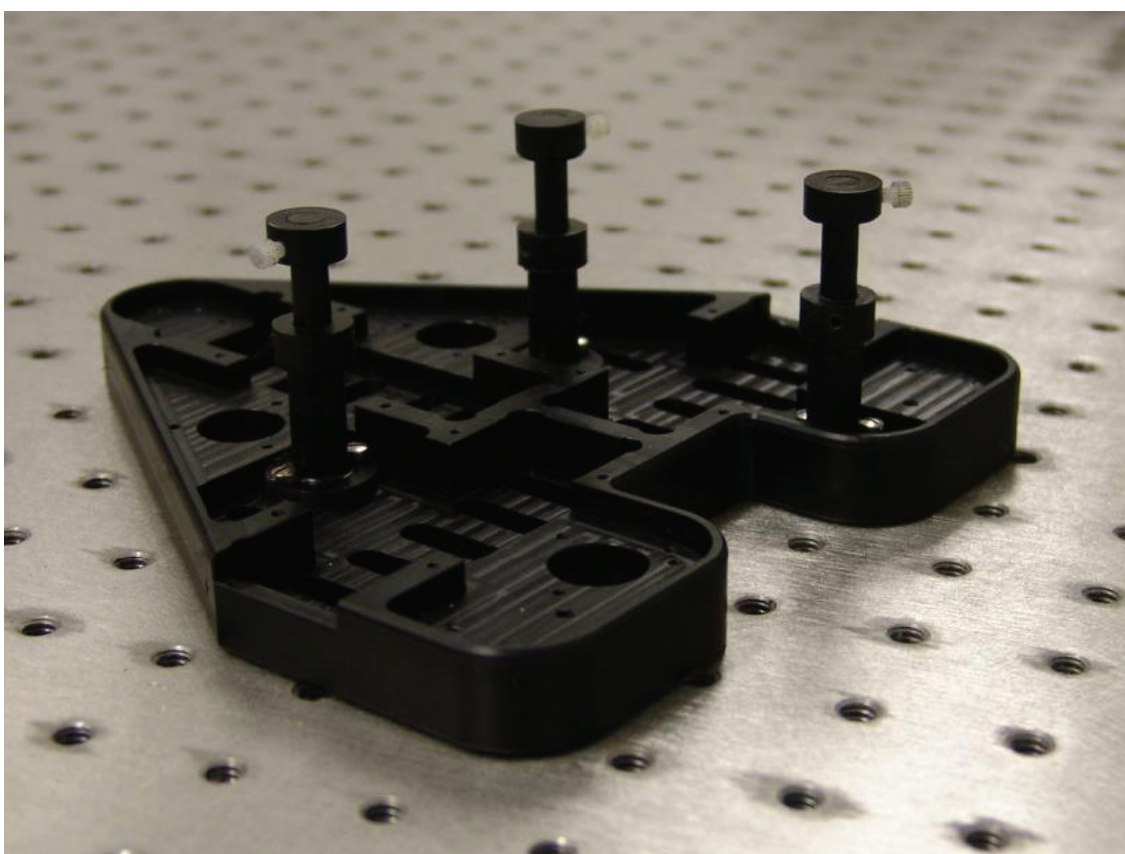
Figure 5-16: Photograph of the Hall-effect sensor mounts attached on the platen
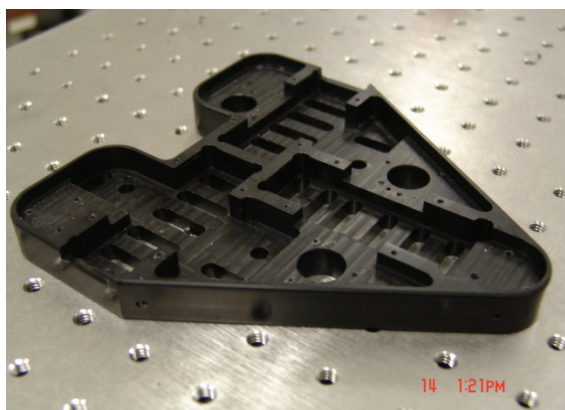
(a)
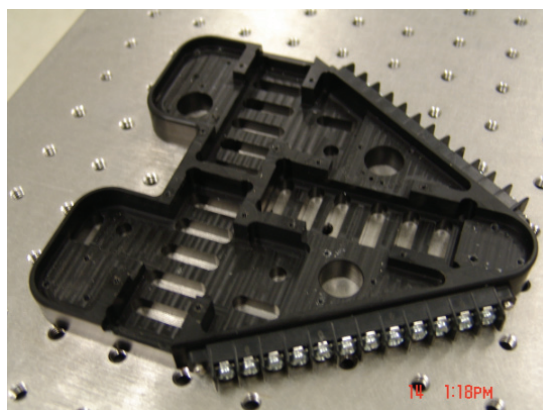
(b)
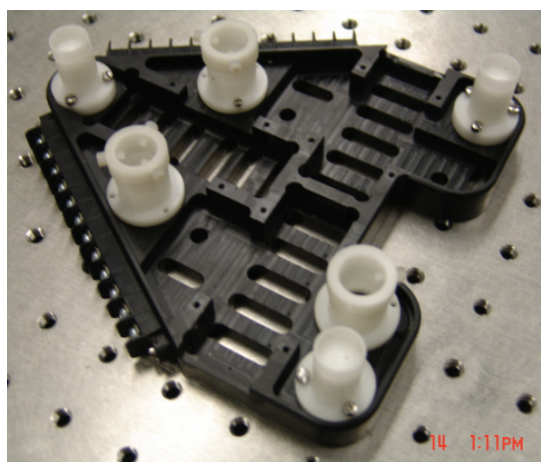
(c)
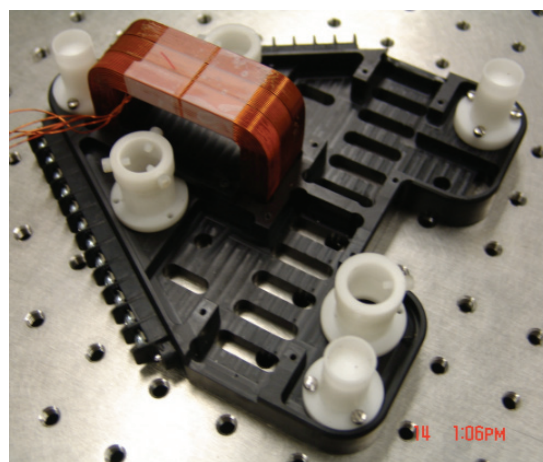
(d)
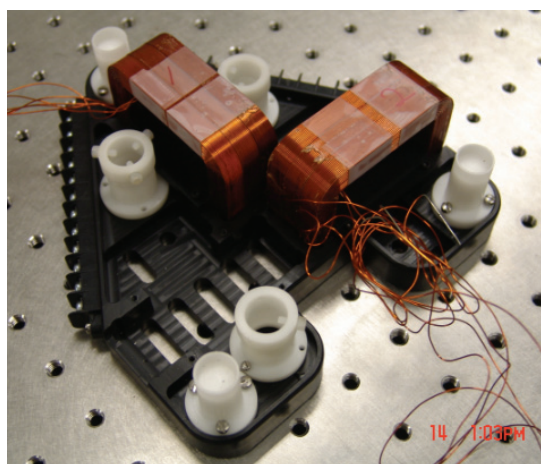
(e)
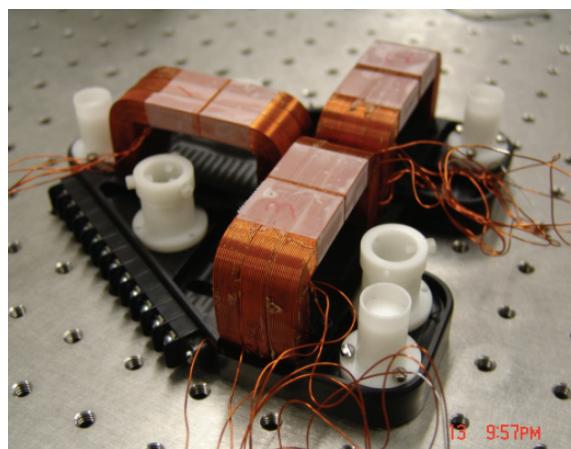
(f)

Figure 5-17: Platen assembly process
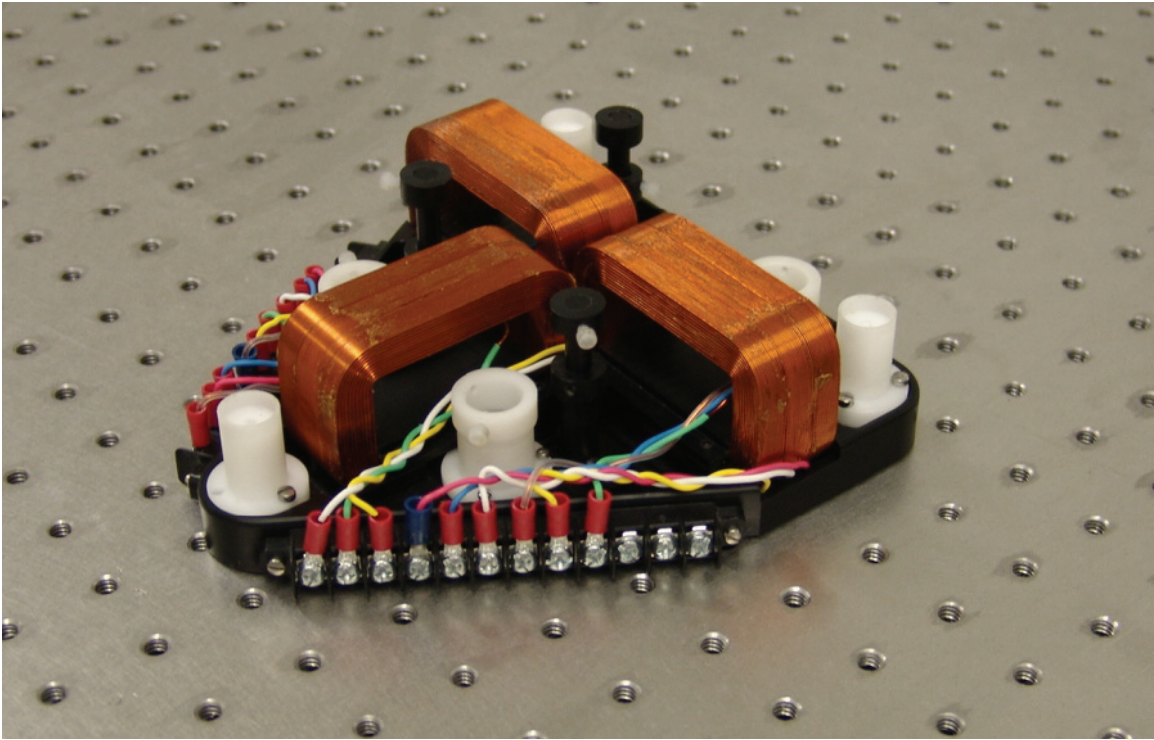
Figure 5-18: Photograph of the assembled platen at the bottom

top sensor mounts

laser distance sensor

air distributor

heat dissipating holes

hall-effect sensor cable holes

terminal block
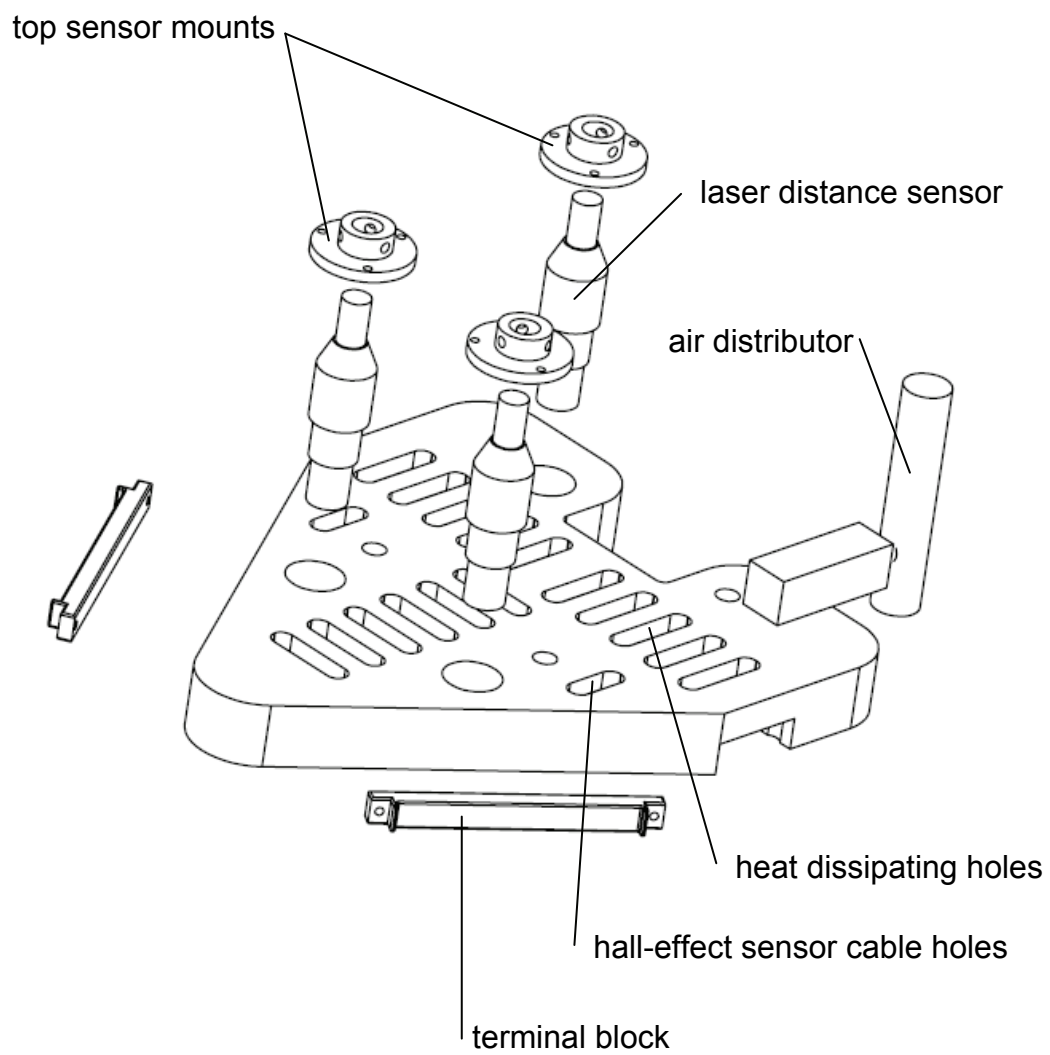
Figure 5-19: Exploded view of the platen at the top
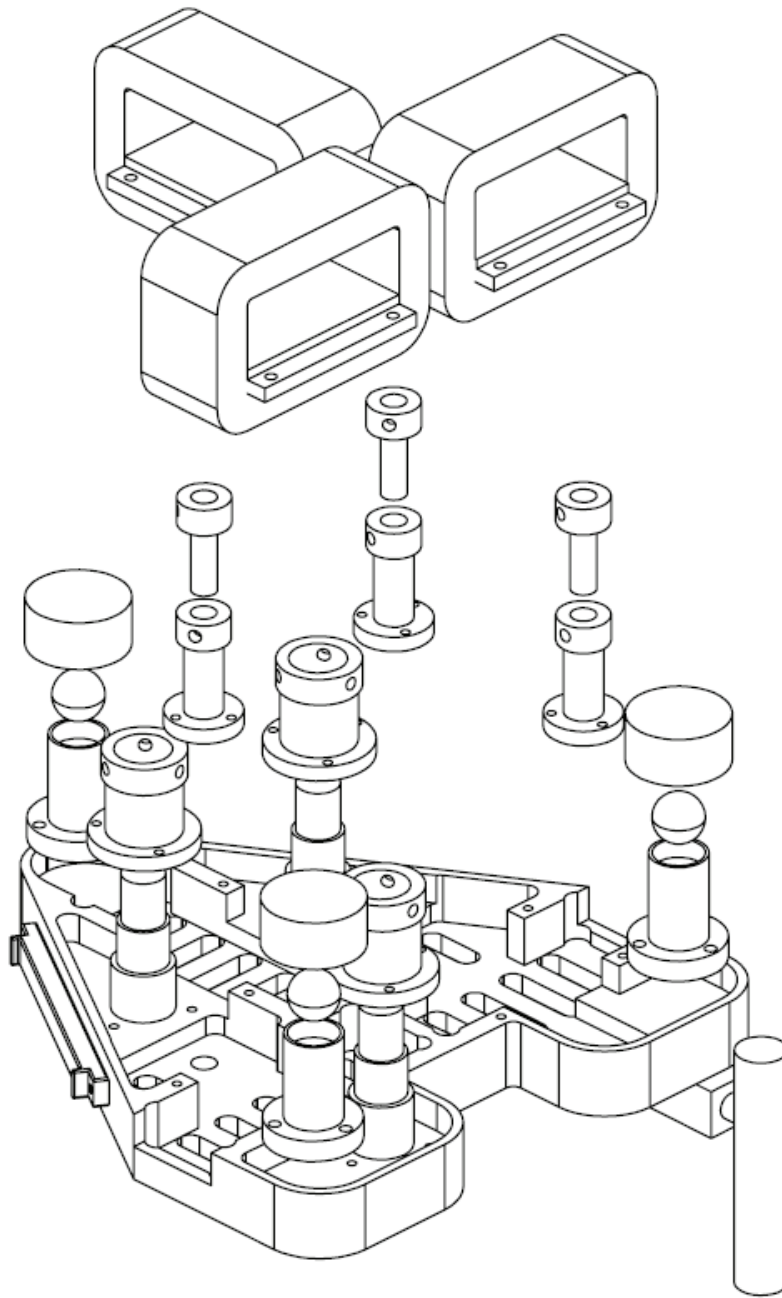
Figure 5-20: Exploded view of the platen at the bottom
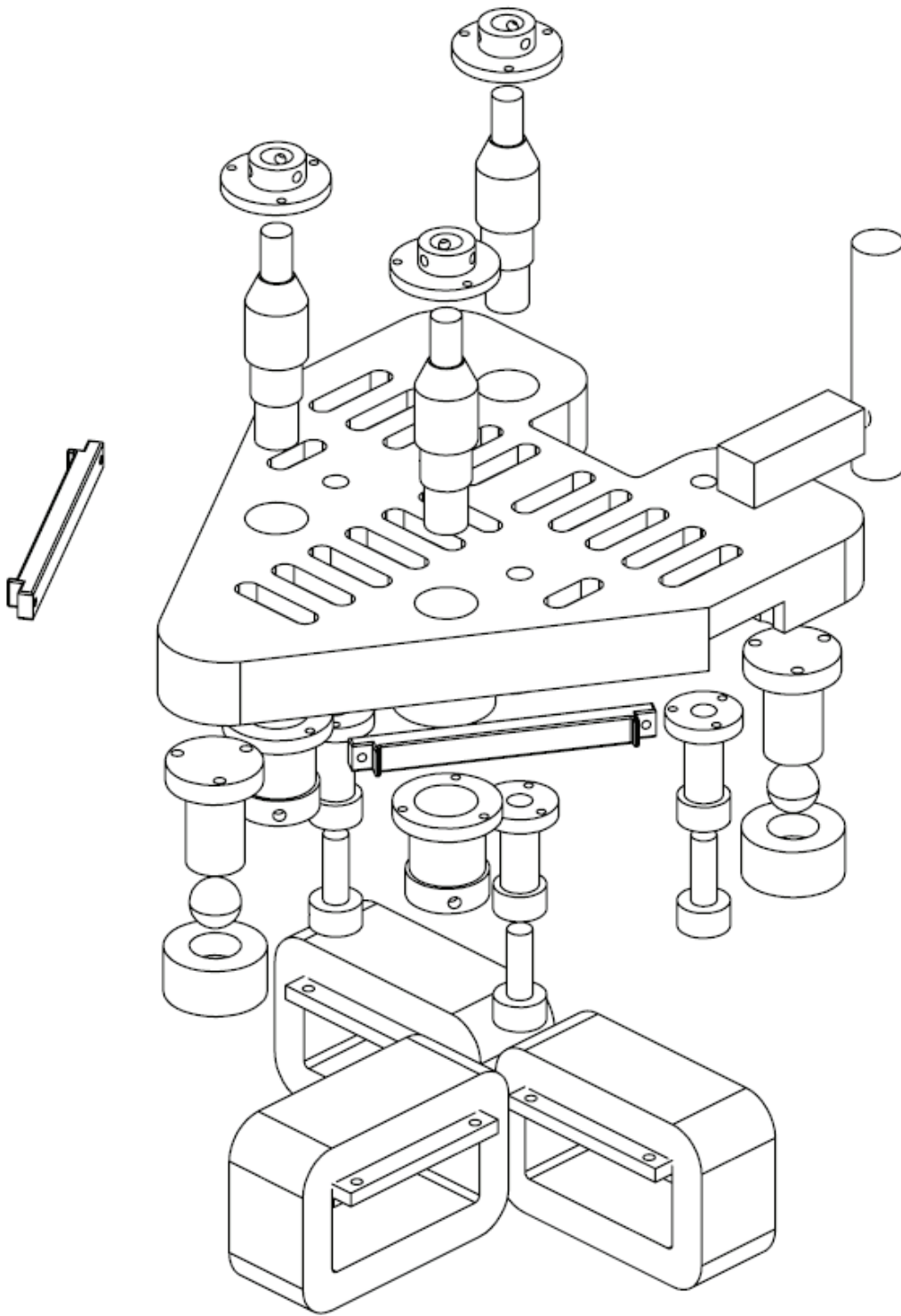
Figure 5-21: Exploded view of the whole platen

magnet matrix
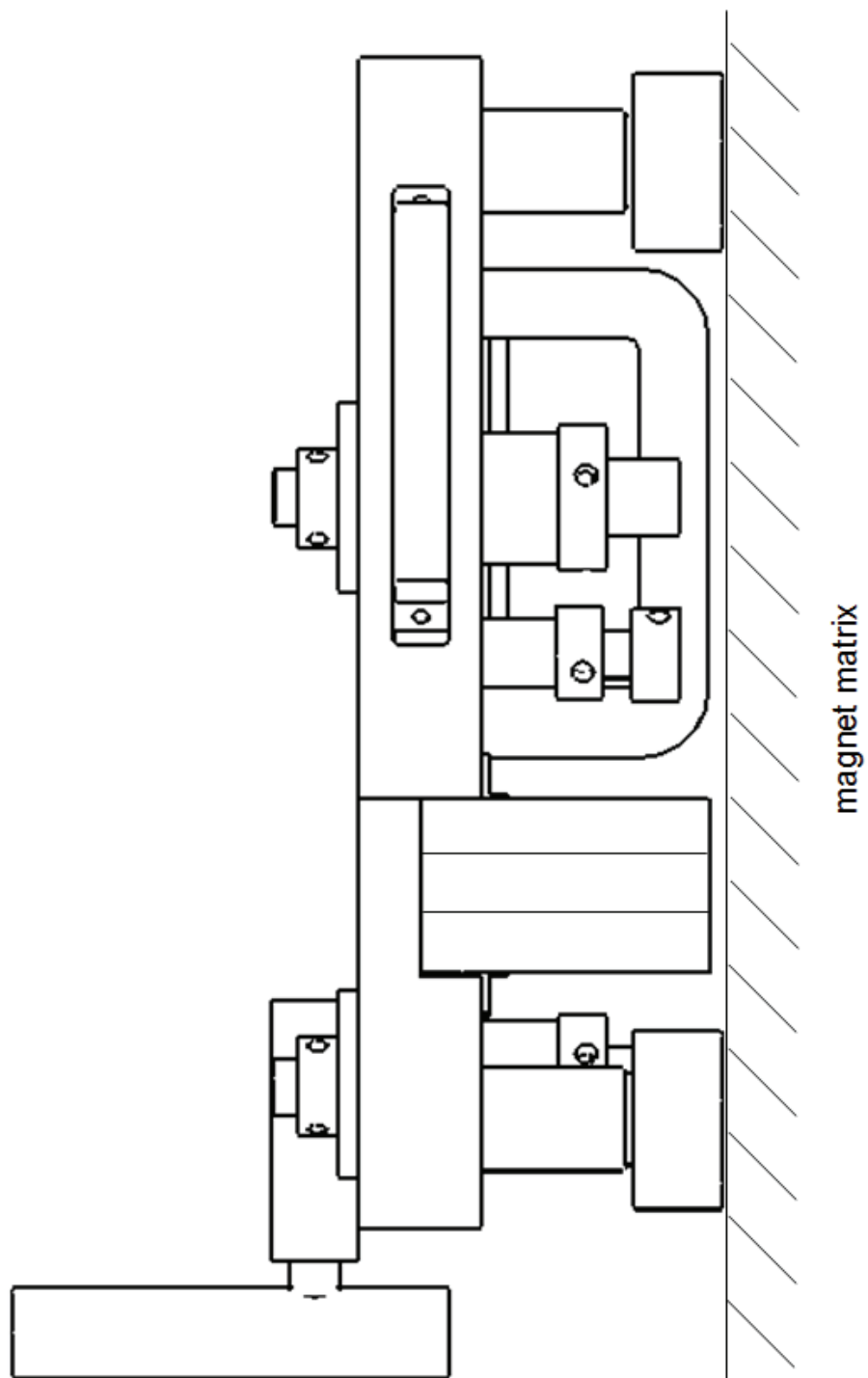
Figure 5-22: Side view of the platen indicating the nominal gaps

CHAPTER VI

DYNAMIC ANALYSIS AND SYSTEM MODELING

The previous chapter addressed mechanical design and fabrication. For precision motion control, the accurate dynamic analysis of the platen is necessary. The mass center and the moment of inertia were determined by software calculation. Repetitive experiments determine parameters, such as spring constants and damping coefficients. Dynamic models for the multidimensional positioner are derived in this chapter.

6.1 Mass and Inertia Tensor of the Platen

The platen carries a main body, vertical sensor mounts, Hall-effect sensor mounts, air-bearing mounts, two terminal blocks, air-support distributor and three planar-motor coils. In order to reduce the total mass of the platen, the main body and all plastic mounts such as sensor mounts and air-bearing mounts are made of Delrin with the mass density of 1.54 g/cm³. The mass of the entire platen was measured to be 1.52 kg by a precision scale with a resolution of 0.1 g. Hence, the weight of the positioner is 14.91 N. The design of the platen was developed so that the platen could generate the driving force in a lateral motion, as well as the vertical force for levitation. The suspension force of 17.15 N could be generated by three planar motors so as to control the vertical motion with magnetic levitation.

The design of the positioner was performed by Solidworks. This software calculates mass properties and the dimensions of each part. The center of mass was calculated using the software with material properties. The coordinate of the mass center is,

$$CM = \begin{bmatrix} CM_x & CM_y & CM_z \end{bmatrix}^T = \begin{bmatrix} 76.72 & 69.07 & -3.1 \end{bmatrix}^T \tag{6.1}$$

in millimeters. Figure 6-1 (a) shows the mass center of the platen. It has the origin at the left bottom side for the mass center calculation. The mass center is not exactly the center of the body in *x-y* plane, because the geometry of the platen is asymmetrical. The compact design concept did not allow the geometry of the positioner to be completely symmetrical. One of vertical sensors and its mount is located on the right and one of Hall-effect sensors and its mount is located on the left side. Those two components do not have corresponding mass properties. The laser sensor and its mount have more mass than the Hall-effect sensor mounts. This asymmetry causes the offset of the platen in order to calculate the mass center.

The inertia matrix at the center of the mass is calculated by Solidwoks, as well. Figure 6-1 (b) illustrates the positioner, its coordinates, and the origin.

$$I = \begin{bmatrix} I_{xx} & -I_{xy} & I_{xz} \\ -I_{yx} & I_{yy} & -I_{yz} \\ -I_{zx} & -I_{zy} & I_{zz} \end{bmatrix} = \begin{bmatrix} 0.001898 & -0.000043 & 0.000041 \\ -0.000043 & 0.002153 & 0.000179 \\ 0.000041 & 0.000179 & 0.003375 \end{bmatrix} \tag{6.2}$$

in kg-m². The principal moments of inertia of the platen in the *x, y,* and *z* axes are denoted as I_{xx}, I_{yy}, and I_{zz}, respectively. The rest of components in the matrix tensor are $I_{xy}, I_{yz}, I_{zx}, I_{yx}, I_{xz}$, and I_{zy}, which are the products of inertia. The moments of inertia a re used to derive equations of motion for the rotational motion dynamics. The products of inertia are over 10 times less than values of the moments of inertia. Hence, we ignored v-
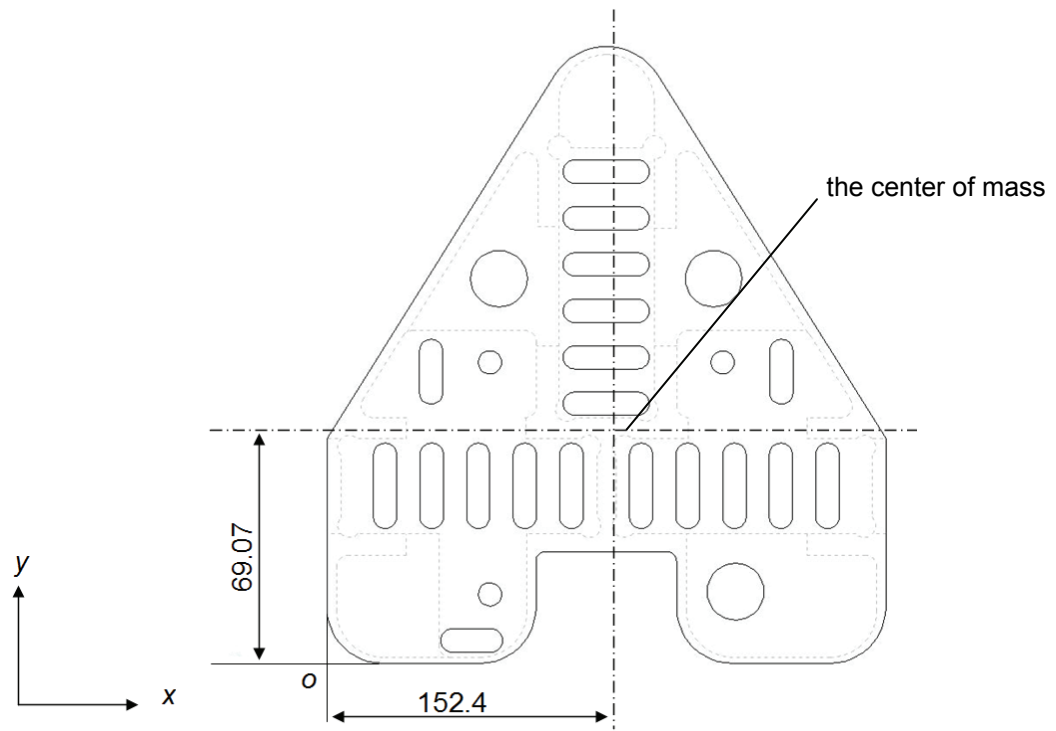
(a)
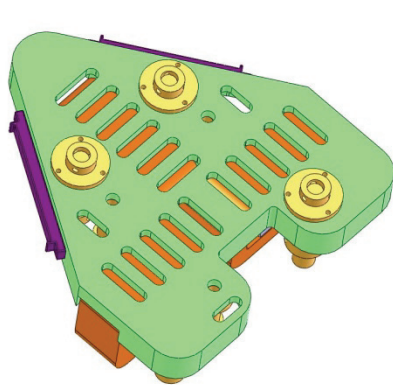
(b)
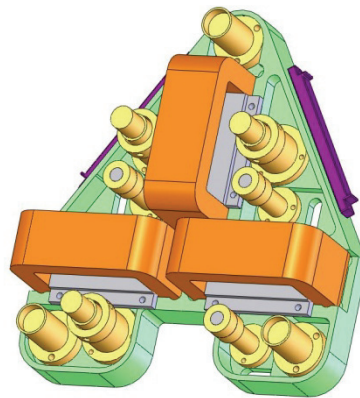
(c)

Figure 6-1: (a) The center of mass, (b) Solidworks drawing of top, and (c) bottom

alues of the product of inertia, because they do not affect the model significantly.

A modeling error in the inertia tensor might happen in the software. That is because the designed model by Solidworks does not include all body components such as many the small screws to fix the mounts, screw halls on the platen, the air-distributor, and the flexible tubes for air-bearings. The umbilical power cables, vertical sensor cables, and Hall-effect sensor cables installed on top of the platen may affect the motion generation, the mass calculation, and/or the inertia matrix calculation.

6.2 *DQ*-Decomposition

The *DQ* decomposition was used in the rotary machinery to generate torque, which is the decomposed stator current [96−97]. The *DQ* coordinates are illustrated in Figure 6-2. The *D*-axis and the *Q*-axis represent the direct-axis and the quadrature-axis, respectively. The two axes of *D* and *Q* are attached to the moving frame and move with the positioner with respect to the global coordinate system. Geometric nonlinearity can partially be eliminated by the *DQ* decomposition. This is because there is no horizontal position dependence in the force equations with respect to the stator. The vertical motion is generated by the *D*-component currents. The *Q*-component currents produce the horizontal driving forces. In order to control the 2-DOF suspension and the driving forces independently, the planar motor generates two decoupled (*D*-axis and *Q*-axis) orthogonal force components. The following sections will introduce linearized equations of motion developed with this *DQ* decomposition methodology.
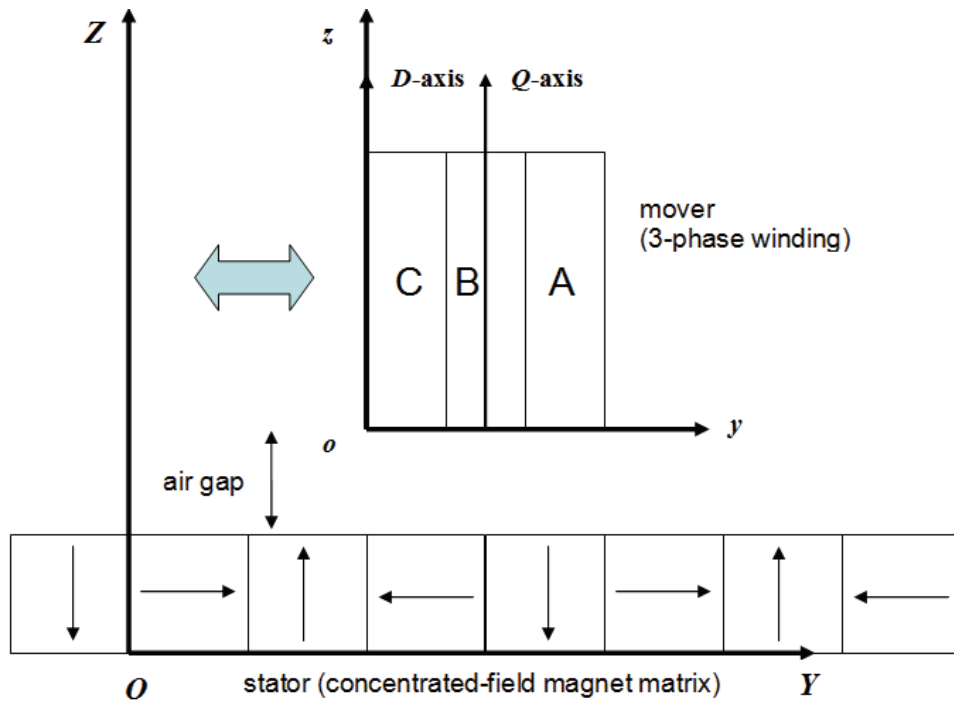
Figure 6-2: *DQ*-decomposition

Figure 6-2 denotes that the *D*-axis corresponds to the *z*-axis, which is the vertical motion in the moving frame. A quarter of the motor pitch difference exists between the *D*-axis and *Q*-axis, where there is the 90° electrical angle in the +*y*-direction. Equation (6.3) shows the transformation between $\begin{bmatrix} J_a & J_b \end{bmatrix}^T$ and $\begin{bmatrix} J_Q & J_D \end{bmatrix}^T$.

$$\begin{bmatrix} J_Q \\ J_D \end{bmatrix} = e^{\gamma_1 y J} \begin{bmatrix} J_a \\ J_b \end{bmatrix}, \tag{6.3}$$

where $\gamma_1 = 2\pi / l$, $e^{\gamma_1 y_0 J}$ is a transformation matrix and $J = \begin{bmatrix} 0 & 1 \\ -1 & 0 \end{bmatrix}$.

$$e^{\gamma_1 y_0 J} = e^{\gamma_1 y \begin{bmatrix} 0 & 1 \\ -1 & 0 \end{bmatrix}} = \begin{bmatrix} \cos \gamma_1 y & \sin \gamma_1 y \\ -\sin \gamma_1 y & \cos \gamma_1 y \end{bmatrix}, \tag{6.4}$$

6.3 Magnetic Force Equation

The Lorentz force law in (6.5) was used to derive the driving force and the levitation force on top of the concentrated-field magnetic matrix.

$$\overline{F} = \overline{J} \times \overline{B} ,$$ (6.5)

The synchronous permanent magnet planar motors (SPMPM) are the Lorentz-force-type actuator. The interaction force for the lateral and the vertical motion are derived through using the Maxwell stress tensor methodology.

$$\begin{bmatrix} f_{y\lambda} \\ f_{z\lambda} \end{bmatrix} = \mu_0 M_0 G e^{-\gamma_1 z_0} \begin{bmatrix} \cos\gamma_1 y & \sin\gamma_1 y \\ -\sin\gamma_1 y & \cos\gamma_1 y \end{bmatrix} \begin{bmatrix} J_a \\ J_b \end{bmatrix} ,$$ (6.6)

Equation (6.6) denotes the force matrix per spatial wavelength, where $f_{y\lambda}$ and $f_{z\lambda}$ are the y-directed and z-directed force per spatial wavelength, respectively [3]. The real and the imaginary parts of the fundamental current density components in the winding are defined by J_a and J_b. The motor geometric constant is represented by G as follows [3],

$$G = \frac{\sqrt{2}wl^2}{\pi^2} \left(1 - e^{-\gamma_1 \Gamma}\right)\left(1 - e^{-\gamma_1 \Delta}\right),$$ (6.7)

The parameters of the positioner's geometry are presented in Table 6-1.

6.4 Linearized Force Equation

The decoupled force in both the driving and the suspension directions are derived in (6.8). The total lateral force and the vertical force are represented as f_y and f_z, and the peak current components are i_a and i_b. Thus, (6.8) presents the relationship between the

Table 6-1 Geometric parameters

Variables	Unit	Values
The motor geometric constant G	m³	1.072×10^{-5}
The magnet remanence $\mu_0 M_0$	T	0.71
The width of one magnet array w	in	0.5
The thickness of the magnet array Δ	mm	12.70
The thickness of the winding Γ	mm	10.16
The on pich length l	mm	50.98
The absolute value of the fundamental wave number $\gamma_1 = 2\pi/l$	m^{-1}	123.25
The nominal motor air gap z_0	mm	2.3

phase currents for the planar motor and the magnetic force generated from the planar motor [3].

$$\begin{bmatrix} f_y \\ f_z \end{bmatrix} = \frac{1}{2}\mu_0 M_0 \eta_0 N_m G e^{-\gamma_1 z_0} \begin{bmatrix} \cos\gamma_1 y & \sin\gamma_1 y \\ -\sin\gamma_1 y & \cos\gamma_1 y \end{bmatrix} \begin{bmatrix} i_a \\ i_b \end{bmatrix}, \tag{6.8}$$

Equations (6.6) and (6.8) demonstrate the forces per spatial wavelength and the total forces, respectively. The relationships of two equations represented by $\begin{bmatrix} f_{y\lambda} & f_{z\lambda} \end{bmatrix}^T$ and $\begin{bmatrix} f_y & f_z \end{bmatrix}^T$ are presented in (6.9) and (6.10).

$$f_y = N_m f_{y\lambda}, \tag{6.9}$$

$$f_z = N_m f_{z\lambda}, \tag{6.10}$$

where N_m is the number of the planar-motor pitches. The relationship between the current densities and the peak current components in the windings are derived as follows,

$$i_a = 2\eta_0 J_a, \tag{6.11}$$

$$i_b = 2\eta_0 J_b, \tag{6.12}$$

where η_0 is the winding turn density of 3.5246×10^6 turns/m³ in each planar motor.

Therefore, substituting (6.9–6.12) into (6.6), the decoupled force equation (6.8) is derived for one of the planar motors.

The relationship between the phase current $\begin{bmatrix} i_A & i_B & i_C \end{bmatrix}^T$ and the peak current $\begin{bmatrix} i_a & i_b \end{bmatrix}^T$ is shown in (6.13) which is based on the inverse Blondel-Park transformation [98–99]. Each planar motor consists of a 3-phase winding set, which has a 1-in motor pitch. Phase differences among windings in the one planar motor are $\pi/3$, which helps the platen generate continuous driving force.

$$
\begin{bmatrix} i_A \\ i_B \\ i_C \end{bmatrix} = \begin{bmatrix} \cos 0 & \sin 0 \\ \cos \dfrac{\pi}{3} & \sin \dfrac{\pi}{3} \\ \cos \dfrac{2\pi}{3} & \sin \dfrac{2\pi}{3} \end{bmatrix} = \begin{bmatrix} 1 & 0 \\ \dfrac{1}{2} & \dfrac{\sqrt{3}}{2} \\ -\dfrac{1}{2} & \dfrac{\sqrt{3}}{2} \end{bmatrix} \begin{bmatrix} i_a \\ i_b \end{bmatrix}, \tag{6.13}
$$

The relationship between $\begin{bmatrix} f_y & f_z \end{bmatrix}^T$ and $\begin{bmatrix} i_A & i_B & i_C \end{bmatrix}^T$ in (6.14) is represented by plugging (6.13) into (6.8).

$$
\begin{bmatrix} f_y \\ f_z \end{bmatrix} = \frac{1}{2} \mu_0 M_0 \eta_0 N_m G e^{-\gamma_1 z_0} \begin{bmatrix} \cos \gamma_1 y & \sin \gamma_1 y \\ -\sin \gamma_1 y & \cos \gamma_1 y \end{bmatrix} \begin{bmatrix} \dfrac{2}{3} & -\dfrac{1}{3} & -\dfrac{1}{3} \\ 0 & \dfrac{1}{\sqrt{3}} & -\dfrac{1}{\sqrt{3}} \end{bmatrix} \begin{bmatrix} i_A \\ i_B \\ i_C \end{bmatrix}, \tag{6.14}
$$

The decoupled magnetic forces are generated by controling each phase current in the planar motor. The following two force equations for the lateral and the vertical motion are derived from (6.3) and (6.6).

$$
f_y = \frac{1}{2} \mu_0 M_0 \eta_0 N_m G e^{-\gamma_1 z_0} i_Q, \tag{6.15}
$$

$$f_z = \frac{1}{2}\mu_0 M_0 \eta_0 N_m Ge^{-\gamma_1 z_0} i_D, \tag{6.16}$$

The multiplicative terms of position z_0 and the current components i_Q and i_D shown in

(6.15) and (6.16) can be linearlized around the operating point by the Taylor series

expansion in (6.17) [100].

$$f(z) = f(z_0) + \frac{z-z_0}{1!}f'(z_0) + \frac{(z-z_0)^2}{2!}f''(z_0) + ... + \frac{(z-z_0)^n}{n!}f^{(n)}(z_0) + R_n(z), \tag{6.17}$$

To linearize the force equations, variables need to be set as,

$$z = z_0 + \tilde{z}, \tag{6.18}$$

$$i_Q = i_{Q0} + \tilde{i}_Q, \tag{6.19}$$

$$i_D = i_{D0} + \tilde{i}_D, \tag{6.20}$$

where z_0 denotes the nominal vertical height. The values of i_{Q0} and i_{D0} are the

constants at equilibrium. We use the first derivative term in the Taylor series.

$$\begin{aligned}
f_y &= f_y(i_{Q0}, z_0) + \left.\frac{\partial f_y}{\partial z}\right|_{\substack{i_Q=i_{Q0} \\ z=z_0}} (z-z_0) + \left.\frac{\partial f_y}{\partial i_Q}\right|_{\substack{z=z_0 \\ i_Q=i_{Q0}}} (i_Q - i_{Q0}) \\
&= \frac{1}{2}\mu_0 M_0 \eta_0 N_m Ge^{-\gamma_1 z_0} i_{Q0} - \frac{1}{2}\mu_0 M_0 \eta_0 N_m Ge^{-\gamma_1 z_0} i_{Q0}\gamma_1(z-z_0), \\
&+ \frac{1}{2}\mu_0 M_0 \eta_0 N_m Ge^{-\gamma_1 z_0}(i_Q - i_{Q0})
\end{aligned} \tag{6.21}$$

$$\begin{aligned}
f_z &= f_z(i_{D0}, z_0) + \left.\frac{\partial f_z}{\partial z}\right|_{\substack{i_D=i_{D0} \\ z=z_0}} (z-z_0) + \left.\frac{\partial f_z}{\partial i_D}\right|_{\substack{z=z_0 \\ i_D=i_{D0}}} (i_D - i_{D0}) \\
&= \frac{1}{2}\mu_0 M_0 \eta_0 N_m Ge^{-\gamma_1 z_0} i_{D0} - \frac{1}{2}\mu_0 M_0 \eta_0 N_m Ge^{-\gamma_1 z_0} i_{D0}\gamma_1(z-z_0), \\
&+ \frac{1}{2}\mu_0 M_0 \eta_0 N_m Ge^{-\gamma_1 z_0}(i_D - i_{D0})
\end{aligned} \tag{6.22}$$

If we let the linear force components be (6.23–6.24), then the Taylor series expanded equations can be rewritten as (6.25–6.26).

$$f_y = f_y(i_{Q0}, z_0) + \tilde{f}_y, \tag{6.23}$$

$$f_z = f_z(i_{D0}, z_0) + \tilde{f}_z, \tag{6.24}$$

$$\tilde{f}_y = -\frac{1}{2}\mu_0 M_0 \eta_0 N_m G e^{-\gamma_1 z_0} i_{Q0} \gamma_1 \tilde{z} + \frac{1}{2}\mu_0 M_0 \eta_0 N_m G e^{-\gamma_1 z_0} \tilde{i}_Q, \tag{6.25}$$

$$\tilde{f}_z = -\frac{1}{2}\mu_0 M_0 \eta_0 N_m G e^{-\gamma_1 z_0} i_{D0} \gamma_1 \tilde{z} + \frac{1}{2}\mu_0 M_0 \eta_0 N_m G e^{-\gamma_1 z_0} \tilde{i}_D, \tag{6.26}$$

Equations (6.25–6.26) are the linearized force equations for the suspension and the driving motion. Since the coefficients of $\tilde{z}_0$, $\tilde{i}_{Q0}$, and $\tilde{i}_{D0}$ are constant, the linearized force equations (6.25–6.26) are functions of variables $\tilde{z}$, $\tilde{i}_Q$, and $\tilde{i}_D$.

6.5 Motion Generations of the Positioner

The force equations for vertical and the translational (lateral) motion were derived in the previous sections. These decoupled force equations are applied to each planar motor in Figure 6-3. The positioner was designed to generate all 6-DOF motions. To make all six independent motions, the system requires at least six individual actuators. Our positioner loads three planar motors. Each planar motor can produce the suspension and the lateral driving force, individually as introduced in the *DQ*-decomposition section. Therefore, all three planar motors together can generate any directional motions by interactions among planar motors. Motor A, B, and C are indicated in Figure 6-3, which represents the bottom view of the platen. The origin of the platen is located at the center

of mass. Motors A and B generate the driving force in the *y*-direction, and Motor C works for the *x*-direction motion. More dynamic motions are generated in the *y*-direction motion than those in *x*-direction, because two planar motors A and B are involved in *y*. Motor C
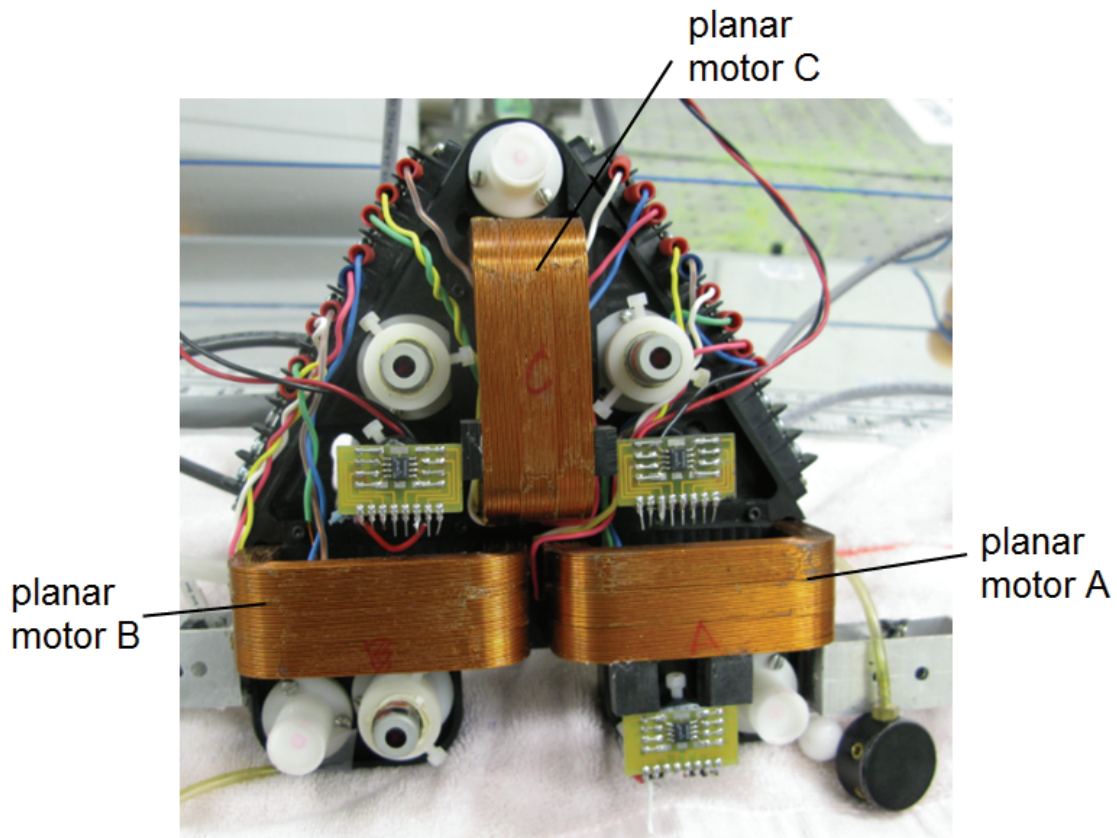
Figure 6-3: Bottom face of the positioner
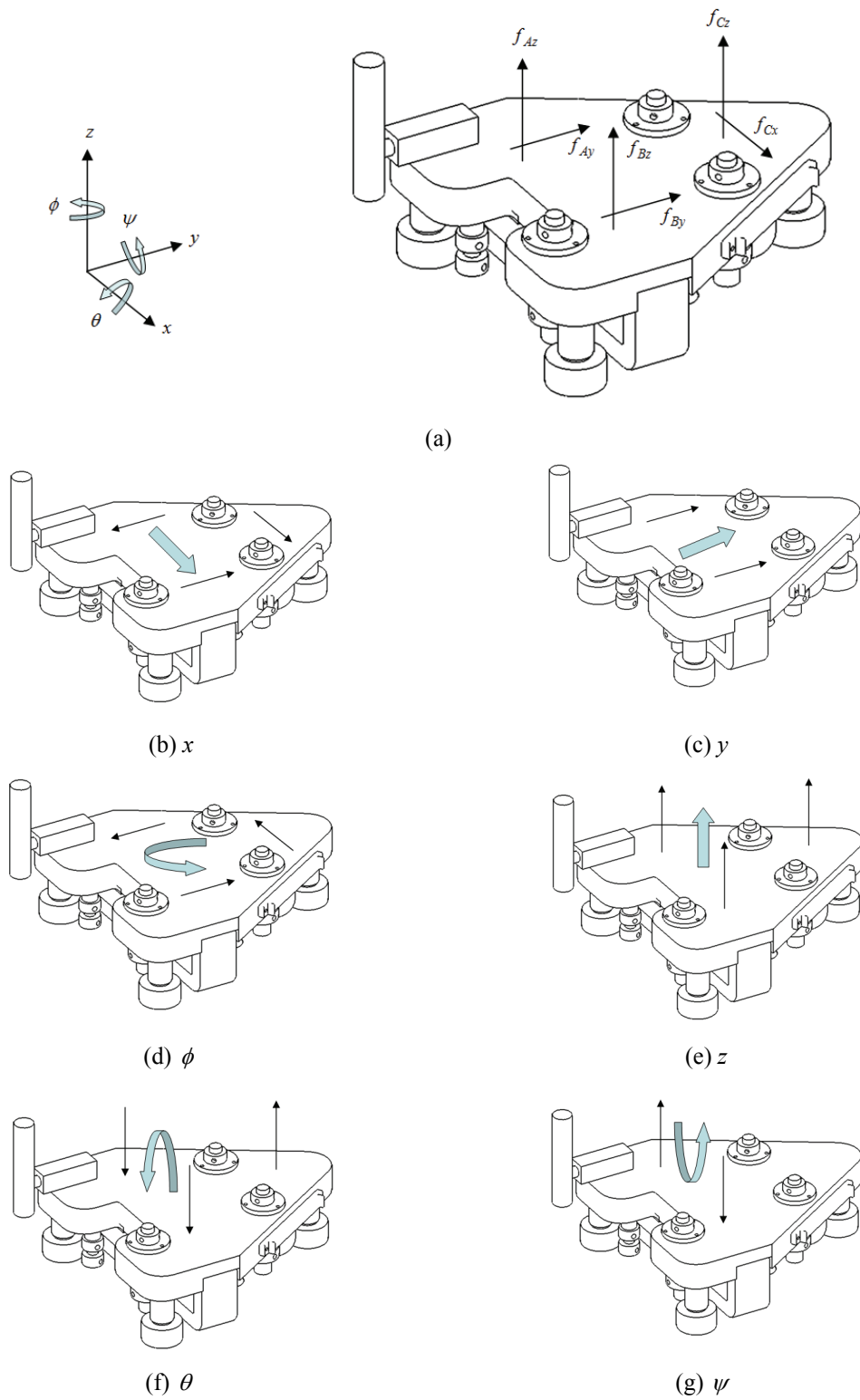
Figure 6-4: Illustration of 6-DOF motion generation

only contributes to the *x*-direction motion. Figure 6-4 illustrates how all motions are controlled by each planar motor. Motors *A* and *B* generate *y*-direction forces of f_{Ay} and f_{By}, respectively. Motor C generates *x*-direction force of f_{Cx}. The magnetic suspension forces f_{Az}, f_{Bz}, and f_{Cz} in the *z*-direction are generated by all planar motors (A, B, and C). Figure 6-4 (a) shows the coordinate and the force directions on each planar motor. The lateral motion configurations are in Figure 6-4 (b), (c), and (d). If the positioner moves to *y*-direction, motors A and B generate the translational forces. There is no torque around the *z*-axis by the planar motor geometry. However, the torque τ_z occurs when the platen moves in the *x*-direction because motor C is not located at the corresponding position with the center of mass. To achieve stable movements in *x*, the torque τ_z need to be cancelled out. Interaction forces generated by motors A and B provide the torque elimination. Figure 6-4 (e), (f), and (g) illustrate how the vertical motions are generated. The magnitude and the force direction determine the control angle in the rotation around *x*, *y* and *z*.

6.6 Euler Angles

The Force equations defined in the previous section depend on the trigonometric functions on the electrical angles of the platen with respect to the inertial frame. So, Euler angles and the coordinate frame will be defined in this section.

The coordinate system in the platen consists of the body frame *xyz* and the inertial frame *XYZ*. The deformation or bending of the platen while it is moving is not considered
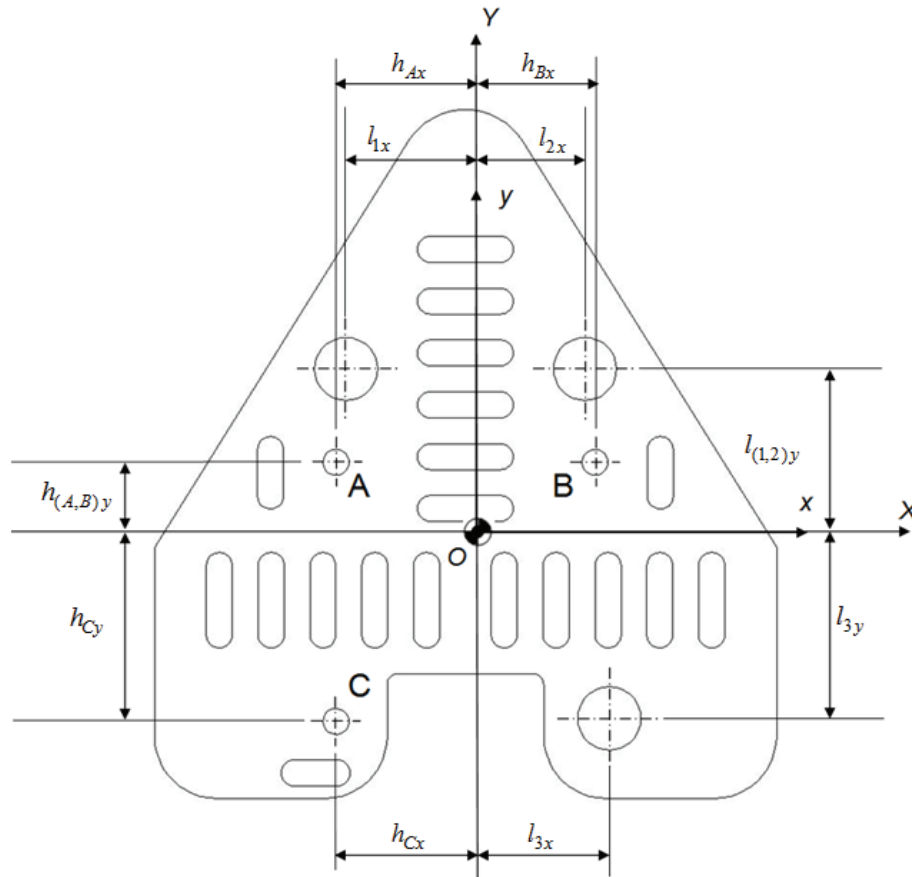
Figure 6-5: Top view of the positioner's coordinate

so that the platen is regarded as a rigid body [101]. The coordinates *xyz* attached on the body has the origin at the center of mass. The coordinates *XYZ* is fixed at the initial position of the positioner body, which is identified with the center of mass at the initial position. Figure 6-5 presents the coordinate system of the positioner.

The coordinate transformation is required for the platen to control the vertical motion. Three laser distance sensors mounted on the platen are employed to measure displacements at each position for the translation in *z*, rotation around the *x*- and *y*-axes.

All measurements are based on the moving frame *xyz* and the coordinate transformation performs the transform the distances with respect to the inertial frame *XYZ*.

For the rotations, there are three motions such as the yaw around the *z*-axis, the roll around the *x*-axis, and the pitch around *y*-axis, which are represented as $[A_\phi]$, $[A_\theta]$, and $[A_\psi]$, respectively. The corresponding transformation matrices are as follows,

$$[A_\phi] = \begin{bmatrix} \cos\phi & \sin\phi & 0 \\ -\sin\phi & \cos\phi & 0 \\ 0 & 0 & 1 \end{bmatrix} \tag{6.27}$$

$$[A_\theta] = \begin{bmatrix} 1 & 0 & 0 \\ 0 & \cos\theta & \sin\theta \\ 0 & -\sin\theta & \cos\theta \end{bmatrix} \tag{6.28}$$

$$[A_\psi] = \begin{bmatrix} \cos\psi & 0 & -\sin\psi \\ 0 & 1 & 0 \\ \sin\psi & 0 & \cos\psi \end{bmatrix}. \tag{6.29}$$

The complete transformation matrix will be obtained by multiplying all three components $[A_\phi]$, $[A_\theta]$, and $[A_\psi]$.

$$[A] = [A_\phi][A_\theta][A_\psi]$$

$$= \begin{bmatrix} \cos\psi\cos\phi & \cos\psi\sin\phi & -\sin\psi \\ \sin\theta\sin\psi\cos\phi - \cos\theta\sin\phi & \sin\theta\sin\psi\sin\phi + \cos\theta\cos\phi & \cos\psi\sin\theta \\ \cos\theta\sin\psi\cos\phi + \sin\theta\sin\phi & \cos\theta\sin\psi\sin\phi - \sin\theta\cos\phi & \cos\psi\cos\theta \end{bmatrix} \tag{6.30}$$

$$\begin{bmatrix} x \\ y \\ z \end{bmatrix} = [A] \begin{bmatrix} X \\ Y \\ Z \end{bmatrix} \tag{6.31}$$

$$\begin{bmatrix} X \\ Y \\ Z \end{bmatrix} = [A^{-1}] \begin{bmatrix} x \\ y \\ z \end{bmatrix} \tag{6.32}$$

Equations (6.31–6.32) present the coordinate transformations between the body frame and the inertial frame with the transformation matrix $[A]$. The inverse of the matrix $[A]$ is

$$[A]^{-1} = \begin{bmatrix} \cos\theta\cos\phi & \sin\theta\sin\psi\cos\phi - \cos\theta\sin\phi & \cos\theta\sin\psi\cos\phi + \sin\theta\sin\phi \\ \cos\psi\sin\phi & \sin\theta\sin\psi\sin\phi + \cos\theta\cos\phi & \cos\theta\sin\psi\sin\phi - \sin\theta\cos\phi \\ -\sin\psi & \cos\psi\sin\theta & \cos\psi\cos\theta \end{bmatrix}. \quad (6.33)$$

The positioner's equations of motion are based on Newton's second law with the coordinate transformation. The following equations (6.34–6.37) present the sums of external forces and the sums of the moments of the external forces with respect to the inertial coordinate origin O.

$$\sum F_x = ma_{ox} \quad (6.34)$$

$$\sum F_y = ma_{oy} \quad (6.35)$$

$$\sum F_z = ma_{oz} \quad (6.36)$$

$$\begin{Bmatrix} \sum M_{ox} \\ \sum M_{oy} \\ \sum M_{oz} \end{Bmatrix} = \begin{bmatrix} I_{xx} & -I_{xy} & I_{xz} \\ -I_{yx} & I_{yy} & -I_{yz} \\ -I_{zx} & -I_{zy} & I_{zz} \end{bmatrix} \begin{Bmatrix} a_x \\ a_y \\ a_z \end{Bmatrix} + \begin{bmatrix} 0 & -\omega_z & \omega_y \\ \omega_z & 0 & -\omega_x \\ -\omega_y & \omega_x & 0 \end{bmatrix} \begin{bmatrix} I_{xx} & -I_{xy} & I_{xz} \\ -I_{yx} & I_{yy} & -I_{yz} \\ -I_{zx} & -I_{zy} & I_{zz} \end{bmatrix} \begin{Bmatrix} \omega_x \\ \omega_y \\ \omega_z \end{Bmatrix}$$

$$(6.37)$$

The positioner is regarded as a pure mass system. Hence, no friction exists between the mover and the ground. The equations of motion in the horizontal motion are as follows,

$$M\frac{d^2x}{dt^2} = f_x \quad (6.38)$$

$$M\frac{d^2y}{dt^2} = f_y \quad (6.39)$$

$$I_{zz}\frac{d^2\phi}{dt^2} = M_{oz} + (I_{xx} - I_{yy})\omega_x\omega_y. \tag{6.40}$$

As introduced in an inertia tensor section, the products of inertia in the inertia tensor matrix were neglected. The equilibrium point of this equation is $\omega_x = \omega_y = 0$ rad/s so that the equation can be linearized.

$$I_{zz}\frac{d^2\phi}{dt^2} = M_{oz} \tag{6.41}$$

The dynamic models of the positioner in the horizontal motion are derived by taking the Laplace transform of (6.38–6.40).

$$\frac{x(s)}{f_x(s)} = \frac{1}{ms^2} \tag{6.42}$$

$$\frac{y(s)}{f_y(s)} = \frac{1}{ms^2} \tag{6.43}$$

$$\frac{\phi(s)}{M_{oz}(s)} = \frac{1}{I_{zz}s^2}. \tag{6.44}$$

The dynamic models for vertical modes are as follows,

$$M\frac{d^2z}{dt^2} = f_z - K_z z \tag{6.45}$$

$$I_{xx}\frac{d^2\theta}{dt^2} = M_{ox} - K_\theta\theta \tag{6.46}$$

$$I_{yy}\frac{d^2\psi}{dt^2} = M_{oy} - K_\psi\psi, \tag{6.47}$$

where K_z is the effective spring constant of the magnetic motor, which is determined by experiments based on Hooke's law. The vertical direction force represented by f_z make possible the platen be levitated. I_{xx} and I_{yy} present the moment of inertia for the rotation

of *x* and *y*, respectively. The effective torsional spring constants around the *x*- and *y*-axes, which are determined by experiments are indicated as K_θ and K_ψ, respectively. By taking the Laplace transform, the ordinary differential equations (ODE) (6.45−6.47) can be converted to the transfer functions. The corresponding dynamic models are as follows,

$$\frac{z(s)}{f_z(s)} = \frac{1}{ms^2 + K_z} \tag{6.48}$$

$$\frac{\theta(s)}{M_{ox}(s)} = \frac{1}{I_{xx}s^2 + K_\theta} \tag{6.49}$$

$$\frac{\psi(s)}{M_{oy}(s)} = \frac{1}{I_{yy}s^2 + K_\psi}. \tag{6.50}$$

6.7 Force Allocation

The force allocation among the three planar motors is discussed in this section. Several commanded forces and the moments of the platen are related to the force allocation of each motor. Figure 6-6 illustrates the free-body diagram for force allocation. We regard that the coordinate for the moving frame and that of the inertial frame coincide at the origin. The magnet force generated by each planar motor is considered as the concentrated force applied at the center of each motor. The origin is the center of mass of the platen. Distances of each planar motor from the center of the platen are indicated as *L*. $L_{(A,B,C)X}$ denotes distances from the center of the planar motors A, B, and C from the *y*-axis. The distances from the center of each planar motor from the *x*-axis are represented as $L_{(A,B,C)y}$ likewise. Table 6-2 presents the each motor distance value from the origin.
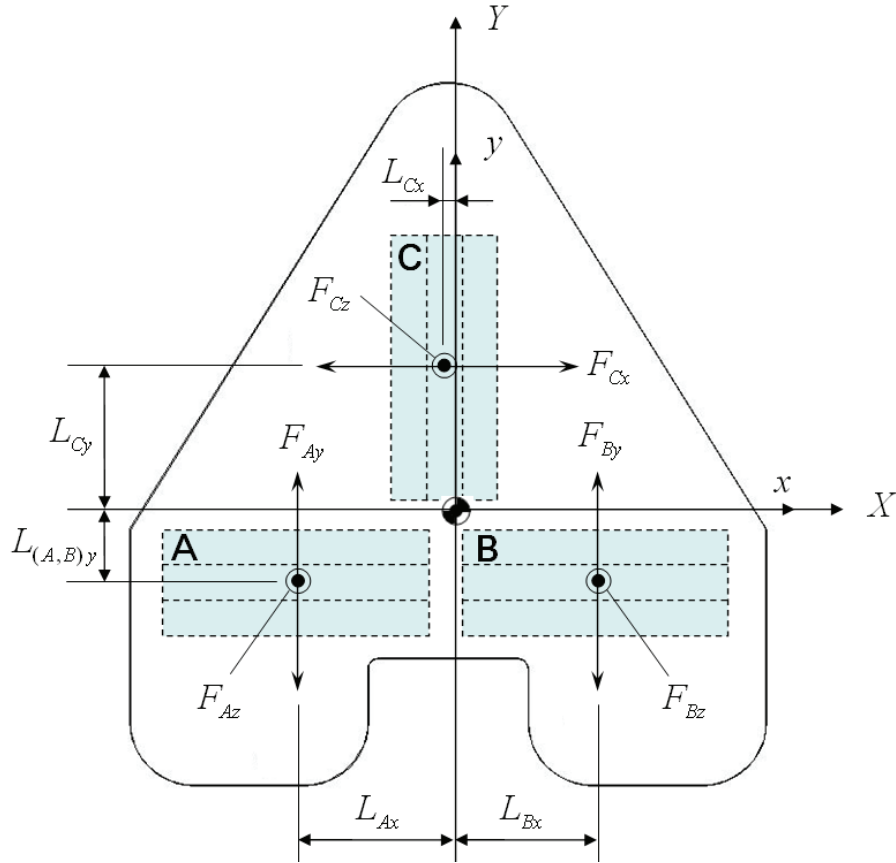
Figure 6-6: Free-body diagram for the force allocation

Table 6-2 Specifications of the planar motor locations

Variables	Distance (mm)
L_{Ax}	39.74
L_{Bx}	37.86
L_{Cx}	1.36
L_{Ay}	19.77
L_{By}	19.77
L_{Cy}	34.89

The forces and the moment in horizontal direction are studied in this section and Figure 6-4 verified how the positioner moves by the motor forces. Translation dynamic motions in x and y have performed as follows.

$$f_x = f_{cx},$$
(6.51)

$$f_y = f_{Ay} + f_{By},$$
(6.52)

The moment term around z is shown in (6.53). All three planar motors are involved in generating torque.

$$M_{oz} = -L_{Az}f_{Ay} + L_{Bx}f_{By} - L_{Cy}f_{Cx},$$
(6.53)

The above equations (6.51–6.53) can be represented in matrix form.

$$
\begin{bmatrix} f_x \\ f_y \\ M_{oz} \end{bmatrix} = \begin{bmatrix} 0 & 0 & 1 \\ 1 & 1 & 0 \\ L_{Ax} & -L_{Bx} & L_{Cy} \end{bmatrix} \begin{bmatrix} f_{Ay} \\ f_{By} \\ f_{Cx} \end{bmatrix} = \begin{bmatrix} 0 & 0 & 1 \\ 1 & 1 & 0 \\ 0.03974 & -0.03786 & 0.03489 \end{bmatrix} \begin{bmatrix} f_{Ay} \\ f_{By} \\ f_{Cx} \end{bmatrix}
$$
(6.54)

By taking the inverse of the matrix, we can obtain the relationship (6.55) from the total force or moment to each planar motor force.

$$
\begin{bmatrix} f_{Ay} \\ f_{By} \\ f_{Cx} \end{bmatrix} = \begin{bmatrix} -\dfrac{L_{Cy}}{L_{Ax}+L_{Bx}} & \dfrac{L_{Bx}}{L_{Ax}+L_{Bx}} & \dfrac{1}{L_{Ax}+L_{Bx}} \\ \dfrac{L_{Cx}}{L_{Ax}+L_{Bx}} & \dfrac{L_{Ax}}{L_{Ax}+L_{Bx}} & -\dfrac{1}{L_{Ax}+L_{Bx}} \\ 1 & 0 & 0 \end{bmatrix} \begin{bmatrix} f_x \\ f_y \\ M_{oz} \end{bmatrix}
$$
(6.55)

If we substitute values from the Table 6-1, the force allocation matrix will become

$$
\begin{bmatrix} f_{Ay} \\ f_{By} \\ f_{Cx} \end{bmatrix} = \begin{bmatrix} -0.449613 & 0.487887 & 12.8866 \\ 0.449613 & 0.512113 & -12.8866 \\ 1 & 0 & 0 \end{bmatrix} \begin{bmatrix} f_x \\ f_y \\ M_{oz} \end{bmatrix}.
$$
(6.56)

In the vertical mode like the horizontal force allocation, the total force and moments can be generated by each planar motor.

$$f_z = f_{Az} + f_{Bz} + f_{Cz}, \tag{6.57}$$

$$M_{ox} = -f_{Az}L_{Ay} - f_{Bz}L_{By} + f_{Cz}L_{Cy}, \tag{6.58}$$

$$M_{oy} = f_{Az}L_{Ax} - f_{Bz}L_{Bz} - f_{Cz}L_{Cx}. \tag{6.59}$$

Equations (6.57–6.59) can be written as the matrix form as follows

$$\begin{bmatrix} f_z \\ M_{ox} \\ M_{oy} \end{bmatrix} = \begin{bmatrix} 1 & 1 & 1 \\ -L_{Ay} & -L_{By} & L_{Cy} \\ L_{Ax} & -L_{Bx} & -L_{Cx} \end{bmatrix} \begin{bmatrix} f_{Az} \\ f_{Bz} \\ f_{Cz} \end{bmatrix} = \begin{bmatrix} 1 & 1 & 1 \\ -0.01977 & -0.01977 & 0.03489 \\ 0.03974 & -0.03786 & -0.00136 \end{bmatrix} \begin{bmatrix} f_{Az} \\ f_{Bz} \\ f_{Cz} \end{bmatrix}.$$

$$\tag{7.60}$$

Equation (6.60) is achieved by plugging all values in from Table 1. The inverse transform

is as follows.

$$\begin{bmatrix} f_{Az} \\ f_{Bz} \\ f_{Cz} \end{bmatrix} = \begin{bmatrix} 0.317762 & -8.60521 & 12.8866 \\ 0.325048 & -9.6897 & -12.8866 \\ 0.36169 & 18.2949 & 0 \end{bmatrix} \begin{bmatrix} f_z \\ M_{ox} \\ M_{oy} \end{bmatrix}, \tag{6.61}$$

Sensor equations are derived in the previous chapter.

6.8 State-Space Model

This section introduces the state-space model. The inputs are the current values, and the outputs are the displacements of the positioner. The state-space dynamics can be developed for the observer and LQG design in Chapter VII. Since the state-space model should have the current input values, the equations (6.38−6.41) and (6.45−6.47) should have the linearlized current forms as follows.

$$M\frac{d^2x}{dt^2} = \frac{1}{2}\mu_0 M_0 \eta_0 N_m G e^{-\gamma_1 z_0} i_{CQ} \tag{6.62}$$

$$M \frac{d^2 y}{dt^2} = \frac{1}{2} \mu_0 M_0 \eta_0 N_m G e^{-\gamma_1 z_0} (i_{AQ} + i_{BQ})$$ (6.63)

$$I_{zz} \frac{d^2 \phi}{dt^2} = \frac{1}{2} \mu_0 M_0 \eta_0 N_m G e^{-\gamma_1 z_0} (-L_{Ax} i_{AQ} + L_{Bx} i_{BQ} - L_{Cy} i_{CQ})$$ (6.64)

Since the term $\frac{1}{2} \mu_0 M_0 \eta_0 N_m G e^{-\gamma_1 z_0}$ is a constant, it is indicated by the character A in the state-space representation.

$$A = \frac{1}{2} \mu_0 M_0 \eta_0 N_m G e^{-\gamma_1 z_0}$$ (6.65)

The state-space form in the horizontal mode is

$$\begin{bmatrix} \dot{x} \\ \dot{y} \\ \dot{r} \\ \dot{d} \\ \dot{f} \\ \dot{v} \end{bmatrix} = \begin{bmatrix} 0 & 0 & 0 & 1 & 0 & 0 \\ 0 & 0 & 0 & 0 & 1 & 0 \\ 0 & 0 & 0 & 0 & 0 & 1 \\ 0 & 0 & 0 & 0 & 0 & 0 \\ 0 & 0 & 0 & 0 & 0 & 0 \\ 0 & 0 & 0 & 0 & 0 & 0 \end{bmatrix} \begin{bmatrix} x \\ y \\ r \\ d \\ f \\ v \end{bmatrix} + \begin{bmatrix} 0 & 0 & 0 \\ 0 & 0 & 0 \\ 0 & 0 & 0 \\ 0 & 0 & \frac{A}{M} \\ \frac{A}{M} & \frac{A}{M} & 0 \\ -\frac{A}{I_{zz}} L_{Ay} & \frac{A}{I_{zz}} L_{By} & -\frac{A}{M} L_{Cy} \end{bmatrix} \begin{bmatrix} i_{AQ} \\ i_{BQ} \\ i_{CQ} \end{bmatrix}$$ (6.66)

$$Y_1 = \begin{bmatrix} 1 & 0 & 0 & 0 & 0 & 0 \\ 0 & 1 & 0 & 0 & 0 & 0 \\ 0 & 0 & 1 & 0 & 0 & 0 \end{bmatrix} \begin{bmatrix} x \\ y \\ r \\ d \\ f \\ v \end{bmatrix}.$$ (6.67)

The values of $\begin{bmatrix} d & f & v \end{bmatrix}^T$ indicate the velocities of $\begin{bmatrix} x & y & r \end{bmatrix}^T$. Equations (6.66–6.67) represent the state-space model of the positioner for the horizontal mode. The output is indicated as Y_1 in the equation (6.66) and the output matrix has a dimension of three by six. Since the Hall-effect sensors only provide the displacement values of positioner, the velocity terms can not be presented in the output matrix. Similarly, the vertical mode

state-space representation based on equations (6.45−6.47) is presented in equations (6.68−6.69).

$$
\begin{bmatrix} \dot{z} \\ \dot{\theta} \\ \dot{\psi} \\ \dot{p} \\ \dot{q} \\ \dot{w} \end{bmatrix} = \begin{bmatrix} 0 & 0 & 0 & 1 & 0 & 0 \\ 0 & 0 & 0 & 0 & 1 & 0 \\ 0 & 0 & 0 & 0 & 0 & 1 \\ -\dfrac{K_z}{M} & 0 & 0 & 0 & 0 & 0 \\ 0 & -\dfrac{K_\theta}{M} & 0 & 0 & 0 & 0 \\ 0 & 0 & -\dfrac{K_\psi}{M} & 0 & 0 & 0 \end{bmatrix} \begin{bmatrix} z \\ \theta \\ \psi \\ p \\ q \\ w \end{bmatrix} + \begin{bmatrix} 0 & 0 & 0 \\ 0 & 0 & 0 \\ 0 & 0 & 0 \\ \dfrac{A}{M} & \dfrac{A}{M} & \dfrac{A}{M} \\ -\dfrac{A}{I_{xx}}L_{Ay} & -\dfrac{A}{I_{xx}}L_{By} & \dfrac{A}{I_{xx}}L_{Cy} \\ \dfrac{A}{I_{yy}}L_{Ax} & -\dfrac{A}{I_{yy}}L_{By} & -\dfrac{A}{I_{yy}}L_{Cy} \end{bmatrix} \begin{bmatrix} i_{AD} \\ i_{BD} \\ i_{CD} \end{bmatrix},
\tag{6.68}
$$

$$
Y_1 = \begin{bmatrix} 1 & 0 & 0 & 0 & 0 & 0 \\ 0 & 1 & 0 & 0 & 0 & 0 \\ 0 & 0 & 1 & 0 & 0 & 0 \end{bmatrix} \begin{bmatrix} z \\ \theta \\ \psi \\ p \\ q \\ w \end{bmatrix},
\tag{6.69}
$$

CHAPTER VII

CONTROLLER DESIGN

This chapter introduces the process of the controller design to run the positioner in real time. The controllers were designed with respect to the dynamic system models derived in Chapter V. The six different second order digital lead-lag digital controllers for each axis were designed with root-locus methodologies and the Bode plots using Matlab. The multivariable controllers based on the LQG methodology for the horizontal mode were also designed.

7.1 Lead-Lag Compensator for Translation Mode

The positioner was designed to generate 6-DOF motion, where each axis requires the independent compensators. First, the three single-input-single-output (SISO) compensators were designed in the x-, y- and ϕ-direction. Since aerostatic bearings support the constant air gap between the positioner and the ground, the designed compensators can be implemented easily without the vertical-mode feedback control. The decoupled lateral dynamic equations of motion were derived in the previous chapter as follows,

$$M\frac{d^2\{x,y\}}{dt^2} - \mu_0 M_0 \eta_0 N_m G e^{-\gamma_1 z} i_D \{x,y\} = \mu_0 M_0 \eta_0 N_m G e^{-\gamma_1 z} i_Q \qquad (7.1)$$

Equations of motion based on Newton's second law are,

$$M\frac{d^2\{x,y\}}{dt^2} = f_{\{x,y\}}, \qquad (7.2)$$

$$I_{zz}\frac{d^2\phi}{dt^2} = \tau.$$ (7.3)

A modal force represented by f_x is a sum of the decomposed lateral force components. As mentioned in the previous chapter, the total mass of the platen is 1.52 kg and the moment of inertia around z is 0.0037 kg-m². The transfer functions as shown in (7.4–7.6) can be derived by taking the Laplace transform. The dynamic models in the x-, y-, and ϕ-direction for the lateral mode are,

$$\frac{X(s)}{F(s)} = \frac{1}{1.52s^2}$$ (7.4)

$$\frac{Y(s)}{F(s)} = \frac{1}{1.52s^2}$$ (7.5)

$$\frac{\Phi(s)}{T(s)} = \frac{1}{0.0037s^2}.$$ (7.6)

From the dynamic equations of motion and the transfer functions, SISO lead-lag controllers can be designed in each axis. The nonlinear term in the magnet force equation is eliminated by using the transfer functions directly between the input magnet force and the output displacement. A continuous-time lead-lag compensators for x and y were first designed with the root-locus methodology. Equation (7.7) shows the lead-lag compensator for the x- and y-direction, where the same compensators are used in both axes.

$$G_{x,y}(s) = 1.5 \times 10^4 \left(\frac{1+0.11s}{1+0.00088s}\right)\left(\frac{1+0.1s}{s}\right).$$ (7.7)

A pure integrator exists in the compensator as shown in (7.7). The dynamics of the positioner was considered a pure mass system, which implies that the positioner originally includes integrators as well. The whole system theoretically does not need an

additional integrator against the steady-state error. However, an additional integrator is very important in the real system, because the actual system is not a perfect pure mass by air-suspension bearings or the magnetic levitation. There are several components that prevent the positioner from being the pure mass such as the power cables, the current signal cables, the plastic air-bearing pipes, and the sensor cables.

Figure 7-1 presents the continuous-time closed-loop control structure with the lead-lag compensator. The controllers for *x* and *y* were first designed, and then controllers for other axes were designed with similar methods.
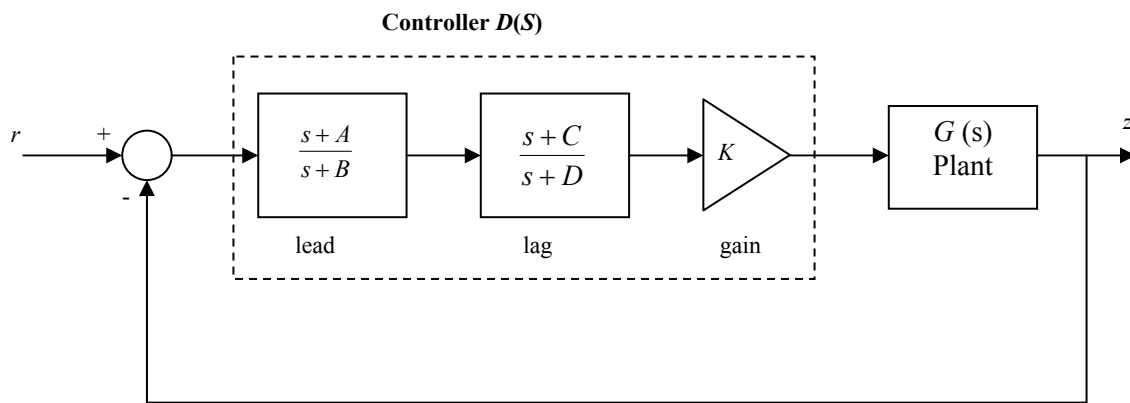
Figure 7-1: Continuous-time decoupled lead-lag controller

There are several methodologies to design a digital controller by different numerical approximations. The commonly used methods are zero-order hold (ZOH), Tustin that is a bilinear approximation, and matched pole-zero (MPZ) methods. After the continuous-time controller in the *s*-domain is designed, the pole-zero matching technique converts the controller to fit the digital system through sampling process [102]. The Matlab SISO

tool equipped with well-organized graphics provides effective methods to convert controllers with following technique,

$$z = e^{sT}.$$ (7.8)

The sampling frequency of 800 Hz was determined by the experiments with respect to the hardware setup. The positioning stage is controlled by the Linux based real-time control with data acquisition boards manufactured by National Instruments (NI). Experimental tests concluded that the optimized sampling frequency was 800 Hz, which means that the whole control routine is completed in 1.25 ms. Although the RTAI and data acquisition boards can generate faster sampling frequency, the Pentium IV personal computer that processes six individual data signals could not support the constant fast speed sampling. The sampling frequency was tested in 1 kHz, 2 kHz, 4 kHz, and 5 kHz. Equation (7.9) represents the converted digital compensator for the x- and y-direction.

$$G_{x,y}(z) = 1.53 \times 10^5 \left(\frac{z - 0.9093}{z - 0.2741}\right)\left(\frac{z - 0.9871}{z - 1}\right),$$ (7.9)

$$G_{\phi}(s) = 35\left(\frac{1 + 0.12s}{1 + 0.00088s}\right)\left(\frac{1 + 0.1s}{s}\right),$$ (7.10)

$$G_{\phi}(z) = 1.42 \times 10^3 \left(\frac{z - 0.9093}{z - 0.2741}\right)\left(\frac{z - 0.9871}{z - 1}\right).$$ (7.11)
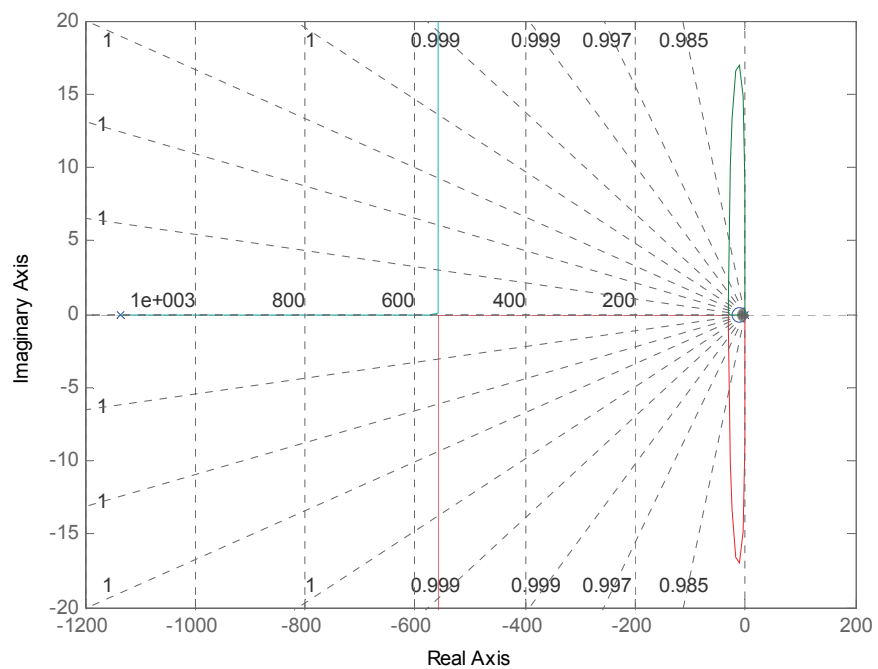
Figure 7-2: Root locus for translation in *x* and *y*
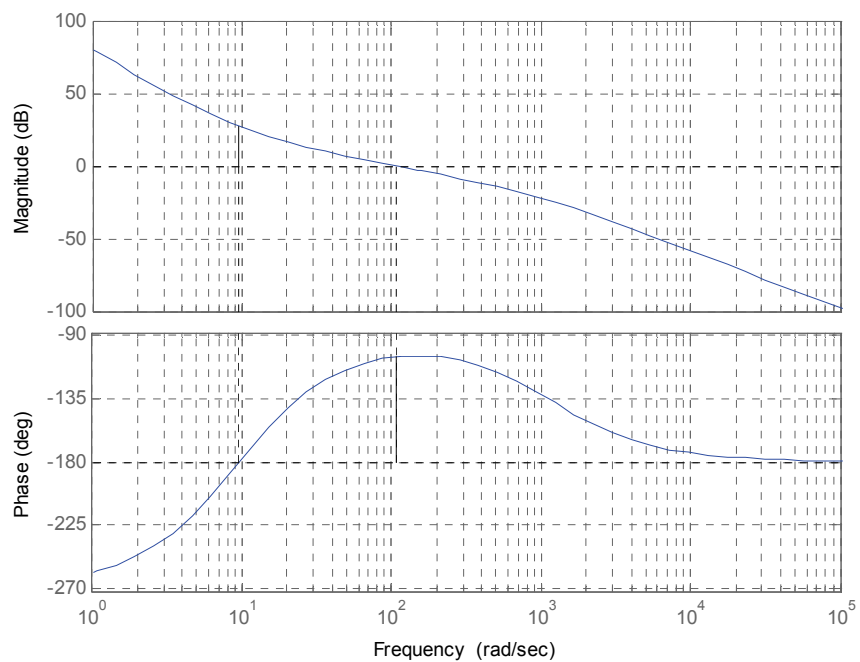
Figure 7-3: Loop transmission for translation in *x* and *y*
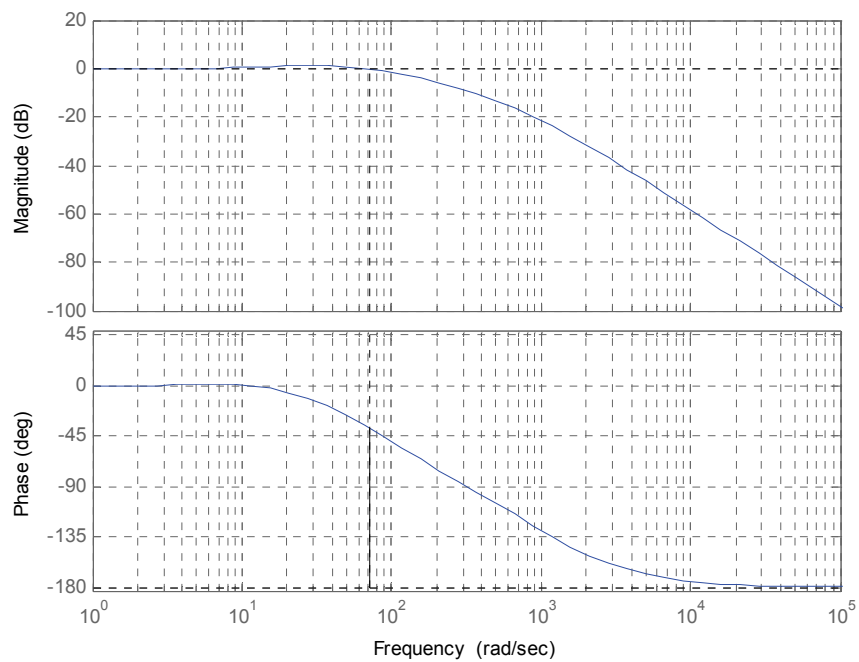
Fig. 7-4 Closed-loop Bode plot for translation in *x* and *y*
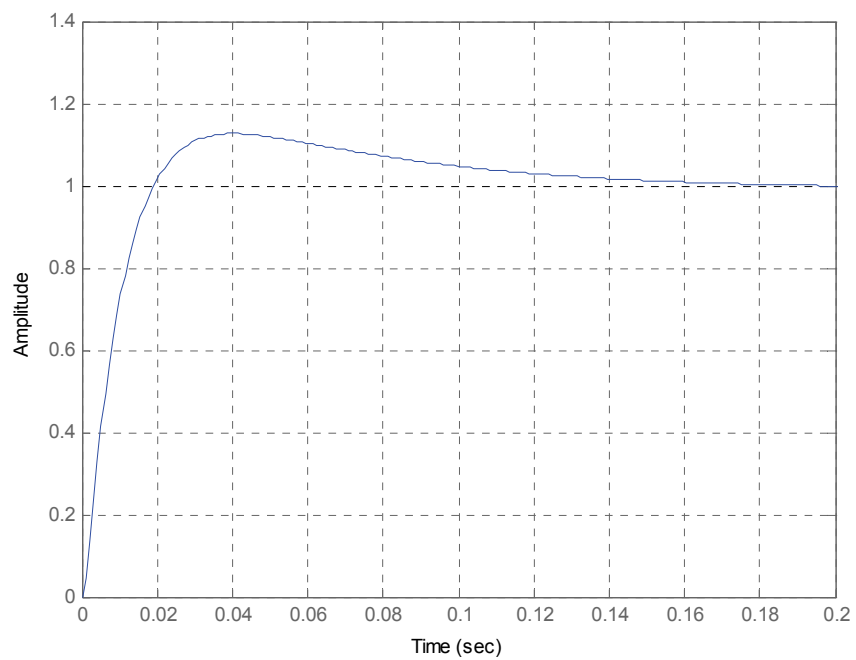
Figure 7-5: Step response in *x* and *y*
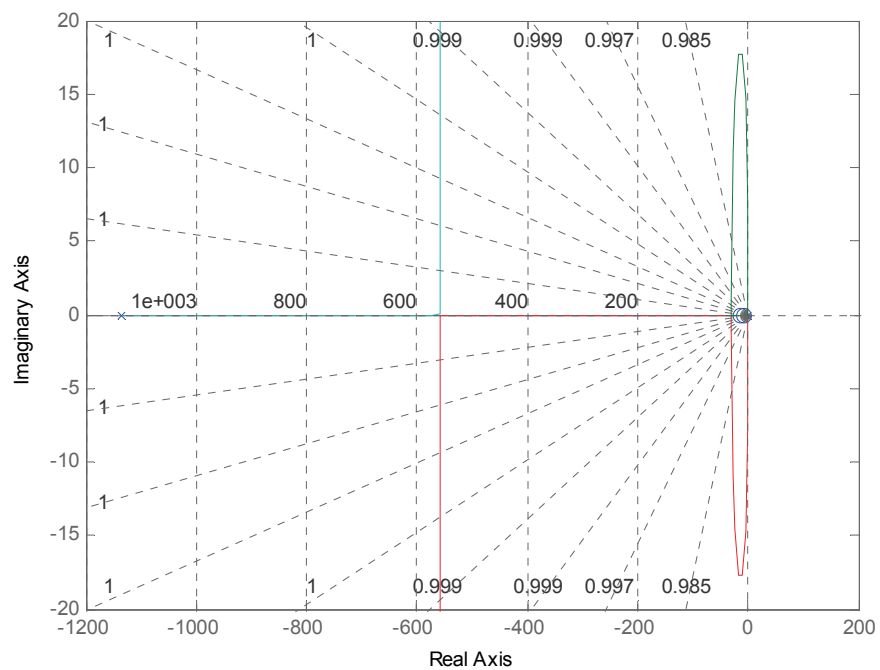
Figure 7-6: Root locus in rotation around z
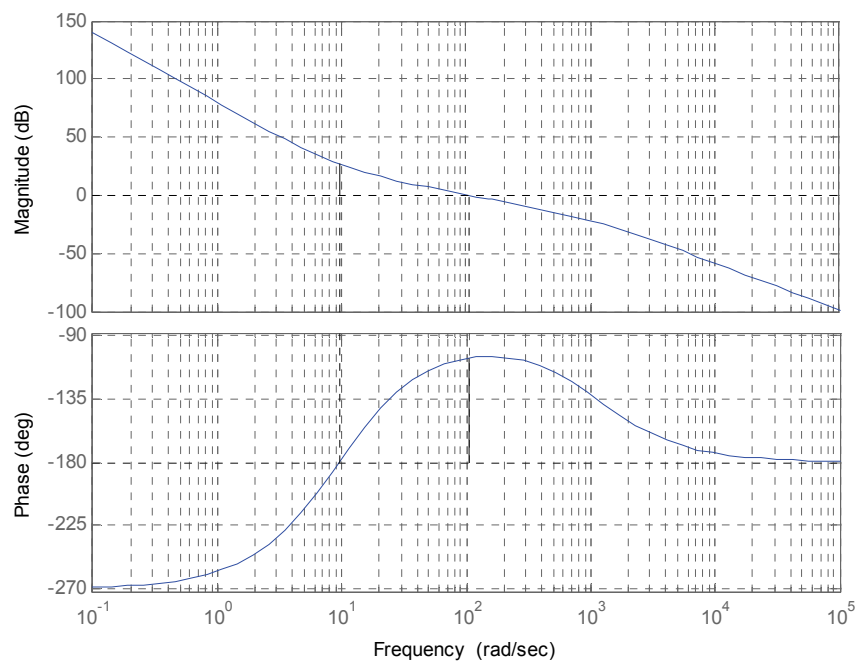
Figure 7-7: Loop transmission in rotation around z
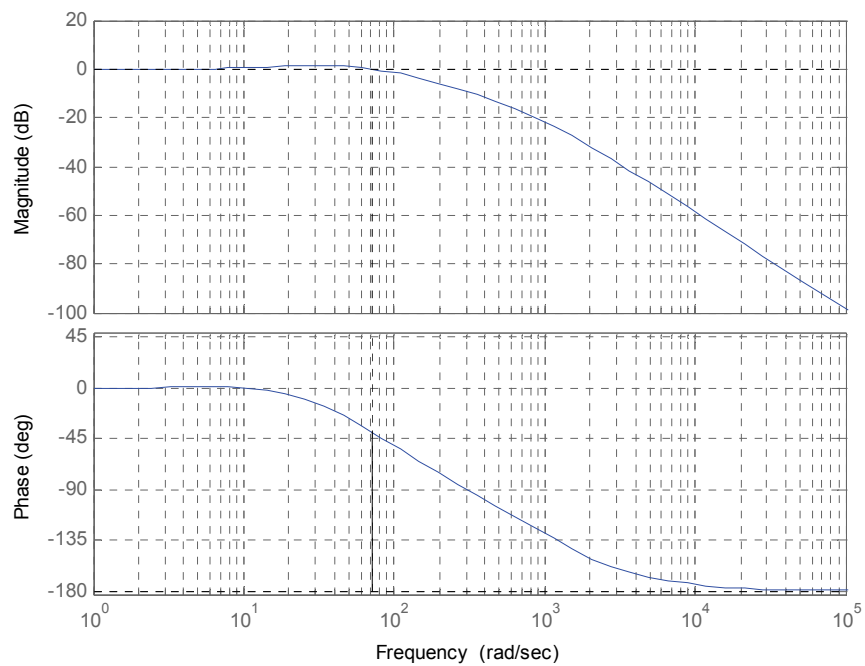
Figure 7-8: Closed-loop Bode plot in rotation around *z*
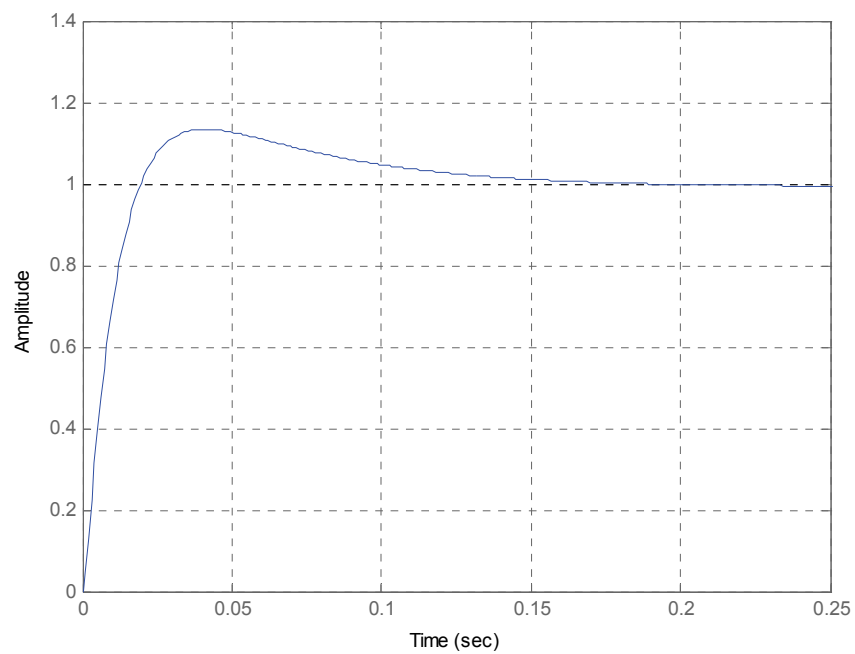
Figure 7-9: Step response in rotation around *z*

7.2 Vertical Mode Control

The dynamic motions for the vertical modes start from the following equation such as the lateral mode.

$$M \frac{d^2z}{dt^2} - \mu_0 M_0 \eta_0 N_m G e^{-\gamma_1 z} i_D z = \mu_0 M_0 \eta_0 N_m G e^{-\gamma_1 z} i_Q.$$

(7.12)

By plugging in parameters in (6.45), the following equation was obtained for z.

$$1.52 \frac{d^2z}{dt^2} + 620z = f_z,$$

(7.13)

A sum of decomposed vertical force is represented by the modal force of f_z such as the lateral mode control. The magnetic spring constant of $K = 620$ N/m was determined by experiments. The transfer function by taking the Laplace transform is,

$$\frac{Z(s)}{F(s)} = \frac{1}{1.52s^2 + 620},$$

(7.14)

The continuous-time lead-lag controller in z was initially set at 45 Hz. The phase margin of 50° was targeted in this design. The continuous-time lead-lag compensator was designed as,

$$G_z(s) = 323252(\frac{s+102.91}{s+776.828})(\frac{s+10}{s}).$$

(7.15)

The phase margin was designed to be 47.9° at crossover frequency of 277 rad/s, which is illustrated in the root locus in Figure 7-10 and the loop transfer function Bode plot in Figure 7-11. The corresponding digital controller in the z-direction was converted at the sampling frequency of 800 Hz.

$$G_z(z) = 298600(\frac{z-0.879}{z-0.379})(\frac{z-0.988}{z-1}),$$

(7.16)
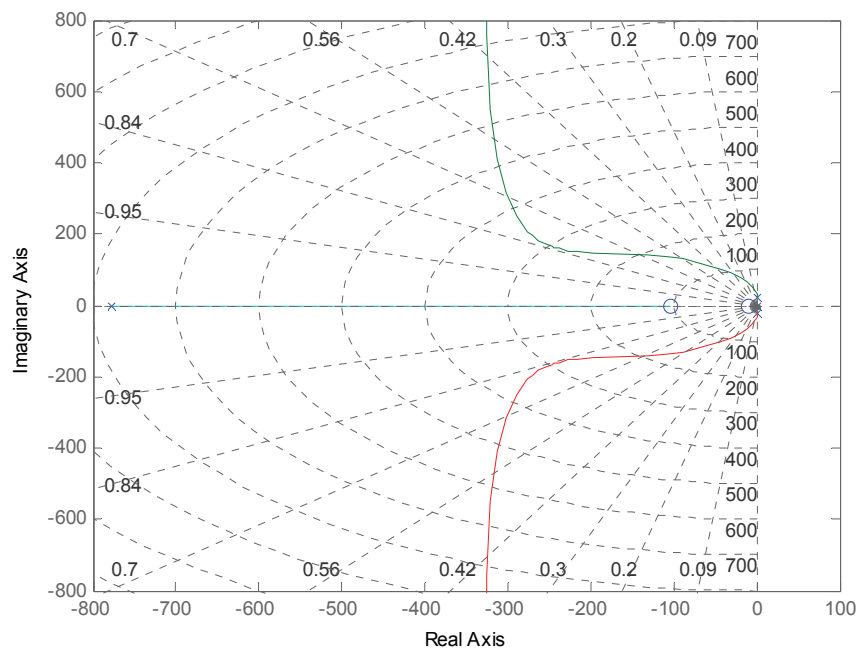
Figure 7-10: Root locus in z
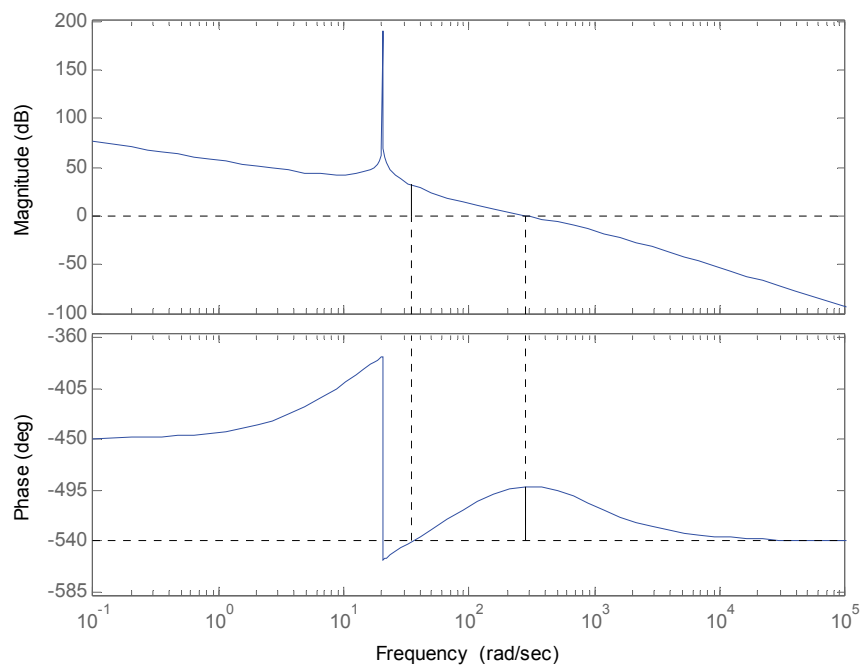
Figure 7-11: Loop transmission in z
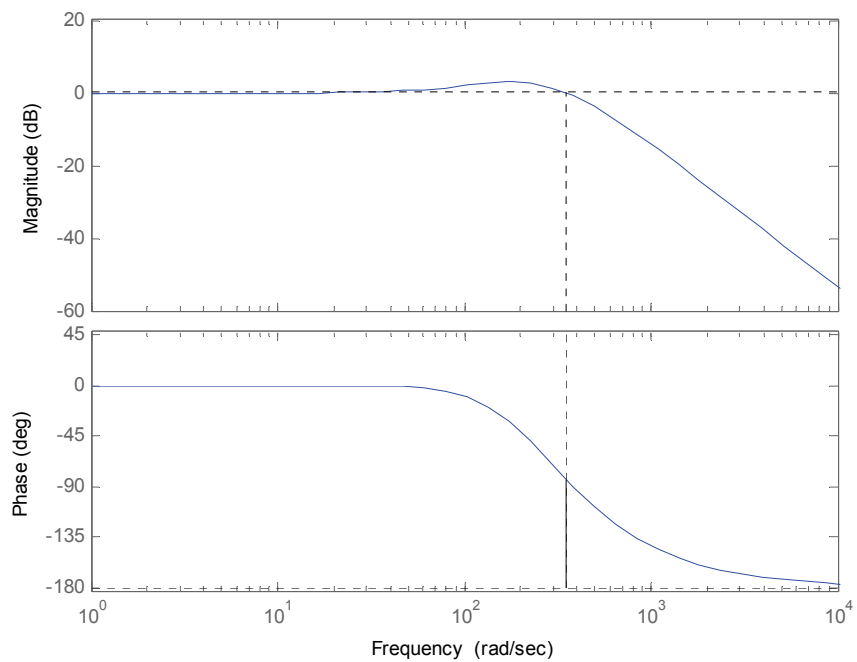
Figure 7-12: Closed-loop Bode plot in z
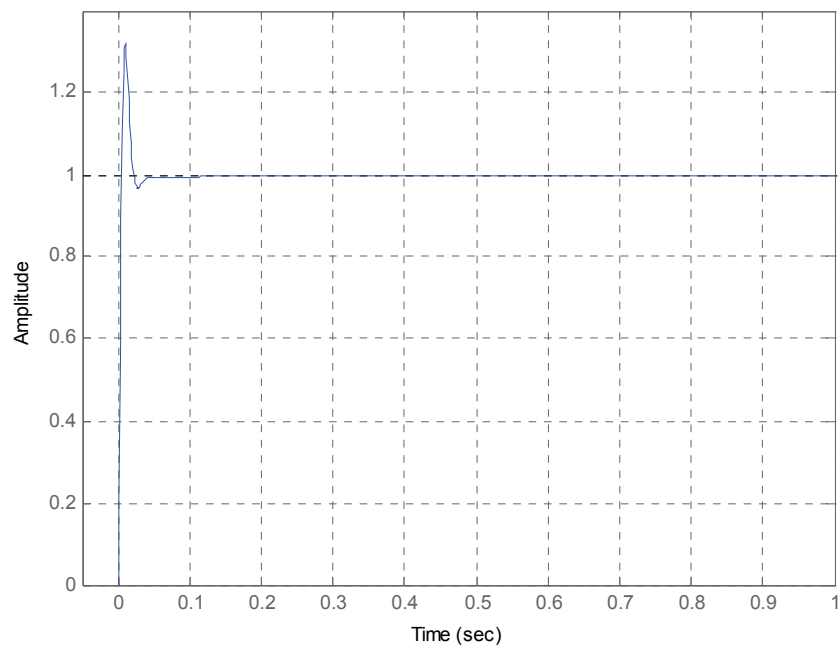
Figure 7-13: Step response in z

The closed-loop Bode plot and the step response plot in the z-axis are presented in Figures 7-12 and 7-13, respectively.

The vertical mode controllers in θ and ψ were designed after closing the loop for the vertical motion in the z-direction. The dynamic models for the vertical mode are presented in the following equations with the parameters.

$$\frac{\Theta(s)}{T(s)} = \frac{1}{0.0019s^2 + 65}, \tag{7.17}$$

$$\frac{\Psi(s)}{T(s)} = \frac{1}{0.0022s^2 + 87}, \tag{7.18}$$

According to the geometrical symmetry of the platen, the moments of inertia of $I_{xx} = 0.0019$ kg-m² and $I_{yy} = 0.0022$ kg-m² were considered. The effective torsional spring constants of $K_\theta = 65$ N-m/rad and $K_\psi = 87$ N-m/rad were determined by experiments. The closed-loop bandwidth was set at 35 Hz and the phase margin of 50° was targeted. The continuous-time controllers in θ and ψ are,

$$G_\theta(s) = 900(\frac{s + 80.0413}{s + 604.199})(\frac{s + 10}{s}), \tag{7.19}$$

$$G_\psi(s) = 1100(\frac{s + 80.0413}{s + 604.199})(\frac{s + 10}{s}), \tag{7.20}$$

$$G_\theta(z) = 854(\frac{z - 0.905}{z - 0.470})(\frac{z - 0.988}{z - 1}), \tag{7.21}$$

$$G_\psi(z) = 1020(\frac{z - 0.905}{z - 0.470})(\frac{z - 0.988}{z - 1}), \tag{7.22}$$

Figures 7-14 and 7-15 present the root-locus plot and the loop transmission plot in the rotation around x. Figures 7-16 and 7-17 present the closed-loop Bode plot and the step responses. Similarly, controller designs in the rotation in y are represented in Figure 7-18
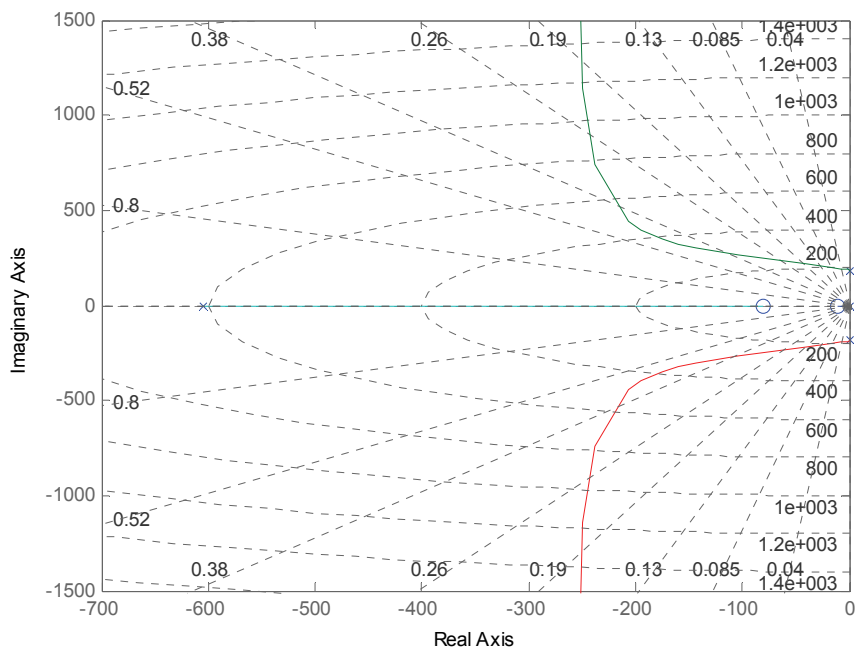
Figure 7-14: Root locus in rotation around *x*
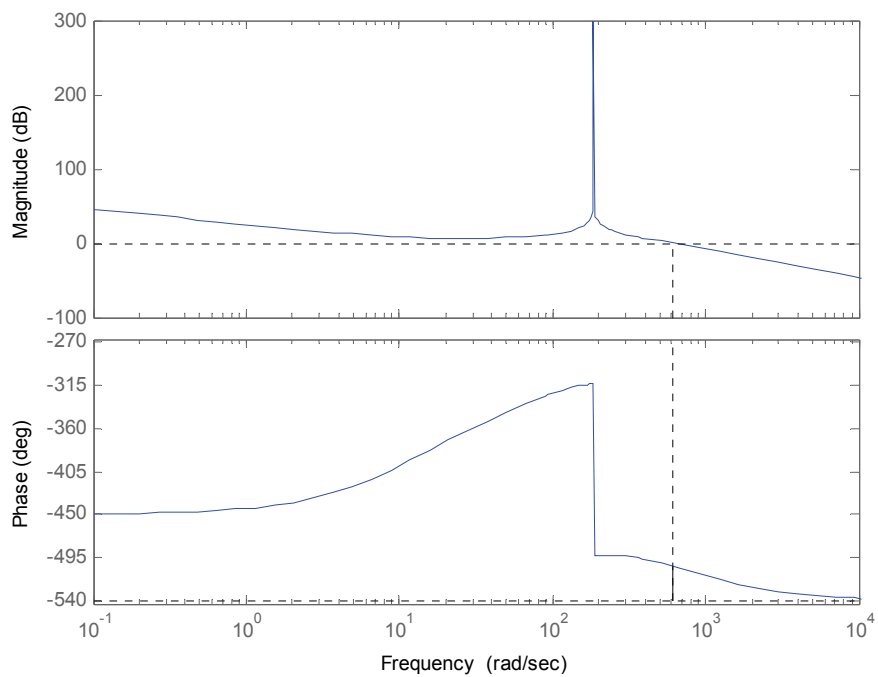
Figure 7-15: Loop transmission in rotation around *x*
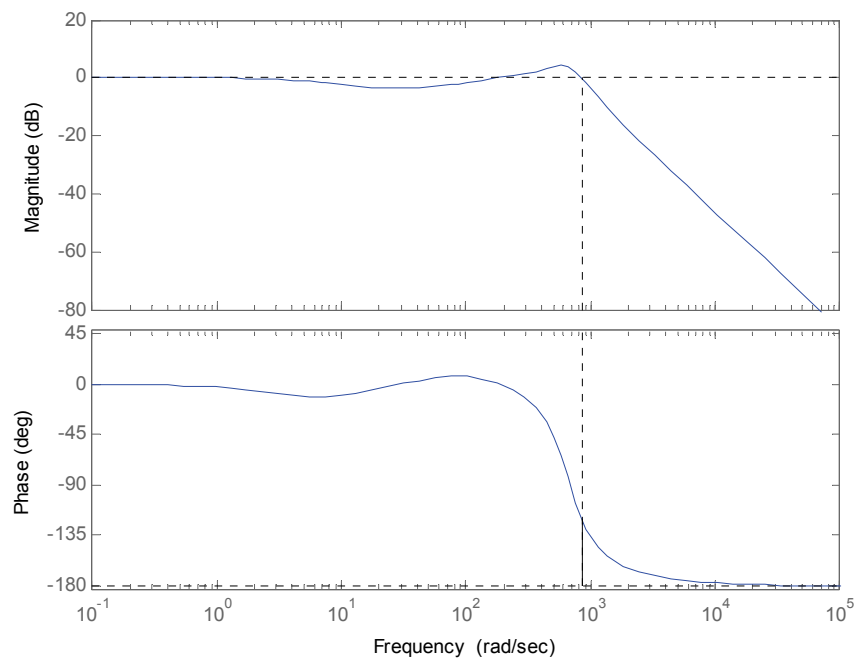
Figure 7-16: Closed-loop Bode plot in rotation around *x*
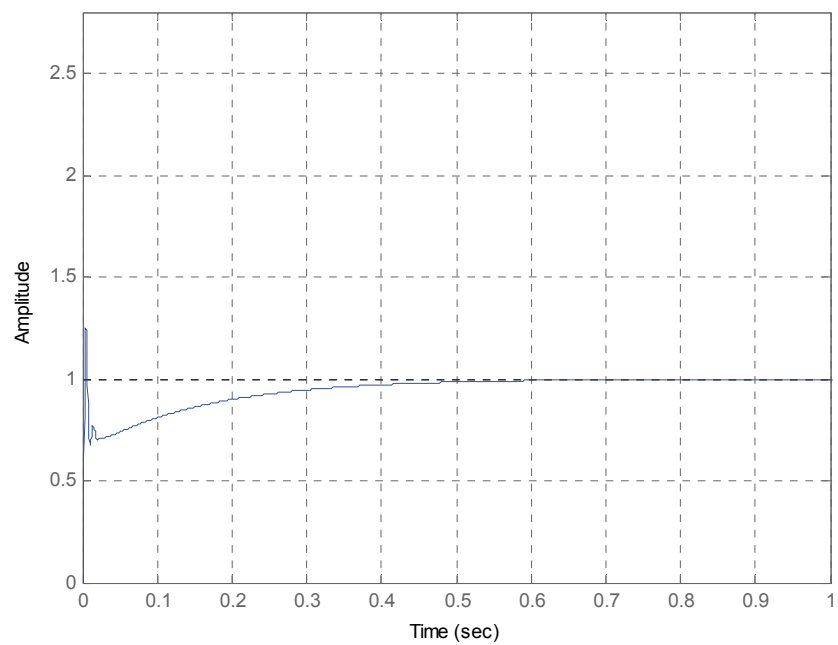
Figure 7-17: Step response in rotation around *x*
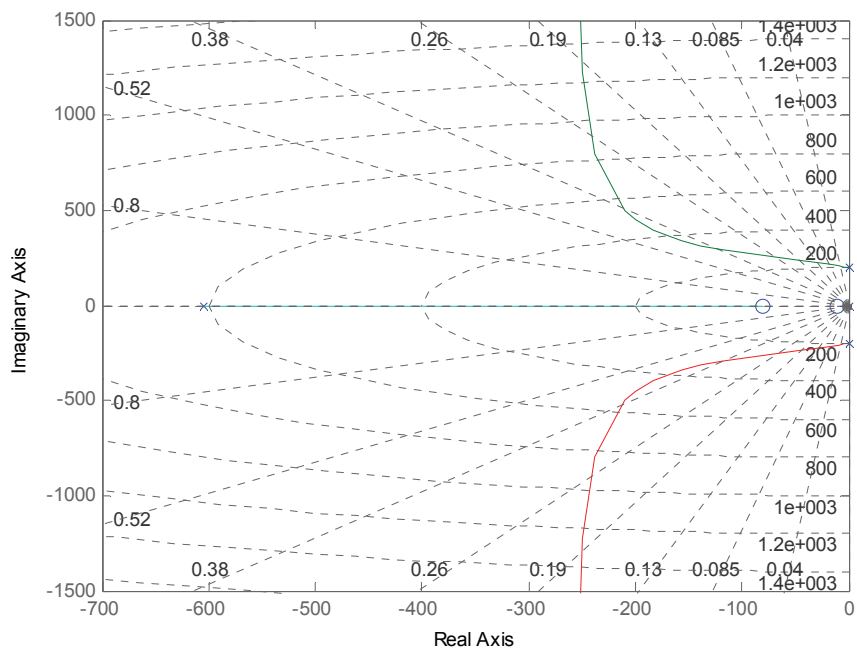
Figure 7-18: Root locus in rotation around *y*
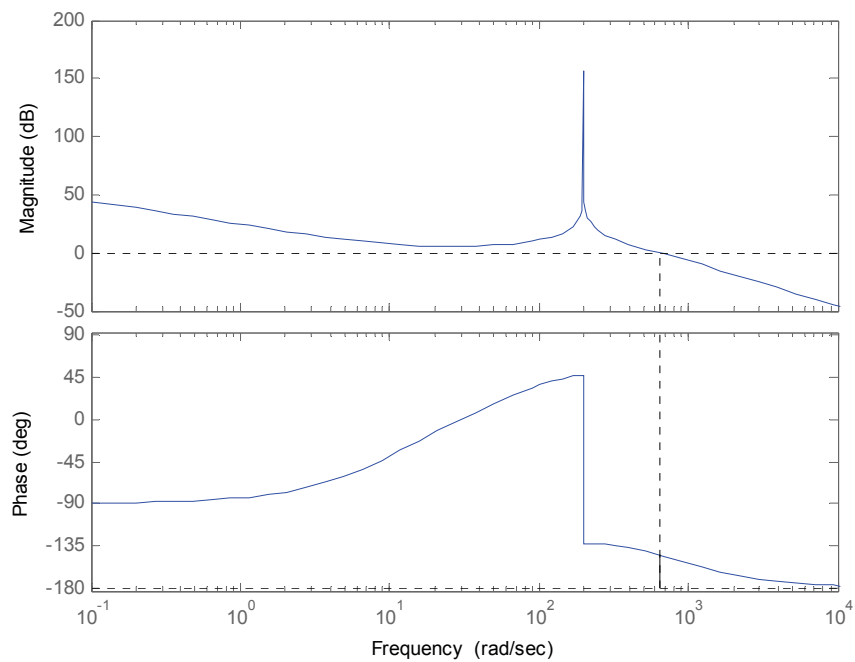
Figure 7-19: Loop transmission in rotation around *y*
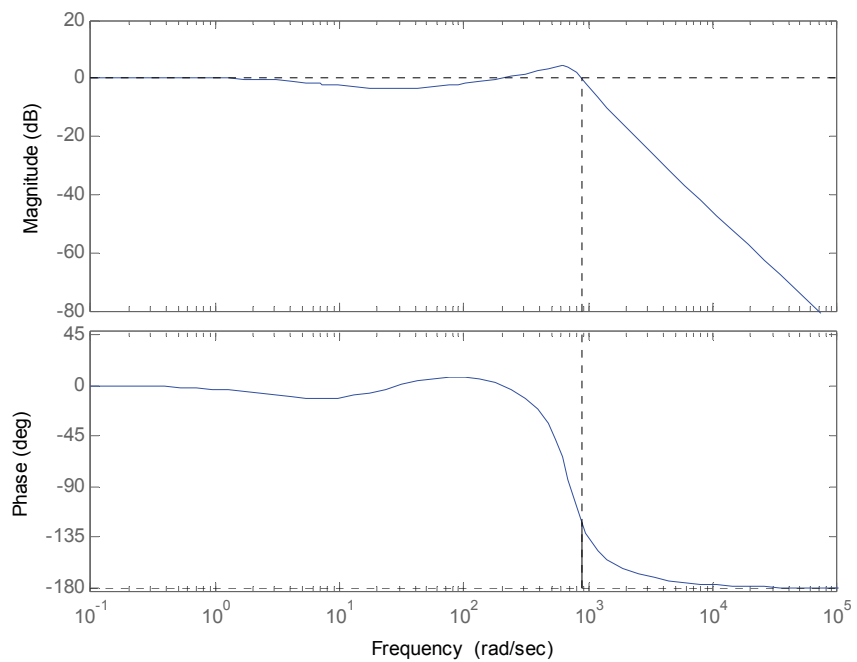
Figure 7-20: Closed-loop Bode plot in rotation around *y*
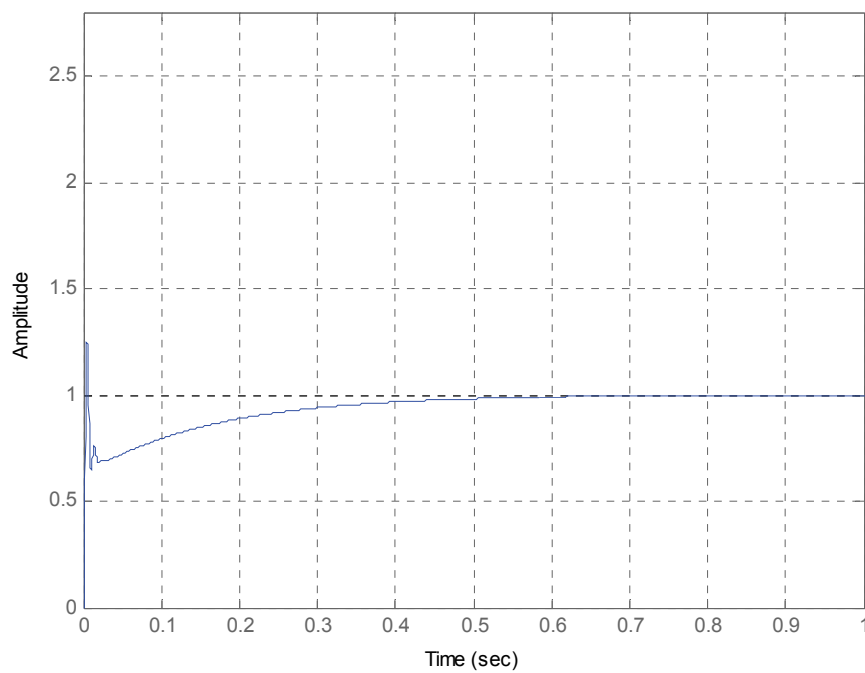
Figure 7-21: Step response in rotation around *y*

to Figure 7-21. Dynamics of the closed-loop system in the rotation around *x* and *y* are slower than those of the *z*-direction and translations. Since the plant models include magnetic spring constants, these cause significant resonances at 30 Hz in the rotation around *x* and *y*. The resonant dynamics make the closed-loop system slow.

7.3 Multivariable Control for Translation Mode

This section discusses multivariable control for the positioner. Based on the system dynamics derived In Chapter VI, the multivariable controllers are developed. The linear quadratic Gaussin (LQG) controller methodology is used for the lateral mode. Experimental results are presented in the following chapter.

7.3.1 Observer-Based Control

The state-space model of the positioning system was derived in equation (6.66–6.67) in Chapter VI. After all corresponding constant values were substituted in those equations,

$$\begin{bmatrix} \dot{x} \\ \dot{y} \\ \dot{r} \\ \dot{d} \\ \dot{f} \\ \dot{v} \end{bmatrix} = \begin{bmatrix} 0 & 0 & 0 & 1 & 0 & 0 \\ 0 & 0 & 0 & 0 & 1 & 0 \\ 0 & 0 & 0 & 0 & 0 & 1 \\ 0 & 0 & 0 & 0 & 0 & 0 \\ 0 & 0 & 0 & 0 & 0 & 0 \\ 0 & 0 & 0 & 0 & 0 & 0 \end{bmatrix} \begin{bmatrix} x \\ y \\ r \\ d \\ f \\ v \end{bmatrix} + \begin{bmatrix} 0 & 0 & 0 \\ 0 & 0 & 0 \\ 0 & 0 & 0 \\ 0 & 0 & 13.2547 \\ 13.2547 & 13.2547 & 0 \\ -117.15 & 117.15 & 0 \end{bmatrix} \begin{bmatrix} i_{AQ} \\ i_{BQ} \\ i_{CQ} \end{bmatrix} \tag{7.23}$$

$$Y_1 = \begin{bmatrix} 1 & 0 & 0 & 0 & 0 & 0 \\ 0 & 1 & 0 & 0 & 0 & 0 \\ 0 & 0 & 1 & 0 & 0 & 0 \end{bmatrix} \begin{bmatrix} x \\ y \\ r \\ d \\ f \\ v \end{bmatrix}. \tag{7.24}$$

Equations (7.23–7.24) present a state-space representation for the horizontal mode of the positioner. Because Hall-effect sensors provide solely displacement values, an observer to estimate velocity states is required in the system in order to achieve full state feedback. In the plant dynamics, if (A, B) is controllable and (A, C) is observable, an observer/state-feedback controller can be designed.

Figure 7-22 shows the structure of the observer. The observer takes the original plant's input and output. An estimate of the plant's state vector is produced by observer. The observer tracks the output from the plant and the output errors $y - \hat{y}$ go into the observer. The observer has identical structure with the plant with additional input $y - \hat{y}$.

$$\dot{\hat{x}} = A\hat{x} + Bu + L(y - \hat{y}), \tag{7.25}$$

$$\hat{y} = C\hat{x} + Du, \tag{7.26}$$

The observer gain matrix L can be computed because (A, C) is observable. The plant dynamics is as follows.

$$\dot{x} = Ax + Bu \tag{7.27}$$

$$y = Cx + Du \tag{8.28}$$

The state feedback is $u = -K\hat{x}$, where the estimated stages $\hat{x}$ will asymptotically converge to the state x. The closed-loop dynamics is represented as

$$\dot{x} = Ax - BK\hat{x} \tag{7.29}$$

$$\dot{\hat{x}} = (A - BK - LC)\hat{x} + LCx. \tag{7.30}$$

A matrix form of the closed-loop dynamics is

$$\begin{bmatrix} \dot{x} \\ \dot{\hat{x}} \end{bmatrix} = \begin{bmatrix} A & -BK \\ LC & A - BK - LC \end{bmatrix} \begin{bmatrix} x \\ \hat{x} \end{bmatrix} \tag{7.31}$$

$$Y = Cx \tag{7.32}$$
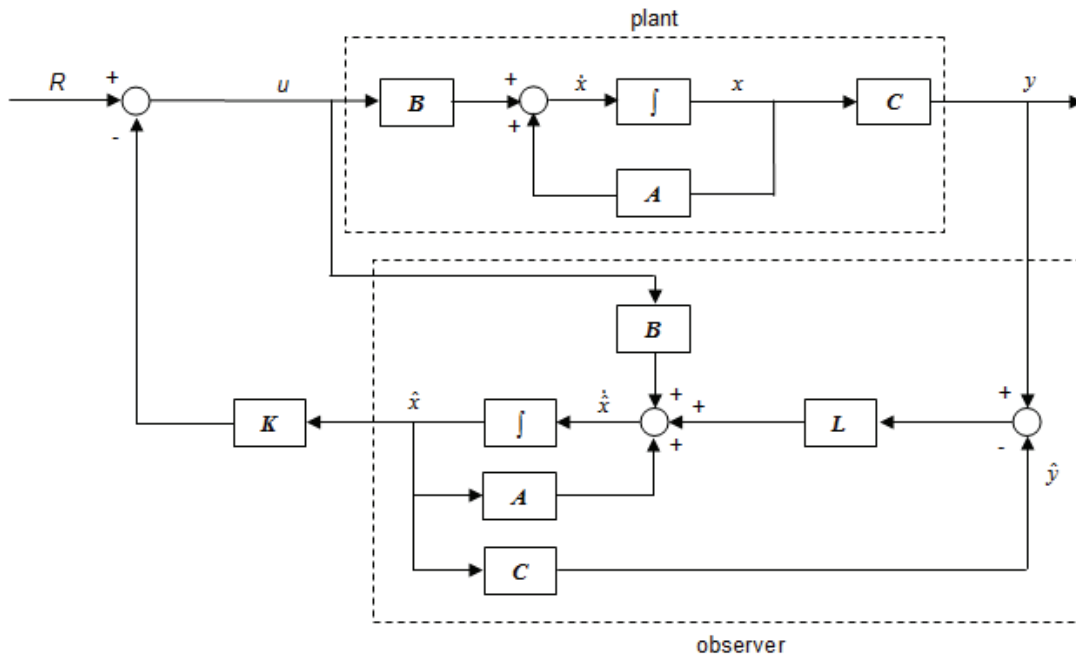
Figure 7-22: Observer structure

The purpose of the positioning system is to achieve high resolution. The precision mainly depends on the position sensors, but the optimized control algorithm can improve the precision positioning performances. Since the original plant and the controller do not include the integrators, steady-state errors in the closed-loop position control may exist. In order to reduce the steady-state errors, three pure integrators are employed in the original system as follows.

$$
\begin{bmatrix} \dot{x} \\ \dot{y} \\ \dot{r} \\ \dot{z}_1 \\ \dot{z}_2 \\ \dot{z}_3 \\ \dot{d} \\ \dot{f} \\ \dot{v} \end{bmatrix} = \begin{bmatrix} 0 & 0 & 0 & 0 & 0 & 0 & 1 & 0 & 0 \\ 0 & 0 & 0 & 0 & 0 & 0 & 0 & 1 & 0 \\ 0 & 0 & 0 & 0 & 0 & 0 & 0 & 0 & 1 \\ 1 & 0 & 0 & 0 & 0 & 0 & 0 & 0 & 0 \\ 0 & 1 & 0 & 0 & 0 & 0 & 0 & 0 & 0 \\ 0 & 0 & 1 & 0 & 0 & 0 & 0 & 0 & 0 \\ 0 & 0 & 0 & 0 & 0 & 0 & 0 & 0 & 0 \\ 0 & 0 & 0 & 0 & 0 & 0 & 0 & 0 & 0 \\ 0 & 0 & 0 & 0 & 0 & 0 & 0 & 0 & 0 \end{bmatrix} \begin{bmatrix} x \\ y \\ r \\ z_1 \\ z_2 \\ z_3 \\ d \\ f \\ v \end{bmatrix} + \begin{bmatrix} 0 & 0 & 0 \\ 0 & 0 & 0 \\ 0 & 0 & 0 \\ 0 & 0 & 0 \\ 0 & 0 & 0 \\ 0 & 0 & 0 \\ 0 & 0 & 13.2547 \\ 13.2547 & 13.2547 & 0 \\ -117.15 & 117.15 & 0 \end{bmatrix} \begin{bmatrix} i_{AQ} \\ i_{BQ} \\ i_{CQ} \end{bmatrix} \quad (7.33)
$$

$$
Y_1 = \begin{bmatrix} 1 & 0 & 0 & 0 & 0 & 0 & 0 & 0 & 0 \\ 0 & 1 & 0 & 0 & 0 & 0 & 0 & 0 & 0 \\ 0 & 0 & 1 & 0 & 0 & 0 & 0 & 0 & 0 \end{bmatrix} \begin{bmatrix} x \\ y \\ r \\ z_1 \\ z_2 \\ z_3 \\ d \\ f \\ v \end{bmatrix} \quad (7.34)
$$

Using full-order states in (7.33–7.34) is inefficient and requires more computations. Thus, a reduced-order LQG controller design based on the vertical mode control of ATP stage by Hu [103–105] is developed. The full states are divided by two subsystems, which are the terms of known state $\bar{x}_1$ and the terms of unknown state $\bar{x}_2$. By estimating only unknown states, the controller structure will be simple. The reduced-order observer structure is

$$
\begin{bmatrix} \dot{\bar{x}}_1 \\ \dot{\bar{x}}_2 \end{bmatrix} = \begin{bmatrix} A_{11} & A_{12} \\ A_{21} & A_{22} \end{bmatrix} \begin{bmatrix} \bar{x}_1 \\ \bar{x}_2 \end{bmatrix} + \begin{bmatrix} B_1 \\ B_2 \end{bmatrix} \bar{u}, \quad (7.35)
$$

$$
Y = \begin{bmatrix} I & 0 \end{bmatrix} \begin{bmatrix} \bar{x}_1 \\ \bar{x}_2 \end{bmatrix}, \quad (7.36)
$$

with

$$A_{11} = \begin{bmatrix} 0 & 0 & 0 & 0 & 0 & 0 \\ 0 & 0 & 0 & 0 & 0 & 0 \\ 0 & 0 & 0 & 0 & 0 & 0 \\ 1 & 0 & 0 & 0 & 0 & 0 \\ 0 & 1 & 0 & 0 & 0 & 0 \\ 0 & 0 & 1 & 0 & 0 & 0 \end{bmatrix}, \; A_{12} = \begin{bmatrix} 1 & 0 & 0 \\ 0 & 1 & 0 \\ 0 & 0 & 1 \\ 0 & 0 & 0 \\ 0 & 0 & 0 \\ 0 & 0 & 0 \end{bmatrix}, \tag{7.37}$$

$$A_{21} = \begin{bmatrix} 0 & 0 & 0 & 0 & 0 & 0 \\ 0 & 0 & 0 & 0 & 0 & 0 \\ 0 & 0 & 0 & 0 & 0 & 0 \end{bmatrix}, \; A_{22} = \begin{bmatrix} 0 & 0 & 0 \\ 0 & 0 & 0 \\ 0 & 0 & 0 \end{bmatrix}, \tag{7.38}$$

$$B_1 = \begin{bmatrix} 0 & 0 & 0 \\ 0 & 0 & 0 \\ 0 & 0 & 0 \\ 0 & 0 & 0 \\ 0 & 0 & 0 \\ 0 & 0 & 0 \end{bmatrix}, \; B_2 = \begin{bmatrix} 0 & 0 & 13.2547 \\ 13.2547 & 13.2547 & 0 \\ -117.15 & 117.15 & 0 \end{bmatrix}, \tag{7.39}$$

The known state vector $\bar{x}_1$ consists of the displacement states (x, y, and r) from the Hall-effect sensors and the integrator states (z_1, z_2, and z_3). The unknown state vector $\bar{x}_2$ includes the velocity states (d, f, and v). The continuous-time system (7.33) is discretized at the sampling frequency of 800 Hz. The closed-loop dynamics of the reduced-order LQG controller is derived in (7.40–7.41) [103].

$$\begin{bmatrix} \dot{\bar{x}}_1 \\ \dot{\bar{x}}_2 \\ \dot{\bar{x}}_3 \end{bmatrix} = \begin{bmatrix} A_{11} - B_1\bar{k}_1 - B_1\bar{k}_2 L & A_{12} & -B_1\bar{k}_2 \\ A_{21} - B_2\bar{k}_1 - B_2\bar{k}_2 L & A_{22} & -B_2\bar{k}_2 \\ (A_{22} - LA_{12})L + A_{21} - LA_{11} - (B_2 - LB_1)(\bar{k}_1 + \bar{k}_2 L) & 0 & A_{22} - LA_{12} - B_2\bar{k}_2 + LB_1\bar{k}_2 \end{bmatrix} \begin{bmatrix} \bar{x}_1 \\ \bar{x}_2 \\ \bar{x}_3 \end{bmatrix} \tag{7.40}$$

$$Y = \begin{bmatrix} I & 0 & 0 \end{bmatrix} \begin{bmatrix} \bar{x}_1 \\ \bar{x}_2 \\ \bar{x}_3 \end{bmatrix}, \tag{7.41}$$

where $\bar{x}_3 = \hat{\bar{x}}_2 - L\bar{x}_1$ and $\hat{\bar{x}}_2$ denotes the estimated vector of the unknown states $\bar{x}_2$. The estimator gain matrix is represented as L. The LQ gain matrix of $K = [\bar{k}_1 \ \bar{k}_2]$ is also divided by the known states $\bar{k}_1$ and estimated states $\bar{k}_2$. By mathematical manipulations, the new state matrix A can be derived as follows

$$\begin{bmatrix} A_{11} - B_1\bar{k}_1 & A_{12} - B_1\bar{k}_2 & -B_1\bar{k}_2 \\ A_{21} - B_2\bar{k}_1 & A_{22} - B_2\bar{k}_2 & -B_2\bar{k}_2 \\ 0 & 0 & A_{22} - LA_{12} \end{bmatrix} = \begin{bmatrix} A - BK & -B\bar{k}_2 \\ 0 & A_{22} - LA_{12} \end{bmatrix} \quad (7.42)$$

7.3.2 Linear Quadratic Gaussian (LQG) Control

The LQG controller is comprised of a Kalman filter and an LQR control law [96]. The Kalman filter as shown in Figure 7-23 is employed as a state estimator, and the LQR controller performs state feedback. Since the Kalman filter and the model-based compensator in Figure 7-24 have similar structure, the Kalman filter can be used in the control system design. Thus, the Kalman filter is regarded as the model-based observer or the state-reconstructor.
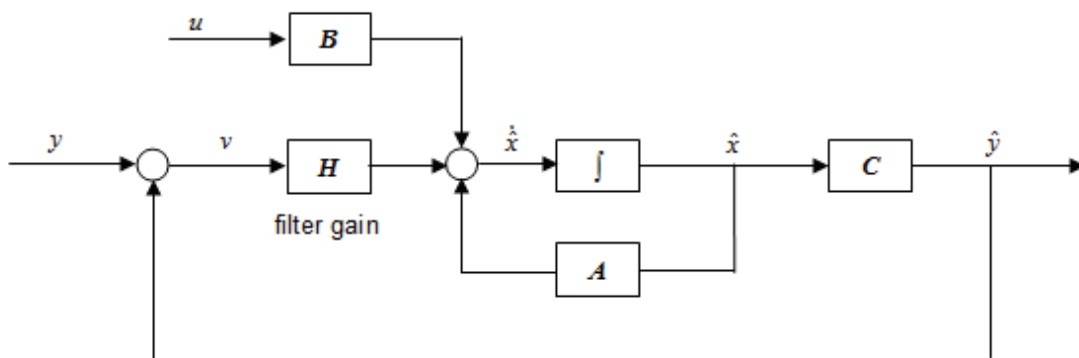
Figure 7-23: Kalman filter structure

Figure 7-24 shows the feedback control loop with a model-based compensator (MBC). The multivariable system using the MBC can basically guarantee the stability of the system and design a proper loop shape when (A, B) is controllable and (A, C) is observable [106]. In addition, it partially guarantees the system dynamic performance, stability, and robustness.
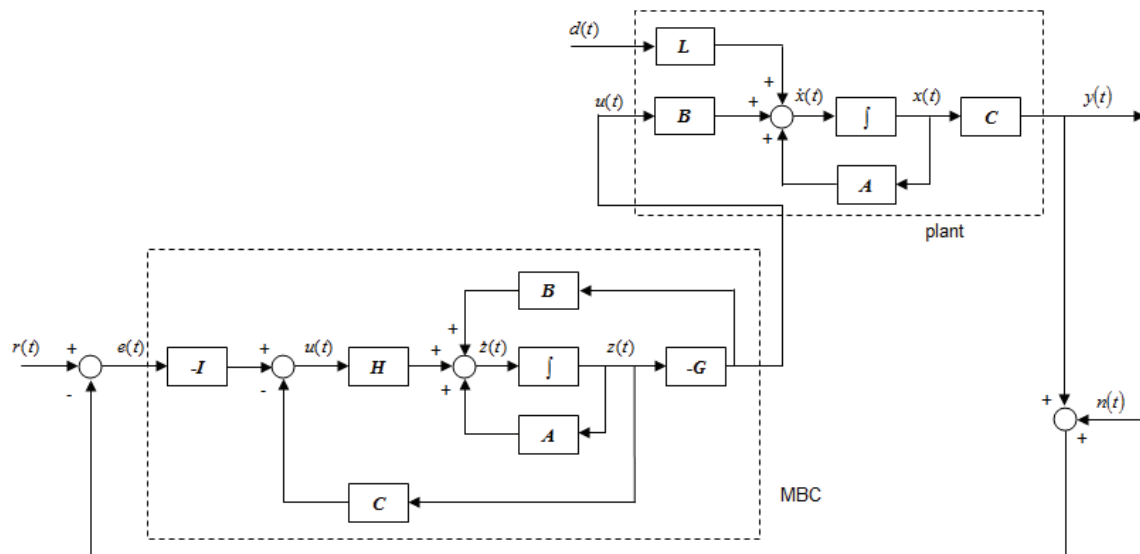
Figure 7-24: Feedback control loop with a model-based compensator (MBC)

The LQG control methodology is the combination of optimal state estimation and optimal state feedback for a deterministic plant. The measurement noise and the disturbance need to be stochastic with known statistical properties [107]. The plant model has a structure as follows

$$\dot{x}(t) = Ax(t) + Bu(t) + L\zeta(t) \tag{7.43}$$

$$y(t) = Cx(t) + \theta(t) \tag{7.44}$$

where the *A*, *B*, *L*, and *C* are constant matrices. Variables of $\zeta(t)$ and $\theta(t)$ are stationary, white Gaussian disturbance and measurement input noise, respectively. The properties of expectation and covariance are as follows

$$E\{\zeta(t)\} = 0 \tag{7.45}$$

$$Cov\{\zeta(t),\zeta(t)\} = \Psi\delta(t-\tau), \ \Psi = \Psi^T > 0 \tag{7.46}$$

$$E\{\theta(t)\} = 0 \tag{7.47}$$

$$Cov\{\theta(t),\theta(t)\} = \Theta\delta(t-\tau), \ \Theta = \Theta^T > 0, \tag{7.48}$$

where $E\{\cdot\}$, $Cov\{\cdot\}$, and $\delta(t-\tau)$ are the expectation operator, a covariance, and a delta function, respectively [108]. The Kalman filter can be designed when (A, L) is controllable and (A, C) is observable and has the following structure.

$$\dot{\hat{x}} = A\hat{x} + Bu + H(y - C\hat{x}) \tag{7.49}$$

$$\dot{\hat{x}} = (A - HC)\hat{x} + Bu + Hy \tag{7.50}$$

$$0 = A\Sigma + \Sigma A^T - \Sigma C^T \Theta^{-1} C\Sigma + L\Psi L^T \tag{7.51}$$

$$H = \Sigma C^T \Theta^{-1}, \tag{7.52}$$

where the stability of the Kalman filter depends on the eigenvalues of matrix $(A–HC)$ in (7.50). $\Sigma = \Sigma^T > 0$ satisfies a filter algebraic Ricatti equation (FARE) in (7.51) with a unique positive-semidefinite solution. The Matlab command "kalman" calculates the matrix of *H*. An optimal control law $u = -K\hat{x}(t)$ is considered to minimize the cost function *J*.

$$J = E\{\lim_{T\to\infty}\frac{1}{T}\int_0^T [x^T Q x + u^T R u]dt\} \tag{7.53}$$

The matrix K is determined by the control algebraic Ricatti equation (CARE). P is the unique positive-semidefinite solution of the CARE in (7.56).

$$K = R^{-1}B^T P \tag{7.54}$$

$$P = P^T > 0 \tag{7.55}$$

$$A^T P + PA - PBR^{-1}B^T P + Q = 0 \tag{7.56}$$

There are three inputs i_{Q1}, i_{Q2}, and i_{Q3}, as well as there are three outputs x, y, and r. The noise covariance coming from the Hall-effect sensors was measured by experiments on the order of 5×10^{-5} m. The noise in the input and output channels is assumed as.

$$L = \begin{bmatrix} 1 & 0 & 0 \\ 0 & 1 & 0 \\ 0 & 0 & 1 \end{bmatrix}, \tag{7.57}$$

The input noise covariance is $\Psi = 5 \times 10^{-5}$ m. The output noise is assumed as

$$\Theta = 5 \times 10^{-5} \begin{bmatrix} 1 & 0 & 0 \\ 0 & 1 & 0 \\ 0 & 0 & 1 \end{bmatrix} \tag{7.58}$$

The Q and R matrices can be designed by the LQR state feedback method, because the (A, B) is stabilizable. The matices Q and R are

$$Q = \text{diag}([1e3\ 1e4\ 1e3\ 1e9\ 1e8\ 1e8\ 1e2\ 1e2\ 1e2]) \tag{7.59}$$

$$R = \begin{bmatrix} 1 & 0 & 0 \\ 0 & 1 & 0 \\ 0 & 0 & 1 \end{bmatrix} \tag{7.60}$$

The design of Q matrix was achieved by many iterations. Heavier weight values to the displacement states (x, y, and r) and the integrator states (z_1, z_2, and z_3) were given than those of the velocity states. In order to remove the steady state errors, the integrator states

weights are much higher than other values [109–110]. The gain matrix K can be

calculated by the LQR methodology in Matlab as follows,

$$K = \begin{bmatrix} 0 & 507.24 & -472.64 & 0 & 19975 & -41394 & 0 & 64304 & -26962 \\ 0 & 507.24 & 472.64 & 0 & 19975 & 41394 & 0 & 64304 & 26962 \\ 1757.55 & 0 & 0 & 84872 & 0 & 0 & 181556 & 0 & 0 \end{bmatrix}$$

(7.61)

The Kalman filter gain matrix H can be also calculated with the noise covariance.

$$H = \begin{bmatrix} 1600 & 0.0006 & 0.0006 & 1 & 0 & 0 \\ 0.0006 & 1600 & 0.0006 & 0 & 1 & 0 \\ 0.0006 & 0.0006 & 1600 & 0 & 0 & 1 \end{bmatrix}$$

(7.62)

The implementation results are presented in Chapter VIII and all programming codes are

attached in Appendix B.

CHAPTER VIII

EXPERIMENTAL RESULTS

This chapter illustrates the experimental results of the compact multidimensional positioner. With the digital controllers designed in the previous chapter, the dynamics performances of the positioner were tested. For the purpose of demonstrating its precision-positioning capabilities, microscale positioning step responses, 2-dimensional trajectories, and extended travel range tests were performed. The 2-D trajectory and the back-and-forth motions show that the positioner is capable of being applied for the wafer inspection, microscopy, and scanning. The results in this section present that the multi-dimensional positioner has the potential to generate the appropriate motions required in precision positioning industries.

8.1 Step Responses

First, several step responses were taken in the x- and y-direction with the step sizes of 1mm, 100 μm, 20 μm, and 10 μm. The perturbations in other axes were also recorded. The perturbations imply the existence of dynamic coupling during the step motions. The step response in x employs the planar motor C. Two motors A and B compensate for the stray torque caused by the geometrical asymmetry. Since the dynamic coupling was well compensated, there are no steady-state errors in each axis.

Step responses in the x-direction based on the controllers (7.7) and (7.9) are first shown in Figures 8-1 and 8-2. A 100-μm step response in x, perturbations in y and z are

presented in Figure 8-1 (a), (b), and (c), respectively. 20-μm step response in x and its perturbations are presented in Figure 8-2. The 500-μm step response and the millimeter scale consecutive stair-case response in y are shown in Figures 8-3 and 8-4, respectively. The 100-μm, 20-μm, and 10-μm stair case motions in y are presented in Figures 8-5, 8-6, and 8-7, respectively. The perturbations in x and in ϕ are accompanied in each motion plot. Step responses in the experimental results show that the rise time is less than 25 ms, the maximum overshoot is around 20%, and the settling time is less than 220 ms without steady-state errors in x and y. As we can see in the figures, the magnitude of perturbation is smaller in the short step response plot such as 10-μm than 1-mm or 100-μm step response.

Step responses in the y-direction with the step sizes of 100 μm, 20 μm, and 10 μm with the perturbations in x and ϕ are shown in Figures 8-8, 8-9, and 8-10, respectively. Figures 8-9 and 8-10 illustrate that the positioner can demonstrate the capability of microscale positioning. The fast Fourier transform (FFT) in Figure 8-10 (b) presents that there is a dominant noise frequency at 60 Hz. The position noise is 6 μm rms in x and y. The position noise is mainly caused by the Hall-effect sensors. Besides it might be generated by the umbilical cables, three aerostatic bearing that blow air flow, the modeling error from dynamic analysis, and inaccurate digital compensators.

Stair-case step responses of 0.1° and 0.01° rotations around z based on (7.9–7.10) are presented in Figures 8-11 and 8-12, respectively. The perturbations of x and y are followed in each figure. Vertical-mode step responses in z, in θ, and in ψ based on (7.15–7.22) are shown in Figure 8-13 (a), (b) and (c), respectively. The vertical motion of

5 μm and 0.001° step responses in θ and in ψ were achieved. These vertical mode controls were performed by only the magnetic force without aerostatic bearing support.

The LQG compensator was designed in Chapter VII. Figure 8-14 presents the step responses of horizontal mode with the LQG compensator. Step responses of 50 μm in both x and y are shown in Figure 8-14 (a) and (b), respectively. Figure 8-14 (c) presents the 0.3° step response in rotation around z. A FFT of the step response in x is presented in Figure 8-14 (d) and exhibits that there is no dominant noise frequency in the system. Step responses with LQG controller have a position noise of 10 μm rms. Compared to the SISO controllers in Figure 8-10, more vibrations are seen in the experimental results. The modeling error and the disturbance noise may cause this problem.
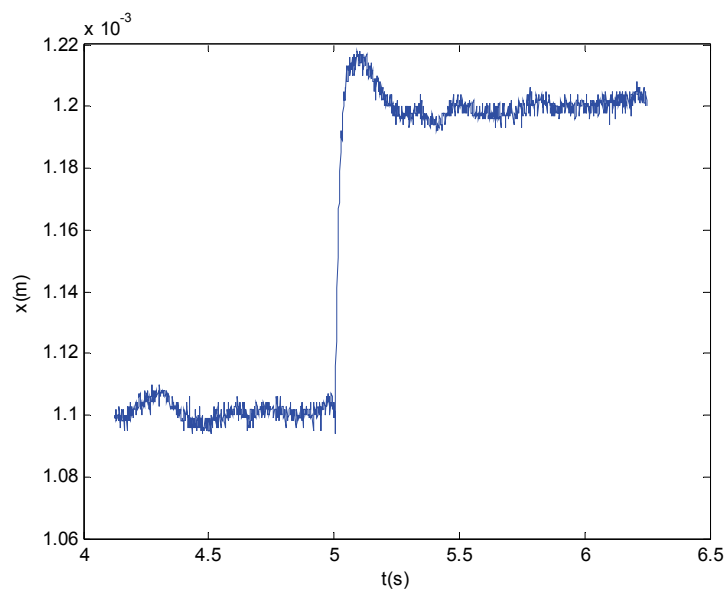
(a)
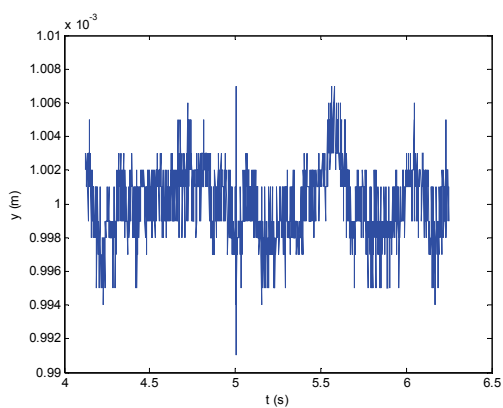
(b)
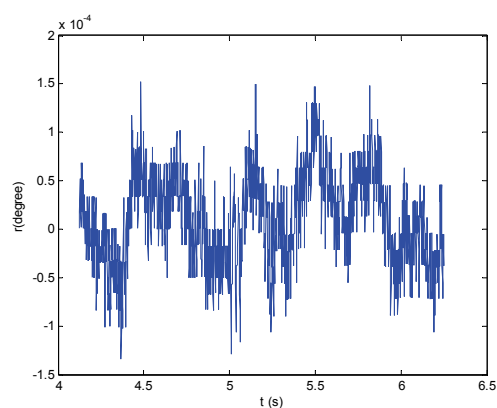
(c)

Figure 8-1: 100-μm step response in *x*, and perturbations (b) in *y* and (c) in ϕ
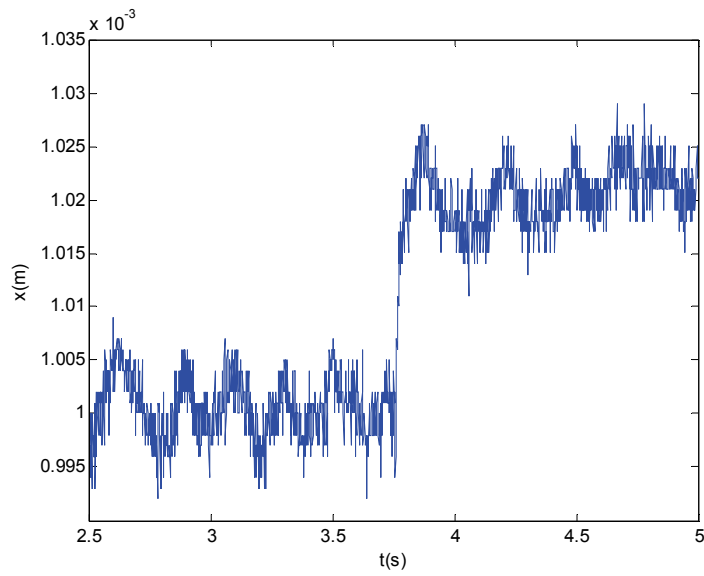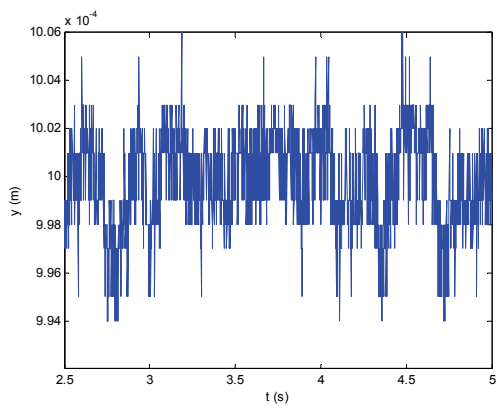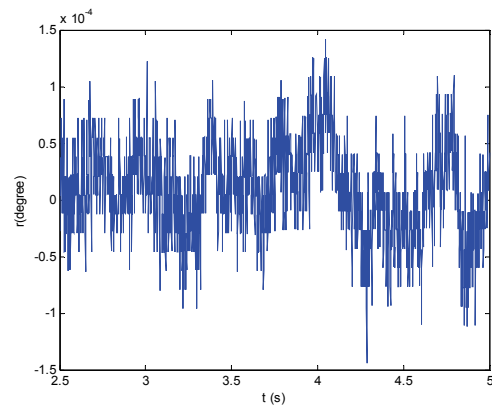
(a)

(b)   (c)

Figure 8-2: 20-µm step response in *x*, and perturbations (b) in *y* and (c) in ϕ

(a)

(b)
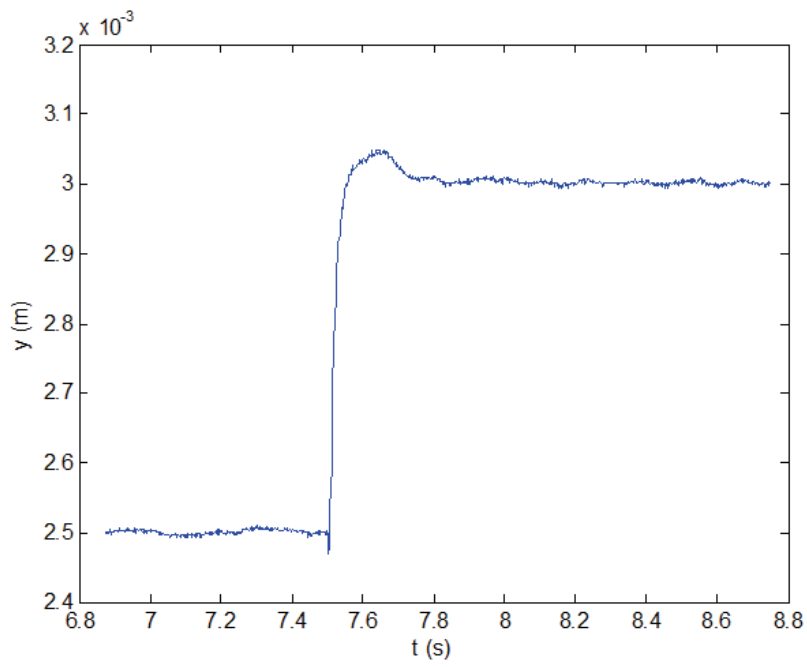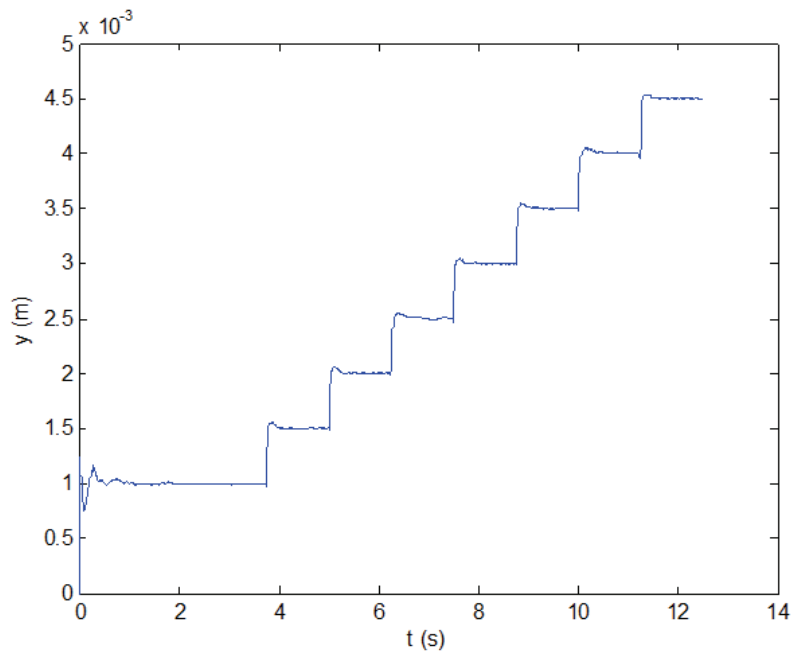
Figure 8-3: 500-µm (a) step response and (b) stair-case response in *y*
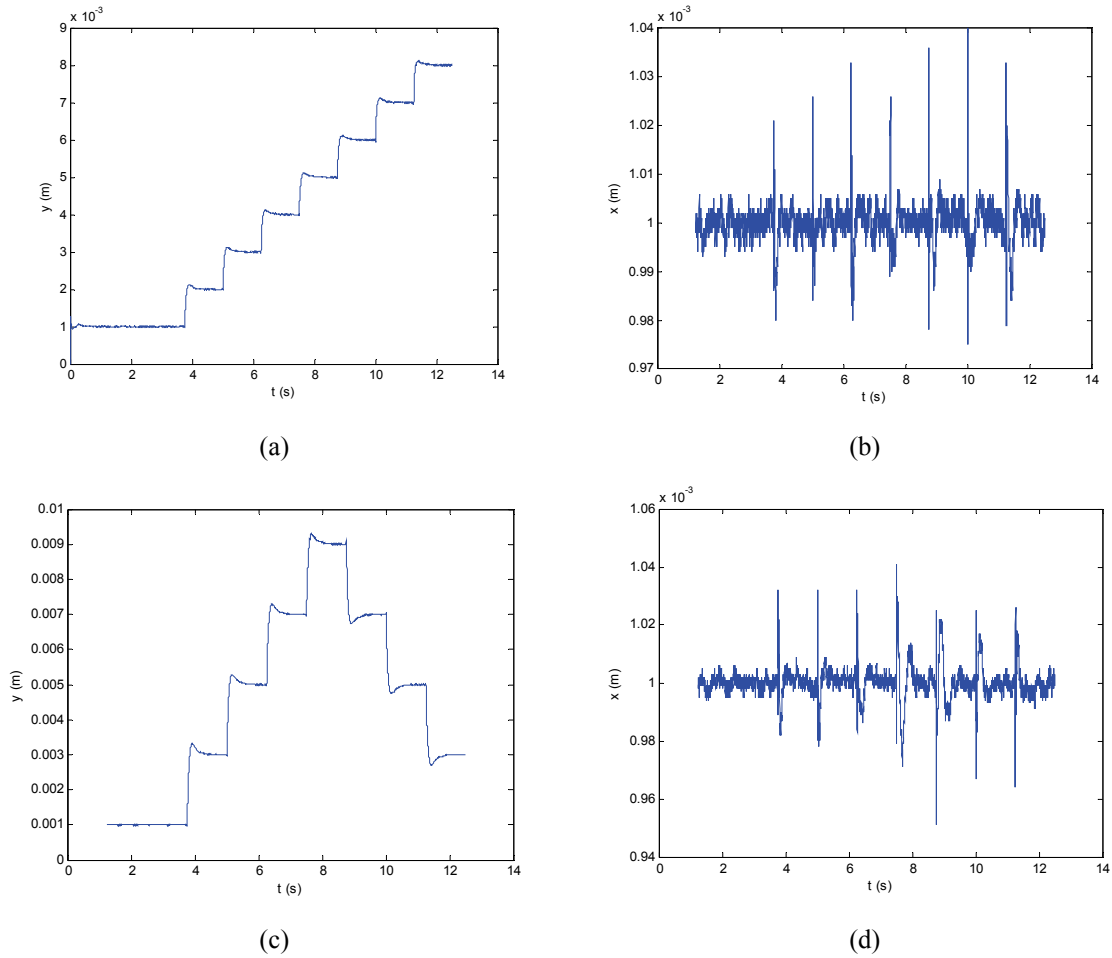
Figure 8-4: (a) 1-mm stair case in *y* and (b) its perturbation in *x*. (c) 2-mm stair case in *y*, and (d) its perturbation in *x*

(a)

(b)

(c)

Figure 8-5 (a) 100-µm stair case in *y*, and perturbation (b) in *x*, and (c) in ϕ
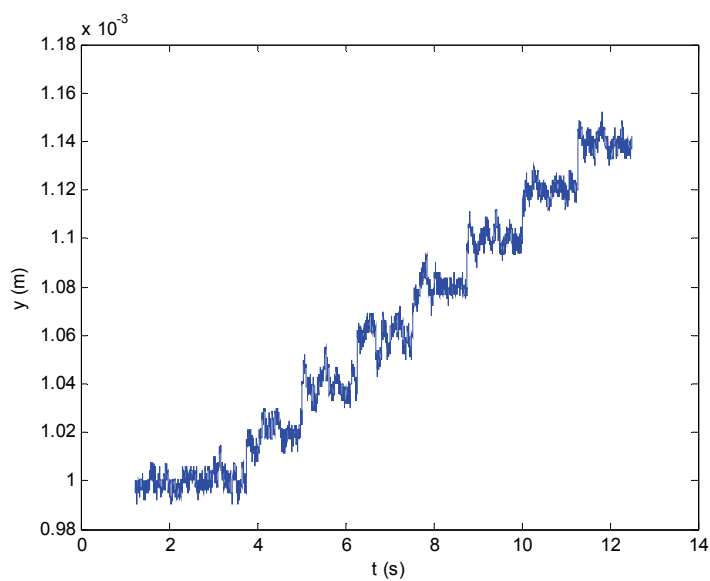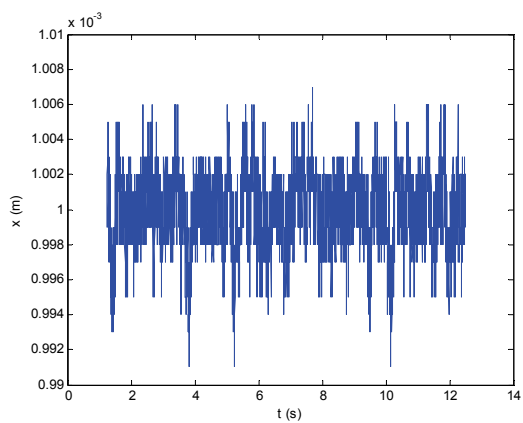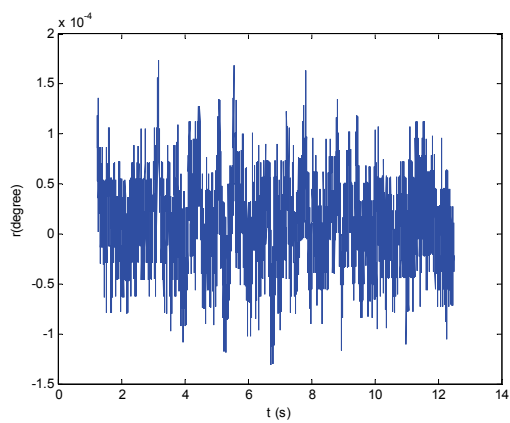
(a)

(b)

(c)

Figure 8-6 (a) 20-µm stair case in *y*, and perturbation (b) in *x*, and (c) in ϕ

(a)

(b)

(c)

Figure 8-7 (a) 10-μm stair case in *y*, and perturbation (b) in *x*, and (c) in ϕ

(a)

(b)

(c)

Figure 8-8 (a) 100-µm step response in *y*, and perturbation (b) in *x*, and (c) in ϕ

(a)

(b)

(c)
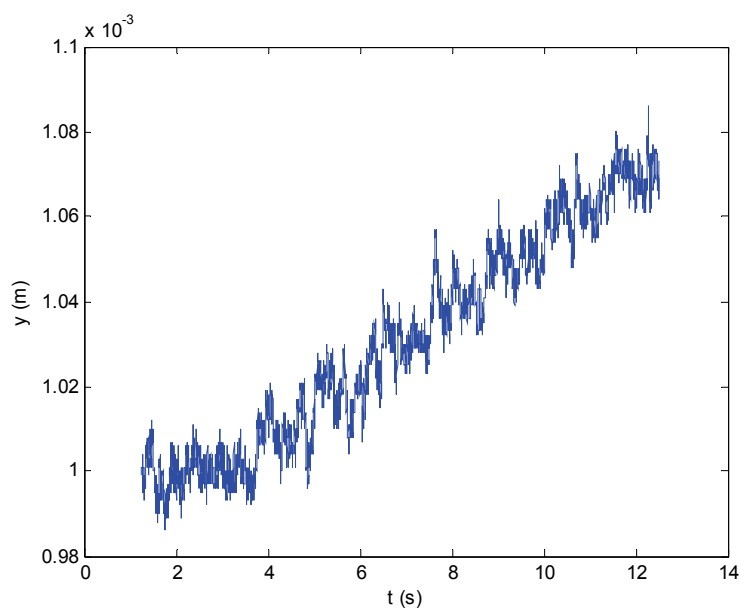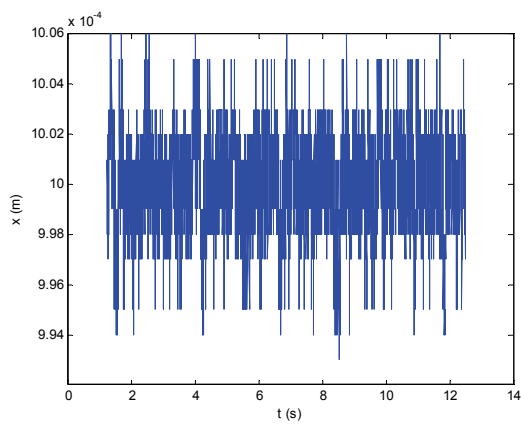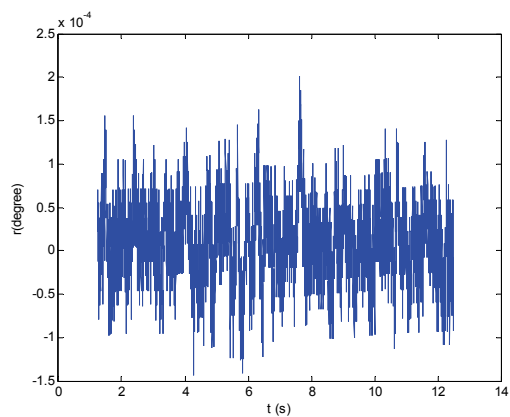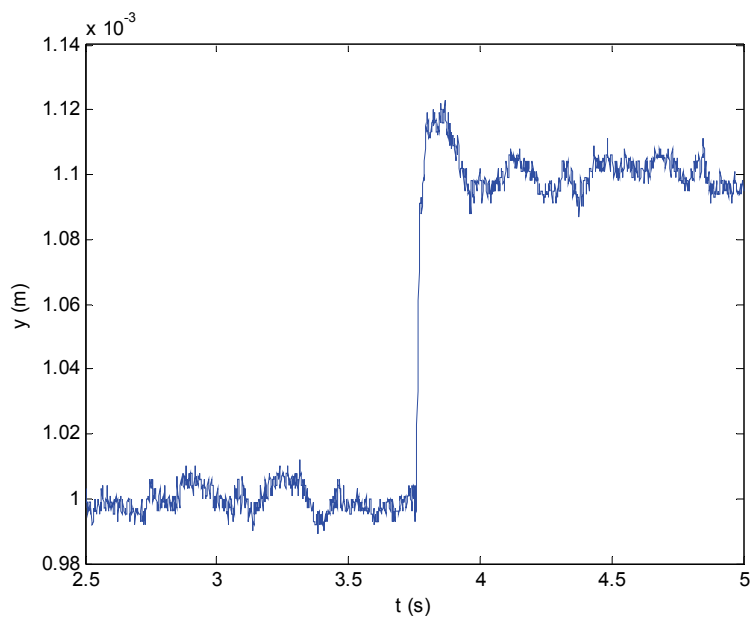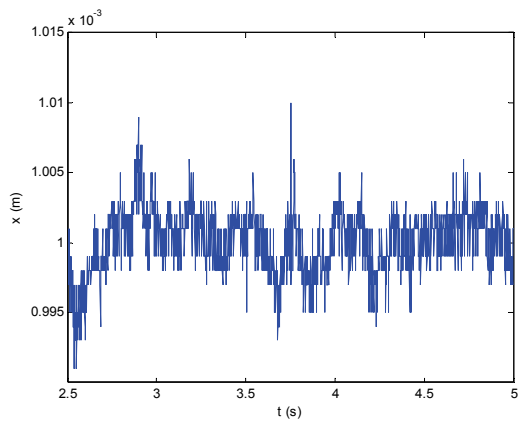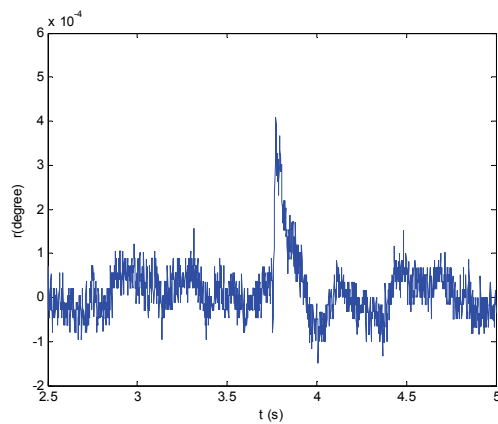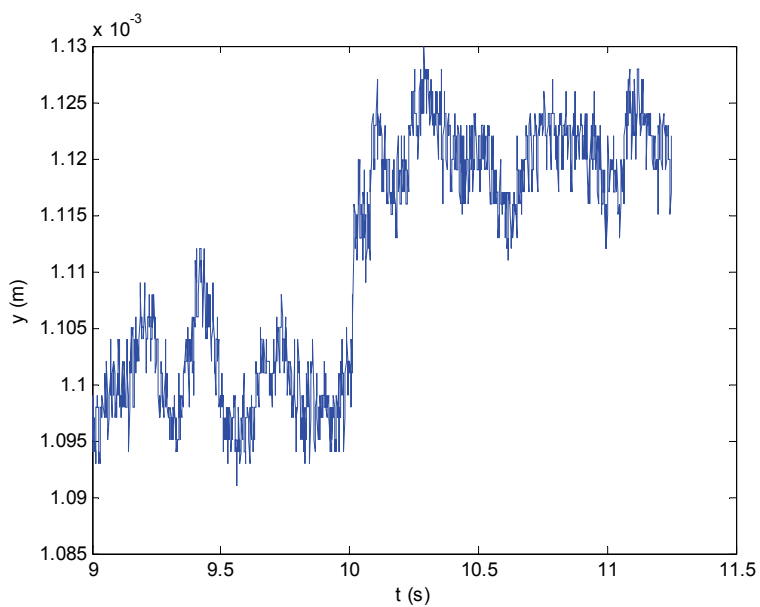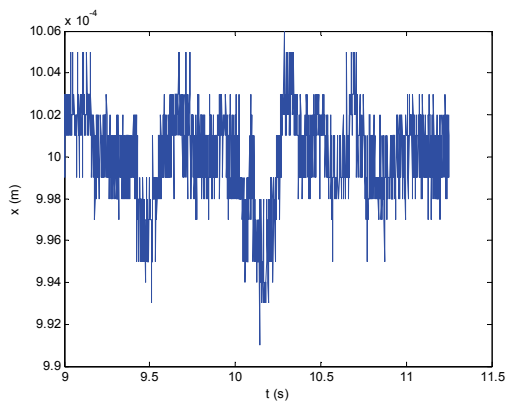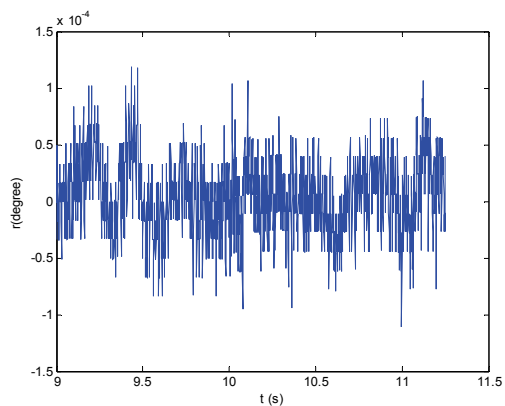
Figure 8-9 (a) 20-μm step response in *y*, and perturbation (b) in *x*, and (c) in *ϕ*
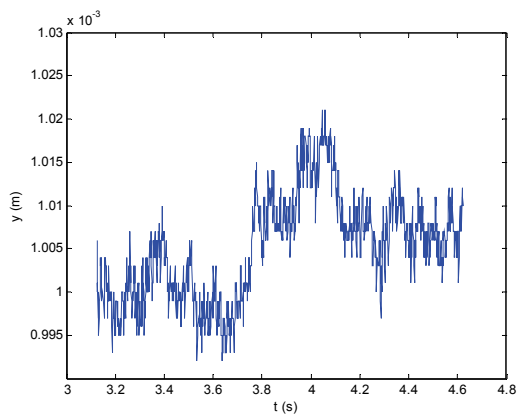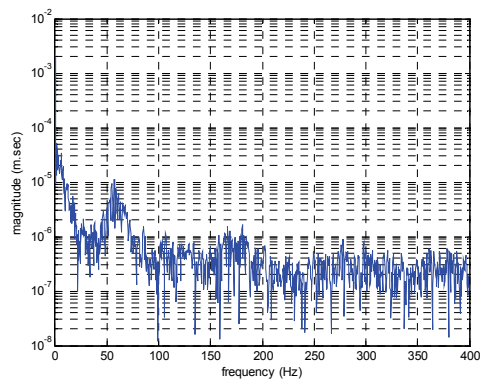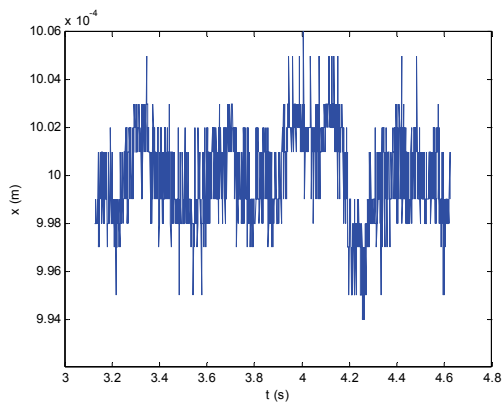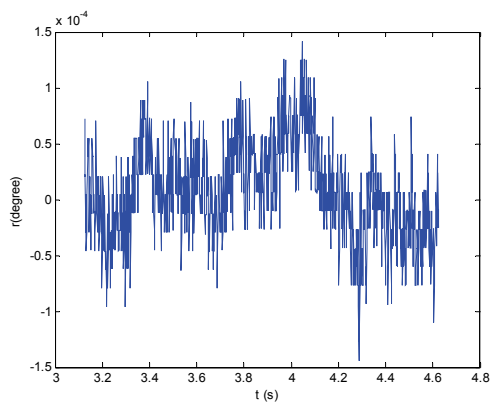
Figure 8-10 (a) 10-µm step response in *y*, (b) FFT, perturbation (c) in *x*, and (d) in ϕ
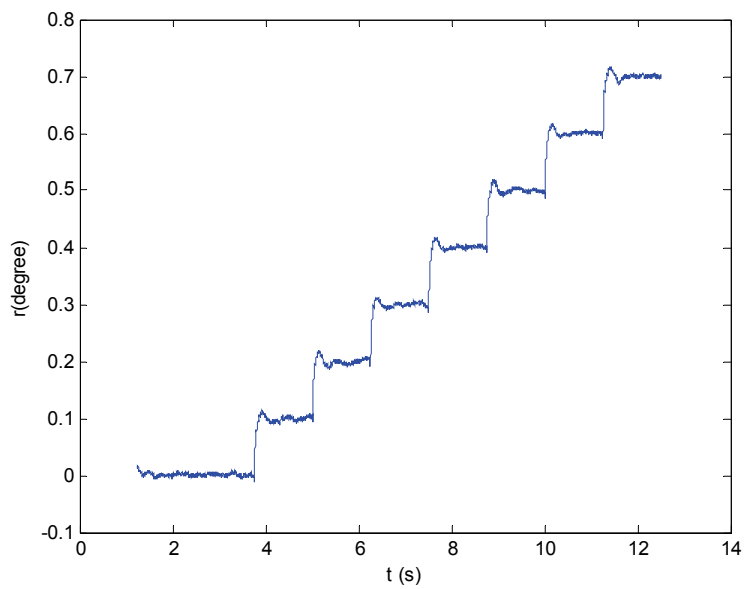
(a)
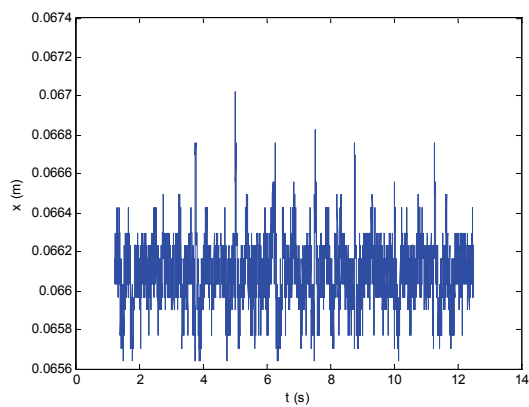
(b)
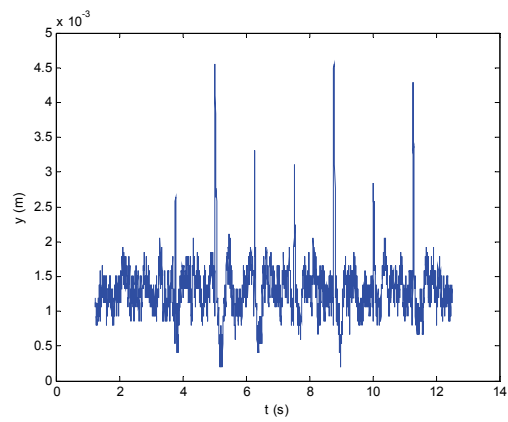
(c)

Figure 8-11: (a) 0.1° step response in ϕ, and perturbation (b) in x, and (c) in y
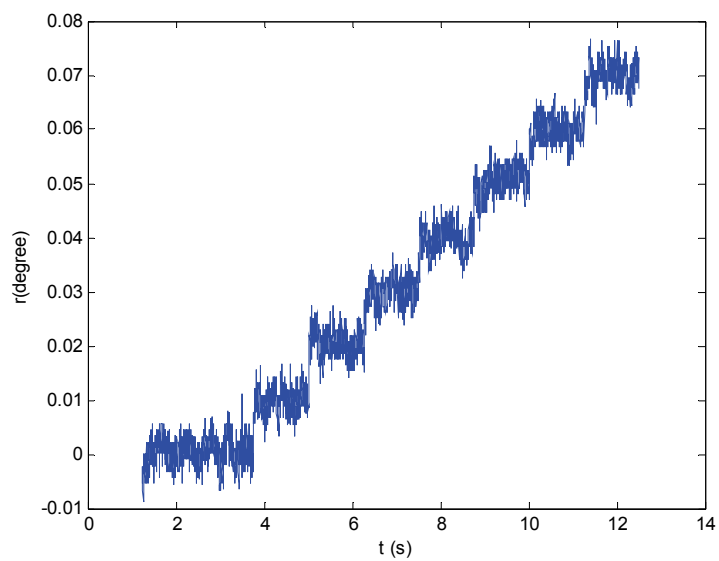
(a)
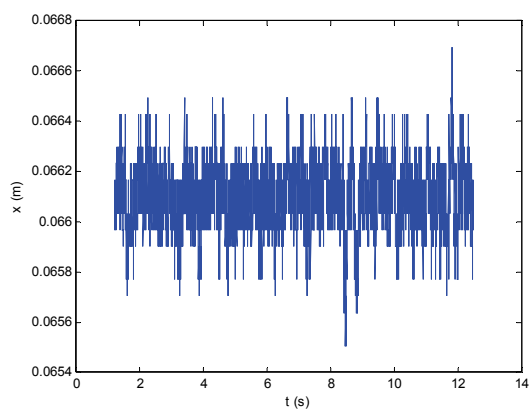
(b)
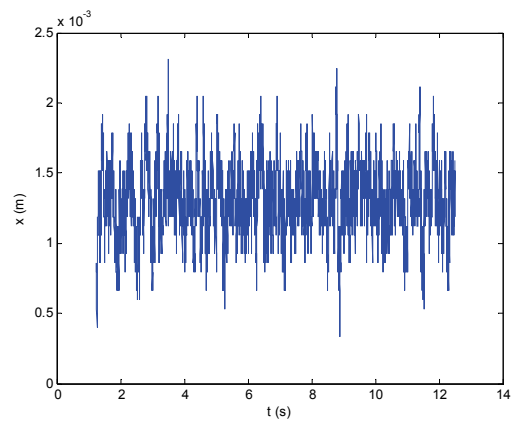
(c)

Figure 8-12: (a) 0.01° step response in ϕ, perturbation (b) in x, and (c) in y
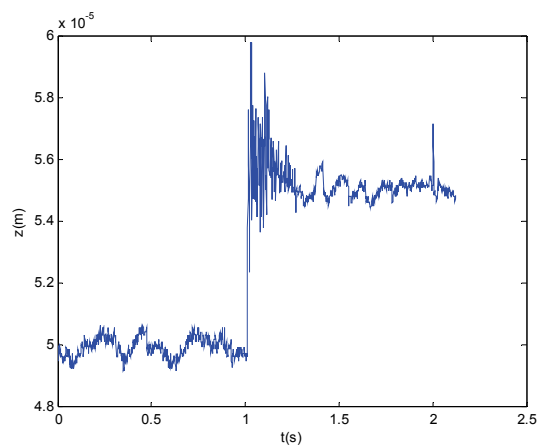
(a)
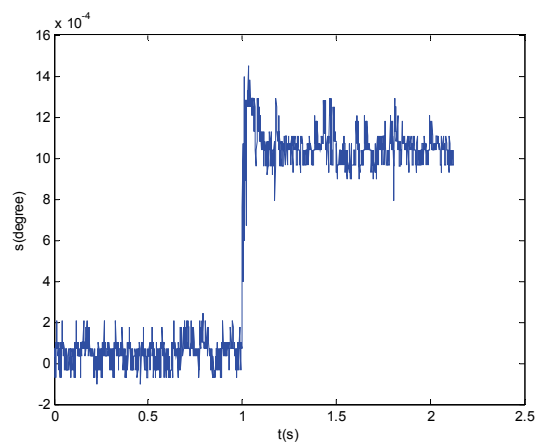
(b)
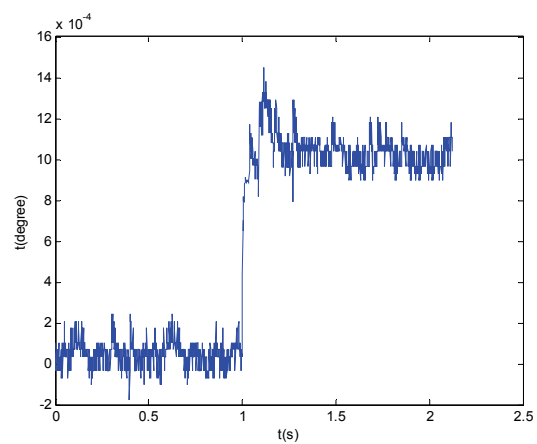
(c)

Figure 8-13: Vertical-mode step responses: (a) 5-µm in *z*, (b) 0.001° in θ, and (d) 0.001° in ψ
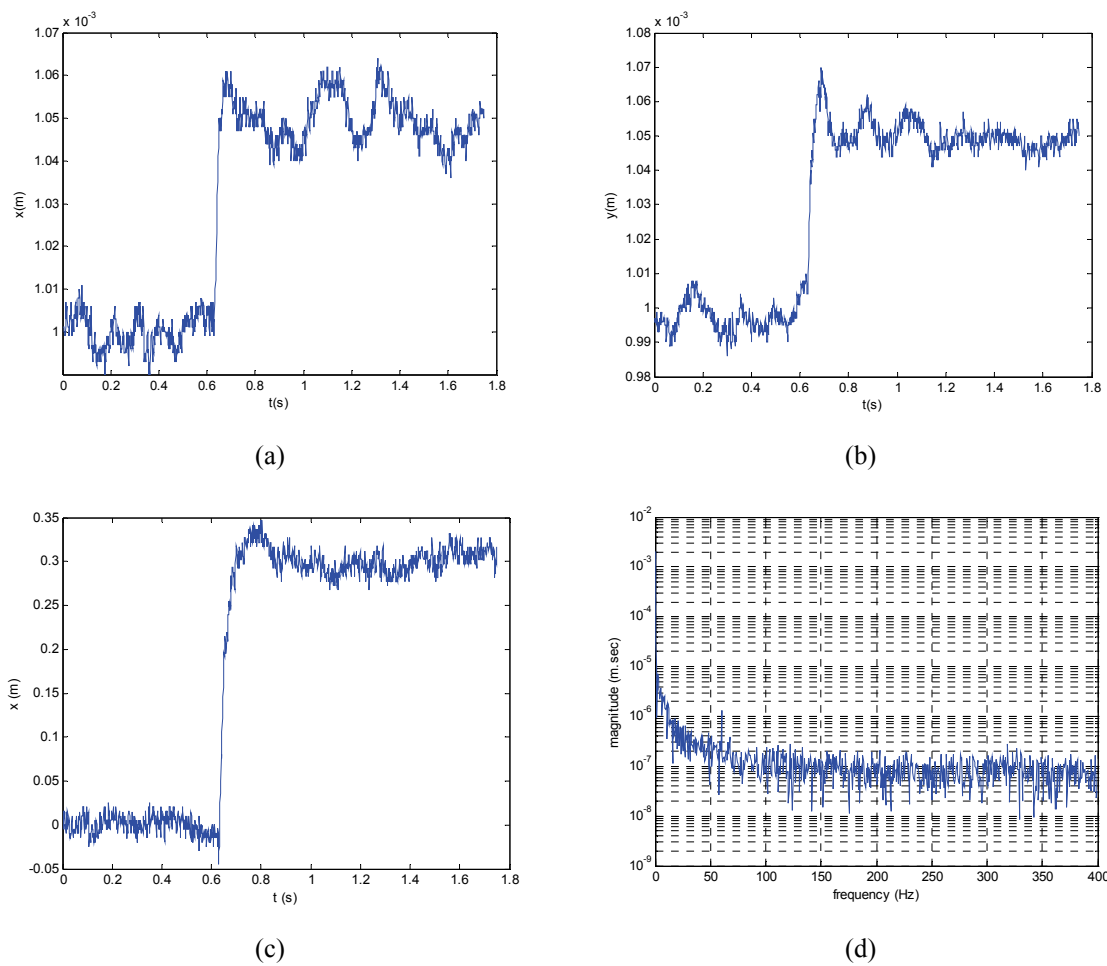
Figure 8-14: 50-µm step responses by LQG controller (a) in *x* and (b) in *y*. (c) 0.3° step response in ϕ and (d) FFT of (a)

8.2 Long-Range Planar Motions

Planar motions in a long-range are commonly used in precision-positioning application, such as scanning, microlithography, and microscopy. Long-range planar motion generation is performed and several experimental results are presented in this section. These experimental results demonstrate the long-range scanning motion capabilities of the positioner.

First, one of the key advantages of this positioning stage is that the angular measurement range with the Hall-effect sensors is larger than that of the laser interferometers. The rotation motion range of the laser interferometer is just a few milliradians, because it uses the reflected laser beam, where laser beams stray off in large angles of motion. However, rotation motion control with Hall-effect sensors does not have this limitation. Hence, it can technically generate much larger angle of rotation motions than the system with laser interferometers. Figure 8-15 presents the large angle of the rotation motion of 12° with the Hall-effect sensors. The positioner started to rotate clockwise up to almost 6° and the counter-clockwise rotation motion of 12° was generated.

The maximum travel ranges that can be generated by this positioner are presented in Figure 8-16. The travel ranges of 220 mm in x and 200 mm in y are achieved in translation. The scanning velocities are 8 mm/s both in x and y. The travel range of the positioner is only limited by the number of pitches in the magnet matrix, currently consisting of 6 by 6 pitches. The platen's geometric asymmetry accounts for the difference in the maximum travel ranges in x and y. The two planar motors are employed

for the *y*-directional motion. Otherwise a single planar motor is employed for the *x*-direction motion. The maximum travel range in translation can be simply enlarged by increasing the number of pitches in the magnet matrix. Since the positioner with Hall-effect sensors does not need to carry the stick mirrors that reflect the laser beam in the laser interferometry, it can generate larger motions than the positioners using laser interferometers.

Figure 8-17 (a) and (b) show the planar back-and-forth motions of 8×8 mm and 16×14 mm that demonstrate the capabilities in the wafer stepping/scanning process. A big circular motion of 200-mm diameter in Figure 8-18 (a) was achieved with the position errors in *x* and *y* shown in Figure 8-18 (b) and (c). The position errors of 0.94 mm in *x* and 1.1 mm in *y* are seen in the figure. The angular velocity of 0.2094 rad/s was obtained to generate circular motion.

A spiral motion with the radius increases from the origin, the position error in *x*, and the position error in *y* are demonstrated in Figure 8-19 (a), (b), and (c), respectively. The position errors of 0.5 mm was measured both in *x* and *y*. Figure 8-20 presents a 30-mm maximum diameter spiral motion with fast angular velocity of 4.74 rad/s. The motion started at the origin and the circle was enlarged until the diameter became 30 mm. The spiral motion includes seven circles, which rotates a total of 2520°.

A variable-amplitude sinusoidal trajectory in the *x-y* plane is presented in Figure 8-21 (a). It also demonstrates that the positioner has the capability of arbitrary 2-D precision positioning. The amplitude of sinusoidal motion started from zero and it was enlarged up to 20 mm. After the amplitude reach the peak, it decreased to zero again. Figure 8-21 (b) and (c) show the single-axis plots in *x* and *y* with respect to time, respectively.

A velocity profile that verifies the dynamic performances is one of the important processes in precision engineering. Hence, the maximum velocity tests were performed in Figures 8-22 and 8-23. This compact multidimensional positioner is currently capable of generating the maximum velocity of 16.25 mm/s in a long range motion, which is over one pitch of 110 mm. The maximum velocity of 17.5 mm/s was achieved in a short distance motion within one pitch. Figure 8-22 illustrates that the velocity of the positioner started at 8.2 mm/s at 3.75 s and the maximum velocity of 16.25 mm/s was achieved after 4.5 s. Figure 8-23 presents the 8 mm back-and-forth motion with the maximum velocity of 17.5 mm/s. Less than 5% overshoot occured at the end of the steps due to the abrupt velocity change. The acceleration of 72.4 mm/s² was achieved until the positioner reached the maximum velocity.

Finally, a step-and-repeat motion was generated as shown in Figure 8-24. It is a useful demonstration for semiconductor-manufacturing applications. Figure 8-24 (a) illustrates the motion trajectory of the process in the x-y plane. The positioner started the motion from the origin with fast step motion of 14 mm/s in the positive x-direction. The slow scanning motion of 1.6 mm/s in the negative y-direction followed. After 18 s, the scanning motions in the y-direction turned positive. Fast step motions in the x-direction were repeated six times in Figure 8-24 (b). Slow scanning motions in the y-direction were repeated three times in negative and three times in positive directions in Figure 8-24 (c). Demonstration codes of step motions and large trajectory motions are presented in Appendix B.
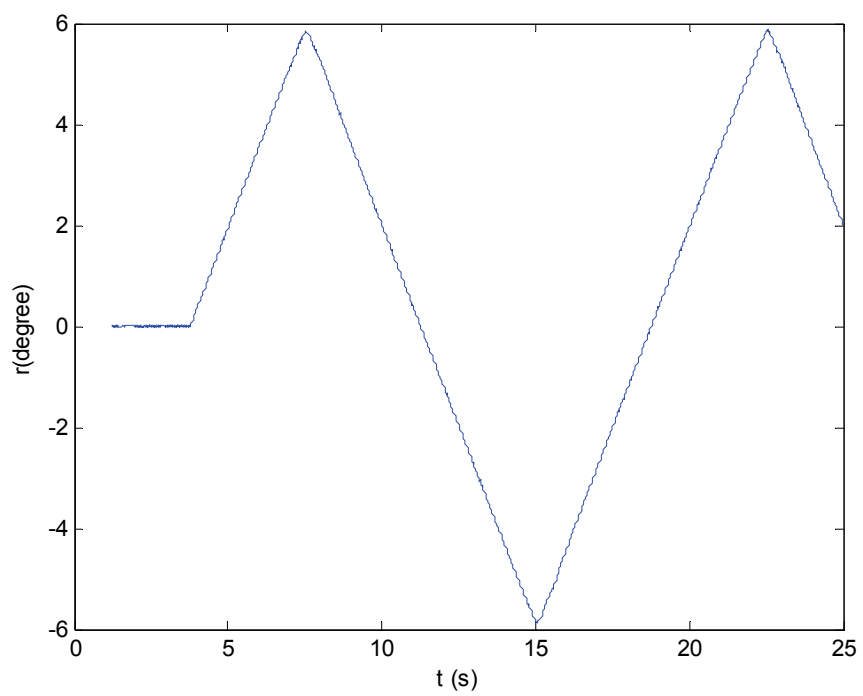
Figure 8-15: 12° rotation motion
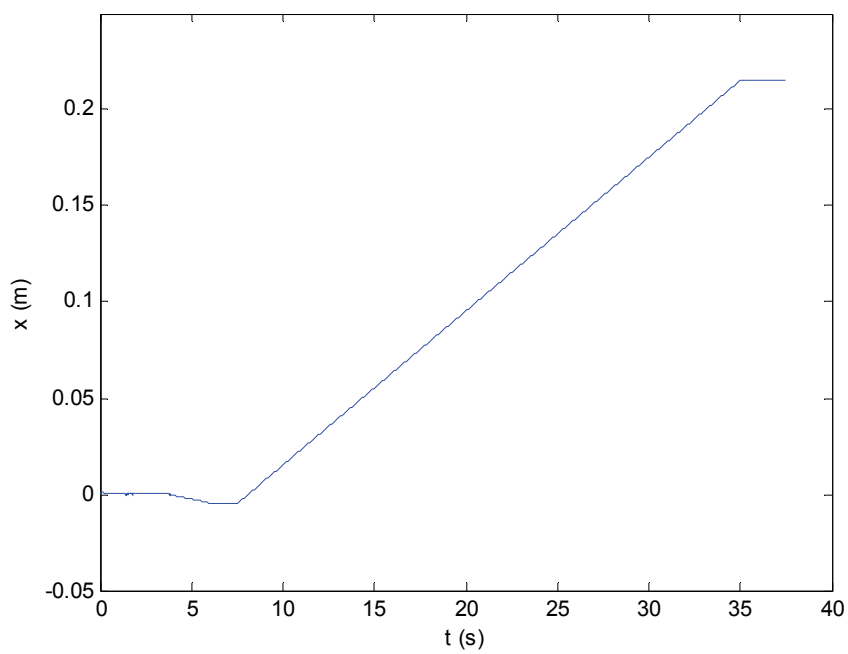
(a)
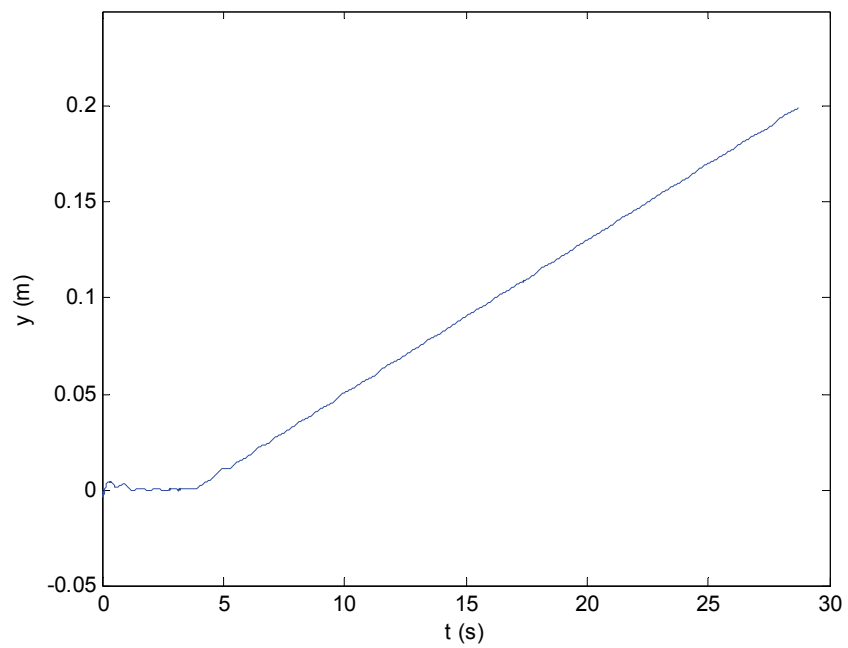
(b)

Figure 8-16: Maximum travel ranges: (a) 220 mm in *x* and (b) 200 mm in *y*
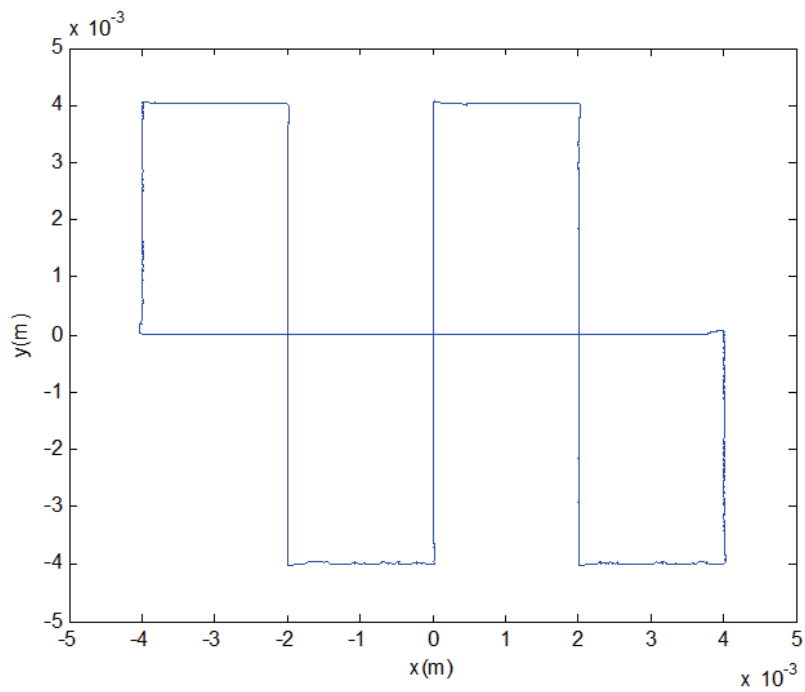
(a)
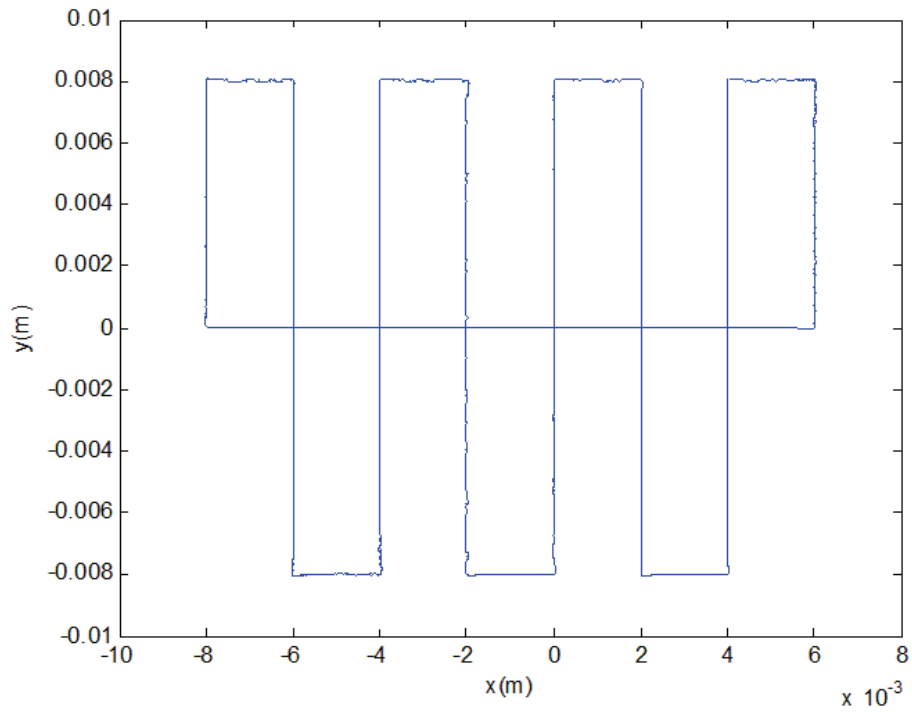
(b)

Figure 8-17: Back-and-forth motions, (a) 8 × 8 mm and (b) 16 × 14 mm
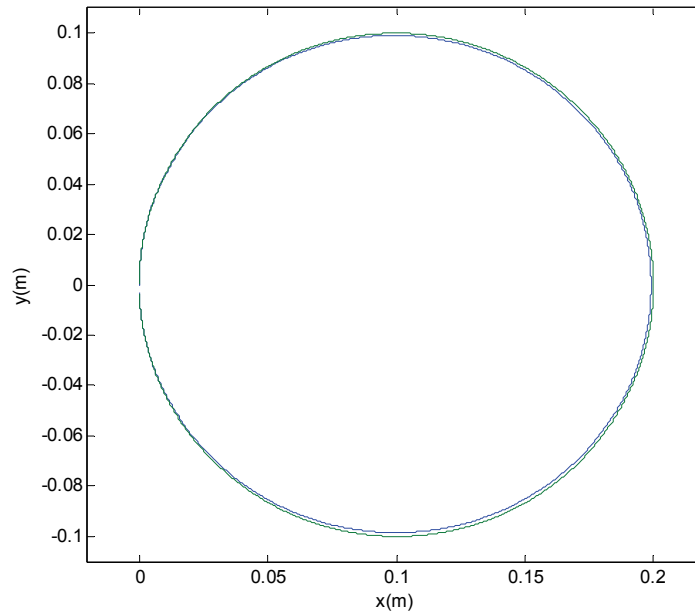
(a)
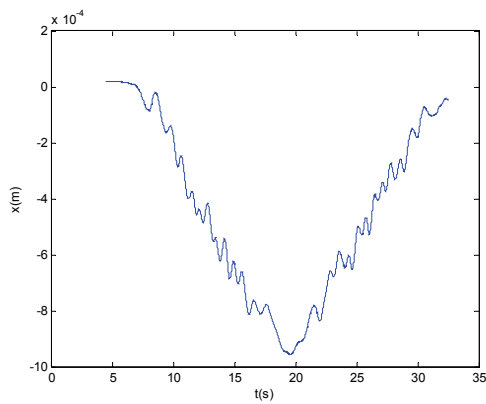
(b)
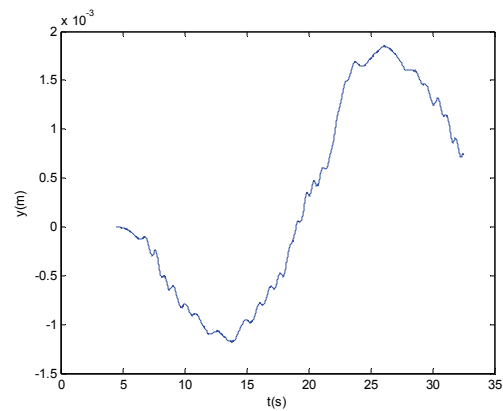
(c)

Figure 8-18: (a) 200-mm diameter circle motion, and position error (b) in *x* and (c) in *y*
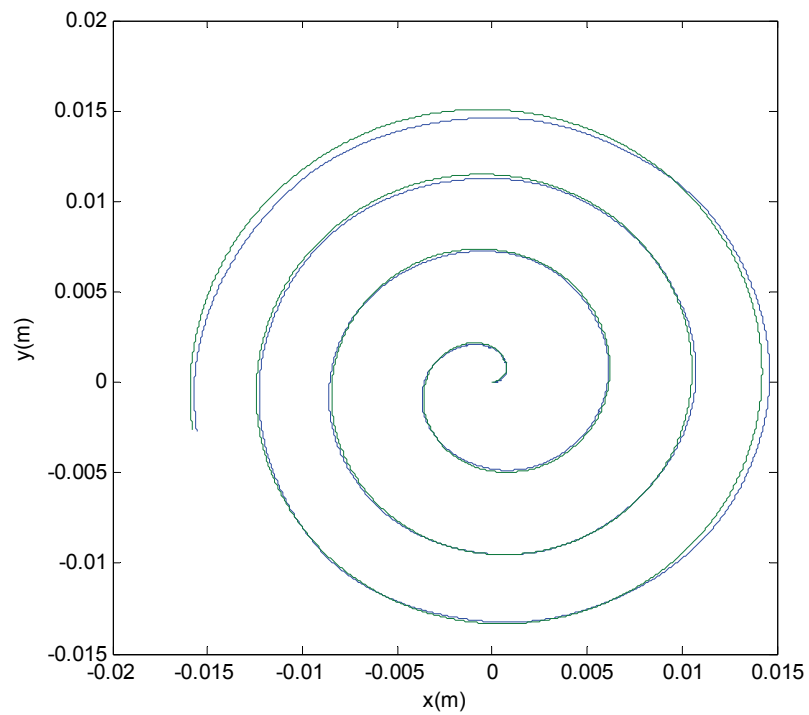
(a)
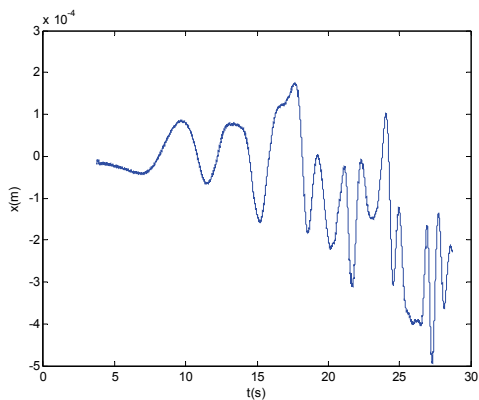
(b)
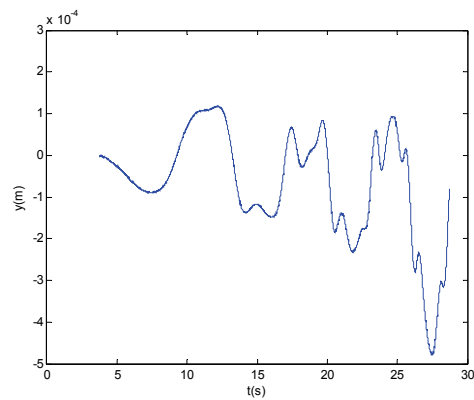
(c)

Figure 8-19: (a) Spiral motion generation, and position error (b) in *x* and (c) in *y*
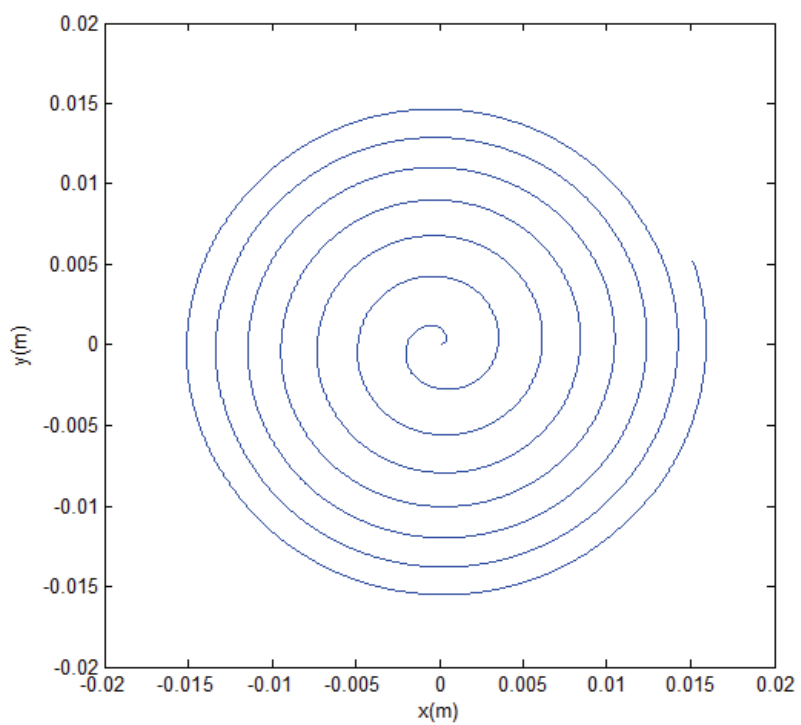
Figure 8-20: 2520° spiral motion generation
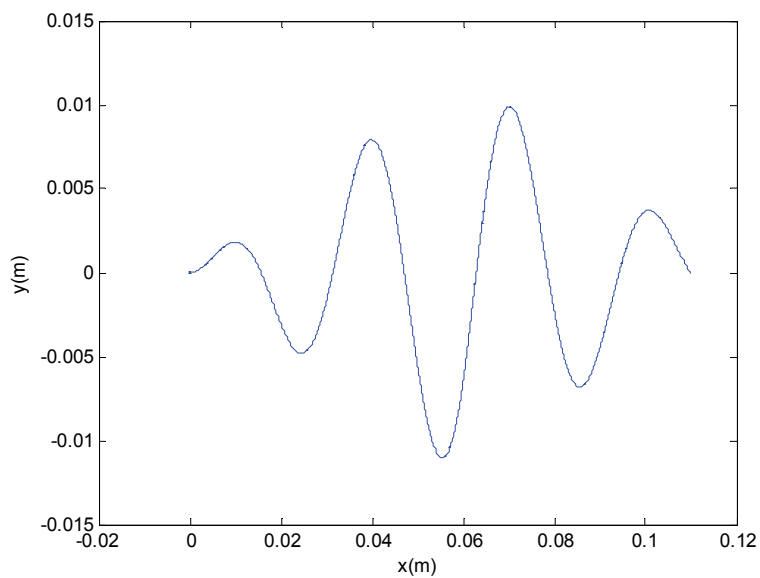
(a)
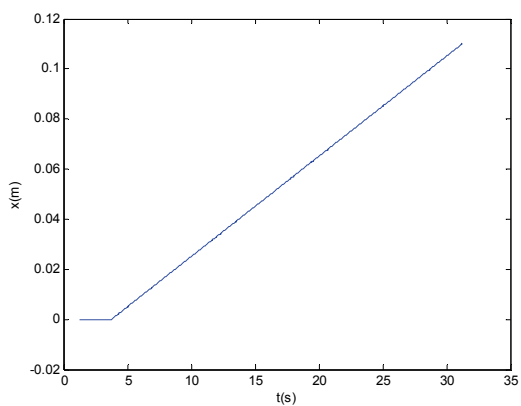
(b)
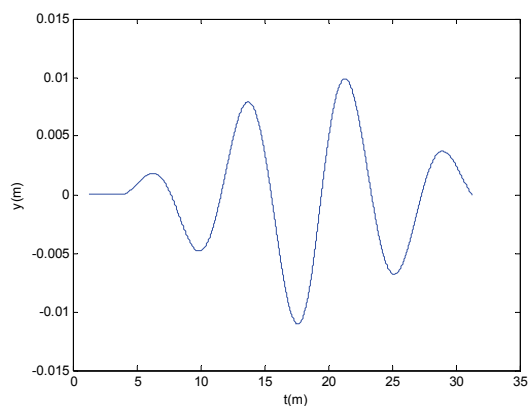
(c)

Figure 8-21: (a) Variable-amplitude sinusoidal motion in the *x-y* plane, (b) in *x*, and (c) in *y*
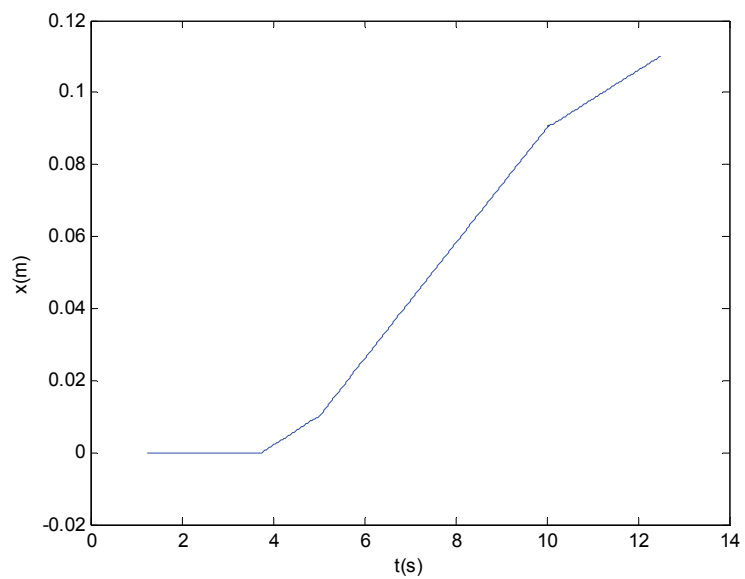
Figure 8-22: Velocity profile in *x* with 16.25 mm/s
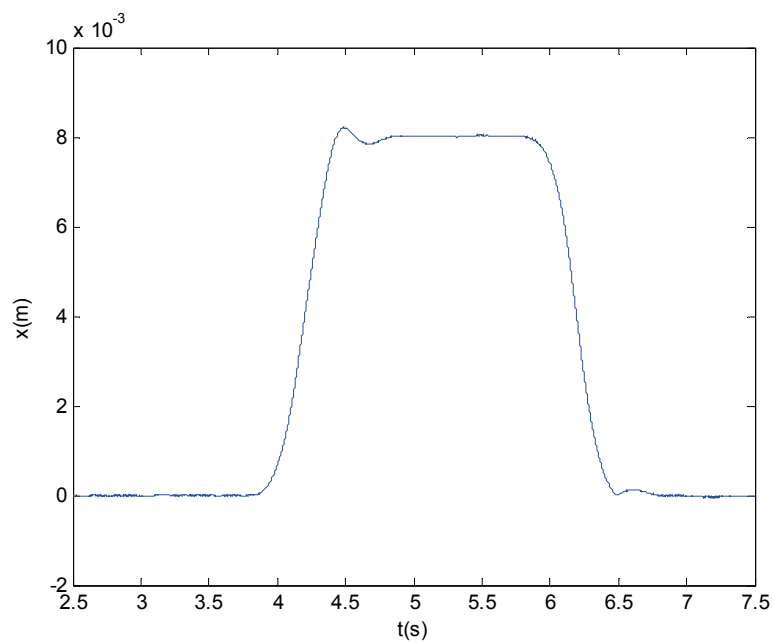
Figure 8-23: 8-mm back-and-forth motion
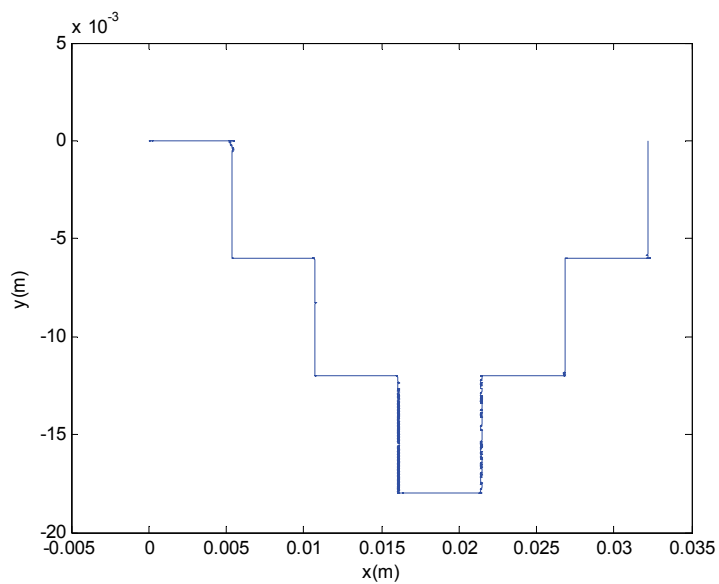
(a)
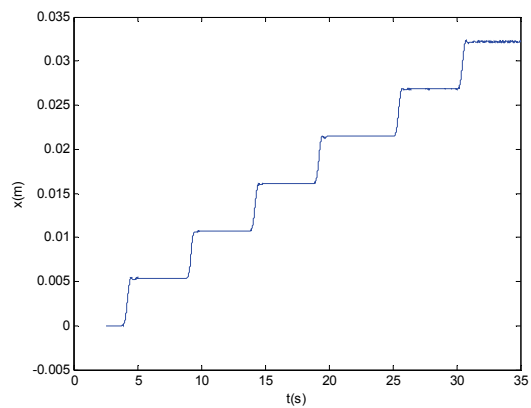
(b)
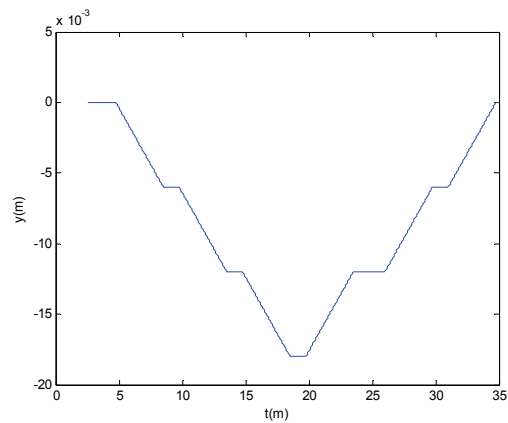
(c)

Figure 8-24: Step-and-repeat motion: (a) in the *x-y* plane, (b) in *x*, and (c) in *y*

CHAPTER IX

CONCLUSIONS AND FUTURE WORK

This final chapter includes the conclusions of this research in the design, analysis of the electromagnetic structures, sensor methodologies, real-time programming, and the experimental achievements. Several suggestions for the future work to improve the design and performance of the positioner are also given in this chapter.

9.1 Conclusions

In this research, a compact high-precision multi-dimensional positioning system was developed and implemented. The design objective was generating both fine and coarse motions with Linux-based real-time control. In order to reduce the size and the mass of the platen, Delrin with a low mass density of 1.54 g/cm³ was used. The CNC machining process made it possible to produce the simplest and the lightest body frame with a single cutting. The platen was comprised of a triangular-shaped Delrin main body, three 3-phase planar-levitation-motor windings, three 2-axis Hall-effect sensors, three laser distance sensors, two terminal blocks, and three aerostatic bearings. As a stator, the novel concentrated-field permanent-magnet matrix was used, which consists of the two orthogonal Halbach magnet arrays. Sinusoidal and periodic magnetic flux densities are generated by the magnetic matrix. The planar motors as actuators, which are the SPMPM can provide both driving and vertical forces based on the Lorenz-force law. With the minimum number of planar motors, the positioner was designed to generate all 6-DOF

motions. Levitation eliminates the mechanical contact between the moving platen and the stationary base plate. In addition, the non-contact moving frame eliminates wear in the mechanical components and does not need lubricants. Furthermore, no friction allows a longer life span of the mechanical parts. Hence, it is highly suitable for the clean-room environment such as a vacuum chamber.

The multi-dimensional positioner has a single moving part, which can generate multi-axis motions. Compared to the traditional positioning system such as the crossed-axis-type and gantry-type positioners, it has several advantages of simple design, more compact size, lower power consumption, and high-precision motion generations. The simple design structure leads to high bandwidth, low manufacturing cost, and high reliability.

The lateral motions are measured by three 2-axis Hall-effect sensor and the vertical motions are controlled by the feedback with three laser distance sensors. Laser interferometers, which are the conventional methodologies in the precision engineering, were used in the previous research presented in Chapter I. Since a laser interferometer has high precision resolution capabilities, it is suitable for precision motion control. However, it has several drawbacks. First, the transversal sensing range of a laser interferometer is limited by the size of the mirror. The motion range can be increased by enlarging the mirror. However, a larger mirror becomes heavy and affects the positioner's dynamics negatively. Another downside of the laser interferometer is that it can only generate very small angular motions. Therefore, this research adopted the novel Hall-effect sensor methodology to control the lateral mode position.

Hall-effect sensors are absolute position sensors and can be placed at any position atop a magnet array. Unrestricted translational and rotational moving ranges with respect to the size of magnet array are the advantage of the Hall-effect sensor. The experimental setup, which is more cost-effective than that of laser interferometer, requires the Hall-effect sensors, ADC and DAC boards, power supplies, and power amplifiers. The recursive discrete Kalman filter (DKF) was used to achieve better position estimation from sensor signals with noise and disturbance.

The positioner was controlled by a Linux-based real-time system. The real-time feedback control includes Ubuntu as a Linux OS, RTAI, and Comedi. The sampling frequency of the control system is 800 Hz. Digital lead-lag compensators were designed for translational motions with a bandwidth of 17.3 Hz. After each compensator was designed, the positioner achieved a position resolution of 10 μm with position noise of 6 μm rms in the x-y plane. A multivariable controller based on the LQG methodology was designed as well for the horizontal mode. Since Hall-effect sensors only provide the position displacement data, a Kalman filter was used to estimate the remaining states. In order to remove the steady-state error, the modified dynamic plant model was constructed with additional integrator terms. Input disturbance and output measurement noise in the controller dynamics were discussed in the thesis. Good experimental results were achieved without steady-state errors.

Experimental results were illustrated to prove the positioner and controller design. Step responses of 10 μm, 20 μm, 100 μm, 500 μm, and 2 mm were implemented in the x-y plane, as well as step responses in the rotation around z were performed. For the vertical mode, levitation, the rotation around x, and the rotation around y were presented. The

compact precision positioner has a planar travel range of 220 mm in x and 200 mm in y. Extending the number of magnets can enlarge the moving range of the positioner. The rotation motion exhibits 12° in ϕ, which is much bigger angle than that could be achieved with a laser interferometer.

The large planar motions such as 200-mm diameter circle with the angular velocity of 0.2094 rad/s and a spiral motion with the angular velocity of 4.74 rad/s were demonstrated. The maximum velocities of 16.25 mm/s over one pitch motion and 17.5 mm/s in 8-mm back-and-forth motion with the acceleration of 72.4 mm/s² were achieved. For the vertical mode control, step responses of 5 μm in z, 0.001° rotation motion around x, and y were implemented. The unrestricted moving range is a result of the periodic magnetic flux density in the x-y plane. As mentioned above, the positioner with Hall-effect sensor has 10 μm resolution and 6 μm rms position noise. The microscale accuracy and position errors are based on following reasons: The sensitivity of Hall-effect sensor and the modeling error mainly affect the position output. The manufacturing error of the magnet array and the inconsistent magnet flux density may exist. The misalignment of Hall-effect sensors and an external magnetic field can interfere the accurate position sensing.

A compact precision positioner with Linux-based real-time control was presented in this thesis. Its potential applications in the semiconductor industry were demonstrated, and the designed controllers were successfully implemented.

9.2 Suggestions for Future Work

This section suggests several possible ways to improve the precision positioner for further research. An advanced positioner that has better dynamic performance and positioning resolutions can be designed with improving mechanical, electromagnetic, and control design.

Currently, the real-time control is performed by a personal computer with Linux operating system. Although Linux can provide stable real-time feedback control in low capacity computer, the sampling speed to obtain high quality dynamic performance is limited. A DSP that can accommodate a high-speed sampling frequency may yield better dynamic performance, as well as other sensors such as a laser interferometer can be used by the DSP and data-acquisition devices.

A Hall-effect sensor exhibits the unlimited travel range with a microscale position resolution. Otherwise, a laser interferometer has nanoscale resolution in spite of its limited moving range. Hence, a hybrid sensing methodology that has advantages both the two sensors can be proposed for a new positioning stage. The scanning motion that requires large moving range can be monitored by Hall-effect sensors, and the step-and-repeat motions that need to be controlled in nanoscale can be measured by laser interferometers.

The clean-room environment can improve performances of the positioner. Due to the mechanical vibrations in the lab transmitted through from building and umbilical signal and power cables, the disturbance can be magnified. The noise isolation against the vibration, temperature, and the debris will enhance the precision accuracy.

REFERENCES

[1]   T. Hu, "Design and control of a 6-degree-of-freedom levitated positioner with high precision," Ph.D thesis, Department of Mechanical Engineering, Texas A&M University, College Station, Texas, 2005.

[2]   T. Hu and W. -J. Kim, "Extended-range 6-DOF high-precision positioner for wafer processing," *IEEE/ASME Trans. Mechatronics*, vol. 11, no. 6, pp. 682–689, 2006.

[3]   W.-J. Kim, "High-precision planar magnetic levitation," Ph.D thesis, Massachusetts Institute of Technology, Cambridge, Massachusetts, 1997.

[4]   H. Yu and W.-J. Kim, "Controller design and implementation of six-degree-of-freedom magnetically levitated positioning system with high precision," in *Proc. of 2008 IMechE, Journal of Science and Control Engineering*, vol. 222, Part I.

[5]   Megamation. [Online]. Available: http://www.megamation.com/hm_frame.htm, 2001.

[6]   Normag, *Northern Magnetics Linear Motor Technology Manual*, 1998.

[7]   W. E. Hinds and B. Nocito, "The Sawyer linear motor," in *Proc. of The Second Symposium on Incremental Motion Control Systems and Devices*, pp. W-1–W-10, 1973.

[8]   E. R. Pelta, "Two Axis Sawyer Motor for two-dimensional drive," *IEEE Control System Magazine*, pp. 20–24, October 1987.

[9]   T. Asakawa, "Two dimensional positioning devices," U.S. patent 4 626 749, December 1986.

[10]   T. Asakawa, "Two dimensional precise positioning devices for use in a semiconductor apparatus," U.S. Patent 4 535 278, August 1985.

[11]   N. Fujii and T. Kihara, "Surface induction motor for two-dimensional drive," *J. Inst. Elect. Eng. Trans.*, pp. 221–228, February 1998.

[12]   A. Chitayat, "Two-axis motor with high density magnetic platen," U.S. patent 5 777 402, July 1998.

[13]   A. Chitayat, "Two axis Sawyer motor," in *Proc. of the 12th Annual IEEE Industrial Electronics Society Conference*, Urbana, Illinois, pp. 3–8, 1986.

[14]   E. R. Pelta, "Two Axis Sawyer Motor," in *Proc. of the 12th Annual IEEE Industrial Electronics Society Conference*, pp. 3–8, 1986.

[15]   D. Ebihara and M. Watada, "Study of a basic structure of surface actuator," *IEEE Trans. on Magnetics*, vol. 25, no. 5, pp. 3916–3918, 1989.

[16]   H. S. Cho and H. K. Jung, "Analysis and design of synchronous permanent-magnet planar motors," *IEEE Trans. on Energy Conversion*, vol. 17, no. 4, pp. 492–499, Dec. 2002.

[17]   G. A. Fries, A. A. Rizzi, and R. L. Hollis, "Fluorescent dye based optical position sensing for planar linear motors," in *Proc. of IEEE International Conference on Robotics & Automation* Detroit, Michigan, vol. 2, pp. 1614–1619, May 1999.

[18]   I. J. C. Compter, "Electro-dynamic planar motor," *Precision Engineering*, vol. 28, pp.171–180, 2004.

[19]   Y. Kawato, "Multi-DOF precision positioning methodology using two-axis Hall-effect sensors," M.S. thesis, Department of Mechanical Engineering, Texas A&M University, College Station, Texas, 2005.

[20]   G. van Engelen and A. G. Bouwer, "Two-step positioning device using Lorentz forces and a static gas bearing," U.S. Patent 5 120 034, June 1992.

[21]   S. Sakino, E. Osanai, M. Negishi, M. Horikoshi, M. Inoue, and K. Ono, "Movement guiding mechanism," U.S. Patent 5 040 431. August 1991.

[22]   Danaher Motion, Washington, D.C. [Online]. Available: http://www.danahermoti on.com

[23]   Aerotech Inc., Pittsburg, PA. [Online]. Available: http://www.aerotech.com

[24]   S. Wittekoek and A. G. Bouwer, "Displacement device, particularly for the photolithographic treatment of a substrate," U.S. Patent 4 655 594, April 1987.

[25]   Z. Xu, Z. Feng, K. Seto, and H. Tamura, "Nonlinear vibration properties of a current-controlled attractive type maglev system," in *Proc. of 2003 ASME International mechanical engineering congress and exposition*, November 2003, paper 41879.

[26]   J. Cao, Y. Zhu, J. Wang, W. Yin, and G. Duan, "Analysis and comparison of two-dimensional permanent-magnet arrays for planar motor," *IEEE Trans. on Magnetics*, vol. 40, no. 6, pp. 3490–3491, November 2004.

[27]   H.-S. Cho, C.-H. Im, and H.-K. Jung, "Magnetic field analysis of 2-D permanent magnet array for planar motor," *IEEE Trans. on Magnetics*, vol. 37, no. 5, pp. 3762–3766, September 2001.

[28]   H.-S. Cho and H.-K. Jung, "Effect of coil position and width on back-EMF constant of permanent magnet planar motors," in *Proc. of International Electric Machines and Drives Conference*, pp. 430–435, June 2001.

[29]   T. Ueta, B. Yuan, and T.-C. Teng, "Moving magnet type planar motor control," U.S. Patent Application Publication 0 102 722, June 5, 2003.

[30]   T. Ueta and B. Yuan, "Moving coil type planar motor control," U.S. Patent Application Publication 0 102 721, June 5, 2003.

[31]   A. J. Hazelton and J.-M. Gery, "Planar electric motor and positioning device having transverse magnets," U.S. Patent 6 285 097, September 4, 2001.

[32]   T. Asakawa, "Two dimensional precise positioning devices for use in a semiconductor apparatus," U.S. Patent 4 535 278, August 13, 1995.

[33]   H. S. Cho, C. H. Im, and H. K. Jung, "Magnetic Field Analysis of 2-D Permanent Magnet Array for Planar Motor," *IEEE Trans. on Magnetics*, vol. 37, no. 5, pp. 3762–3766, September 2001.

[34]   D. L. Trumper, W.-J. Kim, and M. E. Williams (1997), "Magnetic arrays," U.S. Patent Office, Patent5 631 618, May 1997.

[35]   K. Halbach, "Design of permanent multipole magnets with oriented rate earth cobalt material," *Nucl. Instrum. Methods*, vol. 169, no. 1, pp. 1–10, 1980.

[36]   P.-K. Budig, "The application of linear motors," in *Proc. of IEEE Power Electronics and Motion Control Conference*, vol. 3, pp. 1336–1341, Aug. 2000.

[37]   W.-J. Kim and B. C. Murphy, "Development of a novel direct-drive tubular linear brushless permanent-magnet motor," in *Proc. IEEE Ind. Applicat. Soc. 38th Annu. Meeting*, Salt Lake City, UT, vol. 3, pp. 1664–1671, October 2003.

[38]   D. L. Trumper, W.-J. Kim, and M. E. Williams, "Design and analysis framework for permanent-magnet machines," *IEEE Trans. on Industry Applications*, vol. 32, no .2, pp. 371–379, March/April 1996.

[39]   W.-J. Kim, M. T. Berhan, D. L. Trumper, and J. H. Lang, "Analysis and implementation of a tubular motor with Halbach magnet array," *Proc. of the IEEE Industry Applications Society 31st Annual Meeting*, pp. 471–478, October 1996.

[40]   J. H. Park, J. H. Choi, D. H. Kim, and Y.S. Beak, "Parametric design of the levitation mechanism for maglev planar transportation vehicle," *IEEE Trans. Magn.*, vol. 40, no. 4, pp. 3069–3071, July 2004.

[41]   N. Fujii, K. Naotsuka, K. Ogawa, and T. Matsumoto, "Basic characteristics of magnet wheels with rotating permanent magnets," in *Proc. 1994 IEEE Ind. Applicat. Soc. Annu. Meeting,* Denver, CO, vol. 1, pp. 203–209, 1994.

[42]   K. Ogawa, Y. Horiuchi, and N. Fujii, "Calculation of electromagnetic forces for magnet wheels," *IEEE Trans. Magn.*, vol. 33, no. 2, pp. 2069–2072, March 1997.

[43]   N. Fujii, S. Nonaka, and G. Hayashi, "Design of magnet wheel integrated own drive," *IEEE Trans. Magn.*, vol. 35, no. 5, pp. 4013–4015, September 1999.

[44]   N. Fujii, T. Kayasuga, and T. Hoshi, "Simple end effect compensator for linear induction motor," *IEEE Trans. Magn.*, vol. 38, no. 5, pp. 3270–3272, September 2002.

[45]   J. Bird and T. A. Lipo, "An electrodynamic wheel: An integrated propulsion and levitation machine," in *Proc. Int. Electr. Machines and Drives Conf.*, Madison, WI, vol. 3, pp. 1410–1416, 2003.

[46]   Philips applied technology website. [Online]. Available: http://www.apptec h.philips.com/press_center/philips_nforcer_technology.html, 2007.

[47]   J. W. Jansen, C. M. M. van Lierop, A. Lomonova, and A. J. A. Vandenput, "Magnetically levitated planar actuator with moving magnet," *IEEE Trans. on Industry Applications*, vol. 44, no. 4, pp. 1108–1115, July/August 2008.

[48]   C. M. M. van Lierop, J. W. Jansen , A. A. H. Damen, and P. P. J. van den Bosch, "Control of multi-degree-of-freedom planar actuators," *in Proc. IEEE Int. CCA*, Munich, Germany, pp. 2516–2521, October 2006.

[49]   J. W. Jansen, C M. M. van Lierop, E. A. Lomonova, and A. J. A. Vandenput, "Modeling of magnetically levitated planar actuators with moving magnets," *IEEE Trans. Magn.*, vol. 43, no. 1, pp. 15–25, January 2007.

[50]   J. W. Jansen, C. M. M. van Lierop, E. A. Lomonova, and A. J. A. Vandenput, "Magnetically levitated planar actuator with moving magnets," in *Proc. Electric Machines & Drives Conference*, vol. 1, pp. 272–278, May 2007.

[51]   B. A. Sawyer, "Magnetic positioning device," U.S. Patent 3 376 578, April 2, 1968.

[52]   Y. Tomita, M. Sugimine, and Y. Koyanagawa, "Development of six-axis precise positioning system driven by surface motor," *The Japan Society of Mechanical Engineers Trans. C*, vol. 62, no. 597, pp. 1840–1847, 1996.

[53]   S. Dejima, W. Gao, H. Shimizu, S. Kiyono, and Y. Tomita, "Precision positioning of a five degree-of-freedom planar motion stage," *Mechtronics*, vol.

15, no. 8, pp. 969–987, October 2005.

[54] Y. Makino, J. Wang, and T. Koseki, "Control of 6-degree-of-freedom motion and design of a mover consisting of three linear induction motors and three u-type electromagnets," in *Proc. Symp. Power Electronics, Electr. Drive, Autom. & Motion (SPEEDAM 2004)*, Capri, Italy, pp. 430–435, June 2004.

[55] N. Fujii and K. Okinaga, "*X-Y* linear synchronous motors without force ripple and core loss for precision two-dimensional drives," *IEEE Trans. Magn.*, vol. 38, no. 5, pp. 3273–3275, September 2002.

[56] J. Cao, Y. Zhu, J. Wang, W. Yin, and G. Duan, "A novel synchronous permanent magnet planar motor and its model for control applications," *IEEE Trans. Magn.*, vol. 41, no. 6, pp. 2156–2163, June 2005.

[57] T. Yano, "Multi-dimensional drive system," in *Proc, Symp, Power Electronics, Electr. Drive, Autom. & Motion (SPEEDAM 2004)*, Capri, Italy, pp. 446–451, June 2004.

[58] Y. Ueda and H. Ohaski, "A planar actuator with a small mover traveling over large yaw and translational displacements," *IEEE Trans. on magnetics*, vol. 44, no. 5, pp. 609–616, May 2008.

[59] K. Halbach, "Concepts for insertion devices that will produce high quality synchrotron radiation," *Nucl. Instr. Meth. Phys. Res. Sect. A*, vol. 246, no. 1–3, pp. 77–81, May 1986.

[60] Z. O. Zhu and D. Howe, "Halbach permanent magnet machines and applications: A review," *IEEE Proc.-Electr. Power Appl.*, vol. 148. no. 4, pp. 299–308, July 2001

[61] B. Zhang and Z. Zhu, "Developing a linear piezomotor with nanometer resolution and high stiffness," *IEEE/ASME Trans. of Mechatronics*, vol. 2, no. 1, pp. 22–29, March 1997.

[62] L. Juhas, A. Vujani, N. Adamovi, L. Nagy, and B. Borovac, "Development of platform for micro-positioning actuated by piezo-legs," in *Proceedings of the 2000 IEEE International Conference on Robotics and Automation*, San Francisco, CA, pp. 3647–3653, April 2000.

[63] H. Richter, E. Misawa, D. Lucca, H. Lu, "Modeling Nonlinear Behavior in a Piezoelectric Actuator." *Precision Engineering and Nanotechnology*, vol. 25, no. 2, pp. 128–137, April 2001.

[64] Y. K. Yong, S. S. Aphale, and S. O. R. Moheimani, "Design, identification, and control of a flexure-based *xy* stage for fast nanoscale positioning," *IEEE Trans.*

on Nanotechnol., vol. 8, no. 1, pp. 46–53, January 2009.

[65] G. Binning and H. Rohrer, "Scanning tunneling microscope," U.S. Patent 4 343 993, August 10, 1982

[66] G. Binning and D. P. E. Smith, "Single-tube three-dimensional scanner for scanning tunneling microscopy," *Rev. Sci. Instrum.*, vol. 57, no. 8, pp. 1688–1689, August 1986.

[67] S. S. Aphale, S. Devasia, and S. O. R. Moheimani, "High-bandwidth control of a piezoelectric nanopositioning stage in the present of plant uncertainties," *Nanotechnology*, vol. 19, pp. 125503-1–125503-9, January 2008.

[68] S. S. Aphale, B. Bhikkaji, and S. O. R. Moheimani, "Minimizing scanning errors in piezoelectric stack-actuated nanopositioning platforms," *IEEE Trans. Nanotechnol.*, vol. 7, no. 1, pp. 79–90, January 2008.

[69] Y. K. Yong and T.-F. Lu, "The effect of the accuracies of flexure hinge equations on the output compliances of planar micro-motion stages," *Mech. Mach. Theory*, vol. 43, pp. 347–363, June 2007.

[70] W.-J. Kim, D. L. Trumper, and J. H. Lang, "Modeling and vector control of planar magnetic levitator," *IEEE Trans, on Industry Applications*, vol. 34, no. 6, pp. 1254–1262, November/December 1998.

[71] W.-J. Kim and D. L. Trumper, "High-precision magnetic levitation stage for photolithography," *Precision Eng.*, vol. 22, no. 2, pp. 66–77, April 1998.

[72] W.-J. Kim, N. Bhat, and T. Hu, "Integrated multidimensional positioner for precision manufacturing," in *Proc. of the Institution of Mechanical Engineers, Part B: Journal of Engineering Manufacture*, vol. 218, no. 4, pp. 431–442, January 2004.

[73] T. Hu and W.-J. Kim, "Extended-range 6-DOF high-precision positioner for wafer processing," *IEEE/ASME Trans. on Mechatronics*, vol. 11, no. 6, pp. 682–689, December 2006.

[74] Agilent technology, Inc., Santa Clara, CA. [Online]. Available: http://www.agilen t.com, 1999.

[75] HP/Agilent datasheet. [Online]. Available: http://www.artisan-scientific.com/info /Agilent_HP_10898A_Datasheet.pdf, 1999.

[76] S. Verma, W,-J. Kim, and J. Gu, "Six-axis nanopositioning device with precision magnetic levitation technology," *IEEE/ASME Transactions on Mechatronics*, vol. 9, no. 2, pp. 384–391, June 2004.

[77] S. Verma, *Development of novel high-performance six-axis magnetically levitated instruments for nanoscale applications*, Ph.D Thesis, Department of Mechanical Engineering, Texas A&M University, College Station, Texas, May 2005.

[78] Y. Kawato and W.-J. Kim, "Multi-degree-of-freedom precision position sensing and motion control using two-axis Hall-effect sensors," *Journal of Dynamic Systems, Measurement and Control*, vol. 128, issue 4, pp. 980–988, December 2006.

[79] Apex. [Online]. Available: http://apex.cirrus.com/en/, 1984.

[80] J. J. Croat, "Current status and future outlook for bonded neodymium permanent magnets (invited)," *J. Appl. Phys*. vol. 8, issues 8, pp. 4804–4809, April 1997.

[81] Hall-effect sensor. [Online]. Available: http://content.honeywell.com/sensing/pro dinfo/solidstate/technical/chapter2.pdf, 2003.

[82] Sentron AG website. [Online]. Available: http://www.sentron.ch, 2004.

[83] Surfboards. [Online]. Available: http://www.capitaladvanced.com, 1999.

[84] J. L. Crassidis and J. L. Junkins, *Optimal Estimation of Dynamic Systems*, 2nd ed. Boca Raton, FL: Chapman & Hall / CRC Press, 2004.

[85] Optra, Inc., Topsfield, MA. [Online]. Available: http://www.optra.com/nanogag e.html, 1985.

[86] A. Ambike, *Closed-loop real-time control on distributed networks*, Master's thesis, Department of Mechanical Engineering, Texas A&M University, College Station, Texas, August 2004.

[87] RT-Linux Home Page. [Online]. http//www.rtlinux.org, 2006.

[88] M. K. Dalheimer and M. Welsh, *Running Linux, Fifth edition*. Sebastopol, CA: O'Reilly Media, December 2005.

[89] RTAI-Linux Home Page. [Online]. http//www.rtai.org, 2006.

[90] B. Lu, X. Wu, and A. Monti, "Implementation of a low-cost real-time virtue test bed for hardware-in-the-loop testing," in *Proc. Industrial Electronics Society, 31st Annual Conference of IEEE*, pp. 239–244, November 2005.

[91] A. Macchelli, C. Melchiorri, R. Carloni, and M. Guidetti, "Space robotics: An experimental set-up based on RTAI-Linux," in *Proc. of 4th real time Linux*

Workshop, Boston, USA, 2002.

[92]   L. Dozio and P. Mantegazza, "Real time distributed control systems using RTAI," *Proceedings of the Sixth IEEE International Symposium on Object-Oriented Real-Time Distributed Computing (ISORC '03)*, pp. 11–18, May 2003.

[93]   M. Ruiz, E. Barrera, S. Lopez, D. Machon, J. Vega, and E. Sanchez, "Real-time data acquisition and processing platform," *Fusion Engineering and Design*, vol. 71, Issues 1–4, pp. 135–140, June 2004.

[94]   Comedi Home Page. [Online]. http://www.comedi.org, 2004.

[95]   Roland CNC Machine. [Online]. http://www.rolanddg.com, 1981.

[96]   A. E. Fitzgerald, C. Kingsley, Jr., and S. Umans, *Electric Machinery*. Boston, MA: McGraw-Hill, 2003.

[97]   A. Blondel, *Synchronous Motors and Converters*. New York: McGraw-Hill, 1913, pt. III

[98]   X. Z. Liu, G. C. Verghese, J. H. Lang, and M. K. Önder, "Generalizing the Blondel-Park transformation of electrical machines: Necessary and sufficient conditions," *IEEE Transactions on Circuits and Systems*, vol. 36, no. 8, pp. 1058−1067, August 1989.

[99]   R. H. Park, "Two-reaction theory of synchronous machines, generalized method of analysis-Part I," *Transactions AIEE*, vol. 48, pp. 716−730, 1929.

[100] E. Kreyszig, *Advanced Engineering Mathematics* 8th edition. New York, NY, John Wiley & Sons, 1999.

[101] J. H. Ginsberg, *Advanced Engineering Dynamics*. Cambridge, U. K.: Cambridge University Press, 1998.

[102] G. F. Franklin, J. D. Powell, and M. L. Workman, *Digital Control of Dynamic Systems*. Reading, MA:Addison-Wesley, 1990.

[103] T. Hu and W.-J. Kim, "Modeling and multivariable control of a novel multi-dimensional levitated stage with high precision," *IJCAS*, vol. 4, no. 1, pp. 1–9, February 2006.

[104] S. Skogestad and L. Postlethwaite, *Multivariable Feedback Control Analysis and Design*, New York, NY, John Wiley & Sons, 1996.

[105]   J. S. Bay, *Fundamentals of Linear State Space Systems*, Boston, MA, WCB/McGraw-Hill, 1999.

[106]   S. Skogestad and I. Postlethwaite, *Multivariable Feedback Control Analysis and Design*. New York, NY: John Wiley & Sons, 1996.

[107]   L. Dai, "Filtering and LQG problems for discrete-time stochastic singular system." *IEEE Transactions on Automatic Control*, vol. 34, no. 10, pp. 1105–1108, Oct. 1989.

[108]   P. S. Mayback, *Stochastic Models, Estimation, and Control*. New York: Academic Press, 1979.

[109]   T. Glad and L. Ljung, *Control Theory Multivariable and Nonlinear Methods*, New York, NY, Taylor & Francis, 2000.

[110]   G. Tao, *Adaptive Control Design and Analysis*, New York, NY, John Wiley & Sons, 2003.

APPENDIX A
MECHANICAL COMPONENT DESIGNS

Figure A-1: Top view of the platen
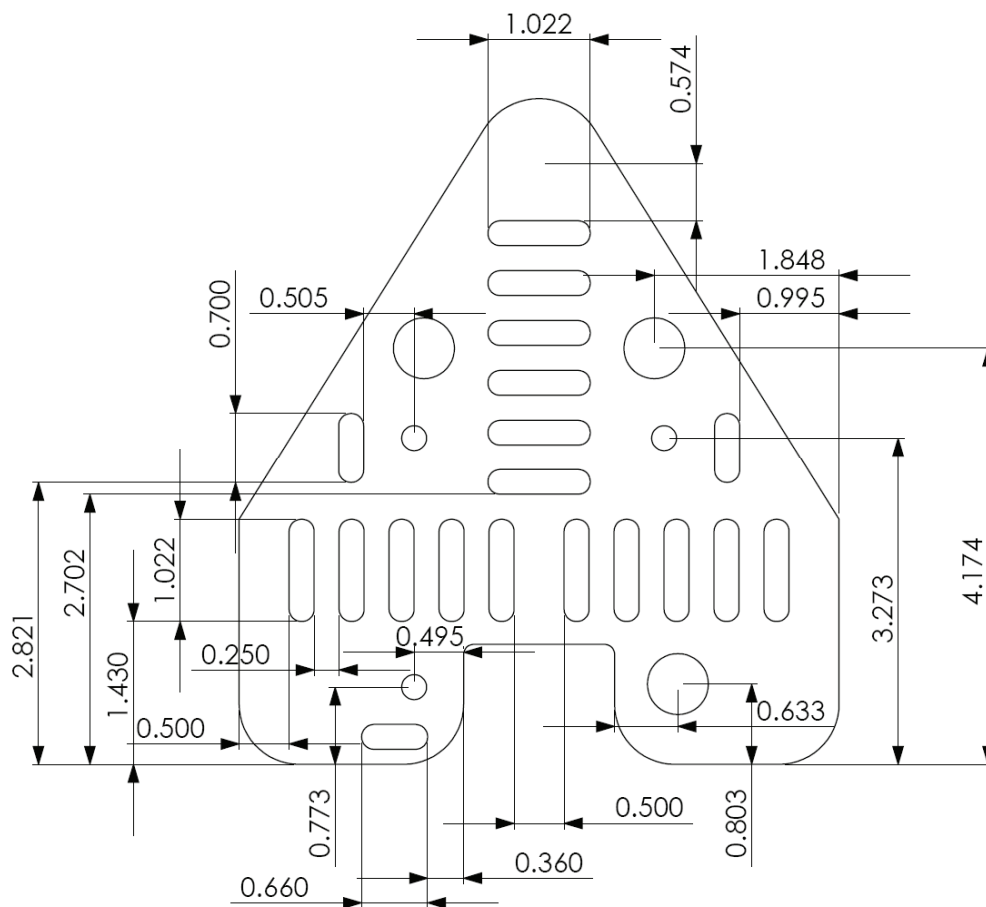
Figure A-2: Top view of the platen 2
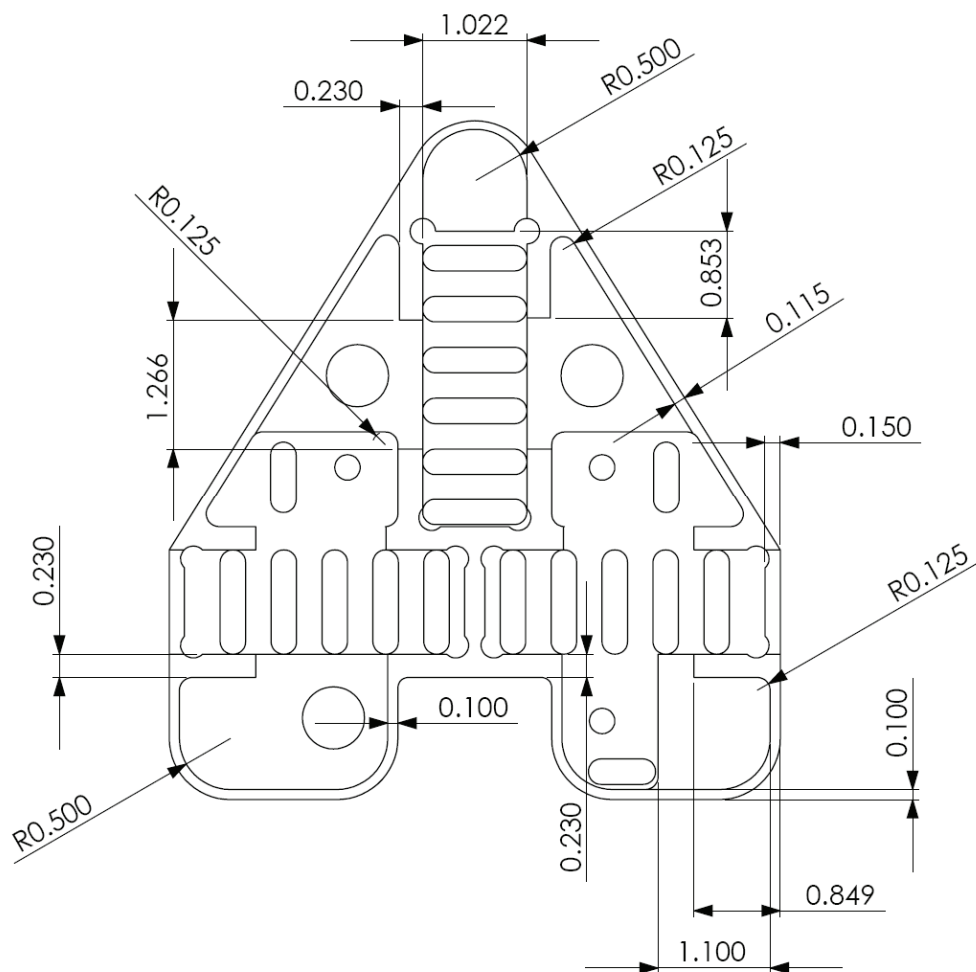
Figure A-3: Bottom view if the pocket 1
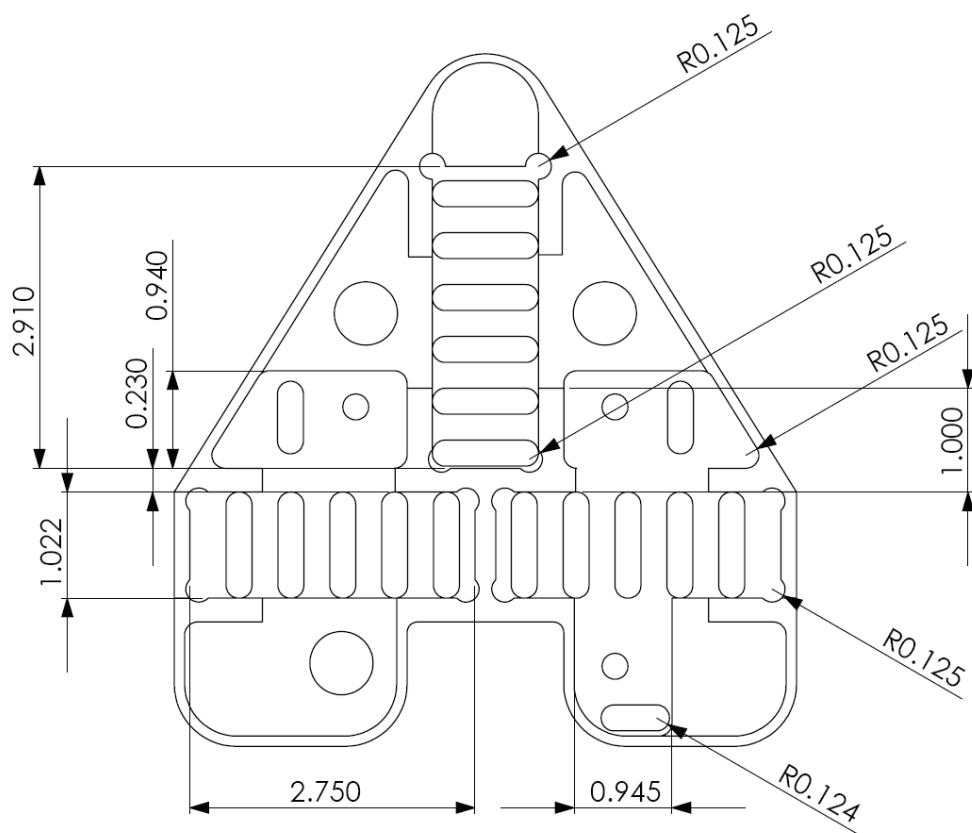
Figure A-4: Bottom view of the pocket 2
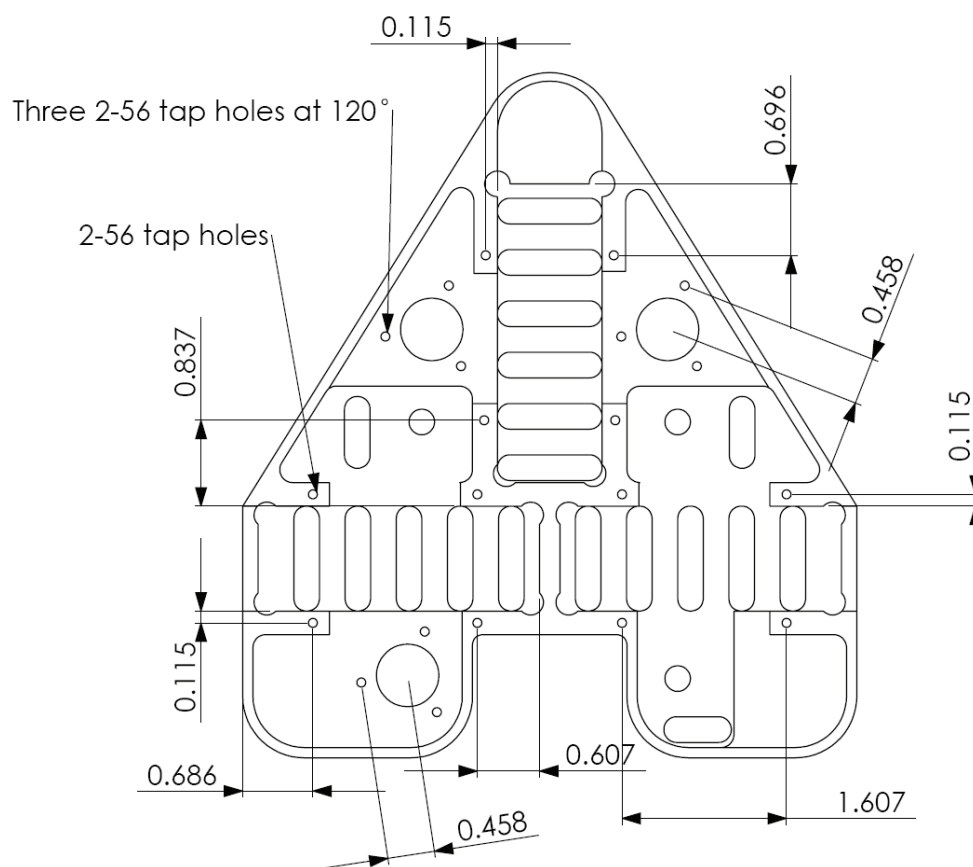
Figure A-5: Bottom view of the drillings and tappings
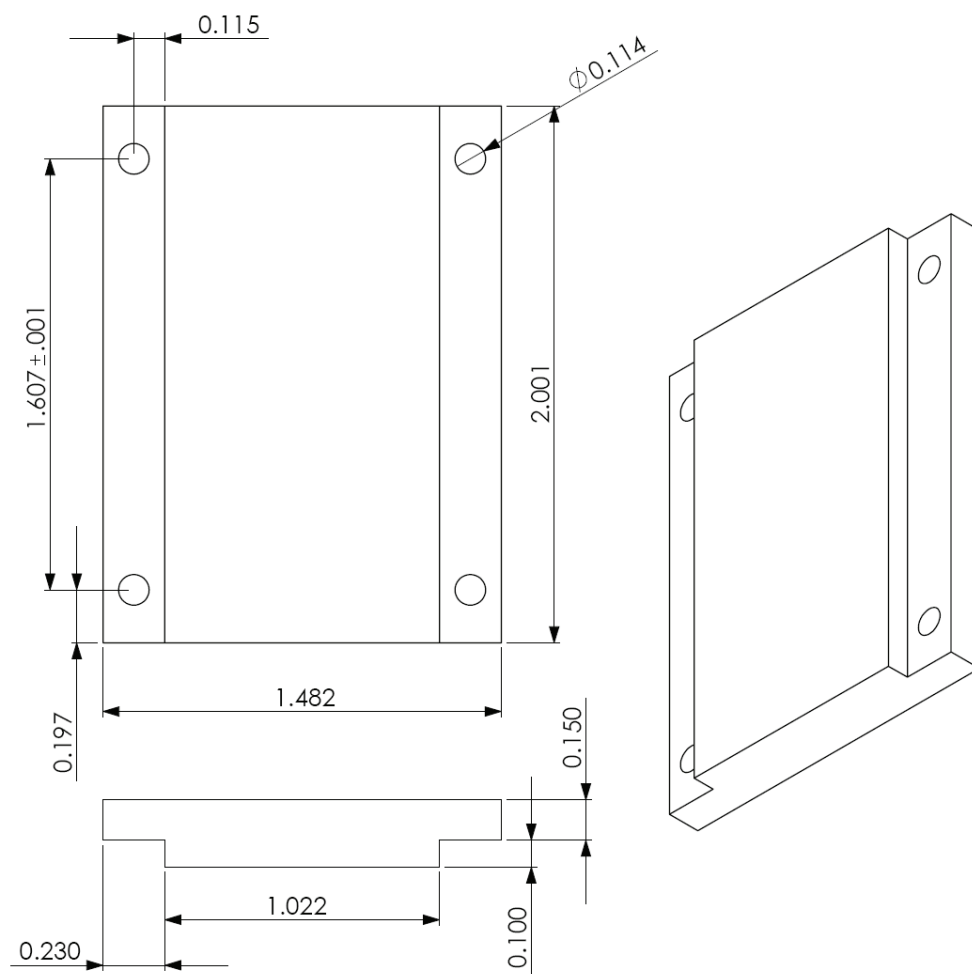
Figure A-6: Schematic view of the winding mount
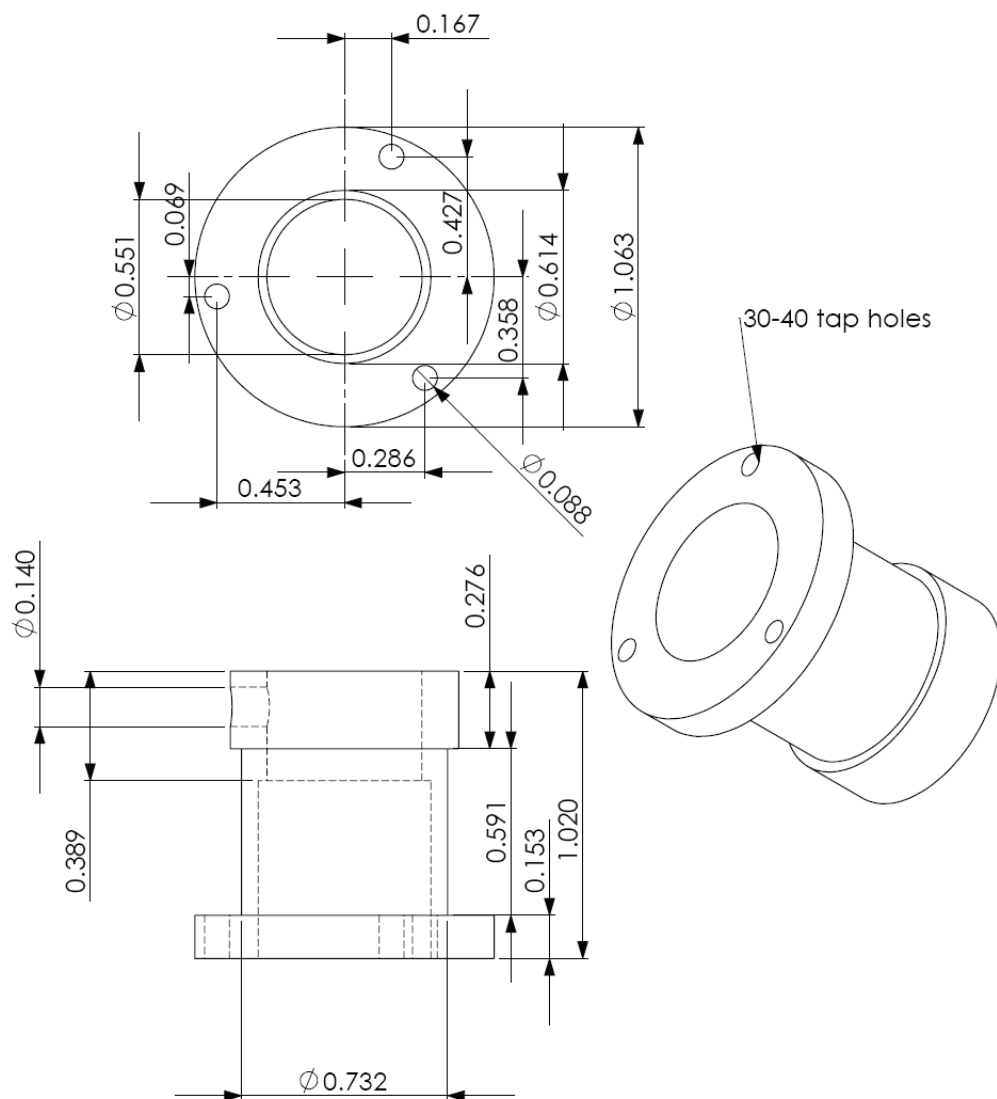
Figure A-7: Schematic view of the bottom mount for Nanogage 100
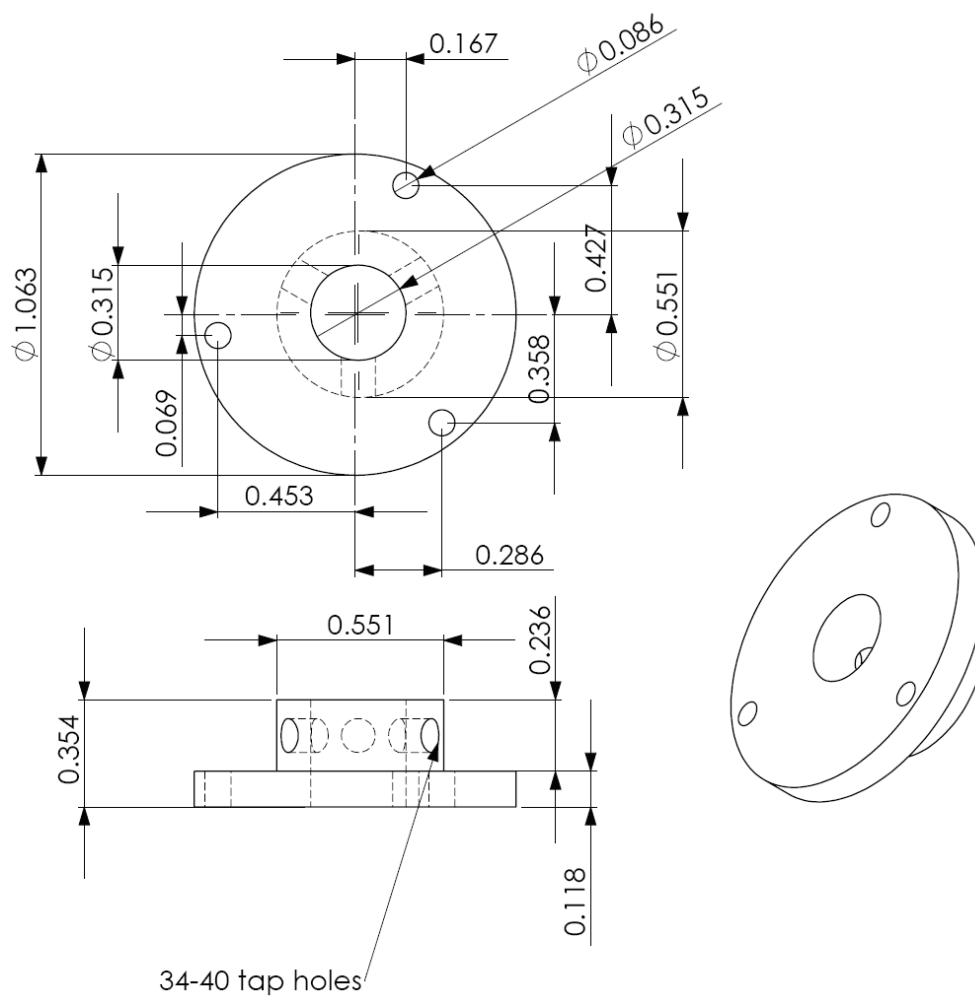
Figure A-8: Schematic view of the top mount for Nanogage 100

0.188

ϕ0.118

ϕ0.945

ϕ0.567

ϕ0.500

0.325

0.325

0.375

0.188

1.122

0.218

0.904

0.200
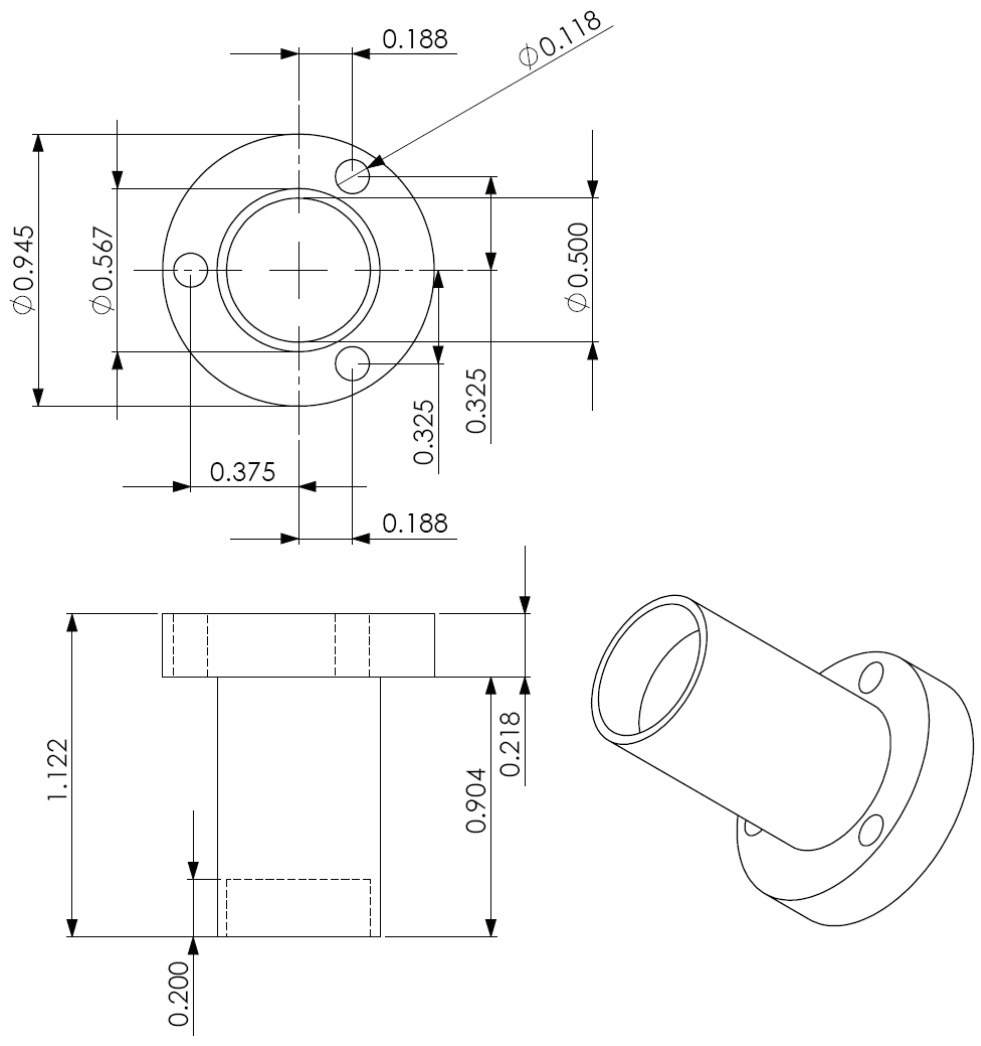
Figure A-9: Schematic view of the aerostatic bearing mount
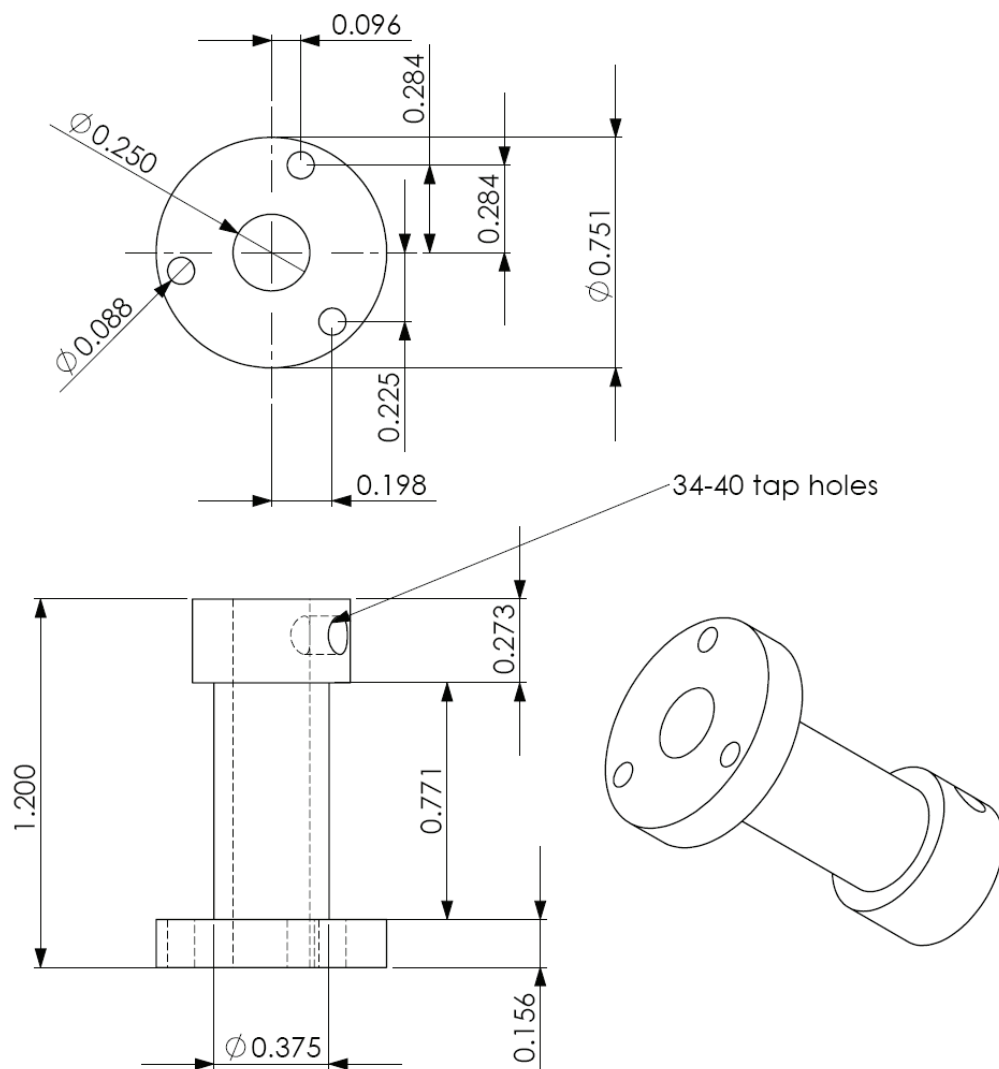
Figure A-10: Schematic view of the Hall-effect sensor mount
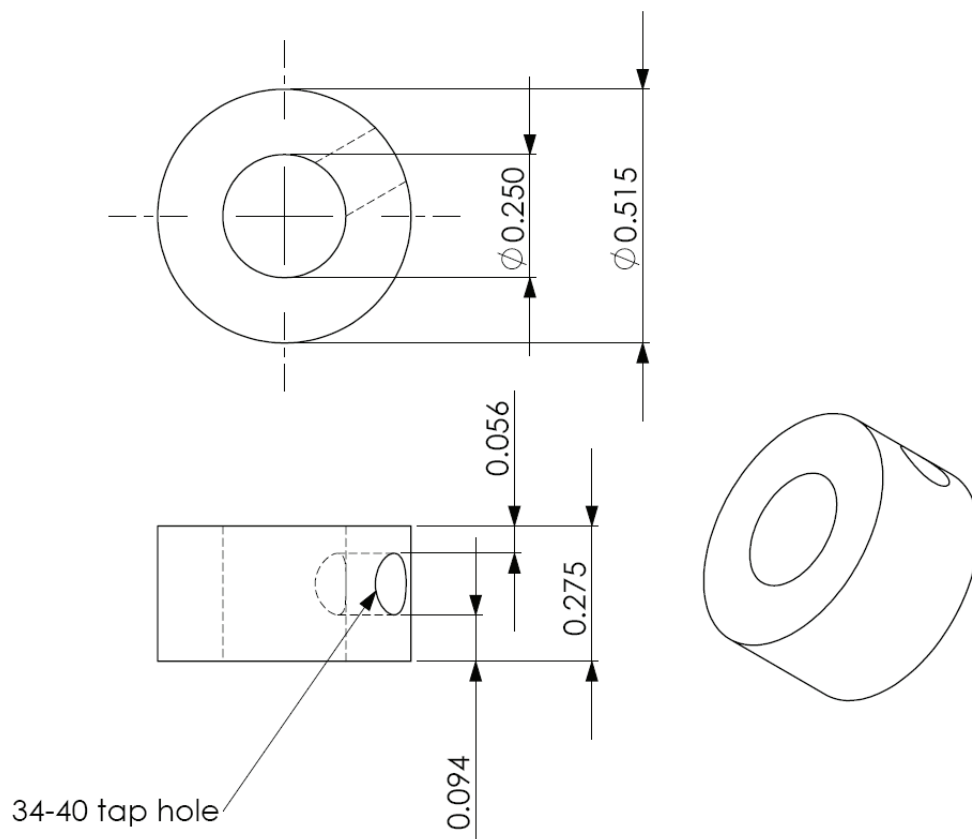
Figure A-11: Schematic view of the Hall-effect sensor mount 2

APPENDIX B

REAL-TIME CONTROL CODES

DIGITAL LEAD-LAG CONTROLLER

```c
#include <stdio.h>
#include <stdlib.h>
#include <unistd.h>
#include <signal.h>
#include <string.h>
#include <asm/errno.h>
#include <sys/types.h>
#include <sys/user.h>
#include <sys/mman.h>
#include <sys/stat.h>
#include <fcntl.h>
//#include <comedilib.h>
#include "/home/comedilib-0.8.0/comedilib/include/comedilib.h"
#include "hall1.h"

#include <rtai_sem.h>
#include <rtai_usi.h>
#include <rtai_lxrt.h>

#define MAX_BANDWIDTH 333000
#define DFLT_FREQUENCY 1000

//Functions
void GLSDC_2(void);
void GLSDC_3(void);
void sensor_test(void);
void EKF_2(void);
```

```
comedi_t *it;
comedi_t *it2;
int in_subdev = 0; //0 is AIO
int out_subdev = 0;
int sigtest = 0;

int in_chan_1 = 0; //Vertical senfor (NANOGAGE100)
int in_chan_2 = 1;
int in_chan_3 = 2;
int in_chan_4 = 3; //A1 Hall-effect sensor
int in_chan_5 = 5; //A2
int in_chan_6 = 6; //B1
int in_chan_7 = 7; //B2
int in_chan_8 = 8; //C1_x
int in_chan_9 = 9; //C2_y

int out_chan_1 = 9; //A
int out_chan_2 = 10;
int out_chan_3 = 11;
int out_chan_4 = 6; //B
int out_chan_5 = 7;
int out_chan_6 = 8;
int out_chan_7 = 3; //C
int out_chan_8 = 4;
int out_chan_9 = 5;

// DIO test
int out_chan_10 = 0;

int in_range = 0;
```

```
int out_range = 0;
int aref = AREF_GROUND;

int i=0;
int j=0,p=0,k=0;
float m1=0,m2=0,m3=0,m4=0,m5=0,m6=0,m7=0,m8=0,m9=0;
char h=0,y=0;
char q;

//rtai declarations
unsigned long mtsk_name;
RT_TASK *mtsk;
struct sched_param mysched;

//comedi declarations
lsampl_t in_data_1;
lsampl_t in_data_2;
lsampl_t in_data_3;
lsampl_t in_data_4; //Hall-effect sensor inputs
lsampl_t in_data_5;
lsampl_t in_data_6;
lsampl_t in_data_7;
lsampl_t in_data_8;
lsampl_t in_data_9;

lsampl_t out_data_1;
lsampl_t out_data_2;
lsampl_t out_data_3;
lsampl_t out_data_4;
lsampl_t out_data_5;
lsampl_t out_data_6;
```

```
lsampl_t out_data_7;

lsampl_t out_data_8;

lsampl_t out_data_9;

lsampl_t out_data_10;


int t=0,zc_lev=0,sc_ang=0,tc_ang=0;

float z_pos1=0, z_pos2=0, z_pos3=0,z1,z2,z3,z_pos10=0,z_pos20=0,z_pos30=0;

float i_Aa,i_Ab,i_Ba,i_Bb,i_Ca,i_Cb,i_Aq,i_Bq,i_Cq,i_Ad,i_Bd,i_Cd;

float xr=0,xr1=0,yr=0,xc=0,yc=0,rr=0,rc=0,f21h=0.04963;

float fA=0,fB=0,fC=0,fZA=0,fZB=0,fZC=0;

float sr=0,tr=0,zc=0,sc=0,tc=0,zr=0,zr10=0,zr_vol=0, izc;

float Ct,St,ho=0,yi,xi,XR,YR,cos_x,cos_y,sin_x,sin_y;

float xA_pos,xB_pos,xB_pos_cal,yA_pos,yB_pos, xrpre=0, yrpre=0, xA_after,xB_after,

delta_x,xC_pos,yC_pos;

float delta_xA, delta_xB, xA_pre, xB_pre, xc1=0,yc1=0,xc2=0,yc2=0;

float va1e=0,va2e=0;


// CALIBRATION FACTORS

float ya1,xa1,yb1,xb1;

float kya= 0.553;

float yaoffset = -0.04;

float kyb = 1.07;

float yboffset = 0.1;

float kxa = 0.54;

float xaoffset = 0.02;

float kxb = 0.55;

float xboffset = 0.095;

float kyc=0.54;

float ycoffset=-0.07;

float kxc=0.54;

float xcoffset=-0.015;
```

```
float z0er=0, z0cer=0, z1cer=0, z0r=0, z1r=0, z0cr=0, z1cr=0;
float er0z=0,er0s=0,er0t=0,u0z=0,
u0s=0,u1s=0,u2s=0,u0t=0,u1t=0,u2t=0,u1z=0,u2z=0,er1z=0,er2z=0;
float
er0x=0,er1x=0,er2x=0,er0y=0,er1y=0,er2y=0,er0r=0,er1r=0,er2r=0,er1t=0,er2t=0,er1s=0
,er2s=0;
float u0x=0,u1x=0,u2x=0,u0y=0,u1y=0,u2y=0,u0r=0,u1r=0,u2r=0;
float stepsize=0,step=0, ux,uy,ur;

float current_A_1 = 0.0, current_A_2 = 0.0, current_A_3 = 0.0;
float current_B_1 = 0.0, current_B_2 = 0.0, current_B_3 = 0.0;
float current_C_1 = 0.0, current_C_2 = 0.0, current_C_3 = 0.0;

int in_maxdata = 0, out_maxdata = 0;
comedi_range *in_range_ptr, *out_range_ptr;

void solve(void);        //* For calculation of control input
void result(void);       //* For Book keeping
void terminate_normally(int signo);

int main(int argc, char* argv[])
{
        FILE *fp1 = NULL; //DATA SAVE
        FILE *fp2 = NULL;
        FILE *fp3 = NULL;
        FILE *fp4 = NULL;
        FILE *fp5 = NULL;
        FILE *fp6 = NULL;
        RTIME start_time = 0;
        RTIME end_time = 0;
```

```
RTIME actual_period = 0;
RTIME difference = 0;

//signal handling
struct sigaction sa;

mtsk_name = nam2num("MTSK");

//Initialize the signal handling structure
sa.sa_handler = terminate_normally;
sa.sa_flags = 0;
sigemptyset(&sa.sa_mask);

if(sigaction(SIGINT, &sa, NULL))
{
        perror("sigaction");
}
if(sigaction(SIGTERM, &sa, NULL))
{
        perror("sigaction");
}

fp1 = fopen("result1.txt", "w"); //*xls -> txt
fp2 = fopen("result2.txt", "w");
fp3 = fopen("result3.txt", "w");
fp4 = fopen("result4.txt", "w");
fp5 = fopen("result5.txt", "w");
fp6 = fopen("result6.txt", "w");
if(fp1 == NULL)
{
        printf("Error opening result1.txt file\n");
```

```c
        exit(1);
    }


    fp1 = fopen("result1.txt", "w");
    if(fp1 == NULL)
    {
            printf("Error opening result1.txt file\n");
            exit(1);
    }
if(fp2 == NULL)
{
    printf("Error opening result2.txt file\n");
    exit(1);
}


fp2 = fopen("result2.txt", "w");
if(fp2 == NULL)
{
    printf("Error opening result2.txt file\n");
    exit(1);
}
if(fp3 == NULL)
{
    printf("Error opening result3.txt file\n");
    exit(1);
}


fp3 = fopen("result3.txt", "w");
if(fp3 == NULL)
{
    printf("Error opening result3.txt file\n");
```

```c
        exit(1);
   }
   if(fp4 == NULL)
   {
           printf("Error opening result4.txt file\n");
           exit(1);
   }
   fp4 = fopen("result4.txt", "w");
   if(fp4 == NULL)
   {
           printf("Error opening result4.txt file\n");
           exit(1);
   }
if(fp5 == NULL)
{
     printf("Error opening result5.txt file\n");
     exit(1);
}
fp5 = fopen("result5.txt", "w");
if(fp5 == NULL)
{
     printf("Error opening result5.txt file\n");
     exit(1);
}
if(fp6 == NULL)
{
     printf("Error opening result6.txt file\n");
     exit(1);
}
fp6 = fopen("result6.txt", "w");
if(fp6 == NULL)
```

```
{
        printf("Error opening result6.txt file\n");
        exit(1);
}


    it = comedi_open("/dev/comedi1");
    it2 = comedi_open("/dev/comedi0");
    if(it == NULL)
    {
        printf("Could not open comedi\n");
        exit(1);
    }
    if(it2 == NULL)
    {
        printf("Could not open comedi\n");
        exit(1);
    }

    in_maxdata = comedi_get_maxdata(it, in_subdev, in_chan_1);
    in_maxdata = comedi_get_maxdata(it, in_subdev, in_chan_2);
    in_maxdata = comedi_get_maxdata(it, in_subdev, in_chan_3);
    in_maxdata = comedi_get_maxdata(it, in_subdev, in_chan_4);
    in_maxdata = comedi_get_maxdata(it, in_subdev, in_chan_5);
    in_maxdata = comedi_get_maxdata(it, in_subdev, in_chan_6);
    in_maxdata = comedi_get_maxdata(it, in_subdev, in_chan_7);
    in_maxdata = comedi_get_maxdata(it, in_subdev, in_chan_8);
    in_maxdata = comedi_get_maxdata(it, in_subdev, in_chan_9);

    out_maxdata = comedi_get_maxdata(it2, out_subdev, out_chan_1);
    out_maxdata = comedi_get_maxdata(it2, out_subdev, out_chan_2);
    out_maxdata = comedi_get_maxdata(it2, out_subdev, out_chan_3);
```

```
        out_maxdata = comedi_get_maxdata(it2, out_subdev, out_chan_4);
        out_maxdata = comedi_get_maxdata(it2, out_subdev, out_chan_5);
        out_maxdata = comedi_get_maxdata(it2, out_subdev, out_chan_6);
        out_maxdata = comedi_get_maxdata(it2, out_subdev, out_chan_7);
        out_maxdata = comedi_get_maxdata(it2, out_subdev, out_chan_8);
        out_maxdata = comedi_get_maxdata(it2, out_subdev, out_chan_9);
        //out_maxdata = comedi_get_maxdata(it2, out_subdev, out_chan_10);

        in_range_ptr = comedi_get_range(it, in_subdev, in_chan_1, in_range);
        in_range_ptr = comedi_get_range(it, in_subdev, in_chan_2, in_range);
        in_range_ptr = comedi_get_range(it, in_subdev, in_chan_3, in_range);
        in_range_ptr = comedi_get_range(it, in_subdev, in_chan_4, in_range);
        in_range_ptr = comedi_get_range(it, in_subdev, in_chan_5, in_range);
        in_range_ptr = comedi_get_range(it, in_subdev, in_chan_6, in_range);
        in_range_ptr = comedi_get_range(it, in_subdev, in_chan_7, in_range);
        in_range_ptr = comedi_get_range(it, in_subdev, in_chan_8, in_range);
        in_range_ptr = comedi_get_range(it, in_subdev, in_chan_9, in_range);

        out_range_ptr = comedi_get_range(it2, out_subdev, out_chan_1, out_range);
        out_range_ptr = comedi_get_range(it2, out_subdev, out_chan_2, out_range);
        out_range_ptr = comedi_get_range(it2, out_subdev, out_chan_3, out_range);
        out_range_ptr = comedi_get_range(it2, out_subdev, out_chan_4, out_range);
        out_range_ptr = comedi_get_range(it2, out_subdev, out_chan_5, out_range);
        out_range_ptr = comedi_get_range(it2, out_subdev, out_chan_6, out_range);
        out_range_ptr = comedi_get_range(it2, out_subdev, out_chan_7, out_range);
        out_range_ptr = comedi_get_range(it2, out_subdev, out_chan_8, out_range);
        out_range_ptr = comedi_get_range(it2, out_subdev, out_chan_9, out_range);
        //out_range_ptr = comedi_get_range(it2, out_subdev, out_chan_10, out_range);
begin:
    printf("Choose your demo (a,b,c,s(NanoGage),n(Exit))\n");
    scanf("%c",&h);
```

```
t=0.0; XR=0; YR=0;
yc=0; yr=0;yi=0; xi=0; ux=0; uy=0; ur=0;
u0z=0; u1z=0; u2z=0; er0z=0; er1z=0; er2z=0;
u0x=0; u1x=0; u2x=0; er0x=0; er1x=0; er2x=0;
u0y=0; u1y=0; u2y=0; er0y=0; er1y=0; er2y=0;
u0r=0; u1r=0; u2r=0; er0r=0; er1r=0; er2r=0;
u0s=0; u1s=0; u2s=0; er0s=0; er1s=0; er2s=0;
u0t=0; u1t=0; u2t=0; er0t=0; er1t=0; er2t=0;
cos_x=0; cos_y=0; sin_x=0; sin_y=0;


mysched.sched_priority = 99;


if( sched_setscheduler(0, SCHED_FIFO, &mysched ) == -1){
puts( "ERROR IN SETTING THE SCHEDULER UP");
perror( "error" );
exit( 0 );
}


mlockall(MCL_CURRENT | MCL_FUTURE);


if (!(mtsk = rt_task_init(mtsk_name, 0, 0, 0))){
        printf("CANNOTINIT MASTER TASK\n");
        exit(1);
}


//start_time = rt_get_cpu_time_ns();
//printf("start_time = %lld\n",start_time);
printf("MASTER TASK STARTS THE ONESHOT TIMER\n");


actual_period = start_rt_timer(nano2count(10000));
```

```
        printf("actual_period = %lld\n", actual_period);

        rt_make_soft_real_time();
        printf("MASTER TASK MAKES ITSELF PERIODIC \n");

        rt_task_make_periodic(mtsk, rt_get_time()+ nano2count(3000),
nano2count(1250000));

        if(h=='a')
        {
                /*printf("Levitation height(10 ~ 90) = ");
                scanf("%d",&zc_lev);
                printf("x-rotation = ");
                scanf("%d",&sc_ang);
                printf("y-rotation = ");
                scanf("%d",&tc_ang);*/

//==   DEMO(a) =====================================================
        while(1)
        {
                sigtest = 0;
                //printf("%d\n", sigtest);
                start_time = rt_get_cpu_time_ns();

                m1=comedi_data_read(it,in_subdev,in_chan_1,in_range,aref,&in_data_1);
                m2=comedi_data_read(it,in_subdev,in_chan_2,in_range,aref,&in_data_2);
                m3=comedi_data_read(it,in_subdev,in_chan_3,in_range,aref,&in_data_3);

        //Hall-effect sensors
                m4=comedi_data_read(it,in_subdev,in_chan_4,in_range,aref,&in_data_4);
```

```
m5=comedi_data_read(it,in_subdev,in_chan_5,in_range,aref,&in_data_5);
m6=comedi_data_read(it,in_subdev,in_chan_6,in_range,aref,&in_data_6);
m7=comedi_data_read(it,in_subdev,in_chan_7,in_range,aref,&in_data_7);
m8=comedi_data_read(it,in_subdev,in_chan_8,in_range,aref,&in_data_8);
m9=comedi_data_read(it,in_subdev,in_chan_9,in_range,aref,&in_data_9);


z1 = comedi_to_phys(in_data_1, in_range_ptr, in_maxdata);
z_pos1 = 50e-6+z1*1.01833e-5;
z_pos10 = z_pos1;
z_pos1 = z_pos1-z_pos10;
z2 = comedi_to_phys(in_data_2, in_range_ptr, in_maxdata);
z_pos2 = 50e-6+z2*1.01833e-5;
z_pos20 = z_pos2;
z_pos2 = z_pos2-z_pos20;
z3 = comedi_to_phys(in_data_3, in_range_ptr, in_maxdata);
z_pos3 = 50e-6+z3*1.01833e-5;
z_pos30 = z_pos3;
z_pos3 = z_pos3-z_pos30;

//Hall-effect sensors data
        va1 = comedi_to_phys(in_data_4, in_range_ptr, in_maxdata);
        vb1 = comedi_to_phys(in_data_5, in_range_ptr, in_maxdata);
        vc1 = comedi_to_phys(in_data_6, in_range_ptr, in_maxdata);
        vd2 = comedi_to_phys(in_data_7, in_range_ptr, in_maxdata);
        va2 = comedi_to_phys(in_data_9, in_range_ptr, in_maxdata);
        vb2 = comedi_to_phys(in_data_8, in_range_ptr, in_maxdata);

        EKF_2();

        ya1 = kya*va1e + yaoffset;
        xa1 = kxa*vb1 + xaoffset;
```

```
        yb1 = kyb*vc1 + yboffset;

        xb1 = kxb*vd2 + xboffset;

        yc1 = kyc*va2e + ycoffset;

        xc1 = kxc*vb2 + xcoffset;


        zr = 0.527327*z_pos1+0.042158*z_pos2+0.430515*z_pos3;

        zr10  = 0.527327*z_pos10+0.042158*z_pos20+0.430515*z_pos30;

        //zr = 0.527327*z1+0.042158*z2+0.430515*z3;

        //sr = -1.16606*z_pos1+12.7953*z_pos2-11.6294*z_pos3;

        //tr = 16.852*z_pos1-16.852*z_pos2;


//***** DEMOS *****
        /*zc = zc_lev*0.000001;

        sc = sc_ang*0.000001;

        tc = tc_ang*0.000001;*/


        /*if(t<500)

        {zc=0.000020;}

        if(t<4000)

        { zc+=4e-9;}*/


        //step += 5e-4;

        //zc=0.000100*sin(step);
//OPEN LOOP TEST X
        /*if(t>10 && t<2000){

                yc=0.00786;

                xr=0.00002;

                rc=0.000006;}

        else if(t>=2000 && t<9990){

                yc=0.00786;

                xr-=0.000025;
```

```
                rc=0.000006;}*/
//OPEN LOOP TEST Y
        /*if(t>10 && t<2000){
                yr=0.00002;
                xc=0.001;
                rc=0.058;}
          else if(t>=2000 && t<9990){
                yr+=0.00002;
                xc=0.001;
                rc=0.058;}*/


//CASE 1 STEP MOTION
        /*if(t>10 && t<2000){
                yc=0.00786;
                xr=0.00002;
                rc=-0.0137;
        }
        if(t>=2001 && t<9990){
                xr+=0.000025;
                yc=0.00786;
                rc=-0.0137;
        }
        else if(8001<=t && t<=9990){
                xr+=0.000025;
                yc=0.00786;
                rc=-0.0137;
        }*/
//CASE 2 STEP AND REPEAT
        /*if(t>1 && t<3000){
                xc = 0.001; yc = 0.00786; rc = -0.0137;
                }
```

```
                else if(t>=3000 && t<4000){
                        xc = 0.0011; yc = 0.00786; rc = -0.0137;
                        }
                else if(t>=4000 && t<5000){
                        xc = 0.0012; yc = 0.00786; rc = -0.0137;
                        }
                else if(t>=5000 && t<6000){
                        xc = 0.0013; yc = 0.00786; rc = -0.0137;
                        }
                else if(t>=6000 && t<7000){
                        xc = 0.0014; yc = 0.00786; rc = -0.0137;
                        }
                else if(t>=7000 && t<8000){
                        xc = 0.0015; yc = 0.00786; rc = -0.0137;
                        }
                else if(t>=8000 && t<9000){
                        xc = 0.0016; yc = 0.00786; rc = -0.0137;
                        }
                else if(t>=9000 && t<9990){
                        xc = 0.0017; yc = 0.00786; rc = -0.0137;
                        }*/
// Y STEPS
    /*if(t>1 && t<3000){
        xc = 0.001; yc = 0.001; rc = 0.000006;
        }
    else if(t>=3000 && t<4000){
        xc = 0.001; yc = 0.00121; rc = 0.000006;
        }
    else if(t>=4000 && t<5000){
        xc = 0.001; yc = 0.00142; rc = 0.000006;
        }
```

```
else if(t>=5000 && t<6000){

    xc = 0.001; yc = 0.00163; rc = 0.000006;

    }
else if(t>=6000 && t<7000){

    xc = 0.001; yc = 0.00104; rc = 0.000006;

    }
else if(t>=7000 && t<8000){

    xc = 0.001; yc = 0.00105; rc = 0.000006;

    }
else if(t>=8000 && t<9000){

    xc = 0.001; yc = 0.00106; rc = 0.000006;

    }
else if(t>=9000 && t<9990){

    xc = 0.001; yc = 0.00107; rc = 0.000006;

    }
    */


//SLOW STEPS BACK AND FORTH
    /*if(t>1 && t<3000){xc = 0.001; yc = 0.00002; rc = -0.0137;}
    else if(t>=3000 && t<6000){xc+= 0.000008; yc = 0.00002; rc =
0.000006;}
    else if(t>=6000 && t<9990){xc+= 0.000008; yc = 0.00002; rc =
0.000006;}*/


    /*if(t>1 && t<3000){xc = 0.001; yc = 0.00002; rc = 0.000006;}
    else if(t>=3000 && t<6000){xc= 0.001; yc-= 0.0000029; rc = 0.000006;}
    else if(t>=6000 && t<9990){xc= 0.001; yc+= 0.0000029; rc = 0.000006;}*/


// ANGULAR TEST
    /*if(t>1 && t<3000){xc = 0.001; yc = 0.00002; rc = 0.000001;} //20000
iterations
```

```
else if(t>=3000 && t<6000){xc= 0.001; yc= 0.00002; rc+= 0.00003;}
else if(t>=6000 && t<12000){xc= 0.001; yc= 0.00002; rc-= 0.00003;}
    else if(t>=12000 && t<18000){xc = 0.001; yc=0.00002; rc+= 0.00003;}
    else if(t>=18000 && t<19990){xc = 0.001; yc=0.00002; rc-= 0.00003;}
    */
/*if(t>1 && t<3000){xc = 0.001; yc = 0.00002; rc = 0.000001;} //20000
iterations
    else if(t>=3000 && t<4000){xc= 0.001; yc= 0.00002; rc= 0.01/66.1;}
    else if(t>=4000 && t<5000){xc= 0.001; yc= 0.00002; rc= 0.02/66.1;}
    else if(t>=5000 && t<6000){xc = 0.001; yc=0.00002; rc= 0.03/66.1;}
    else if(t>=6000 && t<7000){xc = 0.001; yc=0.00002; rc= 0.04/66.1;}
    else if(t>=7000 && t<8000){xc = 0.001; yc=0.00002; rc= 0.05/66.1;}
    else if(t>=8000 && t<9000){xc = 0.001; yc=0.00002; rc= 0.06/66.1;}
    else if(t>=9000 && t<9990){xc = 0.001; yc=0.00002; rc= 0.07/66.1;}*/


    //PLANAR MOTION-BACK AND FORCE 8mm2mm zigzag
    /*if(t>1 && t<3000){xc = 0.00001; yc = 0.00002; rc = 0.000001;} //20000
iterations
    else if(t>=3000 && t<4000){xc-= 0.000004;} // x-left 4 mm
    else if(t>=4000 && t<5000){yc+=0.000004;} // y-up 4 mm
    else if(t>=5000 && t<6000){xc+=0.000002;} // x-right 2 mm
        else if(t>=6000 && t<8000){yc-=0.000004;} // y-down 8 mm
        else if(t>=8000 && t<9000){xc+=0.000002;} // x-right 2 mm
        else if(t>=9000 && t<11000){yc+=0.000004;} // y-up 8 mm
        else if(t>=11000 && t<12000){xc+=0.000002;} // x-right 2 mm
        else if(t>=12000 && t<14000){yc-=0.000004;} // y-down 8 mm
        else if(t>=14000 && t<15000){xc+=0.000002;} // x-right 2 mm
        else if(t>=15000 && t<16000){yc+=0.000004;} // y-up 4 mm
        else if(t>=16000 && t<18000){xc-=0.000002;} // x-left 4 mm*/


    // 16mm2mm zigzag
```

```
/*if(t>1 && t<3000){xc = 0.000001; yc = 0.00002; rc = 0.000001;} //20000
iterations
        else if(t>=3000 && t<5000){xc-= 0.000004;} // x-left 8 mm
        else if(t>=5000 && t<7000){yc+=0.000004;} // y-up 8 mm
        else if(t>=7000 && t<7500){xc+=0.000004;} // x-right 2 mm
        else if(t>=7500 && t<11500){yc-=0.000004;} // y-down 16 mm
        else if(t>=11500 && t<12000){xc+=0.000004;} // x-right 2 mm
        else if(t>=12000 && t<16000){yc+=0.000004;} // y-up 16 mm
        else if(t>=16000 && t<16500){xc+=0.000004;} // x-right 2 mm
        else if(t>=16500 && t<20500){yc-=0.000004;} // y-down 16 mm
        else if(t>=20500 && t<21000){xc+=0.000004;} // x-right 2 mm
        else if(t>=21000 && t<25000){yc+=0.000004;} // y-up 16 mm
        else if(t>=25000 && t<25500){xc+=0.000004;} // x-right 2 mm
            else if(t>=25500 && t<29500){yc-=0.000004;} // y-down 16 mm
            else if(t>=29500 && t<30000){xc+=0.000004;} // x-right 2mm
            else if(t>=30000 && t<34000){yc+=0.000004;} // y-up 16 mm
            else if(t>=34000 && t<34500){xc+=0.000004;} //x-right 2 mm
            else if(t>=34500 && t<36500){yc-=0.000004;} // y-down 8 mm
            //else if(t>=35000 && t<35500){xc+=0.000004;} // x-right 2 mm
            //else if(t>=35500 && t<37500){yc+=0.000004;} // y-up 8 mm
            else if(t>=36500 && t<38500){xc-=0.000004;} // x-left 8 mm*/


        //else if(t>=7000 && t<8000){xc = 0.001; yc=0.00002; rc= 0.000001;}
        //else if(t>=8000 && t<9000){xc = 0.001; yc=0.00002; rc= 0.000001;}
        //else if(t>=9000 && t<9990){xc = 0.001; yc=0.00002; rc= 0.000001;}


    //CIRCULAR MOTION
        /*if(t>1 && t<3000){xc = 0.001; yc=0.00002; rc= 0.000006;}
        else if(t>=3000 && t<9990){step+=1e-5; rc = 0.000006;
            xc2 = 1e-4*(1-cos(0.00001*t)); xc=xc+xc2;
            yc2 = 1e-4*sin(0.00001*t); yc=yc+yc2;}*/
```

```
/*if(t>1 && t<3000){xc = 0.001; yc=0.00002; rc= 0.000006;}
else if(t>=3000 && t<9990){step+=1e-5; rc = 0.000006;
    xc = 0.001+ 1e-2*(1-cos(step));
    yc = 0.00002+ 1e-2*sin(step); }*/


    if(t%2 == 0)
    {ho = 1;}
    else if(t%2 == 1)
    {ho=0;}
    t++;
            //printf("%f\n",u0y);


            fprintf(fp1, "%f\n",rr);
            fprintf(fp2, "%f\n",xr);
            fprintf(fp3, "%f\n",yr);
            fprintf(fp4, "%f\n",vb1);
            fprintf(fp5, "%f\n",vb2);
            fprintf(fp6, "%f\n",ya1-yc1);


    xA_pos=(1/123.25)*asin((1/1)*xa1);
    xB_pos=(1/123.25)*asin((1/1)*xb1);
    xB_pos_cal=(1/123.25)*asin((1/1)*xb1+0.012745);

yA_pos=(1/123.25)*asin((1/1)*ya1);
yB_pos=(1/123.25)*asin((1/1)*yb1);


    xC_pos=(1/123.25)*asin((1/1)*xc1);
    yC_pos=(1/123.25)*asin((1/1)*yc1);
```

```
//x- extended motion CASE I
        /*if (xa1>0 && xb1>=0 && -0.02649<=xrpre<-0.012745){
        xr = -xA_pos-(0.050979);}  // IV
        else if(xa1<0 && xb1<=0){    // II
        xr = xA_pos;
        }
        else if(xa1>=0 && xb1<0){   // III original point
        xr = xA_pos;
        }
        else if(xa1>0 && xb1>=0){   // IV
        xr = -xA_pos+(0.050979/2);
        }
        else if(xa1<=0 && xb1>0){   // I
        xr = -(0.050979/2)-xA_pos;
        }
        else if(xa1<=0 && xb1>0 && 0.012745<xrpre<=0.02649){
        xr = -xA_pos+(0.050979);} // I*/


// x- extended motion CASE II
        /*if(xa1<=0 && xb1>0 && -xa1>xb1){ xr=-xB_pos-0.012745;} //I-2
        else if(xa1<0 && xb1<=0 && xa1<=xb1){ xr=-xB_pos-0.006373-0.007;}
//II-1
        else if(xa1<0 && xb1<=0 && xa1>xb1){ xr = xA_pos; } // II-2
        else if(xa1>=0 && xb1<0 && -xa1<=xb1){ xr=xA_pos; } // III - 1
        else if(xa1>=0 && xb1<0 && xa1>xb1){ xr=xB_pos+0.0115; } // III - 2
        else if(xa1>0 && xb1<0 && xa1>=xb1){ xr=xB_pos + 0.012745; } // IV
- 1
        else if(xa1>0 && xb1<0 && xa1<xb1){ xr=-xA_pos + 0.019118; } // IV -
2
        else if(xa1<=0 && xb1>0 && -xa1<=xb1){ xr=-xA_pos + 0.019118; } //
I-1
```

```
else if(xa1<=0 && xb1>1 && -xa1>xb1){xr=-xB_pos + 0.02549;} // I-
2*/


/*if(-0.006373<=xr<0.006373){ xr = xA_after; } // wrong data
else if(0.00637<=xr<0.01274){xr = -(xB_after); }
else if(0.01274<=xr<0.02549){ xr = -(xA_after)+0.012745; }
else if(-0.00637>xr || 0.02549<=xr){ xr = xA_after; }*/
// x- extension CASE III


/*delta_xA = xA_after-xA_pre; delta_xB=xB_after-xB_pre;


if(xa1<=0 && xb1>0 && -xa1>xb1){ delta_x=-delta_xB;} //I-2
else if(xa1<0 && xb1<=0 && xa1<=xb1){ delta_x=-delta_xB;} //II-1
else if(xa1<0 && xb1<=0 && xa1>xb1){ delta_x=delta_xA; } // II-2
else if(xa1>=0 && xb1<0 && -xa1<=xb1){ delta_x=delta_xA; } // III - 1
else if(xa1>=0 && xb1<0 && xa1>xb1){ delta_x=delta_xB; } // III - 2
else if(xa1>0 && xb1<0 && xa1>=xb1){ delta_x=delta_xB; } // IV - 1
else if(xa1>0 && xb1<0 && xa1<xb1){ delta_x=-delta_xA; } // IV - 2
else if(xa1<=0 && xb1>0 && -xa1<=xb1){ delta_x=-delta_xA; } // I-1
else if(xa1<=0 && xb1>1 && -xa1>xb1){delta_x=-delta_xB;} // I-2


xr = xr + delta_x;
xrpre = xr; xA_pre=xA_after; xB_pre=xB_after;*/


// Y OPEN LOOP TEST
//xr = xB_after;
xr = xC_pos;
// X OPEN LOOP TEST
yr = yA_pos; // X OPEN LOOP TEST
```

```
//rotation z-angle
        rr = (yA_pos - yC_pos); //X OPEN LOOP gain higher than 25000
        //rr = asin((-xA_pos + xC_pos)/0.0635); // Y OPEN LOOP TEST
        //rr = (ya1 - yc1)/10; //gain 5500,rtest_good


    er0x = xc-xr;
    er0y = yc-yr;
    er0r = rc-rr;
        er0z = zc-zr10;
        er0s = sc-sr;
        er0t = tc-tr;


    // x 10Hz PM70
        //u0x=1;
        //u0x = 100; // open loop test
        //u0x = 1.2423*u1x-0.2423*u2x+1500000*(er0x-
1.9773*er1x+0.977428*er2x);//223623.5534
        u0x = 1.2741*u1x-0.2741*u2x+1500000*(er0x-
        1.8965*er1x+0.977428*er2x);//223623.5534
        //u0x = 1.3217*u1x-0.3217*u2x+2020*(er0x-
1.9605*er1x+0.96083*er2x);
        //u0x = 1.7*u1x-0.700*u2x+2000000*(er0x-
1.98231*er1x+0.982308*er2x); //1kHz
        //u0x = 1.837*u1x-0.8368*u2x+130000*(er0x-1.99*er1x+0.99*er2x);
//2kHz
        //u0x = 1.915*u1x-0.915*u2x+10000*(er0x-
1.99462*er1x+0.994615*er2x); //4kHz
        //u0x = 1.641*u1x-0.6406*u2x+13000*(er0x-
1.97846*er1x+0.978462*er2x); //800
        //u0x = 1.931*u1x-0.9312*u2x+153000*(er0x-
1.99615*er1x+0.996154*er2x);
```

```
// y 10Hz PM70
        //u0y=1;
        //u0y = 1; // open loop test
        //u0y = 1.2423*u1y-0.2423*u2y+1500000*(er0y-
1.9773*er1y+0.977428*er2y);
        u0y = 1.2741*u1y-0.2741*u2y+1500000*(er0y-
        1.8965*er1y+0.977428*er2y);


// rot-z 20Hz PM70
        u0r = 1.2741*u1r-0.2741*u2r+75500*(er0r-1.8965*er1r+0.977428*er2r);


        u0z = 1.274*u1z-0.274*u2z+15000*(er0z-1.896*er1x+0.9898*er2x);
        u0s = 1.274*u1z-0.274*u2z+4600*(er0z-1.896*er1x+0.9898*er2x);
        u0t = 1.274*u1z-0.274*u2z+6700*(er0z-1.896*er1x+0.9898*er2x);


//Moment of inertia
    fA = -0.449613*u0x+0.5*u0y+12.8866*u0r; //-0.449613*u0x; //the moment of
inertia 0.487887
        fB = 0.449613*u0x+0.5*u0y-12.8866*u0r; //0.449613*u0x; //0.512113
    //fA = -0.449613*u0x+0.5*u0y-12.8866*u0r;
        //fB = 0.449613*u0x+0.5*u0y+12.8866*u0r;
        //fA = -0.449613*u0x+0.5*u0y;
        //fB = 0.449613*u0x+0.5*u0y;
        //fA = 0.5*u0y;
        //fB = 0.5*u0y;
        fC = u0x;
// Vertical motion
        fZA = 0.317762*u0z-8.60521*u0s+12.8866*u0t;
        fZB = 0.320548*u0z-9.6897*u0s-12.8866*u0t;
        fZC = 0.36169*u0z+18.2946*u0s;
```

```
i_Ad = fZA*f21h;                        //vertical (DQ Decomposition)
i_Bd = fZB*f21h;
i_Cd = fZC*f21h;


i_Aq = fA*f21h;                         //horizontal
i_Bq = fB*f21h;
i_Cq = fC*f21h;


cos_x=cos(123.25*xr);
cos_y=cos(123.25*yr);
sin_x=sin(123.25*xr);
sin_y=sin(123.25*yr);
//XR = 123.25*xr;
//YR = 123.25*yr;


i_Aa = cos_y*i_Aq-sin_y*i_Ad;  //Current a & b
i_Ba = cos_y*i_Bq-sin_y*i_Bd;
i_Ca = cos_x*i_Cq-sin_x*i_Cd;
i_Ab = sin_y*i_Aq+cos_y*i_Ad;
i_Bb = sin_y*i_Bq+cos_y*i_Bd;
i_Cb = sin_x*i_Cq+cos_x*i_Cd;


if(t>5000)
{
        i_Aa=0; i_Ab=0;
        i_Ba=0; i_Bb=0;
        i_Ca=0; i_Cb=0;
        sigtest = 0;
}
```

```
            current_A_1 = i_Aa;                    //Final coil currents
            current_A_2 = 0.5*i_Aa+0.8660254037844*i_Ab;
            current_A_3 = -0.5*i_Aa+0.8660254037844*i_Ab;
            current_B_1 = i_Ba;
            current_B_2 = 0.5*i_Ba+0.8660254037844*i_Bb;
            current_B_3 = -0.5*i_Ba+0.8660254037844*i_Bb;
            current_C_1 = -i_Ca;
            current_C_2 = -0.5*i_Ca-0.8660254037844*i_Cb;
            current_C_3 = 0.5*i_Ca-0.8660254037844*i_Cb;


            out_data_1 = comedi_from_phys(current_A_1, out_range_ptr,
out_maxdata);
            out_data_2 = comedi_from_phys(current_A_2, out_range_ptr,
out_maxdata);
            out_data_3 = comedi_from_phys(current_A_3, out_range_ptr,
out_maxdata);
            out_data_4 = comedi_from_phys(current_B_1, out_range_ptr,
out_maxdata);
            out_data_5 = comedi_from_phys(current_B_2, out_range_ptr,
out_maxdata);
            out_data_6 = comedi_from_phys(current_B_3, out_range_ptr,
out_maxdata);
            out_data_7 = comedi_from_phys(current_C_1, out_range_ptr,
out_maxdata);
            out_data_8 = comedi_from_phys(current_C_2, out_range_ptr,
out_maxdata);
            out_data_9 = comedi_from_phys(current_C_3, out_range_ptr,
out_maxdata);
            out_data_10= comedi_from_phys(sigtest, out_range_ptr, out_maxdata);
```

```
        comedi_data_write(it2, out_subdev, out_chan_1, out_range, aref,
out_data_1);
        comedi_data_write(it2, out_subdev, out_chan_2, out_range, aref,
out_data_2);
        comedi_data_write(it2, out_subdev, out_chan_3, out_range, aref,
out_data_3);
        comedi_data_write(it2, out_subdev, out_chan_4, out_range, aref,
out_data_4);
        comedi_data_write(it2, out_subdev, out_chan_5, out_range, aref,
out_data_5);
        comedi_data_write(it2, out_subdev, out_chan_6, out_range, aref,
out_data_6);
        comedi_data_write(it2, out_subdev, out_chan_7, out_range, aref,
out_data_7);
        comedi_data_write(it2, out_subdev, out_chan_8, out_range, aref,
out_data_8);
        comedi_data_write(it2, out_subdev, out_chan_9, out_range, aref,
out_data_9);
        comedi_dio_write(it, out_subdev, out_chan_10, sigtest);

        rt_task_wait_period();

        end_time = rt_get_cpu_time_ns();

        if(t>6000)
            break;

        difference = end_time - start_time;
        //printf("%d\n", difference);
        xrpre = xr;
    u2z = u1z; u1z = u0z; er2z = er1z; er1z = er0z;
```

```
        u2s = u1s; u1s = u0s; er2s = er1s; er1s = er0s;

        u2t = u1t; u1t = u0t; er2t = er1t; er1t = er0t;

        u2x = u1x; u1x = u0x; er2x = er1x; er1x = er0x;

        u2y = u1y; u1y = u0y; er2y = er1y; er1y = er0y;

        u2r = u1r; u1r = u0r; er2r = er1r; er1r = er0r;


    } //while loop close
    } // if close


    if(h=='b')
    {
//==  DEMO(b) CALIBRATIONS   X================================
    while(1)
    {
        start_time = rt_get_cpu_time_ns();


        m1=comedi_data_read(it,in_subdev,in_chan_1,in_range,aref,&in_data_1);
        m2=comedi_data_read(it,in_subdev,in_chan_2,in_range,aref,&in_data_2);
        m3=comedi_data_read(it,in_subdev,in_chan_3,in_range,aref,&in_data_3);


//Hall-effect sensors
        m4=comedi_data_read(it,in_subdev,in_chan_4,in_range,aref,&in_data_4);
        m5=comedi_data_read(it,in_subdev,in_chan_5,in_range,aref,&in_data_5);
        m6=comedi_data_read(it,in_subdev,in_chan_6,in_range,aref,&in_data_6);
        m7=comedi_data_read(it,in_subdev,in_chan_7,in_range,aref,&in_data_7);
        m8=comedi_data_read(it,in_subdev,in_chan_8,in_range,aref,&in_data_8);
        m9=comedi_data_read(it,in_subdev,in_chan_9,in_range,aref,&in_data_9);


//Hall-effect sensors data
        va1 = comedi_to_phys(in_data_4, in_range_ptr, in_maxdata);
        vb1 = comedi_to_phys(in_data_5, in_range_ptr, in_maxdata);
```

```
vc1 = comedi_to_phys(in_data_6, in_range_ptr, in_maxdata);
vd2 = comedi_to_phys(in_data_7, in_range_ptr, in_maxdata);
//va2 = comedi_to_phys(in_data_9, in_range_ptr, in_maxdata);
//vb2 = comedi_to_phys(in_data_8, in_range_ptr, in_maxdata);


ya1 = kya*va1 + yaoffset;
xa1 = kxa*vb1 + xaoffset;
yb1 = kyb*vc1 + yboffset;
xb1 = kxb*vd2 + xboffset;


    t++;
    fprintf(fp1, "%f\n", ya1);   // y-a
    fprintf(fp2, "%f\n", yb1);   // x-a
    fprintf(fp3, "%f\n", xa1);   // y-b
    fprintf(fp4, "%f\n", xb1);   // x-b
    //GLSDC_2();
            printf("%f\n", xr);


    if(t>4990)
{
    i_Aa=0; i_Ab=0;
    i_Ba=0; i_Bb=0;
    i_Ca=0; i_Cb=0;
}
        out_data_1 = comedi_from_phys(current_A_1, out_range_ptr,
out_maxdata);
        out_data_2 = comedi_from_phys(current_A_2, out_range_ptr, out_maxdata);
        out_data_3 = comedi_from_phys(current_A_3, out_range_ptr, out_maxdata);
        out_data_4 = comedi_from_phys(current_B_1, out_range_ptr, out_maxdata);
        out_data_5 = comedi_from_phys(current_B_2, out_range_ptr, out_maxdata);
        out_data_6 = comedi_from_phys(current_B_3, out_range_ptr, out_maxdata);
```

```
            out_data_7 = comedi_from_phys(current_C_1, out_range_ptr, out_maxdata);
            out_data_8 = comedi_from_phys(current_C_2, out_range_ptr, out_maxdata);
            out_data_9 = comedi_from_phys(current_C_3, out_range_ptr, out_maxdata);


            comedi_data_write(it2, out_subdev, out_chan_1, out_range, aref, out_data_1);
            comedi_data_write(it2, out_subdev, out_chan_2, out_range, aref, out_data_2);
            comedi_data_write(it2, out_subdev, out_chan_3, out_range, aref, out_data_3);
            comedi_data_write(it2, out_subdev, out_chan_4, out_range, aref, out_data_4);
            comedi_data_write(it2, out_subdev, out_chan_5, out_range, aref, out_data_5);
            comedi_data_write(it2, out_subdev, out_chan_6, out_range, aref, out_data_6);
            comedi_data_write(it2, out_subdev, out_chan_7, out_range, aref, out_data_7);
            comedi_data_write(it2, out_subdev, out_chan_8, out_range, aref, out_data_8);
            comedi_data_write(it2, out_subdev, out_chan_9, out_range, aref, out_data_9);


            rt_task_wait_period();


            end_time = rt_get_cpu_time_ns();


            difference = end_time - start_time;
            if(t>5000)
                break;
        } //while loop close
        } // if close


    else if(h=='s')
    {
            printf("Choose your sensor
(1,2,3,4(together),5(Hall_A),6(Hall_B),7(Hall_C),5(exit))\n");
            scanf("%d",&p);
//==   DEMO(sensor test) WHILE LOOP ===============================
    while(1)
```

```
{
    start_time = rt_get_cpu_time_ns();


    m1=comedi_data_read(it,in_subdev,in_chan_1,in_range,aref,&in_data_1);
    m2=comedi_data_read(it,in_subdev,in_chan_2,in_range,aref,&in_data_2);
    m3=comedi_data_read(it,in_subdev,in_chan_3,in_range,aref,&in_data_3);
//Hall-effect sensors
    m4=comedi_data_read(it,in_subdev,in_chan_4,in_range,aref,&in_data_4);
    m5=comedi_data_read(it,in_subdev,in_chan_5,in_range,aref,&in_data_5);
    m6=comedi_data_read(it,in_subdev,in_chan_6,in_range,aref,&in_data_6);
    m7=comedi_data_read(it,in_subdev,in_chan_7,in_range,aref,&in_data_7);
    m8=comedi_data_read(it,in_subdev,in_chan_8,in_range,aref,&in_data_8);
    m9=comedi_data_read(it,in_subdev,in_chan_9,in_range,aref,&in_data_9);


    z1 = comedi_to_phys(in_data_1, in_range_ptr, in_maxdata);
    z_pos1 = 50e-6+z1*1.01833e-5;
    z_pos10 = z_pos1;
    z_pos1 = z_pos1-z_pos10;
    z2 = comedi_to_phys(in_data_2, in_range_ptr, in_maxdata);
    z_pos2 = 50e-6+z2*1.01833e-5;
    z_pos20 = z_pos2;
    z_pos2 = z_pos2-z_pos20;
    z3 = comedi_to_phys(in_data_3, in_range_ptr, in_maxdata);
    z_pos3 = 50e-6+z3*1.01833e-5;
    z_pos30 = z_pos3;
    z_pos3 = z_pos3-z_pos30;


//Hall-effect sensors data
    vc1 = comedi_to_phys(in_data_4, in_range_ptr, in_maxdata);
    vd2 = comedi_to_phys(in_data_5, in_range_ptr, in_maxdata);
    va1 = comedi_to_phys(in_data_6, in_range_ptr, in_maxdata);
```

```
vb1 = comedi_to_phys(in_data_7, in_range_ptr, in_maxdata);
va2 = comedi_to_phys(in_data_8, in_range_ptr, in_maxdata);
vb2 = comedi_to_phys(in_data_9, in_range_ptr, in_maxdata);


zr = 0.527327*z_pos1+0.042158*z_pos2+0.430515*z_pos3;
zr_vol = 0.527327*z1+0.042158*z2+0.430515*z3;
    zr10 = 0.527327*z_pos10+0.042158*z_pos20+0.430515*z_pos30;
//sr = -1.16606*z_pos1+12.7953*z_pos2-11.6294*z_pos3;
//tr = 16.852*z_pos1-16.852*z_pos2;
  if(p==1){printf("%f\n",z_pos10);}
  else if(p==2){printf("%f\n",z_pos20);}
  else if(p==3){printf("%f\n",z_pos30);}
  else if(p==4){printf("%f\n",zr10);}
    else if(p==5){printf("%f %f\n",va1,vb1);}
    else if(p==6){printf("%f %f\n",vc1,vd2);}
    else if(p==7){printf("%f %f\n",va2,vb2);}


t++;
    current_A_1 = 0; current_A_2 = 0; current_A_3 = 0;
        current_B_1 = 0; current_B_2 = 0; current_B_3 = 0;
        current_C_1 = 0; current_C_2 = 0; current_C_3 = 0;


out_data_1 = comedi_from_phys(current_A_1, out_range_ptr, out_maxdata);
out_data_2 = comedi_from_phys(current_A_2, out_range_ptr, out_maxdata);
out_data_3 = comedi_from_phys(current_A_3, out_range_ptr, out_maxdata);
out_data_4 = comedi_from_phys(current_B_1, out_range_ptr, out_maxdata);
out_data_5 = comedi_from_phys(current_B_2, out_range_ptr, out_maxdata);
out_data_6 = comedi_from_phys(current_B_3, out_range_ptr, out_maxdata);
out_data_7 = comedi_from_phys(current_C_1, out_range_ptr, out_maxdata);
out_data_8 = comedi_from_phys(current_C_2, out_range_ptr, out_maxdata);
out_data_9 = comedi_from_phys(current_C_3, out_range_ptr, out_maxdata);
```

```
                    comedi_data_write(it2, out_subdev, out_chan_1, out_range, aref, out_data_1);
                    comedi_data_write(it2, out_subdev, out_chan_2, out_range, aref, out_data_2);
                    comedi_data_write(it2, out_subdev, out_chan_3, out_range, aref, out_data_3);
                    comedi_data_write(it2, out_subdev, out_chan_4, out_range, aref, out_data_4);
                    comedi_data_write(it2, out_subdev, out_chan_5, out_range, aref, out_data_5);
                    comedi_data_write(it2, out_subdev, out_chan_6, out_range, aref, out_data_6);
                    comedi_data_write(it2, out_subdev, out_chan_7, out_range, aref, out_data_7);
                    comedi_data_write(it2, out_subdev, out_chan_8, out_range, aref, out_data_8);
                    comedi_data_write(it2, out_subdev, out_chan_9, out_range, aref, out_data_9);
                    rt_task_wait_period();


                    if(t>30000)
                            break;
            } // while loop close
            } // demo s close


//==   DEMO(s) WHILE LOOP CLOSE


            else if(h=='n')
            {
                    goto answer_no;
            }
                    goto begin;


answer_no:


            out_data_1 = (lsampl_t)2048;
            out_data_2 = (lsampl_t)2048;
            out_data_3 = (lsampl_t)2048;
            out_data_4 = (lsampl_t)2048;
```

```
        out_data_5 = (lsampl_t)2048;
        out_data_6 = (lsampl_t)2048;
        out_data_7 = (lsampl_t)2048;
        out_data_8 = (lsampl_t)2048;
        out_data_9 = (lsampl_t)2048;
        out_data_10= (lsampl_t)2048;


        /*for(i=0;i<20;i++)
        {
                //printf("%d\n",out_data_3);
                comedi_data_write(it2, out_subdev, out_chan_1, out_range, aref,
out_data_1);
                comedi_data_write(it2, out_subdev, out_chan_2, out_range, aref,
out_data_2);
                comedi_data_write(it2, out_subdev, out_chan_3, out_range, aref,
out_data_3);
                comedi_data_write(it2, out_subdev, out_chan_4, out_range, aref,
out_data_4);
                comedi_data_write(it2, out_subdev, out_chan_5, out_range, aref,
out_data_5);
                comedi_data_write(it2, out_subdev, out_chan_6, out_range, aref,
out_data_6);
                comedi_data_write(it2, out_subdev, out_chan_7, out_range, aref,
out_data_7);
                comedi_data_write(it2, out_subdev, out_chan_8, out_range, aref,
out_data_8);
                comedi_data_write(it2, out_subdev, out_chan_9, out_range, aref,
out_data_9);
                comedi_dio_write(it2, out_subdev, out_chan_10, 16);
                rt_task_wait_period();
        }//for loop close*/
```

```c
        //make the process soft real time process
        rt_make_soft_real_time();

        printf("MASTER TASK YIELDS ITSELF\n");
        rt_task_yield();

        printf("MASTER TASK YIELD THE PERIODIC TIMER\n");
        stop_rt_timer();

        printf("MASTER TASK DELETES ITSELF\n");
        rt_task_delete(mtsk);

        comedi_close(it);
        comedi_close(it2);
        fclose(fp1); fclose(fp2); fclose(fp3);

        printf("END MASTER TASK\n");
        printf("%d\n", out_data_1);
        return 0;
}//end of main

void EKF_2(void)
{
        //*********** Extended Kalman filter ***********************

                ytildek[0]=va1;
                ytildek[1]=va2;
                ytildek[2]=0; //theta;
        //gain matriX
                // Hk*Pk*Hk'+Rk=matA matA is symmetric
```

```
for(i=0;i<3;i++){
        for(j=i;j<3;j++){
                matA[i][j]=Pk[i][j]+Rk[i][j];
                matA[j][i]=matA[i][j];
        }
}
// solve for inverse

det=matA[0][0]*matA[1][1]*matA[2][2]+matA[1][0]*matA[2][1]*matA[0][2]+
matA[2][0]*matA[0][1]*matA[1][2]-matA[0][0]*matA[2][1]*matA[1][2]-
matA[2][0]*matA[1][1]*matA[0][2]-matA[1][0]*matA[0][1]*matA[2][2];

        invA[0][0]=(matA[1][1]*matA[2][2]-matA[1][2]*matA[2][1])/det;
        invA[0][1]=(matA[0][2]*matA[2][1]-matA[0][1]*matA[2][2])/det;
        invA[0][2]=(matA[0][1]*matA[1][2]-matA[0][2]*matA[1][1])/det;
        invA[1][1]=(matA[0][0]*matA[2][2]-matA[0][2]*matA[2][0])/det;
        invA[1][2]=(matA[0][2]*matA[1][0]-matA[0][0]*matA[1][2])/det;
        invA[2][2]=(matA[0][0]*matA[1][1]-matA[0][1]*matA[1][0])/det;
        invA[1][0]=invA[0][1];
        invA[2][0]=invA[0][2];
        invA[2][1]=invA[1][2];
        // Pk*Hk' is the left 3 rows of Pk
        // m_times_m(Pk, 9,3,invA,3,3,Kk);
        for(i=0;i<9;i++){
                for(j=0;j<3;j++){
                        Kk[i][j]=0;
                        for(k=0;k<3;k++){
                                Kk[i][j]+=Pk[i][k]*invA[k][j];
                        }
                }
        }
```

```
// update x
    for(i=0;i<9;i++){
        xknew[i]=0;
        for(j=0;j<3;j++){
            xknew[i]+=Kk[i][j]*(ytildek[j]-xk[j]);
        }
            xknew[i]=xknew[i]+xk[i];
    }
        for(i=0;i<9;i++)
            xk[i]=xknew[i];


    // update Pk, Ck is symmetric matrix
        for(i=0;i<9;i++){
            for(j=i;j<9;j++){
                matC[i][j]=0;
                for(k=0;k<3;k++){
                    matC[i][j]+=Kk[i][k]*Pk[k][j];
                }
                matC[j][i]=matC[i][j];
            }
        }
        for(i=0;i<9;i++){
            for(j=i;j<9;j++){
                Pk[i][j]=Pk[i][j]-matC[i][j];
                Pk[j][i]=Pk[i][j];
            }
        }
    // propagation xk
        // m_times_v(Phik,9,9,xk,9,xknew);
        for(i=0;i<9;i++)
            xknew[i]=0;
```

```
xknew[0]=xk[0]+dt*xk[3]+dt22*xk[6];
xknew[1]=xk[1]+dt*xk[4]+dt22*xk[7];
xknew[2]=xk[2]+dt*xk[5]+dt22*xk[8];
xknew[3]=xk[3]+dt*xk[6];
xknew[4]=xk[4]+dt*xk[7];
xknew[5]=xk[5]+dt*xk[8];
xknew[6]=xk[6];
xknew[7]=xk[7];
xknew[8]=xk[8];

for(i=0;i<9;i++)
        xk[i]=xknew[i];

//propagation PK
// Phik*PK*Phik'=Pknew
for(i=0;i<3;i++){
        for(j=i;j<3;j++){

Pknew[i][j]=Pk[i][j]+2*dt*Pk[i][j+3]+dt2*Pk[i][j+6]+dt3*Pk[i+3][j+6]+dt4/4*Pk
[i+6][j+6];

                }
        }
        for(i=0;i<3;i++){
                for(j=i+3;j<6;j++){

Pknew[i][j]=Pk[i][j]+dt*Pk[i][j+3]+1.5*dt2*Pk[i+3][j+3]+dt*Pk[i][j+3]+dt3/2*P
k[i+6][j+3];

                }
        }
        Pknew[1][3]=Pknew[0][4];
```

```
Pknew[2][3]=Pknew[0][5];
Pknew[2][4]=Pknew[1][5];
for(i=0;i<3;i++){
        for(j=i+6;j<9;j++){

Pknew[i][j]=Pk[i][j]+dt*Pk[i+3][j]+dt2*Pk[i+6][j];
        }
}
Pknew[1][6]=Pknew[0][7];
Pknew[2][6]=Pknew[0][8];
Pknew[2][7]=Pknew[1][8];
for(i=3;i<6;i++){
        for(j=i;j<6;j++){

Pknew[i][j]=Pk[i][j]+dt*Pk[i][j+3]+dt2*Pk[i+6][j];
        }
}
for(i=3;i<6;i++){
        for(j=i+3;j<9;j++){
                Pknew[i][j]=Pk[i][j]+dt*Pk[i+3][j];
        }
}
Pknew[4][6]=Pknew[3][7];
Pknew[5][6]=Pknew[3][8];
Pknew[5][7]=Pknew[4][8];
for(i=6;i<9;i++){
        for(j=i;j<9;j++){
                Pknew[i][j]=Pk[i][j];
        }
}
for(i=0;i<9;i++){
```

```
                    for(j=i;j<9;j++){
                            Pknew[j][i]=Pknew[i][j];
                    }
            }

            for(i=0;i<9;i++){
                    for(j=i;j<9;j++){
                            Pk[i][j]=Pknew[i][j]+UpskQkUpskT[i][j];
                            Pk[i][j]=Pk[i][j];
                    }
            }
            va1e=xk[0]; va2e=xk[1]; rr=xk[2];
    }
//sensor_test function
void sensor_test(void)
{
    if(h=='1')
    {
            printf("%f\n",z_pos10);
    }
    else if(h=='2')
    {
            printf("%f\n",z_pos20);
    }
    else if(h=='3')
    {
            printf("%f\n",z_pos30);
    }
    else if(h=='t')
    {
            printf("%f\n",zr10);
```

```
        }
}

void terminate_normally(int signo)
{
        fflush(stdin);

        if(signo==SIGINT ||signo==SIGTERM)
        {
                printf("Terminating the program normally\n");
                out_data_1 = (lsampl_t)2048;
                out_data_2 = (lsampl_t)2048;
                out_data_3 = (lsampl_t)2048;
                out_data_4 = (lsampl_t)2048;
                out_data_5 = (lsampl_t)2048;
                out_data_6 = (lsampl_t)2048;
                out_data_7 = (lsampl_t)2048;
                out_data_8 = (lsampl_t)2048;
                out_data_9 = (lsampl_t)2048;
                out_data_10= (lsampl_t)2048;
                //printf("Sending %d to analog output\n",out_data_3);
                for(i=0;i<20;i++)
                {
                        comedi_data_write(it2, out_subdev, out_chan_1, out_range, aref,
out_data_1);
                        comedi_data_write(it2, out_subdev, out_chan_2, out_range, aref,
out_data_2);
                        comedi_data_write(it2, out_subdev, out_chan_3, out_range, aref,
out_data_3);
                        comedi_data_write(it2, out_subdev, out_chan_4, out_range, aref,
out_data_4);
```

```
                comedi_data_write(it2, out_subdev, out_chan_5, out_range, aref,
out_data_5);
                comedi_data_write(it2, out_subdev, out_chan_6, out_range, aref,
out_data_6);
                comedi_data_write(it2, out_subdev, out_chan_7, out_range, aref,
out_data_7);
                comedi_data_write(it2, out_subdev, out_chan_8, out_range, aref,
out_data_8);
                comedi_data_write(it2, out_subdev, out_chan_9, out_range, aref,
out_data_9);
                comedi_dio_write(it2, out_subdev, out_chan_10,16);
                rt_task_wait_period();
        }

        //make the process soft real time process
        rt_make_soft_real_time();

        printf("MASTER TASK YIELDS ITSELF\n");
        rt_task_yield();

        printf("MASTER TASK STOPS THE PERIODIC TIMER\n");
        stop_rt_timer();

        printf("MASTER TASK DELETES ITSELF\n");
        rt_task_delete(mtsk);

        comedi_close(it);
        comedi_close(it2);

        printf("END MASTER TASK\n");
    }
```

```
        exit(0);
    }
```

MATLAB CODE

LQG COMPENSATOR

```
clear all;

A=[0       0       0       0       0       0       1       0
0;
    0       0       0       0       0       0       0       1
0;
    0       0       0       0       0       0       0       0
1;
    1       0       0       0       0       0       0       0
0;
    0       1       0       0       0       0       0       0
0;
    0       0       1       0       0       0       0       0
0;
    0       0       0       0       0       0       0       0
0;
    0       0       0       0       0       0       0       0
0;];
B=[0                   0                   0;
    0                   0                   0;
    0                   0                   0;
    0                   0                   0;
    0                   0                   0;
    0                   0                   0;
    0                   13                  13.2547;
    13.2547             13.2547             0;
    -117.15             117.15              0];

C=[1 0 0 0 0 0 0 0 0;
    0 1 0 0 0 0 0 0 0;
```

```
   0 0 1 0 0 0 0 0 0];
Q=diag([1e3 1e3 1e3 1e9 1e10 1e10 1e1 1e1 1e1]);

R=eye(3);

psi=5e-6;
thida=5e-6*eye(6);
L=[1 1 1]';

sysC=ss(A_c,B_c,C_c,0);
sysD=c2d(sys_c,0.00125);
[As,Bs,Cs,Ds,Es,Ts]=dssdata(sys_d);

A11=As(1:6,1:6); A12=As(1:6,7:9); A21=As(7:9,1:6);
A22=As(7:9,7:9);
B1=Bs(1:6,1:3);B2=Bs(7:9,1:3);

ob=obsv(A22,A12);
unob=length(A22)-rank(ob)
co=ctrb(As,Bs);
unco=length(As)-rank(co)

Kcs=lqrd(A,B,Q,R,0.00125);
kc2=lqr(A,B,Q,R);

k1=Kcs(1:3,1:6)
k2=Kc(1:3,7:9)

syst=ss(A22,L,A12,0);
[kest,H,P]=kalman(syst,psi,thida);
Hs=H

An=[A11-B1*k1 A12    -B1*k2;
    A21-B2*k1 A22    -B2*k2;
    A21-B2*k1 Hs*A12 A22-Hs*A12-B2*k2];
```

```matlab
Cn=eye(12);
sysn=dss(An,[],Cn,[],eye(12),Ts);


cx=(A22-Hs*A12)*Hs+A21-Hs*A11-(B2-Hs*B1)*(k1+k2*Hs);
cz=(A22-Hs*A12-B2*k2+Hs*B1*k2);
cxz=[cx cz]
opx=-k1-k2*Hs;
opz=-k2;
opxz=[opx opz]
ku=-pinv(Bs)*As


t=0:0.00125:0.5;
x0=[2e-4 5e-4 2e-5 0 0 0 0 0 0 0 0 0]';


[y,t]=initial(sysn,x0,t);


figure(22);
subplot(2,2,1);
plot(t,y(:,7),'-',t,y(:,10),'--');
xlabel('t (s)');ylabel('x-vel (m/s)');


subplot(2,2,2);
plot(t,y(:,8),'-',t,y(:,11),'--');
xlabel('t (s)');ylabel('y-dot (m/s)');


subplot(2,2,3);
plot(t,y(:,9),'-',t,y(:,12),'--');
xlabel('t (s)');ylabel('r-dot (degree/s)');


subplot(2,2,4);
plot(t,y(:,1),'-',t,y(:,2),'--',t,y(:,3),'+');
xlabel('t (s)');ylabel('x, y, r-direction');


figure(3)
```

```
plot(t,y(:,7),'-',t,y(:,10),'--');
xlabel('t (s)');ylabel('x-vel (m/s)');


figure(4)
plot(t,y(:,8),'-',t,y(:,11),'--');
xlabel('t (s)');ylabel('y-dot (m/s)');


figure(5)
plot(t,y(:,9),'-',t,y(:,12),'--');
xlabel('t (s)');ylabel('r-dot (degree/s)');


figure(6)
plot(t,y(:,1),'-',t,y(:,2),'--',t,y(:,3),'+');
xlabel('t (s)');ylabel('x, y, r-direction');
```

VITA

The author, Ho Yu, was born in Seoul, Korea. He graduated from Hanyang University, Seoul, Korea with the Bachelor of Engineering degree in mechanical engineering in February 2003. After that, he received his masters degree from Texas A&M University in August 2005 in mechanical engineering. He received his Ph.D. degree at Texas A&M University in August 2009. His dissertation advisor was Dr. Won-jong Kim in the Mechanical Engineering Department.

His permanent address is:

       Dongangu Pyongchon life 108-602

       Kyonggi Anyang, Korea, 431-070

His e-mail address is:

       jameskaten@gmail.com